MECHANICAL RESPONSES OF ENGINEERING MATERIALS AND LITHIUM-ION BATTERIES UNDER COMPRESSION, INDENTATION AND ROLLING WITH EXTENSIVE PLASTIC DEFORMATION

by

Mohammed Yusuf Ali

A dissertation submitted in partial fulfillment
of the requirements for the degree of
Doctor of Philosophy
(Mechanical Engineering)
in the University of Michigan
2013

Doctoral Committee:

Professor Jwo Pan, Chair
Professor Will Hansen
Professor Katsuo Kurabayashi
Associate Professor Wei Lu
Jagadish Sorab, Ford Motor Co.

Dedication

To my wife. To our family: past, present, and future.

Acknowledgements

I would like to express my sincere appreciation and gratitude to Professor Jwo Pan for his constant guidance, encouragement, support and unlimited patience throughout this research work. His intellectual support at various stages of this work has been invaluable in enabling me to carry this work to completion. I would like to thank my doctoral committee Professor Will Hansen, Professor Katsuo Kurabayashi, Professor Wei Lu and Dr. Jagadish Sorab of Ford Motor Company for their guidance and valuable suggestions. I also thank the academic support staff at the Department of Mechanical Engineering for their invaluable assistance at various stages.

I am very grateful to Dr. Petr Michlik of Caterpillar Inc. for providing the experimental data on bar rolling and helpful suggestions. I would like to thank William Lai of University of Michigan for the experimental results in chapters 5 and 6 which would not have been possible without his contributions. I express my well wishes to Dr. Kyoo-Sil Choi, Dr. Kamran Asim, Dr. Jaewon Lee, Dr. Kulthilda Sripichai, Catherine Amodeo, Teresa Franklin, Katherine Avery and Seung Hoon Hong.

Helpful discussions with Dr. Simon Ho, Yibing Shi, Guy Nusholtz, and Ronald Elder of Chrysler, Saeed Barbat, Bill Stanko, Mark Mehall and Tau Tyan of Ford, Jenne-Tai Wang, Ravi Nayak, Kris Yalamanchili and Stephen Harris of GM, Christopher Orendorff of Sandia National Laboratory, Seung-Hoon Hong of University of Michigan, and Natalie Olds of USCAR are greatly appreciated.

I would like to express my special thanks and gratitude to Rick Renwick, Chief Engineer and Dr. Jagadish Sorab, Technical Leader of Ford Motor Company for their generous support and help. I am very grateful to Ford Motor Company for providing the financial support to complete the academic and research work. I would like to thank Jeffrey Chottiner and Dr. Misha Ejakov for their valuable suggestions. I am also thankful to my management at Ford Motor Company - Dr. Raymond Kach, Barb Kaput, Dr. C. Jerry Hsieh, Dr. Kristofor Norman, Jeffrey Bautz, and Steve Wilkie for their support at various stages of this endeavor.

Finally, I would like to offer my deepest thanks to my wife, Mahbuba, for her love and incredible support during this unique period. To my wife, and my wonderful son, Ayan, - your sacrifice, patience and moral support have made this dissertation possible. I wish to express my love and gratitude to our family and thanks to all my friends for their encouragement at all times.

Table of Contents

List of Figures

List of Tables

Chapter 1
Introduction

The challenge for the automotive industry is to reduce engine weight and increase the fuel economy in response to changes in federal regulations and to address environmental concerns. For high power density, fuel efficient engine, the weight can be improved by a robust design procedure for crankshafts with high fatigue resistance. Deep fillet rolling has been used for years to introduce compressive residual stresses near crankshaft fillets and, consequently, to improve fatigue strengths of the crankshafts. Deep rolling or burnishing is also applied to achieve dimensional tolerances and improved fatigue strength for large casting components. Therefore, understanding the residual stress distributions due to rolling at high rolling loads is very important.

This dissertation systematically investigates mechanical responses of engineering materials under very large contact pressure and lithium-ion batteries under compression with extensive plastic deformation. Chapters 2, 3 and 4 are related to understanding the physics and the resulting residual stresses due to indentation and rolling at very high loads for different configurations. Chapters 5 and 6 are related to understanding the deformation of cells and modules of lithium-ion batteries under compression loads.

Chapter 2 represents a paper on residual stresses due to indentation and rolling at high rolling loads under plane strain conditions. This investigation is aimed to quantify the differences between the residual stresses distributions due to single indentation and

rolling with very large contact pressure. The rolling model and its boundary conditions selected for this study are to identify whether the results of the finite element analyses for single indentation of crankshaft sections conducted by previous researchers are sufficient to represent the residual stresses distribution for further strength/fatigue analyses by comparing the stresses in the rolling and the out-of-plane directions. While a three-dimensional finite element analysis is more appropriate to calculate the residual stresses due to rolling, a two-dimensional model is useful for the initial design iterations.

In this chapter, the elastic Hertzian solution for contact of two elastic cylinders is first reviewed. A crankshaft fillet rolling process along the circumference of the main journal is idealized to a two-dimensional flat plate plane strain rolling model with appropriate boundary conditions. The roller is assumed to be rigid and the contact between the roller and the plate is frictionless. The roller load per unit width for the two-dimensional model is based on that for the corresponding three-dimensional finite element analysis for single indentation. Then, the elastic plane strain finite element analysis of single indentation on a flat plate is carried out. For this case, the plate is modeled as linear elastic. The results of the elastic finite element analysis are then compared with that of the elastic Hertzian solutions in order to establish the guideline for development of the finite element model for acceptable contact pressure and subsurface stress distributions. Next, the plate material is modeled as an elastic-plastic power-law strain hardening material with the non-linear kinematic hardening rule of ABAQUS for loading and unloading. An elastic-plastic plane strain finite element analyses of single indentation on a flat plate are carried out for the development of the computational model for rolling simulation. A single pass rolling is simulated. Then, the results of elastic-

plastic plane strain finite element analyses of single indentation and rolling are presented and compared. The plastic zone development and the residual stress distributions on the plate upper surface and in the subsurface under the roller center induced by the single indentation and the rolling are also presented and compared. In addition, the effects of the boundary conditions on the residual stresses are presented.

Chapter 3 represents a paper on effect of a deformable roller on residual stress distribution for elastic-plastic flat plate rolling under plane strain conditions. This investigation is aimed to quantify the differences between the residual stress distributions in an elastic-plastic plate due to single indentation and rolling by rigid and elastic rollers with a very large contact pressure. More importantly, the advantages of using a rigid roller instead of an elastic roller give the convenience of applying the roller load with a smaller model size. Both conditions of indentation and rolling are selected for this study to identify whether a rigid roller model can be used to replace an elastic roller model for rolling simulations at very high rolling loads with a sufficient accuracy to obtain the residual stresses distribution for further fatigue strength analyses. A two-dimensional model is chosen here to save computational effort.

Chapter 4 represents a paper on effects of high rolling loads on residual stress distributions in a rectangular bar of gray cast iron. In this paper, the details of the results of finite element analyses for a roll burnishing experiment conducted at Caterpillar are presented. It is important to realize that compressive residual stresses are largely dependent on the rolling loads, component material and boundary conditions. The current investigation is aimed to quantify the differences between the residual stresses distributions in a finite rectangular bar due to very large contact pressures from two

different rolling loads. The rolling parameters for this investigation includes smaller roller radius, high rolling loads (with p_0/k ratio of about 12.5 to 15 with the rigid roller assumption), and finite rectangular bar dimensions. Therefore, a thorough investigation is required to understand the residual stresses due to rolling using three-dimensional finite element analyses. In this paper, a three-dimensional prismatic bar with a rectangular cross section is used for rolling simulations with the appropriate boundary conditions. The roller is assumed to be rigid and the roller rolls on the flat surface of the bar with a low coefficient of friction. The bar material is modeled as an elastic-plastic strain hardening material with a non-linear kinematic hardening rule of ABAQUS for loading and unloading. Effects of the two rolling loads with the material data variability are investigated. A single pass rolling is simulated. The longitudinal residual stress distributions in the bar along the width and the thickness directions are compared for both rolling loads. Also, the longitudinal residual stress distributions in the vertical direction (thickness) are then compared with the measurement data.

In recent years the automotive industry is transitioning from cars and trucks powered primarily by petroleum to vehicles powered by electricity. Lithium-ion batteries have been considered as the solution for electric vehicles for the automotive industry due to its lightweight and high energy density. The major design considerations of the lithium-ion batteries involve electrochemistry, thermal management and mechanical performance. Other than dealing with the multi-physics problem, one of the challenges of developing the computational models for the battery behavior is the length scale. Therefore, understanding the basic mechanical behavior of the lithium-ion batteries for automotive applications is very important to develop homogenized models based on

representative volume elements (RVEs) that are needed for efficient crashworthiness analyses.

Chapter 5 represents a paper on computational models for simulations of lithium-ion battery cells under constrained compression tests. This investigation is focused on developing the computational models for simulations of RVE specimens of lithium-ion battery cells under in-plane constrained compression tests and then comparing the computational results with those of the tests. Two approaches are used for the modeling of these battery cells and modules: a detailed model (micro approach) and a less detailed model (macro approach). This investigation will focus on the detailed modeling of a cell RVE specimen of lithium-ion batteries. In the detailed model, the pouch cell battery is modeled as a layered composite and the RVE material nominal stress-strain response is obtained based on the properties of the cell components of layered anode, cathode, separator and active sheets. The less detailed models were investigated in chapter 6. In those less detailed models, a small-scale battery module was considered as a homogenized material based on the response of the physical testing of the module RVE specimens. Both approaches are useful to investigate the mechanical behavior of lithium-ion pouch cell batteries and modules.

The purpose of this detailed model investigation is twofold: one is to enhance understanding of the mechanical behavior of lithium-ion battery cells used for automotive applications and the other is to pave the groundwork for the development of user material models to represent the battery cells and modules by homogenized materials which are a subject of the future research. In this paper, the compressive behavior of cell RVE specimens under quasi-static in-plane compression tests is investigated using the

ABAQUS explicit finite element solver. The experimental results for cell RVE specimens under in-plane compression tests are first reviewed briefly for understanding the physical deformation pattern of the porous cell RVE specimens. Next, the Gurson's model for porous material is presented for characterization of the separator and the electrodes with the active materials. Then the available material data are discussed and adopted for the input of the computational model. The details of the computational model are presented. The computational results of the deformation pattern and nominal stress-strain behavior are then compared with the test results. Based on the computational model, the effects of the friction coefficient between the cell components and the constrained surfaces on the deformation pattern, plastic deformation, void compaction, and the load-displacement curve are examined. The usefulness of the computational model is then presented by further exploring the effects of the initial clearance and biaxial compression on the deformation patterns of cell RVE specimens.

Chapter 6 represents a paper on computational models for simulation of a lithium-ion battery module specimen under punch indentation. In this investigation, less detailed macro homogenized material models are adopted to simulate a small-scale module specimen under the punch test. Here, the test data of module RVE specimens were used to calibrate the inputs of the hyperfoam and crushable compressible foam models available in commercial finite element code ABAQUS for the punch test simulation. The computational results of the load-displacement responses of the punch test are then compared with the experimental results.

Chapter 2
Residual Stresses due to Indentation and Rolling at High Rolling Loads under Plane Strain Conditions

2.1. Introduction

For automotive crankshafts, fatigue damages are initiated near the fillets due to stress concentration. The fillet rolling process has been used for years to introduce compressive residual stresses near crankshaft fillets and, consequently, to improve fatigue strengths of crankshafts [1-3]. During the rolling process, the material near the roller is loaded into plastic range. Once the rolling load is removed, compressive residual stresses are induced. The residual stresses can significantly affect the fatigue lives of the crankshafts under high cycle fatigue loading conditions. Therefore, understanding the residual stresses near crankshaft fillets are important. Previously, researchers estimated the residual stresses near crankshaft fillets either using two-dimensional or three-dimensional finite element analyses [2-8]. Chien et al. [4] conducted two-dimensional elastic-plastic finite element analyses of crankshaft fillet rolling to estimate the residual stresses. They also investigated the behavior of crack initiation and growth near crankshaft fillets with consideration of residual stresses based on linear elastic fracture mechanics. Chien et al. [4] used the rolling depth of crankshaft fillets after the unloading of the roller as the calibration parameter in their two-dimensional finite element analyses. The rolling depth was determined by the fillet surface profiles obtained from the shadowgraphs taken before and after the fillet rolling process. Spiteri et al. [2] examined

the bending fatigue limit of crankshaft sections with consideration of residual stresses based on the results of three-dimensional finite element analyses. Most of the previous analyses for the fatigue behavior of crankshaft sections are based on the residual stresses from single indentation of rollers. Spiteri et al. [2] showed the subsurface axial stress distributions due to single indentation and rolling of a disk based on plane strain finite element analyses. However, the effects of single indentation and rolling on the circumferential and out-of-plane stress components have not been explained in details.

Numerous studies were conducted to understand the stress distributions and deformation patterns near rolling contact surfaces. Researchers mainly conducted indentation and rolling contact analyses to examine the stress-strain histories near the contact surfaces. Some of the previous elastic-plastic analyses were on the indentation of elastic-plastic half spaces using rigid spheres. Mesarovic and Fleck [9] conducted finite element analyses of the normal indentation of an elastic-plastic half-space by a rigid sphere. Indentation maps were constructed with axes of contact radius a (normalized by the indenter radius R) and the yield strain of the half-space. Kral et al. [10] investigated the elastic-plastic contact problem of a rigid sphere indentation of a homogeneous half-space using finite element analyses. The rigid sphere with a radius of 1.5 mm was modeled by contact elements. The results for the contact pressure, surface and subsurface stresses, initiation and growth of the plastic zone, and yielding of the half-space during unloading were presented. The results for the indentations with loads up to 300 times the load necessary for the initial yield were obtained on materials with different elastic and plastic properties. It was shown that the resulting pressure distributions are significantly different from the Hertzian pressure distribution. Komvopoulos [11]

analyzed the plane-strain indentation of a layered half-space by a rigid cylinder using contact elements instead of an assumed distribution of the surface tractions or the displacements on the contact surface. It was shown that the pressure distribution is considerably different from the Hertzian pressure distribution, particularly for stiff and relatively thick layers and/or under large plastic deformation.

Several previous elastic-plastic analyses of rolling were based on translating a Hertzian [12-16] or modified Hertzian pressure distribution [17,18] across the surface of an elastic-plastic half space. Merwin and Johnson [12] analyzed the plane-strain rolling of a rigid cylinder on a half-space. Bhargava et al. [17,18] conducted finite element analyses to investigate the plane-strain problem of a cylinder rolling on a semi-infinite body, both for single and multiple passes. They assumed elastic-plastic linear kinematic hardening material behavior and represented the cylinder by a translating Hertzian or modified Hertzian pressure distribution for a maximum p_0/k ratio of 5, where p_0 is the maximum Hertzian pressure and k is the shear yield stress of the material (see Merwin and Johnson [12] and Bhargava et al. [17] for the bounds of characteristic deformation regimes). Yu et al. [15,16] presented an analytical method for elastic-plastic rolling contact and shakedown, and demonstrated its application to obtain steady-state solutions for two- and three-dimensional repeated rolling contact problems. They used a moving Hertzian pressure distribution to simulate the rolling process for a maximum p_0/k ratio of 6. Chen et al. [19] presented a three-dimensional numerical model for simulating the repeated rolling or sliding contact of a rigid sphere over an elastic-plastic half-space for a p_0/k ratio of 5.2. Jiang and Sehitoglu [20] analyzed the residual stresses for the line rolling contact problems utilizing an analytical approach in conjunction with a new

plasticity model for p_0/k ratios ranging from 5 to 9. Jiang et al. [21] also conducted three-dimensional elastic-plastic rolling analyses incorporating elastic and plastic shakedown concepts for a p_0/k ratio of 6. For both cases, a prescribed Hertzian pressure distribution was traversed over the surface to simulate the loading history experienced by a wheel and rail.

Most researchers used the moving Hertzian pressure distribution to represent the contact pressure for rolling with p_0/k ratios ranging from 5 to 9. Bijak-Zochowski and Marek [22] used elastic rollers with spring contact elements for rolling simulations. They modeled the process of a cylinder running on the strip by finite element analyses, using a program SEGLA developed by the authors. Their work gives good insight on the residual stress distribution in the strip due to rolling. However, the results were obtained for a relatively large wheel radius (R = 457 mm) and the normal force corresponding to the average load values of the train wheel on the track, giving a p_0/k ratio of 4. For the crankshaft rolling, the roller radius is much smaller and the rolling load is high, with a p_0/k ratio of about 22.

This investigation is aimed to quantify the differences between the residual stresses distributions due to single indentation and rolling with very large contact pressure. The rolling model and its boundary conditions selected for this study are to identify whether the results of the finite element analyses for single indentation of crankshaft sections conducted by previous researchers are sufficient to represent the residual stresses distribution for further strength/fatigue analyses by comparing the stresses in the rolling and the out-of-plane directions. While a three-dimensional finite

element analysis is more appropriate to calculate the residual stresses due to rolling, a two-dimensional model is useful for the initial design iterations.

In this paper, the elastic Hertzian solution for contact of two elastic cylinders is first reviewed. A crankshaft fillet rolling process along the circumference of the main journal is idealized to a two-dimensional flat plate plane strain rolling model with appropriate boundary conditions. The roller is assumed to be rigid and the contact between the roller and the plate is frictionless. The roller load per unit width for the two-dimensional model is based on that for the corresponding three-dimensional finite element analysis for single indentation. Then, the elastic plane strain finite element analysis of single indentation on a flat plate is carried out. For this case, the plate is modeled as linear elastic. The results of the elastic finite element analysis are then compared with that of the elastic Hertzian solutions in order to establish the guideline for development of the finite element model for acceptable contact pressure and subsurface stress distributions. Next, the plate material is modeled as an elastic-plastic power-law strain hardening material with the non-linear kinematic hardening rule of ABAQUS [23] for loading and unloading. An elastic-plastic plane strain finite element analyses of single indentation on a flat plate are carried out for the development of the computational model for rolling simulation. A single pass rolling is simulated. Then, the results of elastic-plastic plane strain finite element analyses of single indentation and rolling are presented and compared. The plastic zone development and the residual stress distributions on the plate upper surface and in the subsurface under the roller center induced by the single indentation and the rolling are also presented and compared. In

addition, the effects of the boundary conditions on the residual stresses are presented. Finally, some conclusions will be made based on the results of this investigation.

2.2. Preliminaries on elastic Hertzian solutions and elastic finite element analyses

Consider two infinitely long cylinders with their longitudinal axes both lying parallel are pressed in contact by a force P per unit length as schematically shown in Figure 2.1(a). The Cartesian coordinates are also shown. The two cylinders make contact over a long strip of width $2a$ lying parallel to their axes as shown in Figure 2.1(a). The expressions for the load P, the half contact width a and the pressure $p(x)$ are [24]:

$$P = \frac{\pi a^2 E^*}{4R} \tag{2.1}$$

$$a^2 = \frac{4PR}{\pi E^*} \tag{2.2}$$

where

$$E^* \equiv \left(\frac{1-\nu_1^{\,2}}{E_1} + \frac{1-\nu_2^{\,2}}{E_2} \right)^{-1}$$

and

$$R \equiv \left(\frac{1}{R_1} + \frac{1}{R_2} \right)^{-1}$$

Here, E represents the modulus of elasticity, ν represents the Poisson's ratio, and R represents the radius. The subscripts 1 and 2 represent the upper and lower cylinders, respectively.

The contact pressure distribution is

$$p(x) = \frac{2P}{\pi a^2}\left(a^2 - x^2\right)^{\frac{1}{2}} \tag{2.3}$$

The maximum pressure is expressed as

$$p_0 = \frac{2P}{\pi a} = \left(\frac{PE^*}{\pi R}\right)^{1/2} \tag{2.4}$$

The stresses at a point (x, y) are [24]

$$\sigma_{11} = -\frac{p_0}{a}\left\{m\left(1 + \frac{y^2 + n^2}{m^2 + n^2}\right) - 2y\right\} \tag{2.5}$$

$$\sigma_{22} = -\frac{p_0}{a} m\left(1 - \frac{y^2 + n^2}{m^2 + n^2}\right) \tag{2.6}$$

$$\sigma_{12} = -\frac{p_0}{a} n\left(\frac{m^2 - y^2}{m^2 + n^2}\right) \tag{2.7}$$

where

$$m^2 = \frac{1}{2}\left[\left\{(a^2 - x^2 + y^2)^2 + 4x^2y^2\right\}^{1/2} + (a^2 - x^2 + y^2)\right] \tag{2.8}$$

$$n^2 = \frac{1}{2}\left[\left\{(a^2 - x^2 + y^2)^2 + 4x^2y^2\right\}^{1/2} - (a^2 - x^2 + y^2)\right] \tag{2.9}$$

and the signs of m and n are the same as the signs of y and x, respectively.

Under plane strain conditions, the third principal stress σ_{33} is

$$\sigma_{33} = \nu(\sigma_{11} + \sigma_{22}) \tag{2.10}$$

The von Mises stress is expressed as a function of the stress components as

$$\sigma_{Mises} = \frac{1}{\sqrt{2}}\sqrt{(\sigma_{11} - \sigma_{22})^2 + (\sigma_{22} - \sigma_{33})^2 + (\sigma_{33} - \sigma_{11})^2 + 6\sigma_{12}^2} \tag{2.11}$$

The stresses in equations (2.5)-(2.7), (2.10) and (2.11) based on the elastic Hertzian solution will be plotted in Figures 2.7(a) and 2.7(b) as discussed later. When the radius

R_2 of the lower cylinder becomes infinity, the lower cylinder becomes a semi-infinite solid which is schematically represented by a flat plate as shown in Figure 2.1(b). When the elastic modulus E_1 of the upper roller becomes infinity, the roller becomes rigid. This corresponds to the case of an elastic flat plate indented by a rigid roller as shown in Figure 2.1(c). The elastic Hertzian solutions presented in this section will be used to benchmark the elastic finite element analyses that will be discussed later. The Young's modulus E_2 is set for 207 GPa and the Poisson's ratio ν_2 is set for 0.29 for typical steel crankshaft materials.

2.3. Material model

A Typical steel for crankshafts is considered for the plate. The steel has the Young's modulus of 207 GPa and the Poisson's ratio of 0.29. The tensile stress-strain curve of the steel is shown in Figure 2.2. The nonlinear kinematic hardening rule of the ABAQUS is assumed based on the tensile stress-plastic strain curve shown in Figure 2.2. The nonlinear kinematic hardening rule in ABAQUS is based on the Mises yield function. For the loading/unloading/reloading process, the yield function can be expressed as

$$f\left(\sigma_{ij}-\alpha_{ij},\sigma^0\right)=\left[\frac{3}{2}\left(\sigma'_{ij}-\alpha'_{ij}\right)\left(\sigma'_{ij}-\alpha'_{ij}\right)\right]^{\frac{1}{2}}-\sigma^0=0 \tag{2.12}$$

where σ_{ij} is the stress tensor, σ'_{ij} is the deviatoric stress tensor, α_{ij} represents the center of the yield surface, α'_{ij} is the deviatoric part of α_{ij}, and σ^0 represents the size of the yield surface. Here, σ'_{ij} and α'_{ij} are defined, respectively, as

$$\sigma'_{ij} = \sigma_{ij} - \frac{1}{3}\sigma_{kk}\delta_{ij} \tag{2.13}$$

$$\alpha'_{ij} = \alpha_{ij} - \frac{1}{3}\alpha_{kk}\delta_{ij} \tag{2.14}$$

where δ_{ij} is the kronecker delta.

The associated plastic flow is expressed as

$$\dot{\varepsilon}^p_{ij} = \dot{\bar{\varepsilon}}^p \frac{\partial f\left(\sigma_{ij} - \alpha_{ij}, \sigma^0\right)}{\partial \sigma_{ij}} \tag{2.15}$$

where $\dot{\varepsilon}^p_{ij}$ represents the plastic strain rate tensor and $\dot{\bar{\varepsilon}}^p$ is the equivalent plastic strain rate defined as

$$\dot{\bar{\varepsilon}}^p = \left(\frac{2}{3}\dot{\varepsilon}^p_{ij}\dot{\varepsilon}^p_{ij}\right)^{\frac{1}{2}} \tag{2.16}$$

In ABAQUS, the nonlinear kinematic hardening rule is defined to be an additive combination of a purely kinematic term of the Ziegler linear hardening law and a relaxation term which introduces the nonlinearity. The evolution of α_{ij} is expressed as

$$\dot{\alpha}_{ij} = \frac{C}{\sigma_0}\dot{\bar{\varepsilon}}^p\left(\sigma_{ij} - \alpha_{ij}\right) - \gamma\dot{\bar{\varepsilon}}^p\alpha_{ij} \tag{2.17}$$

where σ_0 is constant and represents the size of the initial yield surface, α_{ij} represents the center of the yield surface, $\dot{\bar{\varepsilon}}^p$ is again the equivalent plastic strain rate, and C and γ are material parameters that must be calibrated from cyclic test data. Here, C is the initial kinematic hardening modulus and γ determines the rate at which the kinematic hardening modulus decreases with increasing plastic deformation. When C and γ are zero, the model reduces to the isotropic hardening rule. When γ is zero, the Ziegler linear hardening law is recovered. Note that, for the nonlinear kinematic hardening rule of ABAQUS, the option of "HALF CYCLE" for data type was adopted in order to use the cyclic stress-strain curve of the material as the input stress-strain data [23].

2.4. Rolling load

The crankshaft rolling process of interest involves 12 rotations of a crankshaft in a rolling machine. For example, Figure 2.3(a) shows an actual rolling load history for the crankshaft fillet rolling where the load is increased linearly up to the full rolling load for the first 3 rotations of the crankshaft. The load is then kept as a constant level for the next 6 rotations. Finally, the load is decreased linearly to zero for the final 3 rotations. However, in this investigation, only one pass of the rolling load is applied as shown in Figure 2.3(b). The full rolling load for the crankshaft fillet rolling is assumed to be 5700 N applied to the primary roller with the direction that is 34^o inclined from the vertical direction. The details of the geometric arrangement of the primary and secondary rollers and crankshafts can be found in [3]. The details to convert the 5700 N load for the crankshaft fillet rolling to the load per unit thickness for plane strain plate rolling are

outlined in Appendix A. After the conversion, a load per unit thickness of 3847.0 (N/mm) was used in the plane strain plate rolling model as the roller load for single indentation and rolling.

2.5. Computational model development for indentation and rolling

Figure 2.4 shows a schematic of a two-dimensional model of a flat plate rolling process. The roller is assumed to be rigid and the contact between the roller and the plate is frictionless. Figure 2.4 shows the phases of the rolling simulation. Initially, the roller is sitting on the starting position of the flat plate. Then the roller is moved down with a given load. The roller is then rolled horizontally to the right. After traveling the full rolling length, the roller is moved up and the rolling is completed.

The finite element analyses were performed using the commercial finite element code ABAQUS. Figure 2.5(a) shows a two-dimensional finite element model of a rigid cylinder rolling on a finite flat plate. The Cartesian coordinate system is also shown in the figure. Two-dimensional plane strain 4-noded CPE4R elements of size 0.4 mm by 0.4 mm are used in this model. The selection of the sizes of the finite elements to simulate single indentation and rolling follows the guidelines that will be presented later. The bottom of the plate is fixed, and the displacements on both end surfaces AB and CD of the plate in the x direction are constrained. The length of the plate is 300 mm with the rolling start point on the upper surface at x = 62 mm and the rolling end point at x = 216.264 mm to eliminate possible end effects. One goal of this investigation is to use the results obtained here to examine the residual stresses in crankshafts after fillet rolling. The diameter of the rigid cylinder is 14 mm which represent the radius of the primary

roller for the crankshaft rolling as discussed in Appendix A. The total rolling length 154.264 mm and the plate thickness 24.552 mm are corresponding to the circumferential length and the radius of the main journal of a crankshaft of interest, respectively. The primary roller is modeled as the rigid cylinder.

2.5.1 Mesh sensitivity for elastic finite element analyses

For elastic contact analyses, two finite element models are developed. The finite element model Mesh-1 has the element size of 0.4 mm and the finite element model Mesh-2 has element size of 0.1 mm. Magnified views of the finite element models for Mesh-1 and Mesh-2 are shown in Figures 2.5(b) and 2.5(c), respectively. The results based on the finite element model Mesh-2 showed better correlations with the elastic Hertzian solutions presented here. Figure 2.6 shows a comparison of the contact widths ($2a$) between the flat plate and the rigid roller obtained by the elastic Hertzian solution and the elastic finite element analysis as a function of the indentation load up to the maximum value of 3847 N/mm used in this investigation. As the indentation proceeds with the increasing load, the indentation depth increases. However, until the next node makes contact, the contact width ($2a$) remains the same in the elastic finite element analysis.

Figure 2.7(a) shows the distributions of the stresses directly under the roller in the –y direction from the top surface of the plate for indentation by the rigid roller at the full rolling load of 3847 N/mm. It should be mentioned again that the plate is modeled to be linear elastic. Figure 2.7(b) is a zoom-in view of Figure 2.7(a) to show the stresses for the top 5 mm of the plate. For the elastic Hertzian solution, at the contact interface σ_{11}

$= \sigma_{22} = -p(x)$. At the contact point, the values of the stresses σ_{11} and σ_{22} obtained from the finite element analysis are 23% and 11% lower than the elastic Hertzian solution. This may be attributed to the mesh discretization [9]. Beyond the contact surface, the stress σ_{22} obtained from the finite element analysis is within 3% of the elastic Hertzian solution. The shear stress component σ_{12} should be zero directly under the roller center. However, the stresses are obtained from the nodal points which are not exactly under the center of the roller. Therefore, very small values of σ_{12} are shown in Figures 2.7(a) and 2.7(b) due to a small offset of these nodal points from the centerline of the roller. Accordingly, the elastic Hertzian solutions based on the appropriate value of the x coordinate for these nodal points are also plotted in Figures 2.7(a) and 2.7(b) for comparison. However, at the contact point, the values of the stresses σ_{11} and σ_{22} obtained from the finite element analysis based on Mesh-1, are 68% and 43% lower than the elastic Hertzian solution. Thus with the element size of 0.1 mm finite element model Mesh-2 is found reasonable for the elastic single indentation with the given high indentation load. Figure 2.8 shows the contact pressure distributions on the plate surface based on the elastic Hertzian solution and the results of the elastic finite element analysis due to indentation by the rigid roller based on the finite element model Mesh-2 with the element size of 0.1 mm at the load of 3847 N/mm. The contact pressure distribution obtained by the elastic finite element analysis is in good agreement with the elastic Hertzian solution except near the boundary of the contact region due to the mesh discretization [9]. It should be noted that for the elastic finite element analysis the results based on both linear element CPE4 and CPE4R were identical. Based on this parametric study of the contact stress distribution at the different load levels, it is suggested that for

the linear element CPE4 or CPE4R, a total of four to five finite elements for the half contact width are needed to obtain acceptable contact pressure and subsurface stress distributions.

2.5.2. Mesh sensitivity for elastic-plastic finite element analyses

Similar to the elastic finite element analyses, a mesh sensitivity study was conducted for simulation of the rigid cylinder indenting on the elastic-plastic finite plate. The finite element models Mesh-1 and Mesh-2 with the element sizes of 0.4 mm and 0.1 mm are again used in this study. The results based on Mesh-1 and Mesh-2 are compared. Figure 2.9(a) shows the contact pressure distributions for both Mesh-1 and Mesh-2. The elastic Hertzian solution is also shown for reference. As shown in the figure, the contact pressure distributions for both Mesh-1 and Mesh-2 are in agreement with each other except near the boundary of the contact region due to the differences in mesh size and the differences of the area under the curve is within 9%. For mesh-1 there are four contact elements for the half contact width. Figure 2.9(b) shows the displacement components u_1 and u_2 of the upper surface nodes and Figure 2.9(c) shows the stress distributions directly under the roller center in the –y direction from the top surface of the elastic-plastic plate when the roller is down for the cases of Mesh-1 and Mesh-2. For the indentation, the peak values of the compressive stress components σ_{11}, σ_{22} and σ_{33} occur at the contact surface directly under the roller center. With the value of the stress component σ_{33} is in between the stress components σ_{11} and σ_{22}, the distributions of σ_{11}, σ_{22} and σ_{33} are nearly parallel until the end of the plastic zone. Figure 2.9(d) shows a

comparison of the residual stresses distributions in the –y direction from the top surface of the plate for both Mesh-1 and Mesh-2 after the roller load for single indentation is removed. The results based on Mesh-1 and Mesh-2 show that the subsurface stresses and residual stresses based on both meshes were in good agreement except the stresses on the contact surface with acceptable differences. For the elastic-plastic plate material, as the load increases and the material under the contact surface becomes plastic, the material acts much softer and the contact width increases. Therefore, more nodes come in contact with the roller and the contact load is distributed to more elements. Therefore, Mesh-1 can give reasonable contact pressure and subsurface stress distributions and was used for the subsequent rolling simulation for saving computational time. It seems that the guideline of four linear elements for half contact width is still applicable to the elastic-plastic finite element analyses.

2.6. Stress distributions due to plate rolling

Based on the coarse Mesh-1, the entire rolling simulation is carried out. However, many computational results presented are based on the fine Mesh-2. Figure 2.10(a) shows the Mises stress distribution and the plastic zone size and shape as the roller is moved down at the full rolling load of 3847 N/mm based on Mesh-1. The inner area of the lightest contour line represents the material that is yielded and hence the lightest contour line represents the plastic zone size and shape. The total contact width is about $6a$ for the rolling. As the rolling continues, the Mises stress contours reaches almost a steady state at a distance of nearly $6.5a$ from the start point, as compared to $6.4a$ obtained by Bhagava et al. [17] and the steady state plastic zone extends to

approximately $5a$. Here, a is the half contact width based on the elastic Hertzian theory of contact. For the given roller radius, the half contact width a is obtained as 0.3895 mm. Figure 2.10(b) shows the Mises stress contours and plastic zone size and shape when the roller is rolled to the half rolling length. Figure 2.10(c) shows the Mises stress contours and plastic zone size and shape after the roller is moved up and the rolling is completed.

Figure 2.11(a) shows again the displacement components u_1 and u_2 of the upper surface nodes when the roller is moved down at the full applied rolling load based on the coarse Mesh-1. The displacement component u_1 is asymmetric with respect to the center of the roller contact area and has negative and positive values behind and in front of the center of the roller contact area, respectively. The displacement component u_2 is negative and symmetric with respect to the center of the roller contact area. Figure 2.11(b) shows the residual displacement components u_1 and u_2 of the upper surface nodes after the rolling is completed based on the coarse Mesh-1. As the rolling progresses, the residual values of the displacement component u_1 of the upper surface nodes between the start and end points increase as shown in Figure 2.11(b). This indicates that plastic deformation continues to accumulate along the rolling direction of the rolled surface. On the other hand, the residual values of the displacement component u_2 between the start and end points are quite stable as shown in Figure 2.11(b). Three nodes are selected on the plate surface as shown in Figure 2.12(a) and the histories of the nodal displacement components of u_1 and u_2 of these nodes are plotted in Figures

2.12(b) and 2.12(c), respectively. The plot also confirms that the displacement component u_2 is stable throughout the rolling process.

Figure 2.13(a) shows again the contact pressure distribution between the roller and the plate due to single indentation based on the fine Mesh-2 and the elastic-plastic finite element analysis at the maximum load of 3847 N/mm. The elastic Hertzian solution is also plotted for comparison. The results of the elastic-plastic finite element analysis shows that the contact pressure distribution is no longer Hertzian pressure distribution but rather flatter and wider, and they are in general agreement with the findings of Kral et al. [10] and Komvopoulos [11]. This is due to the subsurface plastic flow that leads to a flatter and wider pressure distribution. Figure 2.13(b) shows a representative contact pressure distribution between the roller and the plate during rolling after the steady state of the contact pressure distribution based on the fine Mesh-2 is reached. The results confirm that the contact pressure distribution is neither Hertzian pressure distribution nor symmetric. A finer mesh size of 0.1 mm was used for this purpose to capture the detailed pressure distribution. It should be noted that the computational time for the finite element analysis based on the 0.1 mm mesh is prohibitively high to conduct a full rolling analysis.

Figure 2.14 shows the stress distributions of the upper surface during rolling at the half rolling length. During the rolling process, depending on the indentation depth, a zone of material in front of the roller is being pushed and hence results in a non-symmetric contact pressure distribution. At the same time, a small zone of material behind the roller is being pulled away by the roller and is less compressive shown as a peak of the longitudinal stress σ_{11} in Figure 2.14. As the roller moves further, the very

thin top layer with the less compressive stress returns to a more compressive stress state due to a relatively larger subsurface zone that is in a compressive stress state (Figure 2.21). The roller needs to always push the rise-up material in front of it during rolling. Therefore, a very thin top layer on the rolling surface passes through a compressive-tensile-residual compressive loading cycle. This loading pattern causes a relatively less compressive longitudinal stress in the thin top layer than that of the subsurface (Figure 2.21). Also this loading pattern is different from the single indentation case where the material is loaded by only a compressive loading.

Figure 2.15 shows the stress distributions directly under the roller center in the –y direction from the top surface when the roller is down for the cases of single indentation and during rolling as the roller is rolled to the half rolling length based on the coarse Mesh-1. For the single indentation, the peak compressive values of the stress components σ_{11}, σ_{22} and σ_{33} occur at the contact surface directly under the roller center. During rolling, the peak compressive values of the stress components σ_{11}, σ_{22} and σ_{33} still occur at the surface but are located in front of the roller. In the rolling case, directly under the roller center, the peak compressive value of the stress component σ_{11} occurs at a depth to the contact surface and can be explained in the following. Figure 2.16 shows the contours of the longitudinal stress component σ_{11} when the roller load is applied for both the single indentation and rolling cases. For the single indentation, the σ_{11} contour lines are symmetric about the roller center whereas for the rolling, the compressive zone is moving to the front of the roller such that it is leaving a compressive stress trail zone behind it and is no longer symmetric about the roller center line. Therefore, the peak value of the compressive stress σ_{11} for the rolling case occurs in the

subsurface directly under the roller center. The distribution of the stress component σ_{11} under the roller center during the rolling is different from that of the single indentation case. The peak value of the compressive stresses σ_{22} and σ_{33} for the rolling case occurs at the contact surface directly under the roller center as in the single indentation case.

Note also that the stresses are obtained from the nodal points which are not exactly under the roller center. Therefore, for the single indentation case, very small values of σ_{12} exist due to a small offset of these nodal points from the roller centerline as shown in Figure 2.15. The results of the finite element analysis shows that for the rolling case, the zero value of σ_{12} occurs at a distance approximately $2.16a$ in front of the roller. The shear stress component σ_{12} shows the peak value at the location of the peak compressive stress σ_{11} and thus indicating the rolling effect on the subsurface layer. Directly under the roller center, the magnitudes of the stress components σ_{11}, σ_{22} and σ_{33} during rolling are 24%, 10% and 9% lower at the contact surface than those of the single indentation case. Figure 2.17 shows the displacement components u_1 and u_2 directly under the roller center in the –y direction from the top surface for single indentation and during rolling. The displacement component u_1 for the rolling case is significantly higher than the nearly vanishing u_1 of the single indentation case. Note that for the single indentation case, the u_1 component exists due to a small offset of these nodal points from the roller centerline as mentioned above. However, the displacement components u_2 are nearly the same for both cases. Figure 2.18 shows the distributions of the equivalent plastic strain directly under the roller center for single indentation and during rolling. As shown in the figure, the maximum value of the equivalent plastic strain

(PEEQ) for the rolling is almost 5 times higher than that of the single indentation case and appears at a depth equal to about $2a$ for both cases.

Figure 2.19 shows a comparison of the residual stresses of the rolling and single indentation cases after the roller load is removed. The results for the single indentation case show a small tensile longitudinal residual stress (σ_{11}) at the contact surface (Figures 2.19 and 2.21). The results for the rolling case show a compressive residual stress component σ_{11} at the contact surface. The results also showed a significantly higher subsurface compressive residual stress component σ_{11} after rolling when compared to that for single indentation. Overall, the distributions of the out-of-plane residual stress components σ_{33} for the single indentation and the rolling cases are similar, except within a few millimeters of the contact surface where the residual stress σ_{33} on the surface for the rolling case is lower than that of the single indentation case. The residual stress component σ_{12} have small values near the surface for the single indentation case, and the residual stress components σ_{12} and σ_{22} have small values near the surface for the rolling case. These small values could not be shown clearly in Figure 2.19 due to the scale of the figure. Figure 2.20 shows the residual displacement components u_1 and u_2 in the –y direction from the top surface for the single indentation and rolling cases after the roller load is removed. The residual value of the displacement component u_1 on the surface for the rolling case is higher than that of the single indentation case. On the other hand, the residual value of the displacement component u_2 on the surface for the rolling case is significantly lower than that of the single indentation case. Figure 2.21 shows the distributions of the residual longitudinal stress σ_{11} after the roller load is removed for the

single indentation and rolling cases. Figure 2.22 shows the residual stress distributions of the upper surface after the rolling is completed. These plots show that residual stress component σ_{11} (along the plate length) is the dominant component and the out-of-plane residual stress component σ_{33} is also significant.

Now consider the scenario of using a two-dimensional plane strain finite element analysis of a crankshaft section under single indentation with loading/unloading phases similar to those in Chien et al. [4]. Note that σ_{11} and σ_{33} of the flat plate single indentation/rolling from the current study can be related to the out-of-plane stress σ_{zz} and the hoop stress $\sigma_{\theta\theta}$, respectively, for the crankshaft section based on the cylindrical coordinate system used by Chien et al. [4]. Since the residual out-of-plane stress σ_{zz} would be higher with the rolling as found for σ_{11} in the current investigation, the hoop stress $\sigma_{\theta\theta}$ would be affected too in a similar sense as σ_{33}. Chien et al. [4] matched their two-dimensional finite element rolling depth after the unloading of the roller with the fillet surface profiles measured by the shadowgraphs taken before and after the fillet rolling process without direct use of the actual rolling load and thus may have obtained a good correlation. However, using the fillet surface profiles to calibrate the two-dimensional finite element analysis may not be available upfront in many actual design iteration processes. The current study suggests that the effect of rolling must be taken into consideration to interpret the results of finite element analyses based on the two-dimensional crankshaft sections under single indentation with loading/unloading phases using the rolling loads.

2.7. Effects of boundary conditions on residual stresses

The rolling gives a relatively longer longitudinal length of the plate material that is plastically deformed than the single indentation. The compatibility and equilibrium between the plastic and the elastic layers in the plate typically results in a compressive stress in the top deformed (rolled) layer after the roller load is removed. For a plate with a finite dimension in this investigation, the boundary conditions will have significant impact on the residual stresses and are examined here. The physical reasons for the constrained displacement in the x direction for the surfaces AB and CD and the constrained displacements in the x and y directions for the surface BC come from the fact that the plate is used to represent the cross section of a crankshaft journal. Figure 2.23 shows the contours of the residual Mises stress after the roller load is removed for the single indentation and rolling cases. Figures 2.24(a) and 2.24(b) show the distributions of the residual stress components on the surface AB of the plate in the –y direction from the top after the roller load is removed for the single indentation and rolling cases, respectively. It should be noted that the single indentation was conducted at the location of the rolling start point that is closer to the boundary surface AB. For the rolling case, the maximum value of the longitudinal residual stress component σ_{11} on the boundary surface AB of the plate as shown in Figure 2.24(b) was found four times more compressive than that of the single indentation case (Figure 2.24(a)).

Figures 2.25(a) and 2.25(b) show the distributions of the residual stress components on the surface CD of the plate in the –y direction from the top after the roller load is removed for the single indentation and rolling cases, respectively. The stress components are nearly zero on the boundary located on the surface CD of the plate that is

far away from the location of the single indentation as shown in Figure 2.25(a). For the rolling case, the longitudinal stress is compressive and around 10 MPa on the boundary surface CD of the plate as shown in Figure 2.25(b) compared to the near zero value for the single indentation case. For an infinite solid subjected to a single indentation, one might expect that the longitudinal residual stress component directly under the roller center may be in self-equilibrium. However, for a finite plate with the dimensions relatively large compared to the roller dimension and the contact width, the boundary conditions have effects on the residual stresses. It is found that the distribution of the longitudinal residual stress component σ_{11} along the roller centerline (Figure 2.19) is no longer in self equilibrium due to the change in the length of the top layer of the plate by rolling and the reaction forces at the boundary surfaces.

For a finite plate, the residual stresses in the plastically deformed zone are also affected by the boundary conditions. For the single indentation, consider a hypothetical condition where all the boundary conditions are released. Figure 2.26(a) shows the effects of the boundary conditions on the residual stresses in the plastically deformed zone for the single indentation case. After the boundary conditions are released, the changes in the residual stresses are recorded for a few nodes marked as node-1, node-2 and node-3 in the top portion of the plate located directly under the roller center and closer to the indentation center as shown in Figure 2.26(a). Note that the rigid roller is shown in the figure to show the locations of these nodes. After the boundary conditions are released, the value of the residual longitudinal stress σ_{11} becomes around 2.7 times more tensile at node-1 on the top surface. As shown in the figure, the changes are not so drastic at node-2 and node-3. Figure 2.26(b) shows the effects of the boundary condition

on the residual stresses in the plastically deformed zone for the rolling case. For the rolling case, the boundary conditions are also important since any constraint will restrict the plate to take any deformed shape due to the compatibility and equilibrium of the plastic and the elastic layers after the roller load is removed. For the rolling case, after the rolling load is removed and the displacement boundary conditions on both the boundary surfaces AB and CD are released successively, the changes in the residual stresses are recorded for few nodes marked as node-1, node-2 and node-3 in the top portion of the plate located at the half rolling length as shown in Figure 2.26(b). Note that the rigid roller is shown to show the locations of these nodes relative to the starting of the rolling. At node-1 located on the top surface, the absolute value of the compressive residual longitudinal stress (σ_{11}) is reduced by 17% and the stress becomes less compressive. Next, the fixed boundary condition on the bottom surface BC is also removed so that the plate can deform freely in the longitudinal direction. The value of the compressive residual longitudinal stress is further reduced by 54% at node-1 on the top surface at the location of half rolling length. That results in a total drop of 62% in the value of the compressive longitudinal stress component due to the release of all the boundary conditions. For the rolling case, after all the boundary conditions are released, the plate takes a convex shape and the values of the compressive residual stresses reduce.

2.8. Conclusions

In this paper, residual stresses due to single indentation and rolling on a finite plate at very high rolling loads are investigated by two-dimensional plane strain finite element analyses using ABAQUS. In the finite element analyses, the roller is modeled as

rigid and has frictionless contact with the finite plate. Finite element analyses with different meshes for single indentation on elastic flat plate under plane strain conditions are first carried out and the results are compared with those of the elastic Hertzian solutions to understand the need of the finite element model for elastic-plastic analyses of indentation and rolling. Then the plate material is modeled as an elastic-plastic power-law strain hardening material with a non-linear kinematic hardening rule for loading and unloading. Finite element analyses with different meshes for single indentation on an elastic-plastic flat plate under plane strain conditions are also carried out to validate the finite element models. Based on the computational models for indentation and rolling at high rolling loads with extensive plastic deformation, the computational results show that the contact pressure distributions are quite different and they are also significantly different from the elastic Hertzian pressure distribution. The computational results for the rolling case show a significantly higher longitudinal compressive residual stress and a lower out-of-plane compressive residual stress along the contact surface when compared to those for the single indentation case. Moreover, the residual stresses at the boundary surfaces due to rolling are found to be four to five times higher than those of the single indentation case. Also, the longitudinal residual stress distribution under the roller is no longer in self equilibrium due to a length change of the top portion of the plate by rolling and the boundary reaction forces which are no longer negligible compared to those of the single indentation case. The results suggest that the effects of rolling must be accounted for when two-dimensional finite element analyses of crankshaft sections are used to investigate the residual stresses due to fillet rolling of the crankshafts under prescribed loading conditions.

Acknowledgements

The encouragement of Dr. Jagadish Sorab of Ford Motor Company to conduct this research work is greatly appreciated. Helpful discussions with Dr. Simon Ho of Chrysler LLC are also greatly appreciated.

References

1. Love, R. J. and Waistall, D. N., "The Improvement in the Bending Fatigue Strength of Production Crankshafts by Cold Rolling," M.I.R.A. Report No. 1954/1:1-8, 1954.
2. Spiteri, P., Ho, S., and Lee, Y. L., "Assessment of Bending Fatigue Limit for Crankshaft Sections with Inclusion of Residual Stresses," *Int. J. Fatigue*, **29**:318-329, 2007, doi:10.1016/j.ijfatigue.2006.03.009.
3. Choi, K. S., Pan, J., and Ho, S., "Fatigue Failures of Rollers in Crankshaft Fillet Rolling," SAE Technical Paper 2004-01-1498, 2004.
4. Chien, W. Y., Pan, J., Close, D., and Ho, S., "Fatigue Analysis of Crankshaft Sections under Bending with Consideration of Residual Stresses," *Int. J. Fatigue*, **27**:1–19, 2005, doi:10.1016/j.ijfatigue.2004.06.009.
5. Choi, K. S. and Pan, J., "Simulations of Stress Distributions in Crankshaft Sections under Fillet Rolling and Bending Fatigue Tests," *Int. J. Fatigue*, **31**:544-557, 2009, doi:10.1016/j.ijfatigue.2008.03.035.
6. Choi, K. S. and Pan, J., "A Generalized Anisotropic Hardening Rule Based on the Mroz Multi-Yield-Surface Model for Pressure Insensitive and Sensitive Materials," *Int. J. of Plasticity*, **25**(7):1325-1358, 2009, doi:10.1016/j.ijplas.2008.09.005.
7. Choi, K. S., Pan, J., and Ho, S., "Effects of Roller Geometry on Contact Pressure and Residual Stress in Crankshaft Fillet Rolling," SAE Technical Paper 2005-01-1908, 2005.
8. Ho, S., Lee, Y-L, Kang, H.-T., and Wang, C. J., "Optimization of a Crankshaft Rolling Process for Durability," *Int. J. Fatigue*, **31**:799-808, 2009, doi:10.1016/j.ijfatigue.2008.11.011.
9. Mesarovic, S. Dj. and Fleck, N. A., "Spherical Indentation of Elastic-Plastic Solids," Proc. R. Soc. Lond. A, **455**:2707-2728, 1999.
10. Kral, E. R., Komvopoulos, K., and Bogy, D. B., "Elastic-Plastic Finite Element Analysis of Repeated Indentation of Half-Space by a Rigid Sphere," *J. Appl. Mech.*, **60**:829-841, 1993, doi:10.1115/1.2900991.
11. Komvopoulos, K., "Elastic-Plastic Finite Element Analysis of Indented Layered Media," *J. Tribol.*, **111**(3):430-439, 1989, doi:10.1115/1.3261943.
12. Merwin, J. E. and Johnson, K. L., "An Analysis of Plastic Deformation in Rolling Contact," Proc. Instn. Mech. Engrs., **177**(25):676-690, 1963.
13. Kulkarni, S. M., Hahn, G. T., Rubin, C. A., and Bhargava, V., "Elastoplastic Finite Element Analysis of Three-Dimensional, Pure Rolling Contact at the Shakedown Limit," *J. Appl. Mech.*, **57**:57-65, 1990, doi:10.1115/1.2888324.
14. Kulkarni, S. M., Hahn, G. T., Rubin, C. A., and Bhargava, V., "Elasto-Plastic Finite Element Analysis of Three-Dimensional Pure Rolling Contact Above the Shakedown Limit," *J. of Appl. Mech.*, **58**:347-353, 1991, doi:10.1115/1.2897192.
15. Yu, M., Moran, B., and Keer, L. M., "A Direct Analysis of Two-Dimensional Elastic-Plastic Rolling Contact," *J. Tribol.*, **115**:227–236, 1993, doi:10.1115/1.2920996.
16. Yu, M. M. H., Moran, B., and Keer, L. M., "A Direct Analysis of Three-Dimensional Elastic-Plastic Rolling Contact," *J. Tribol.*, **117**:234–243, 1995, doi:10.1115/1.2831236.

17. Bhargava, V., Hahn, G. T., and Rubin, C. A., "An Elastic-Plastic Finite Element Model of Rolling Contact Part 1: Analysis of Single Contacts," *J. of Appl. Mech.*, **52**:67-74, 1985, doi:10.1115/1.3169028.
18. Bhargava, V., Hahn, G. T., and Rubin, C. A., "An Elastic-Plastic Finite Element Model of Rolling Contact Part 2: Analysis of Repeated Contacts," *J. of Appl. Mech.*, **52**:75-82, 1985, doi:10.1115/1.3169030.
19. Chen, W. W., Wang, Q. J., Wang, F., Keer, L. M., and Cao, J., "Three-Dimensional Repeated Elasto-Plastic Point Contacts, Rolling, and Sliding," *J. of Appl. Mech.*, **75**:021021, 2008, doi:10.1115/1.2755171.
20. Jiang, Y. and Sehitoglu, H., "Rolling Contact Stress Analysis with the Application of a New Plasticity Model," *Wear*, **191**:35-44, 1996, doi:10.1016/0043-1648(95)06663-2.
21. Jiang, Y., Xu, B., and Sehitoglu, H., "Three-Dimensional Elastic-Plastic Stress Analysis of Rolling Contact," *J. Tribol.*, **124**:699–708, 2002, doi:10.1115/1.1491978.
22. Bijak-Zochowski, M. and Marek, P., "Residual Stress in Some Elasto-Plastic Problems of Rolling Contact with Friction," *Int. J. Mech. Sci.*, **39**(1):15-32, 1997, doi:10.1016/0020-7403(96)00018-5.
23. ABAQUS Version 6.8 User Manual, SIMULIA, Providence, RI, 2008.
24. Johnson, K. L, "Contact Mechanics", Cambridge University Press, ISBN 0-521-34796-3, 1987.

Appendix 2.A: Conversion of the roller load for the plane strain model

Figure 2.A1(a) shows a three-dimensional finite element model for a crankshaft section under fillet rolling. A portion of the secondary roller on one side of the symmetry line is also modeled by finite elements. Figure 2.A1(b) shows a magnified view of the crankshaft section and the primary roller. As shown in Figure 2.A1(b), very fine elements are used near the fillet region of the crankshaft section. The crankshaft and rollers are mainly modeled by hexagonal elements (C3D8) in ABAQUS. The primary and secondary rollers also have fine elements near the contact zone. The nonlinear kinematic hardening material model of ABAQUS based on the tensile stress-plastic strain curve shown in Figure 2.2 is used for the crankshaft section in the finite element analyses. The diameters of the primary and secondary rollers are assumed to be 14 mm and 80 mm, respectively. The roller load is assumed to be 5700 N. The material data for the primary and secondary rollers are obtained from Choi et al. [3] and they are treated as elastic.

Figure 2.A2(a) shows the contact pressure distribution between the crankshaft and the primary roller from the three-dimensional finite element analysis when the roller load is applied. Figure 2.A2(b) shows the contact pressure distributions along the two circumferential paths, path 1 and 2, as marked in Figure 2.A2(a). The results in Figure 2.A2(b) indicate that the contact pressure distributions are quite similar along the two circumferential paths. Based on the area under the contact pressure distribution of path 2, the load per unit thickness is calculated as 3847.0 (N/mm) which is the rolling load used for the simulations of plane strain indentation and rolling in this investigation.

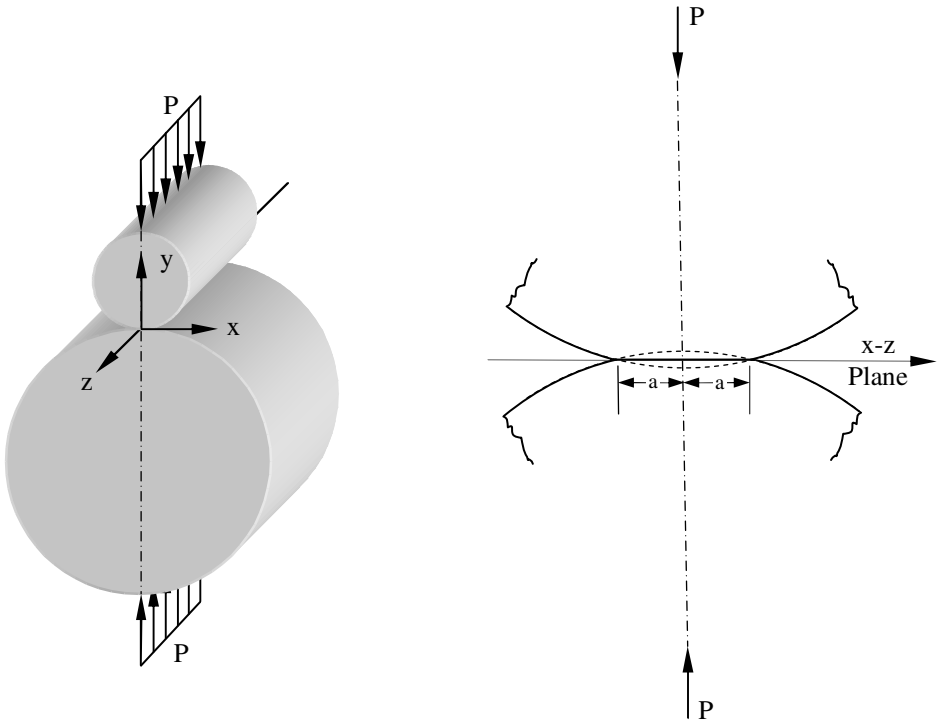

(a)

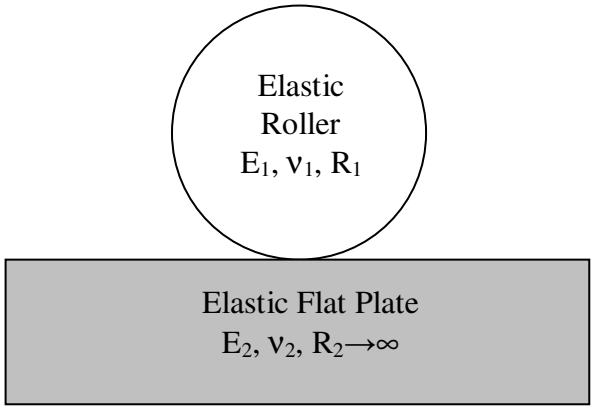

(b)

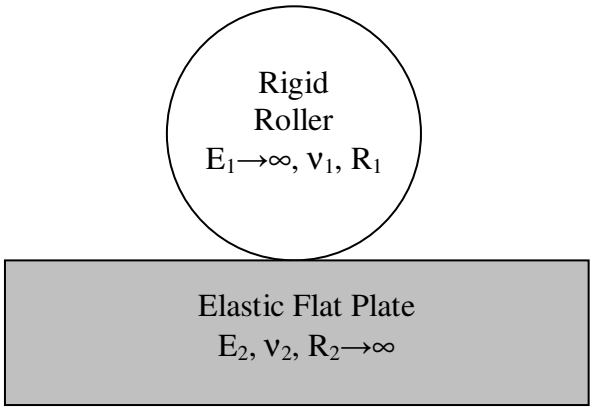

(c)

Figure 2.1. (a) Contact between two elastic cylinders, (b) contact between an elastic roller and an elastic flat plate, and (c) contact between a rigid roller and an elastic flat plate.

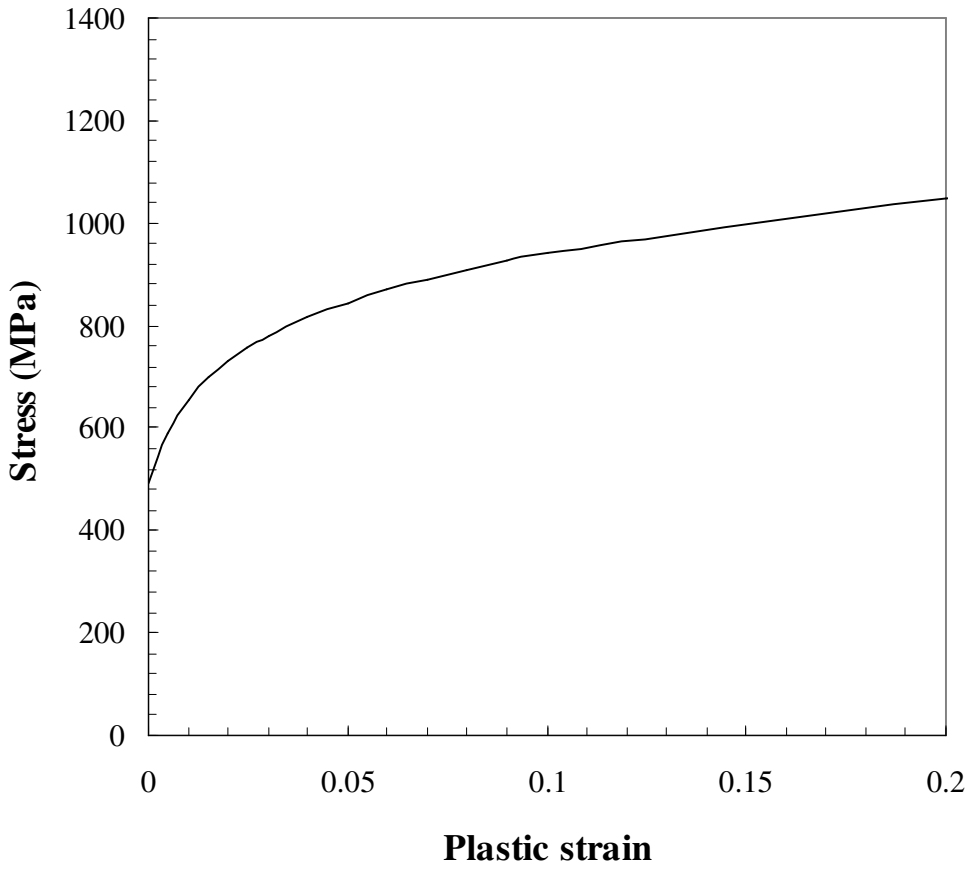

Figure 2.2. The tensile stress–strain curve of the plate material used in the finite element analyses.

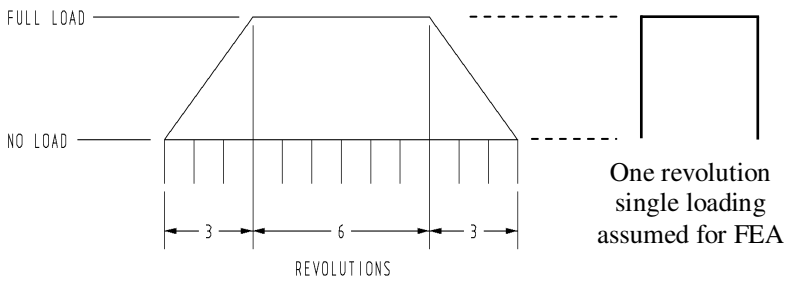

Figure 2.3. (a) One actual rolling load history for the crankshaft fillet rolling and (b) the assumed rolling load history for finite element analyses.

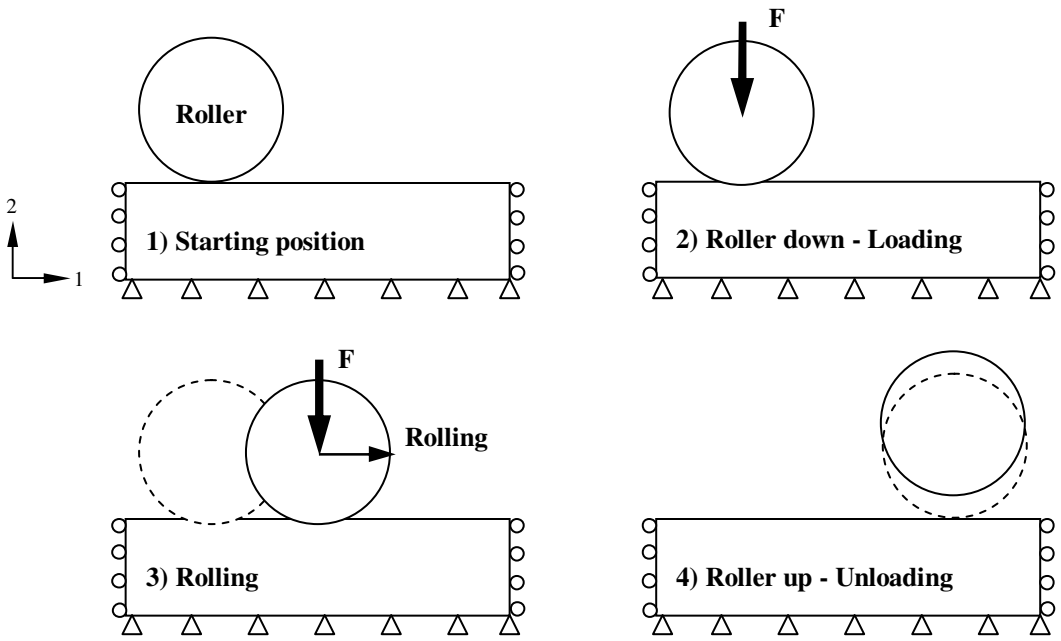

Figure 2.4. A schematic of a two-dimensional model of a flat plate rolling process. The roller is assumed to be rigid and the contact between the roller and the plate is frictionless.

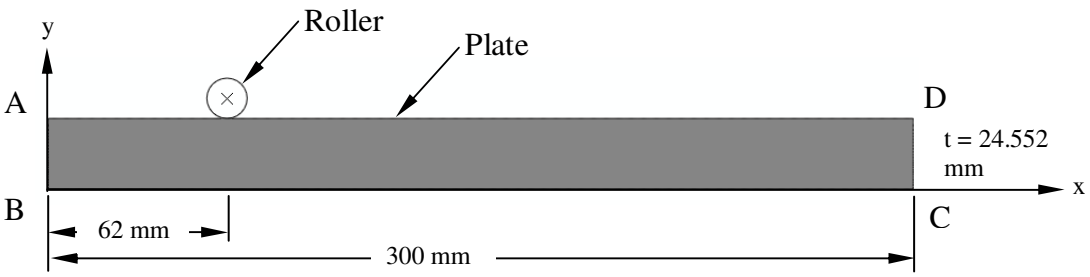

(a)

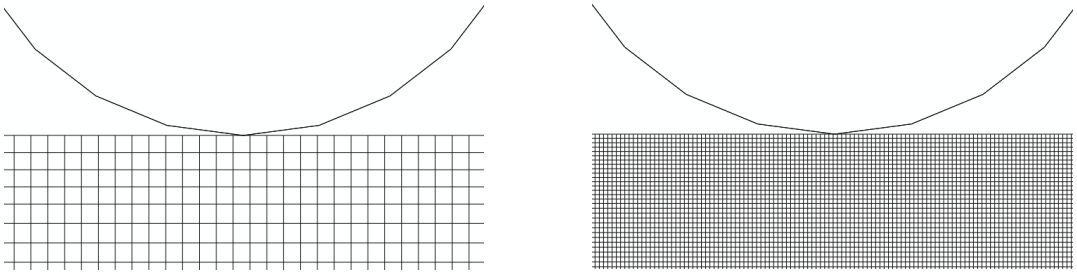

(b) (c)

Figure 2.5. (a) A two-dimensional finite element model of a rigid cylinder rolling on a finite flat plate and magnified views of the finite element models for (b) Mesh-1 with the element size of 0.4 mm and (c) Mesh-2 with the element size of 0.1 mm.

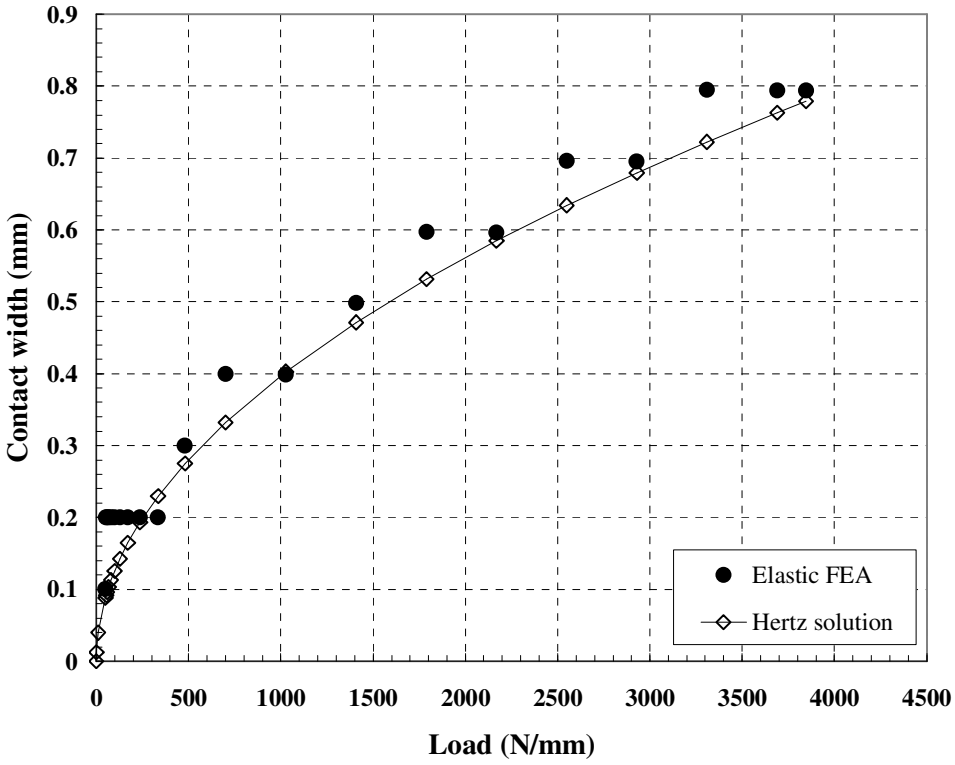

Figure 2.6. A comparison of the contact widths between the flat plate and the rigid roller obtained by the elastic Hertzian solution and the elastic finite element analysis as functions of the indentation load up to the maximum load of 3847 N/mm based on Mesh-2.

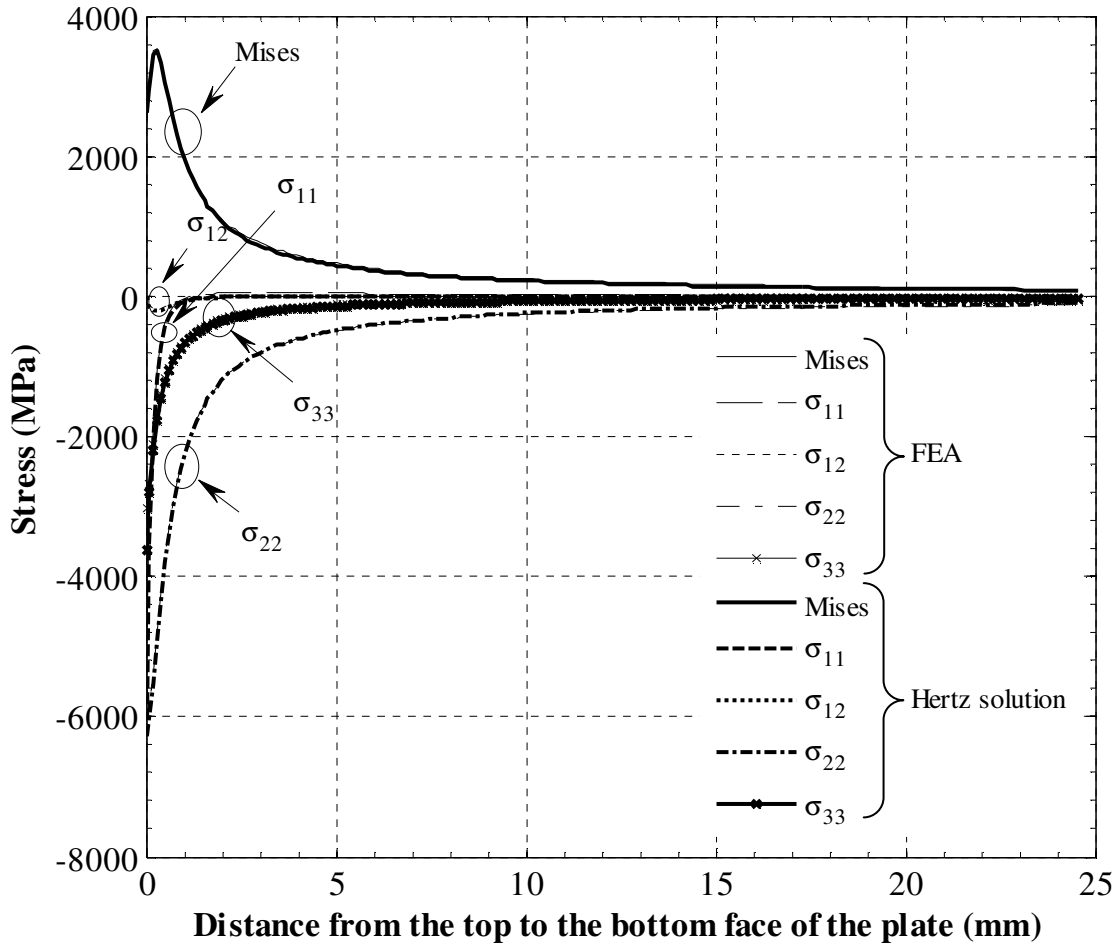
4000
2000
0
-2000
-4000
-6000
-8000
0
5
10
15
20
25
Stress (MPa)
Distance from the top to the bottom face of the plate (mm)
Mises
σ11
σ12
σ33
σ22
Mises
σ11
σ12
σ22
σ33
FEA
Mises
σ11
σ12
σ22
σ33
Hertz solution

(a)

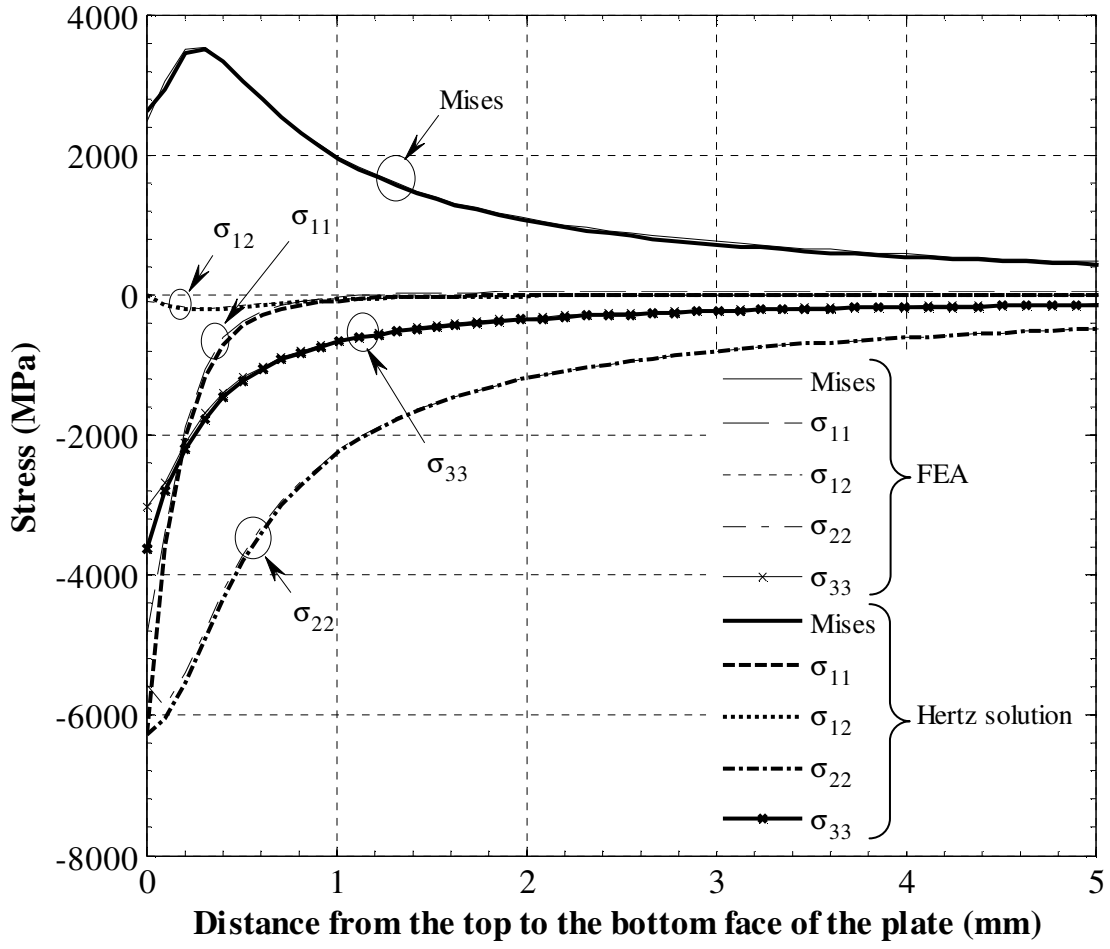

(b)

Figure 2.7. A comparison of the results from the finite element analysis and the elastic Hertzian solution for contact between the elastic plate and the rigid roller. (a) The stress distributions in the –y direction from the top surface for single indentation and (b) a zoom-in view of the stress distribution in the top 5 mm strip of the plate.

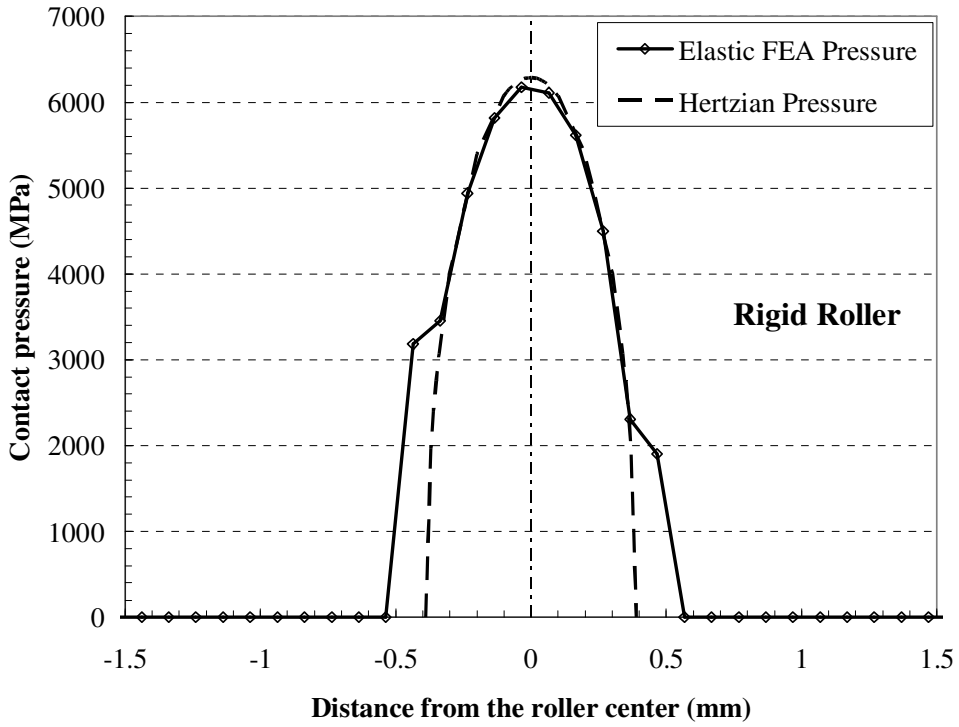

Figure 2.8. The contact pressure distributions on the plate surface based on the elastic Hertzian solution and the results of the elastic finite element analysis with a fine plate mesh size of 0.1 mm due to single indentation by the rigid roller.

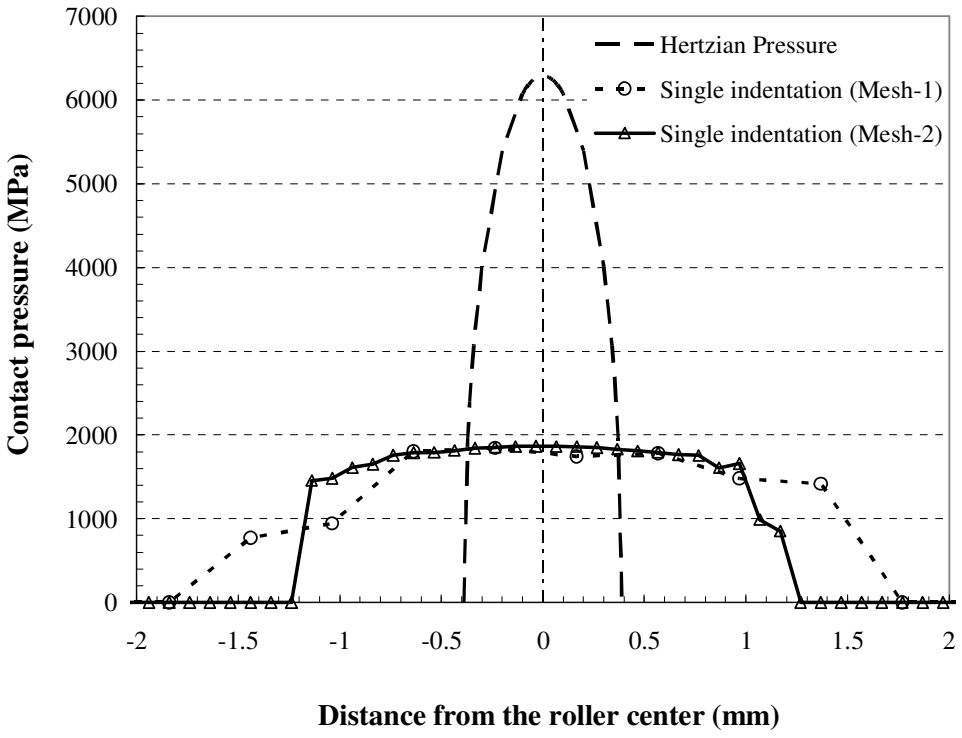
Hertzian Pressure
Single indentation (Mesh-1)
Single indentation (Mesh-2)
Contact pressure (MPa)
7000
6000
5000
4000
3000
2000
1000
0
-2
-1.5
-1
-0.5
0
0.5
1
1.5
2
Distance from the roller center (mm)

(a)

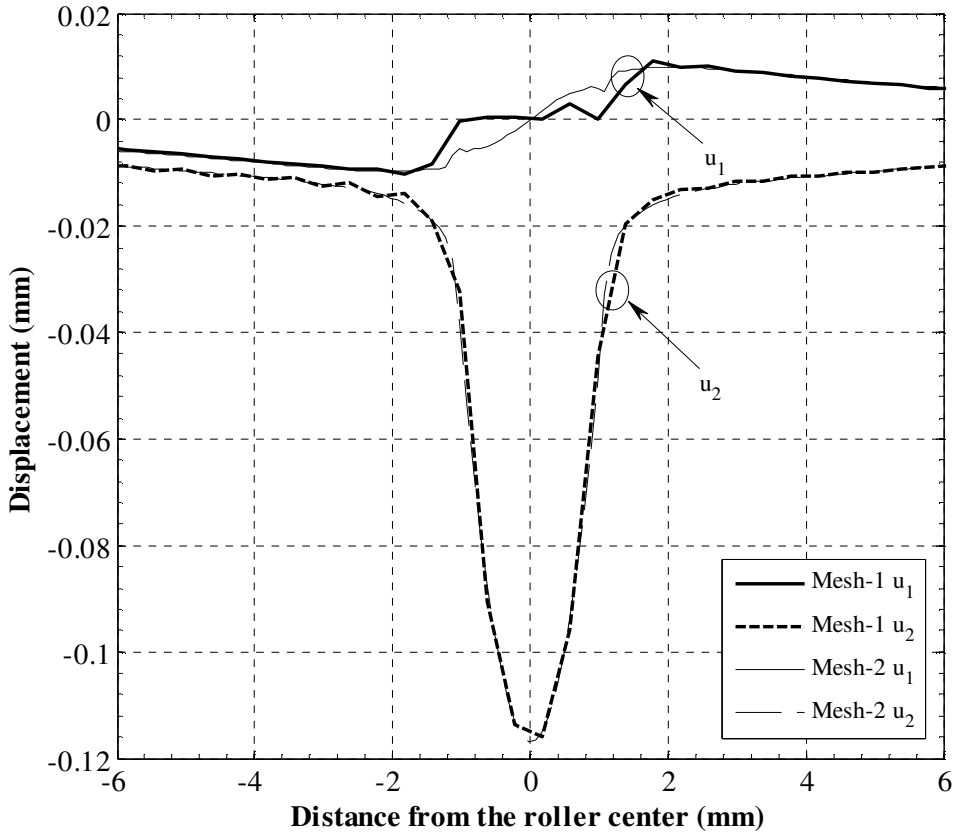
0.02
0
-0.02
-0.04
-0.06
-0.08
-0.1
-0.12
-6
-4
-2
0
2
4
6
Displacement (mm)
Distance from the roller center (mm)
u1
u2
Mesh-1 u1
Mesh-1 u2
Mesh-2 u1
Mesh-2 u2

(b)

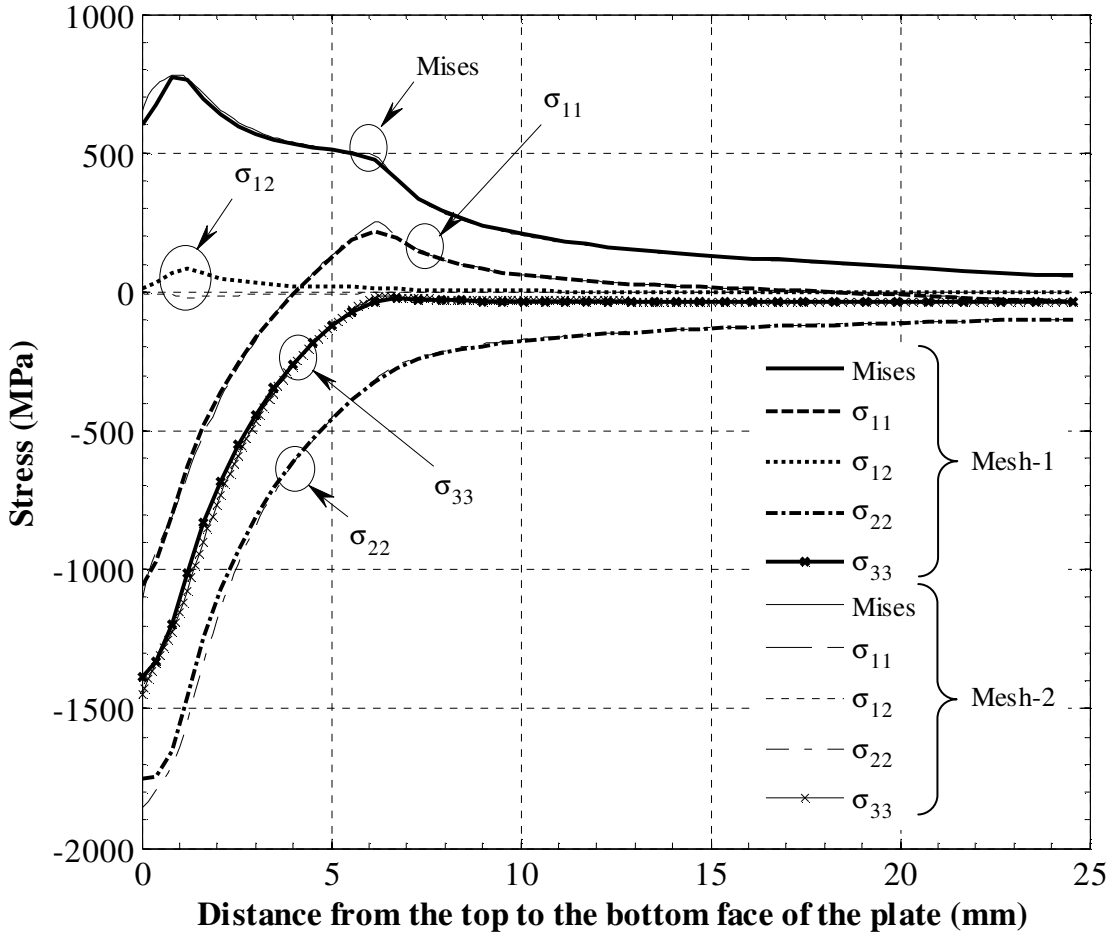
1000
500
0
-500
-1000
-1500
-2000
0
5
10
15
20
25
Stress (MPa)
Distance from the top to the bottom face of the plate (mm)
Mises
σ11
σ12
σ33
σ22
Mises
σ11
σ12
σ22
σ33
Mesh-1
Mises
σ11
σ12
σ22
σ33
Mesh-2

(c)

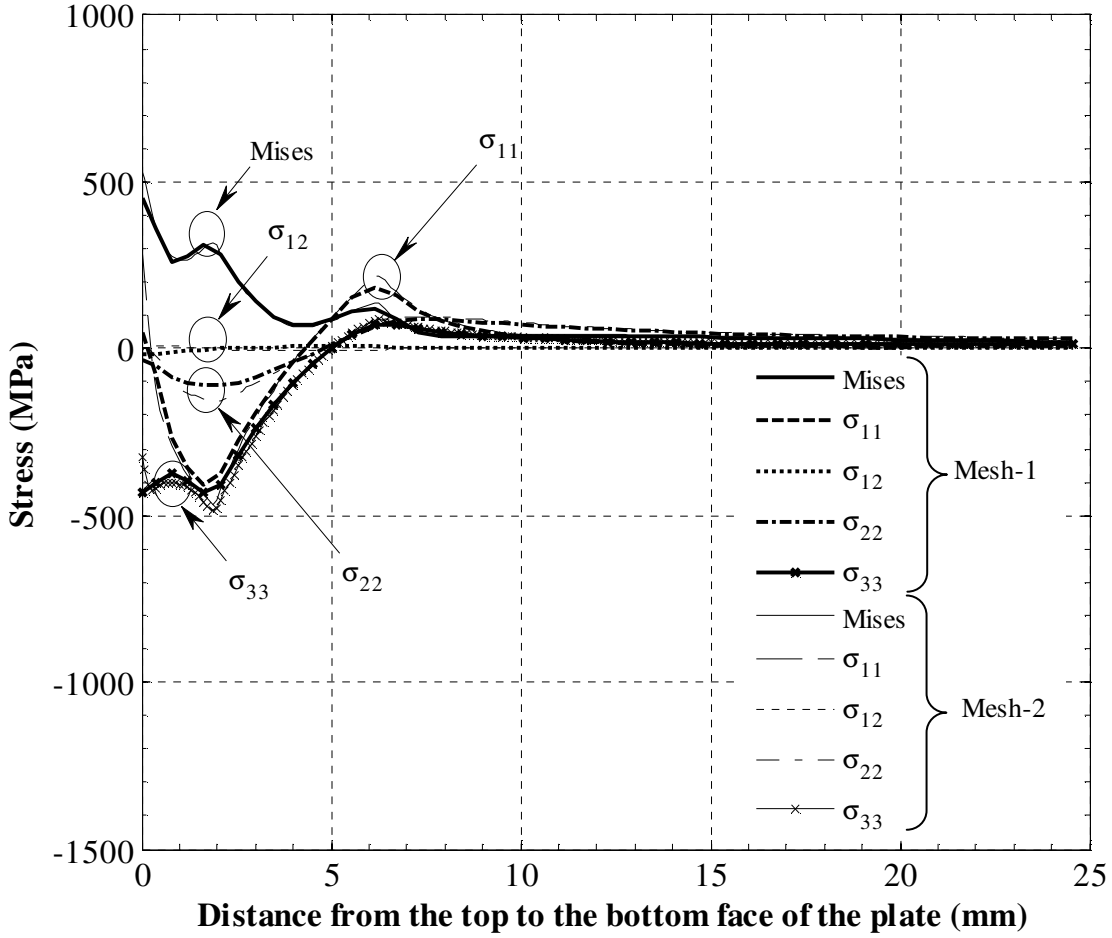

(d)

Figure 2.9. (a) The contact pressure distributions, (b) the displacement components u_1 and u_2 of the plate surface nodes, (c) the stress distributions and (d) the residual stress distributions in the –y direction from the top surface based on Mesh-1 and Mesh-2 after single indentation on the elastic-plastic plate.

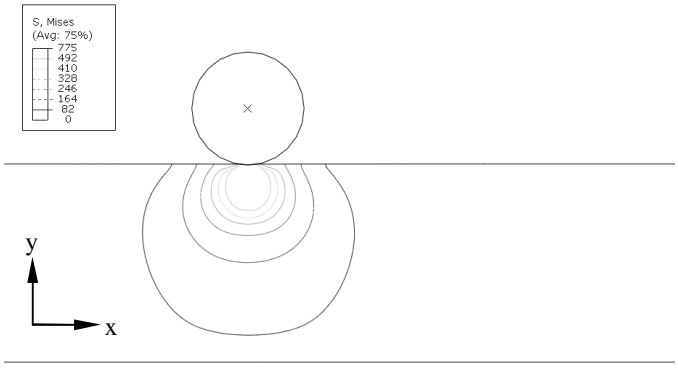

(a)

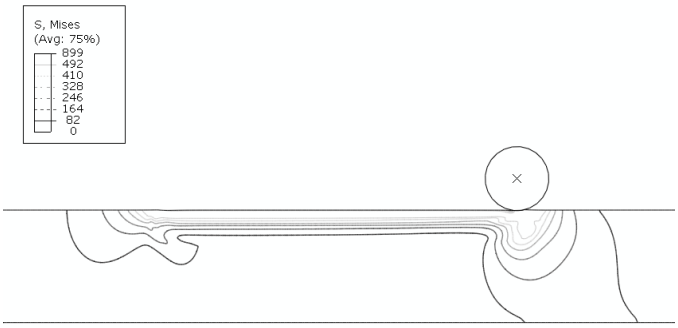

(b)

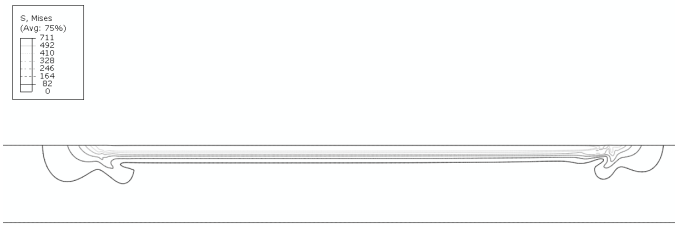

(c)

Figure 2.10. The Mises stress distributions and the plastic zone sizes and shapes represented by the lighter contours due to the rolling when (a) the roller is moved down at the full rolling load, (b) the roller is rolled to the half rolling length, and (c) the roller is moved up after the rolling is completed.

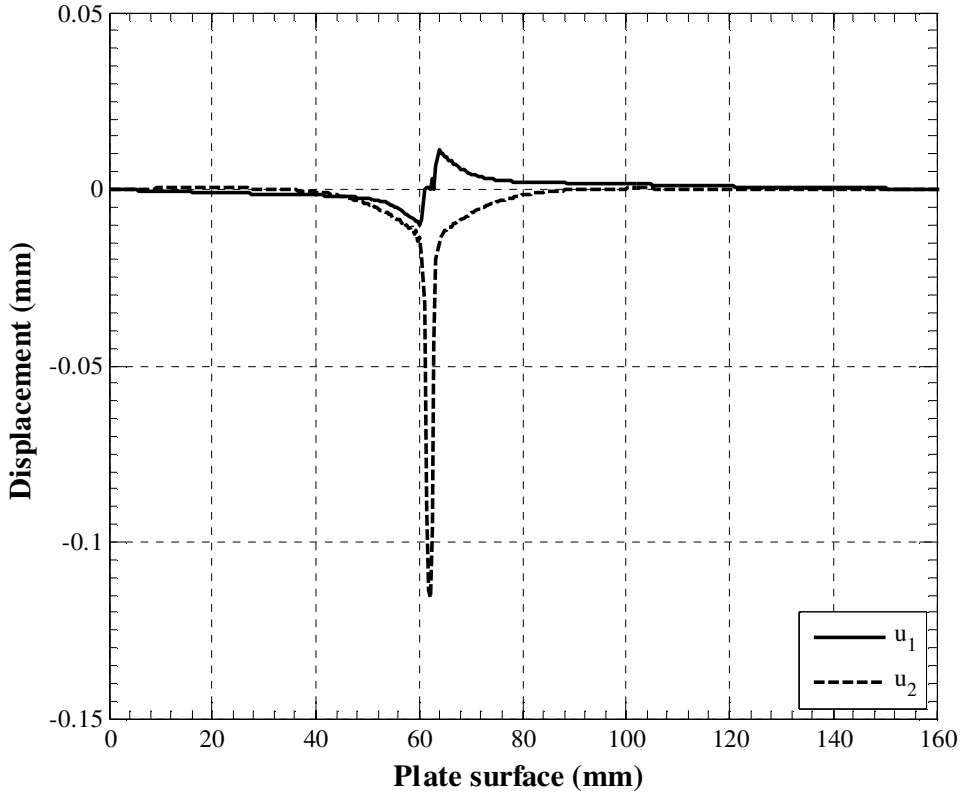
0.05
0
-0.05
-0.1
-0.15
0
20
40
60
80
100
120
140
160
Displacement (mm)
Plate surface (mm)
u1
u2

(a)

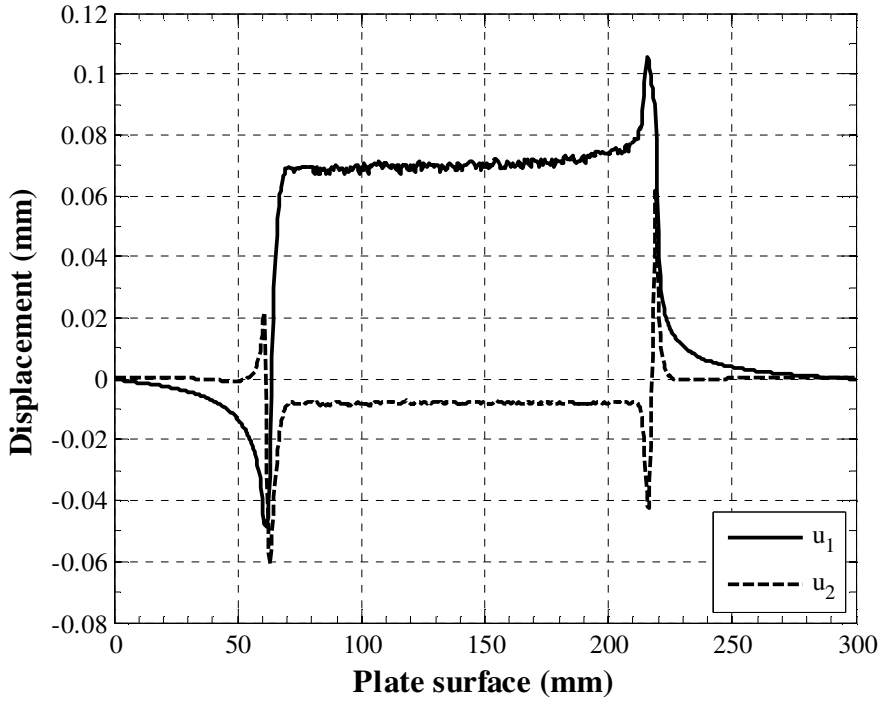

(b)

Figure 2.11. (a) The displacement components u_1 and u_2 of the upper surface nodes when the roller is moved down at the full applied rolling load, and (b) the residual displacement components u_1 and u_2 of the upper surface nodes after the rolling is completed.

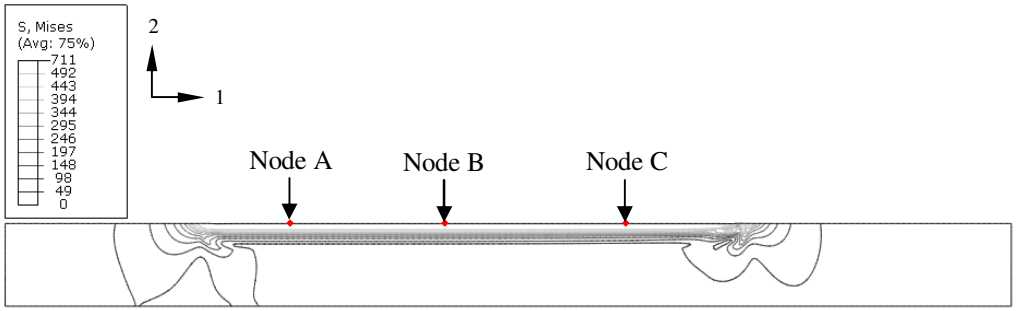
S, Mises
(Avg: 75%)
711
492
443
394
344
295
246
197
148
98
49
0
2
1
Node A
Node B
Node C

(a)

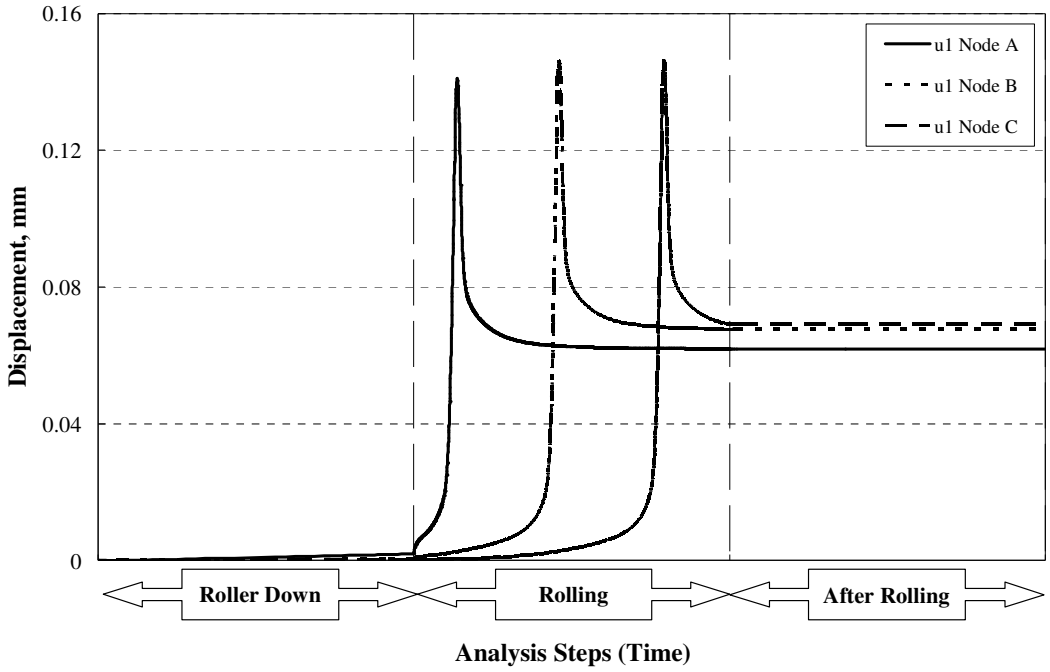
0.16
0.12
0.08
0.04
0
Displacement, mm
u1 Node A
u1 Node B
u1 Node C
Roller Down
Rolling
After Rolling
Analysis Steps (Time)

(b)

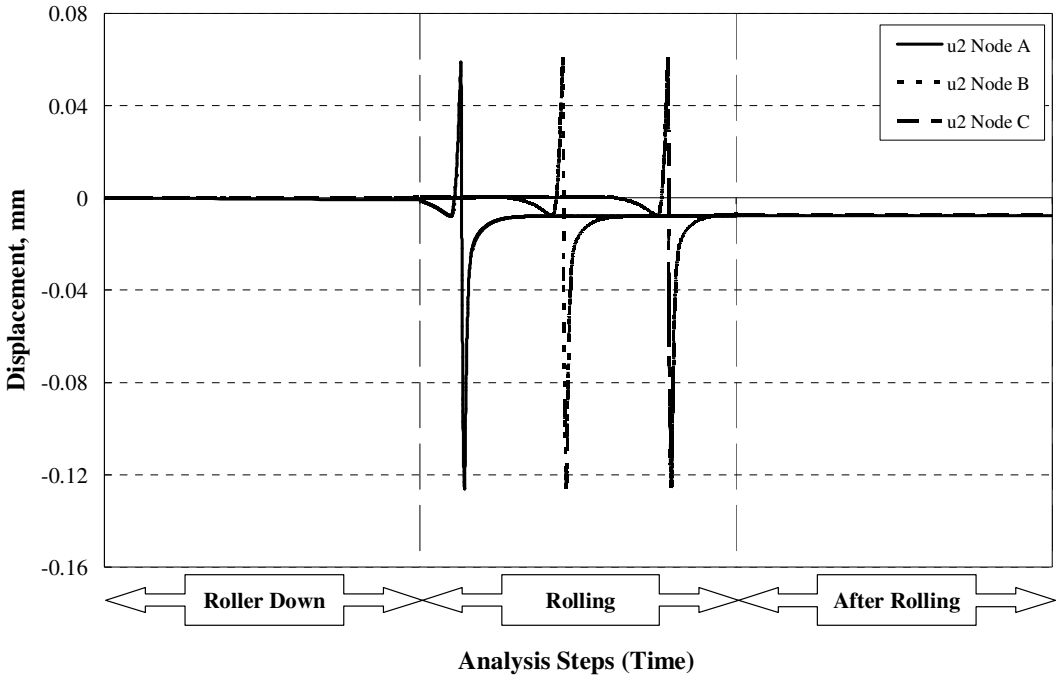

(c)

Figure 2.12. (a) Three nodes are arbitrarily selected on the plate surface, and the histories of the nodal displacement components (b) u_1 and (c) u_2 of the selected nodes on the plate surface.

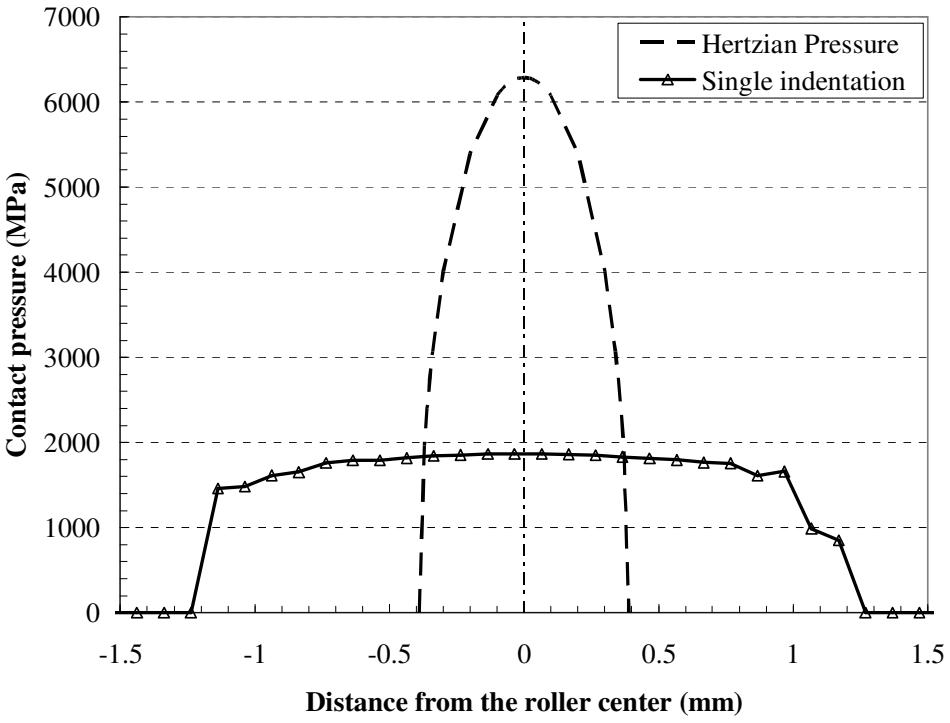
Hertzian Pressure
Single indentation
Contact pressure (MPa)
7000
6000
5000
4000
3000
2000
1000
0
-1.5
-1
-0.5
0
0.5
1
1.5
Distance from the roller center (mm)

(a)

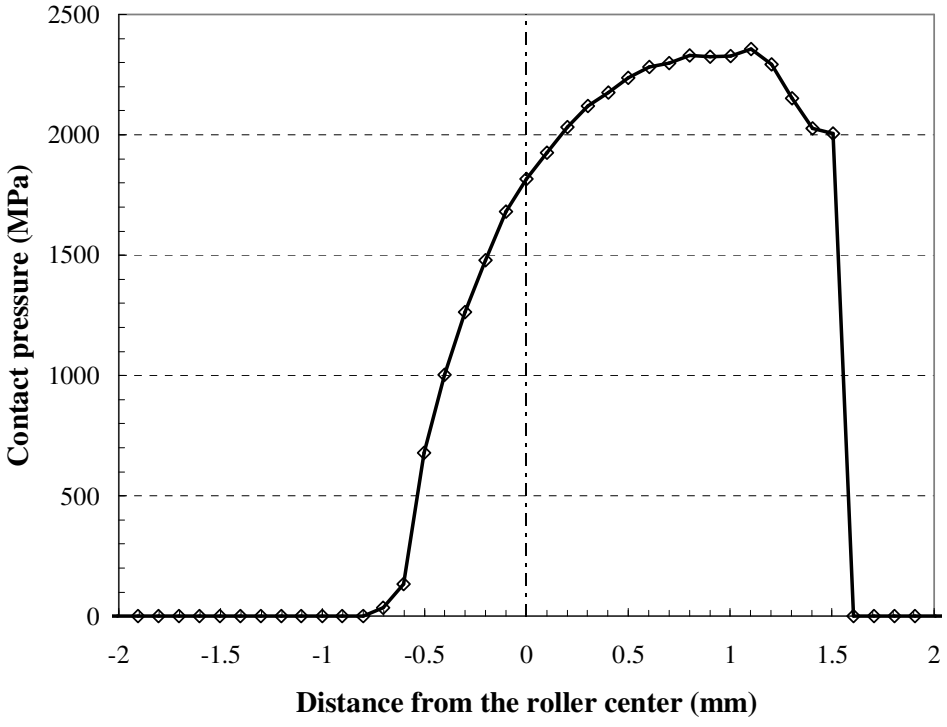

(b)

Figure 2.13. Contact pressure distributions (a) for single indentation and (b) during rolling based on a finer mesh size of 0.1 mm.

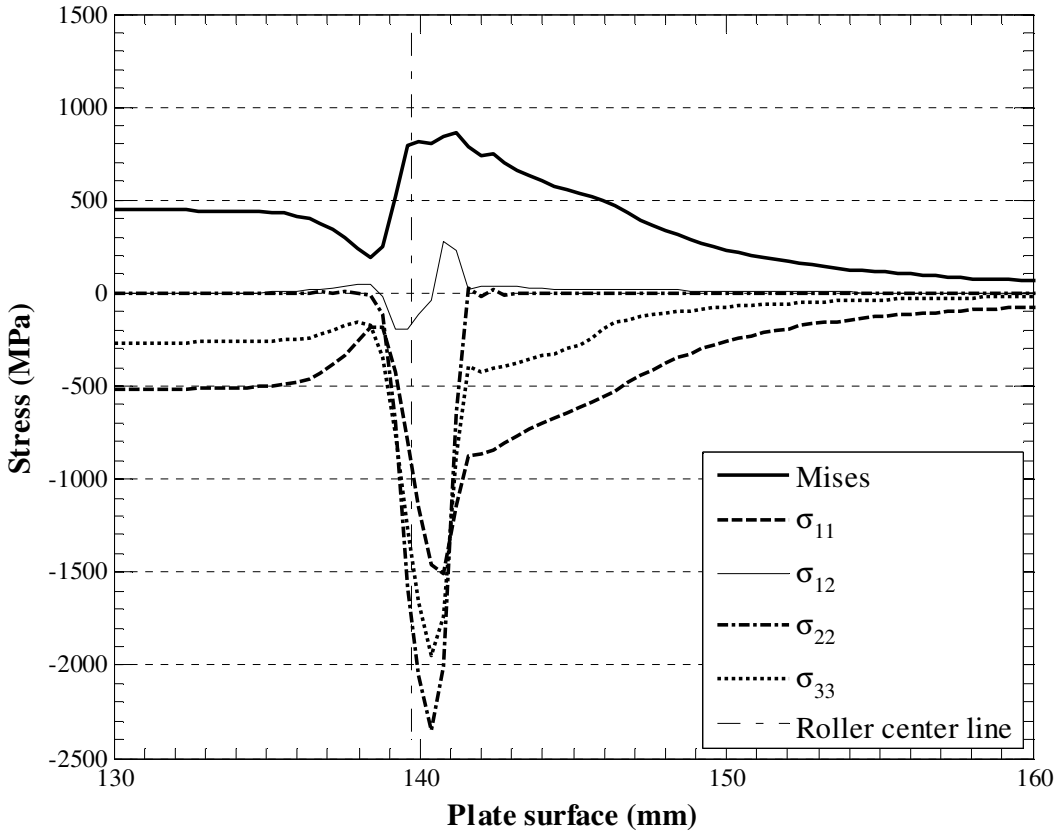

Figure 2.14. The stress distributions of the upper surface during rolling at the half rolling length.

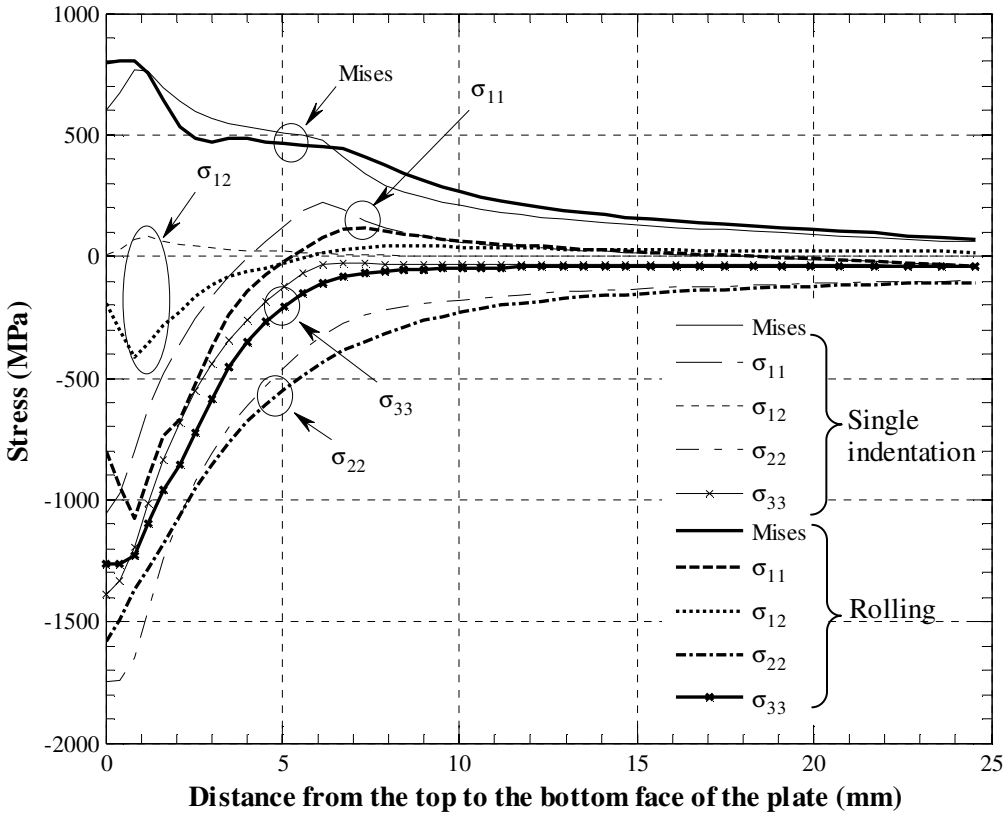

Figure 2.15. The stress distributions in the –y direction from the top surface for single indentation and during rolling.

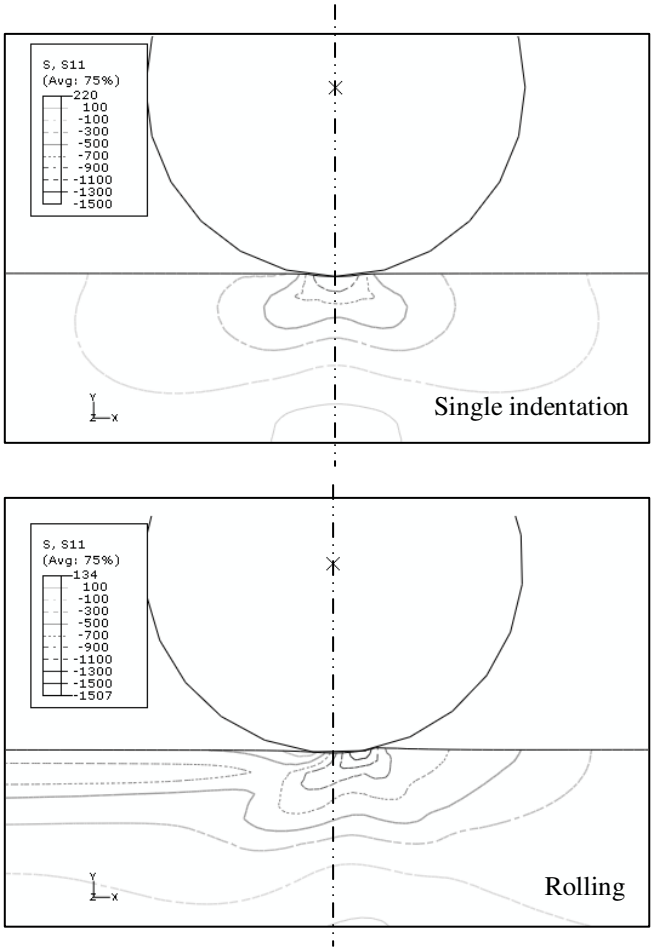

Figure 2.16. The contours of the longitudinal stress component σ_{11} for single indentation and during rolling.

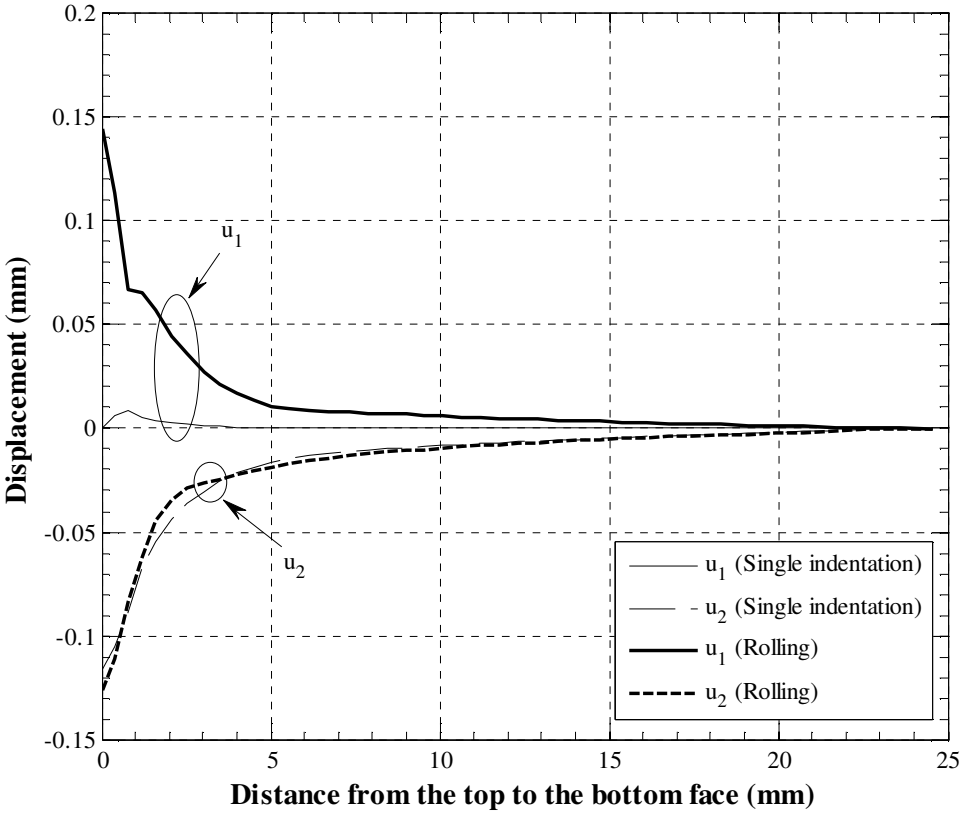

Figure 2.17. The displacement components u_1 and u_2 in the –y direction from the top surface for single indentation and during rolling.

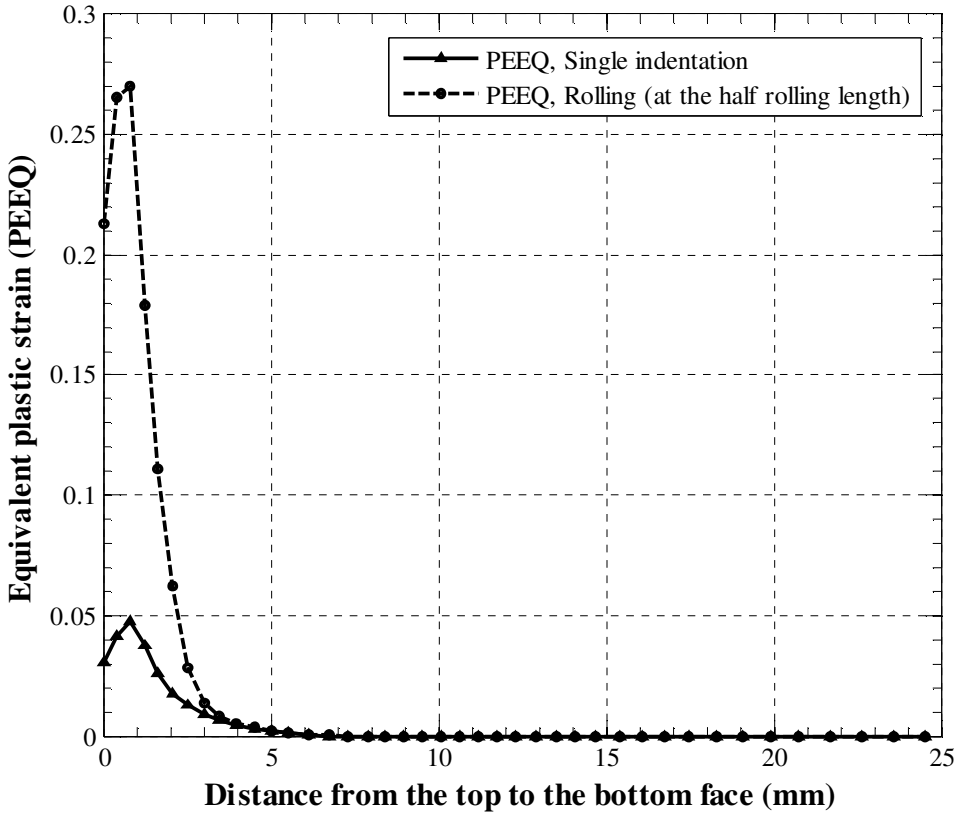

Figure 2.18. The distributions of the equivalent plastic strain (PEEQ) directly under the roller center in the –y direction from the top surface for single indentation and during rolling.

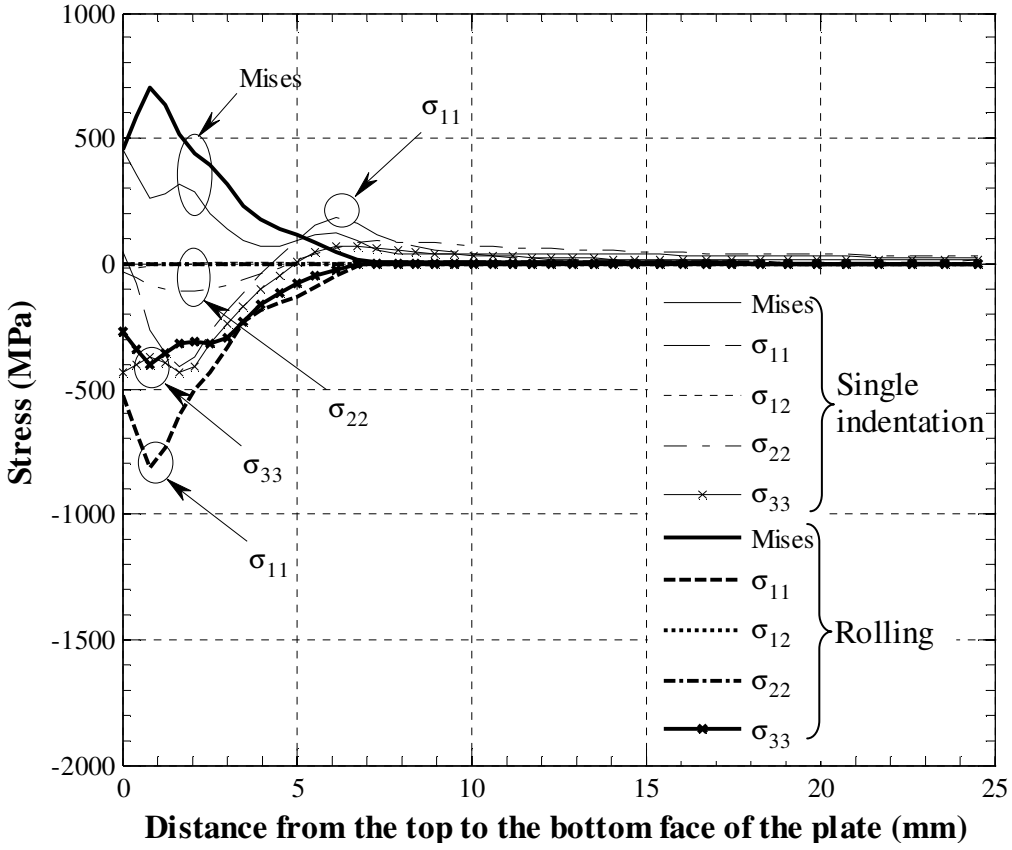

Figure 2.19. The residual stress distributions in the –y direction from the top surface after the roller load is removed for the single indentation and rolling cases.

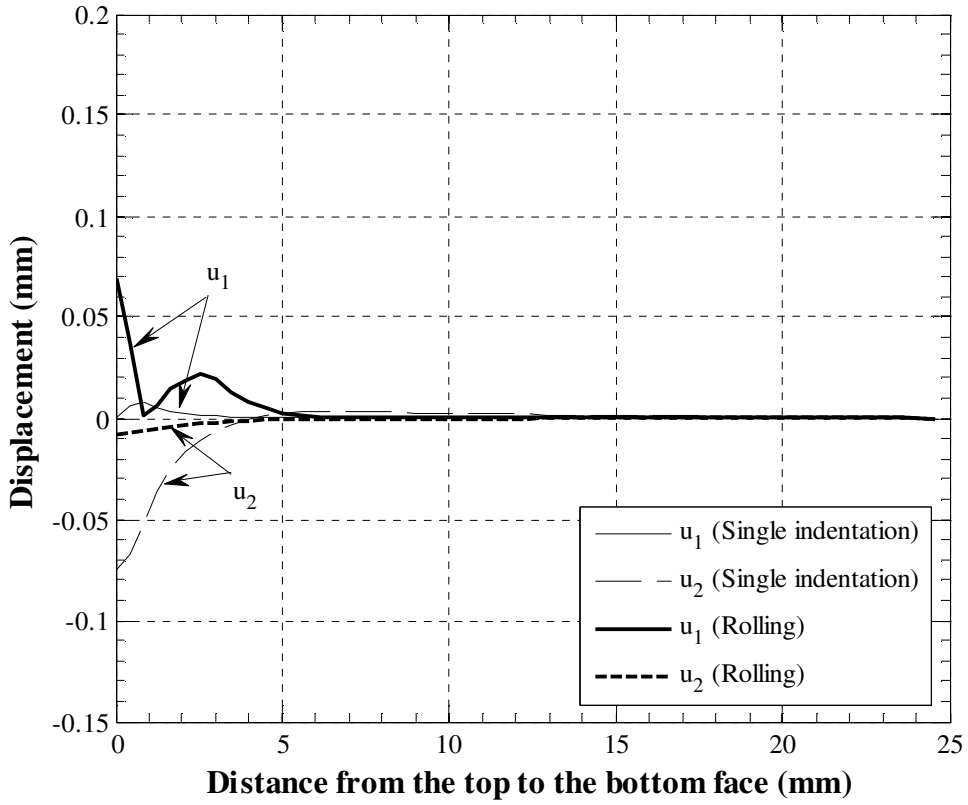

Figure 2.20. The residual displacement components u_1 and u_2 in the –y direction from the top surface after the roller load is removed for the single indentation and rolling cases.

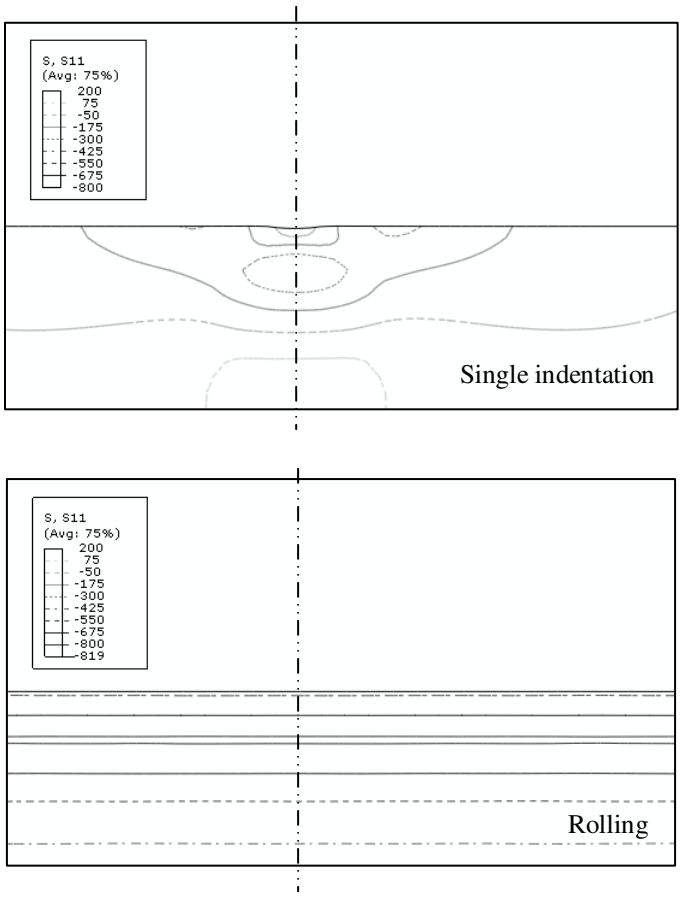

Figure 2.21. The distributions of the residual longitudinal stress σ_{11} after the roller load is removed for the single indentation and rolling cases.

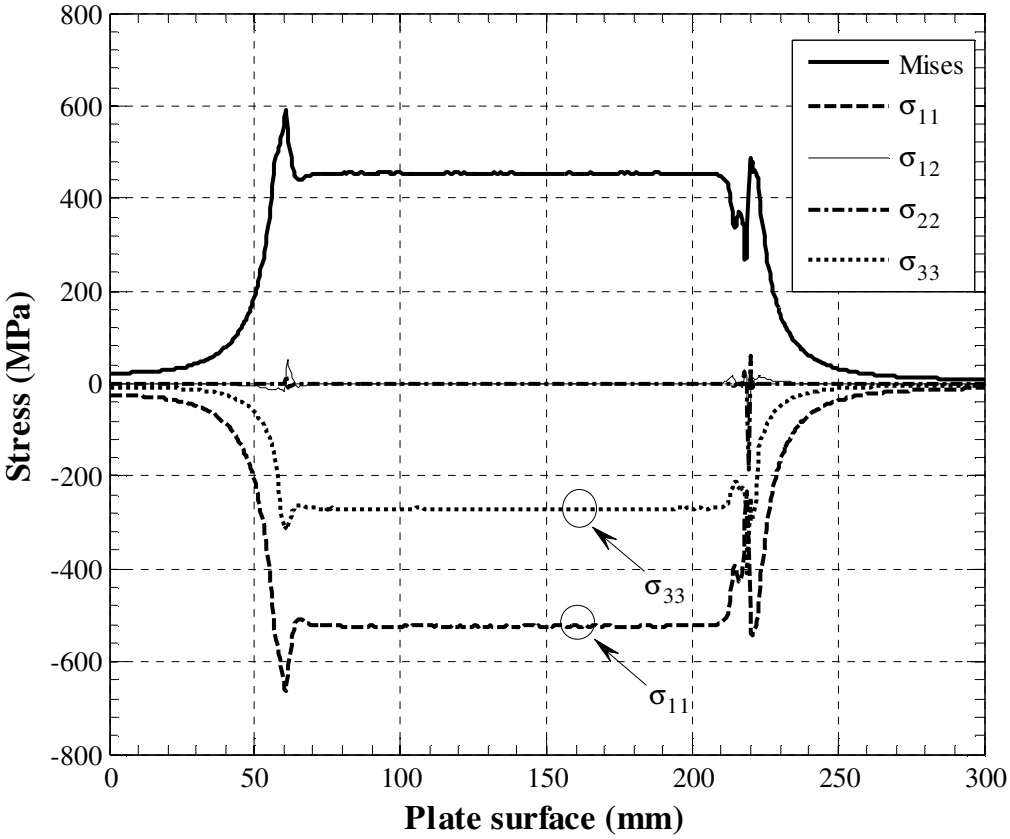

Figure 2.22. The residual stress distributions of the upper surface after the rolling is completed.

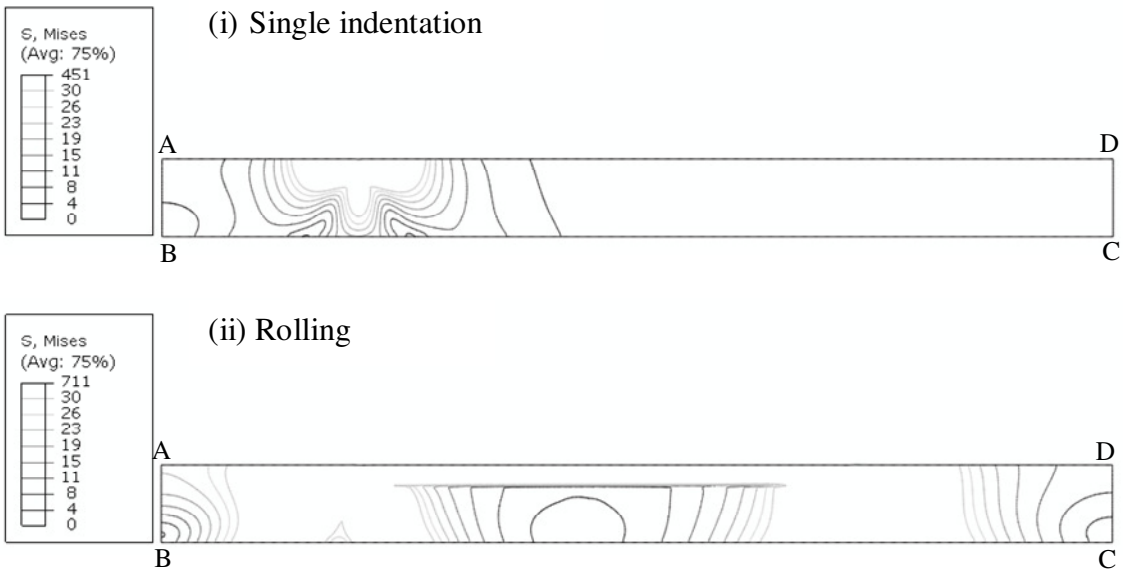

Figure 2.23. The contours of the residual Mises stress after the roller load is removed for the single indentation and rolling cases.

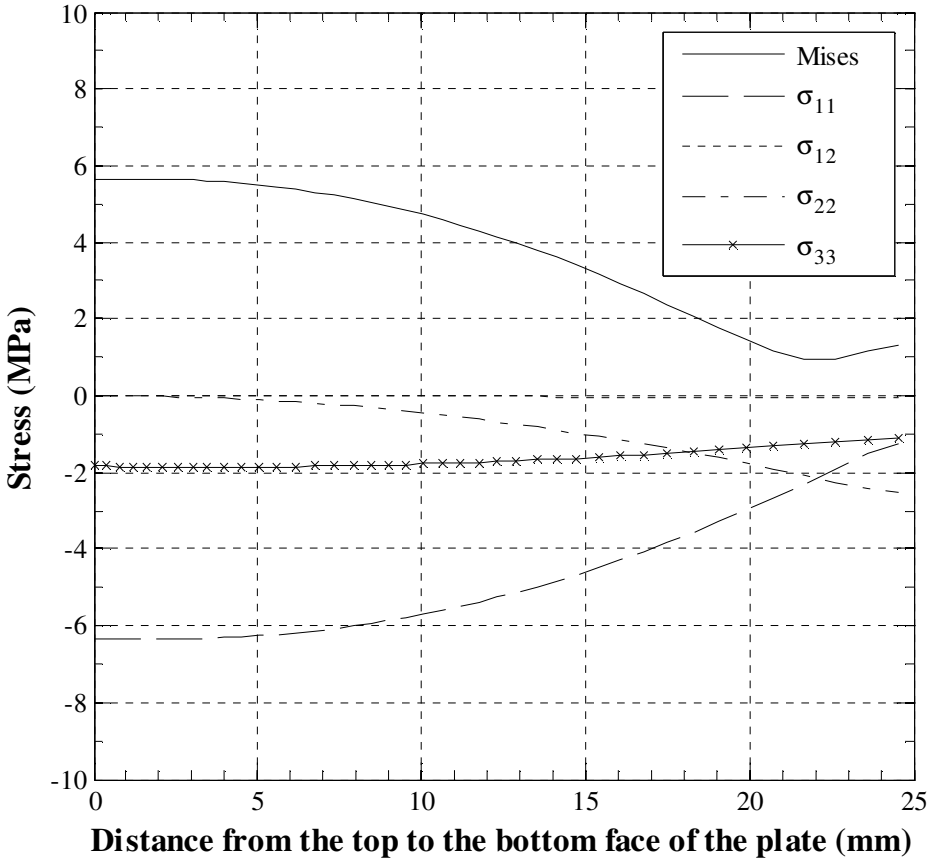
Mises
σ11
σ12
σ22
σ33
Stress (MPa)
Distance from the top to the bottom face of the plate (mm)
10
8
6
4
2
0
-2
-4
-6
-8
-10
0
5
10
15
20
25

(a)

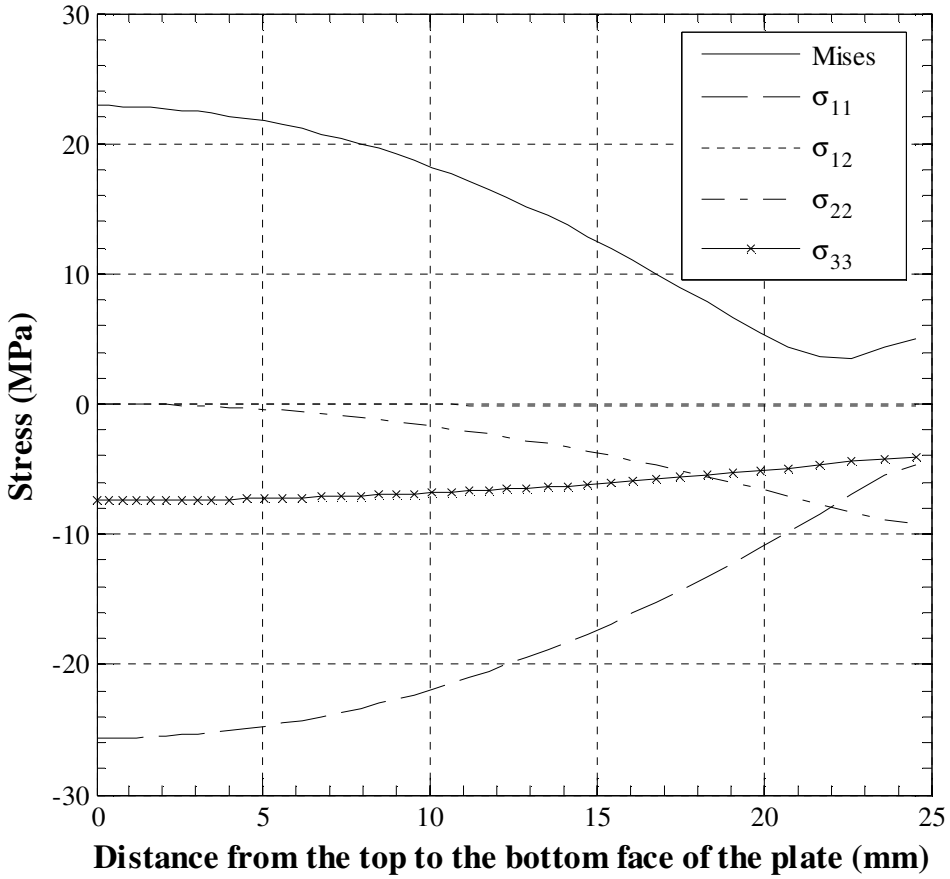

(b)

Figure 2.24. The distributions of the residual stresses on the boundary surface AB of the plate in the –y direction from the top after the roller load is removed for (a) the single indentation and (b) the rolling cases.

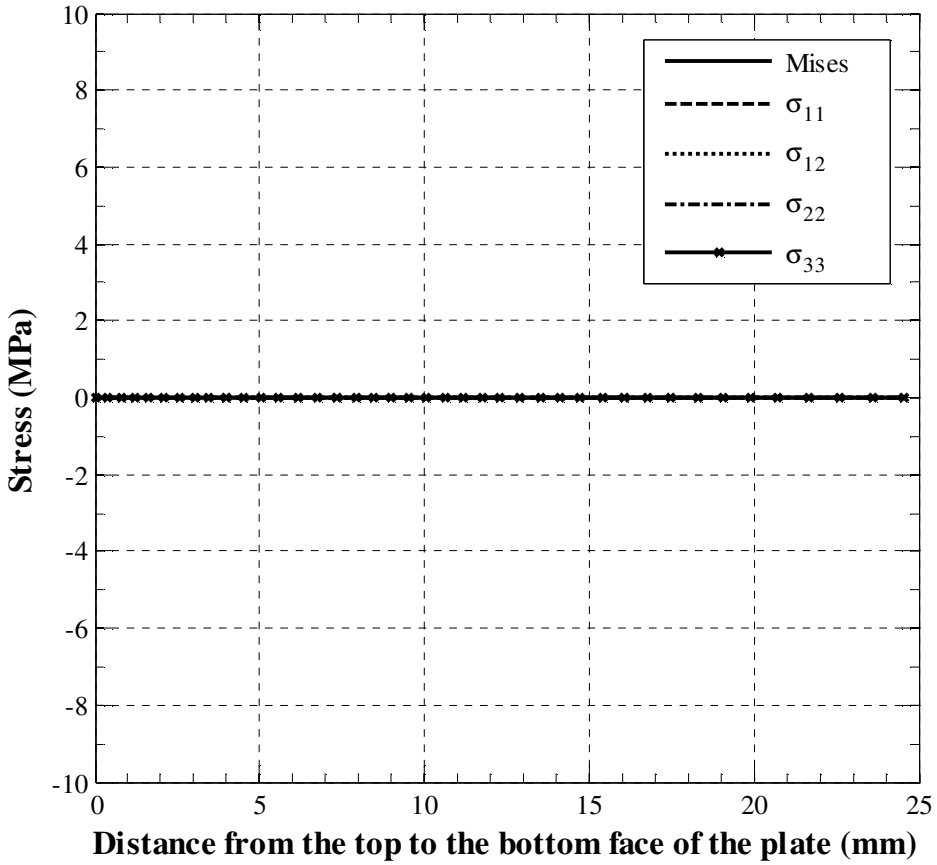
Mises
σ11
σ12
σ22
σ33
Stress (MPa)
Distance from the top to the bottom face of the plate (mm)
10
8
6
4
2
0
-2
-4
-6
-8
-10
0
5
10
15
20
25

(a)

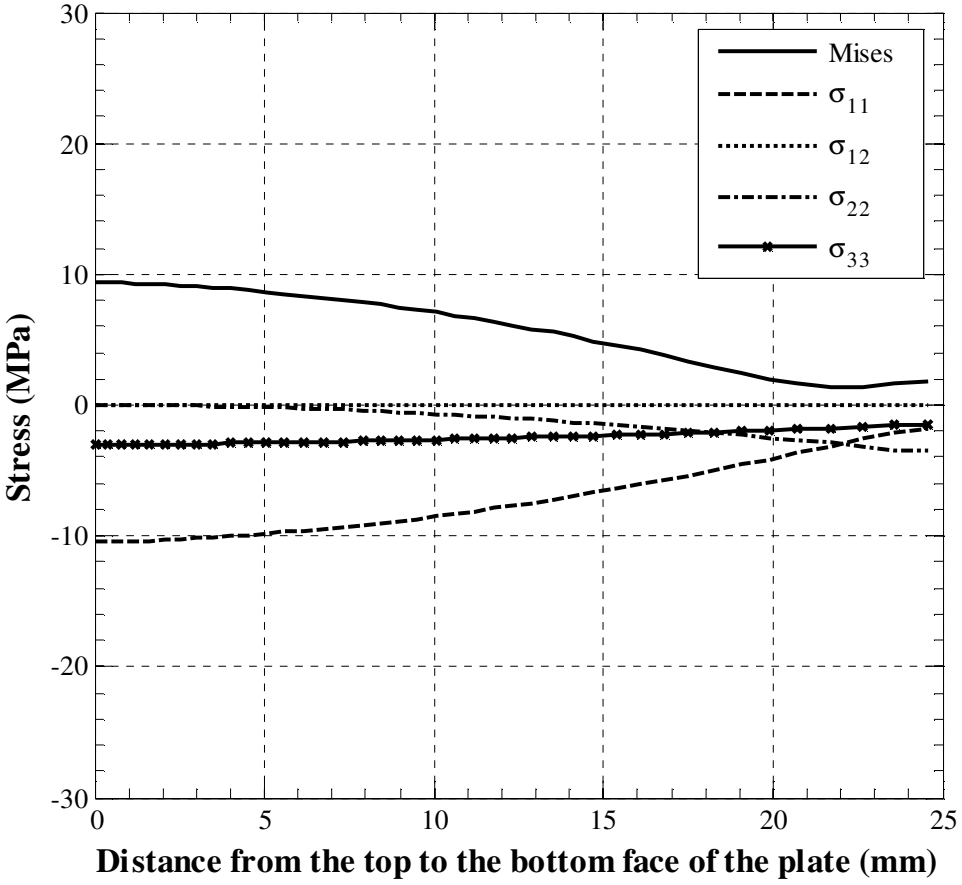

(b)

Figure 2.25. The distributions of the residual stresses on the boundary surface CD of the plate in the –y direction from the top after the roller load is removed for (a) the single indentation and (b) the rolling cases.

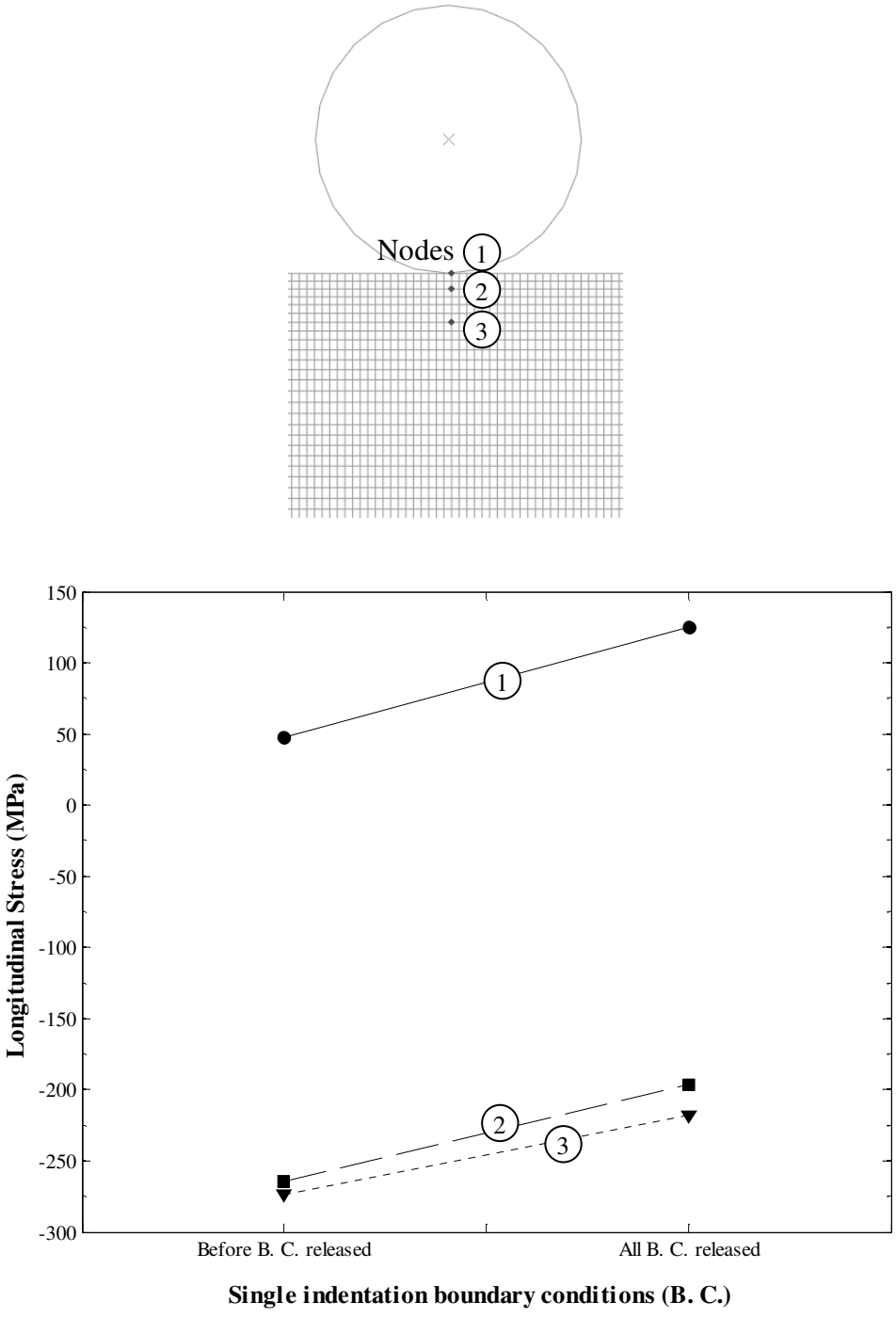
Nodes
1
2
3
150
100
50
0
-50
-100
-150
-200
-250
-300
Longitudinal Stress (MPa)
Before B. C. released
All B. C. released
Single indentation boundary conditions (B. C.)

(a)

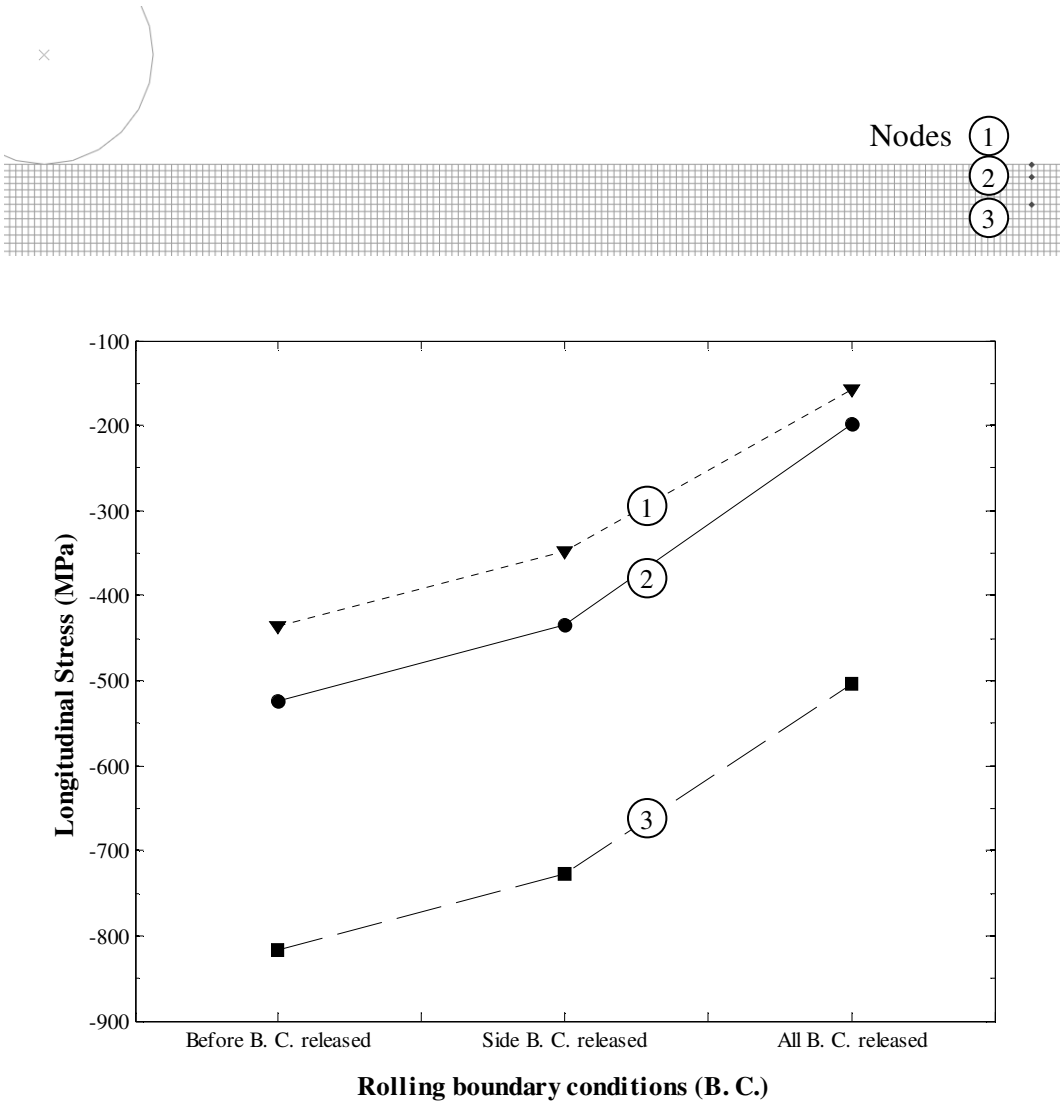

(b)

Figure 2.26. The effects of the boundary conditions on the residual stresses at the marked locations (a) at the marked locations for the single indentation case and (b) at the marked locations at the half rolling length for the rolling case.

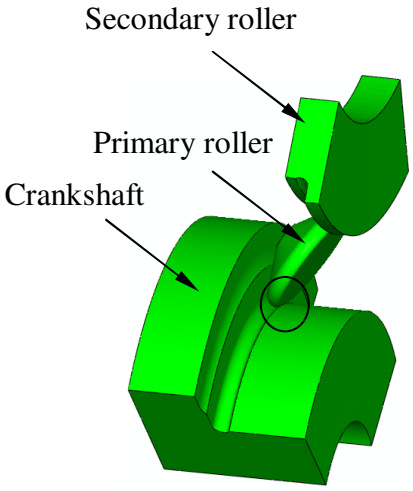

(a)

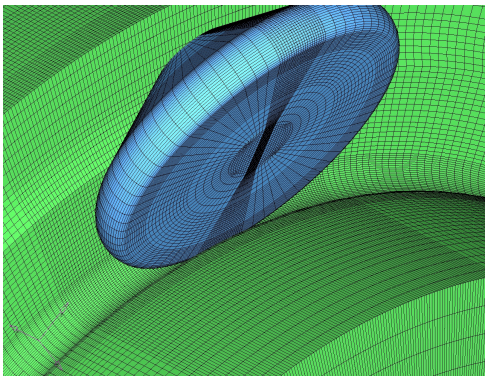

(b)

Figure 2.A1. (a) A three-dimensional finite element model of a crankshaft section under fillet rolling and (b) a magnified view.

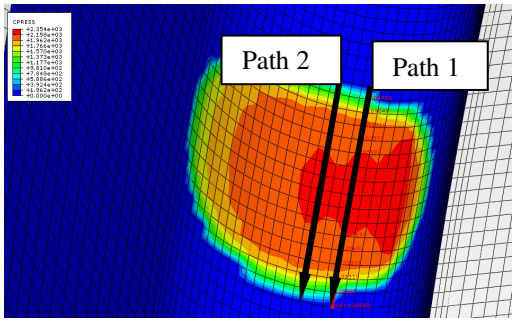

(a)

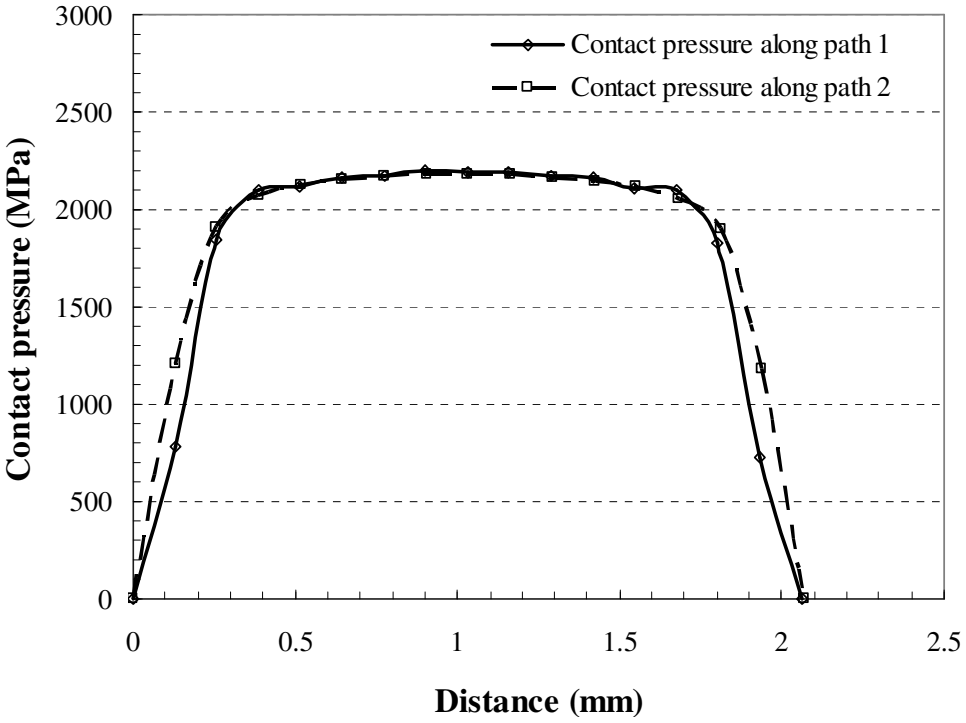

(b)

Figure 2.A2. (a) The contact pressure distribution between the crankshaft and the primary roller, and (b) the contact pressure distributions for paths 1 and 2 as marked in (a).

Chapter 3
Effect of a Deformable Roller on Residual Stress Distribution for Elastic-Plastic Flat Plate Rolling under Plane Strain Conditions

3.1. Introduction

For automotive crankshafts, fatigue damages have been observed near the fillets due to stress concentration. The fillet rolling process has been used for years to introduce compressive residual stresses near crankshaft fillets and, consequently, to improve fatigue strengths of crankshafts [1-3]. The residual stresses can significantly affect the fatigue lives of the crankshafts under high cycle fatigue loading conditions. Previously, researchers estimated the residual stresses near crankshaft fillets either using two-dimensional or three-dimensional finite element analyses [2-8]. Numerous studies were conducted to understand the stress distributions and deformation patterns near rolling contact surfaces [9-22]. A brief discussion of these works can be found in [23].

Most researchers used the moving Hertzian pressure distribution to represent the contact pressure for rolling with p_0/k ratios ranging from 5 to 9, where p_0 is the maximum Hertzian pressure and k is the shear yield stress of the material. For crankshaft rolling, the p_0/k ratio can be as high as 22 as indicated in [23]. Ali and Pan [23] investigated the differences of the residual stresses distributions due to single indentation and rolling by a rigid roller on a finite plate with a very large contact pressure that is relevant to the crankshaft rolling process with a high p_0/k ratio of 22 based on two-dimensional plane strain finite element analyses. The computational results for the

rolling case show a significantly higher longitudinal compressive residual stress and a lower out-of-plane compressive residual stress along the contact surface when compared to those for the single indentation case. Their investigation is further extended in this work to understand the effect of an elastic deformable roller on the residual stresses due to single indentation and rolling with a high p_0/k ratio of 22. A high p_0/k ratio of 22 referred to in this paper is based on the results of a rigid roller indenting an elastic body. For a similar contact configuration, if a rigid roller is replaced by an elastic roller, the p_0/k ratio becomes about 16 due to the elastic deformation of the roller to lower the value of p_0.

This investigation is aimed to quantify the differences between the residual stress distributions in an elastic-plastic plate due to single indentation and rolling by rigid and elastic rollers with a very large contact pressure. As shown later in this paper, the maximum contact pressure and contact width for an elastic roller indenting an elastic plate are significantly lower and higher than those for a rigid roller on elastic plate, respectively. More importantly, the advantages of using a rigid roller instead of an elastic roller give the convenience of applying the roller load with a smaller model size. Both conditions of indentation and rolling are selected for this study to identify whether a rigid roller model can be used to replace an elastic roller model for crankshaft rolling simulations with a sufficient accuracy to obtain the residual stresses distribution for further fatigue strength analyses. While a three-dimensional finite element analysis is more appropriate to calculate the residual stresses due to single indentation and rolling, a two-dimensional model is chosen here to save computational effort.

In this paper, a crankshaft fillet rolling along the circumference of the main journal is idealized to a two-dimensional plane strain flat plate rolling with appropriate boundary conditions. The roller is assumed to be both rigid and linear elastic and the contact between the roller and the plate is frictionless. The roller load per unit width for the two-dimensional model is obtained from the corresponding three-dimensional finite element analysis of single indentation on the crankshaft fillet [23]. Here, the elastic Hertzian solution for contact of two elastic cylinders is first reviewed. Then, the results of elastic plane strain finite element analyses of single indentation on a flat plate are presented for both roller models in order to examine the differences of the elastic contact pressure distributions obtained from both roller models. For this case, the plate is modeled as linear elastic. Next, the results of the elastic-plastic plane strain finite element analyses of single indentation and rolling on a flat plate are presented and compared at a high rolling load with extensive plastic deformation. For this case, the plate material is modeled as an elastic-plastic power-law strain hardening material with the non-linear kinematic hardening rule of ABAQUS [24] for loading and unloading. For the rolling case, only a single pass rolling is simulated. The subsurface stress and residual stress distributions under the roller center induced by the rolling are then compared for the rigid and elastic roller cases. Finally, some conclusions will be made based on the results of this investigation.

3.2. Modeling procedures

Figure 3.1 shows a schematic of a two-dimensional model of a flat plate rolling process. The cylindrical roller is assumed to be both rigid and linear elastic, and the

contact between the roller and the plate is frictionless. Figure 3.1 shows the phases of the rolling simulation. Initially, the roller is sitting on the starting position of the flat plate. Then the roller is moved down with a given load. The roller is then rolled horizontally to the right. After traveling the full rolling length, the roller is moved up and the rolling is completed.

The finite element analyses were performed using the commercial finite element code ABAQUS. The numerical scheme of a two-dimensional finite element analysis of a rigid cylindrical roller rolling on a finite flat plate was presented in Ali and Pan [23] and will not be repeated here. Figure 3.2(a) shows a two-dimensional finite element model of an elastic cylindrical roller rolling on a finite flat plate. The Cartesian coordinate system is also shown in the figure (throughout this paper the Cartesian coordinate notations x, y, z and 1, 2, 3 will be used interchangeably for convenience). The length and the thickness of the plate are 300 mm and 24.552 mm, respectively. Two-dimensional plane strain 4-noded CPE4R elements of size 0.4 mm by 0.4 mm are used in this model. The selection of the sizes of the finite elements to simulate single indentation and rolling follows the guidelines that were established in Ali and Pan [25] and will not be reported here. The diameter of the roller is 14 mm. The bottom of the plate is fixed, and the displacements on both end surfaces AB and CD of the plate in the x direction are constrained. The rolling start point on the upper surface is located at x = 62 mm and the rolling end point is located at x = 216.264 mm to eliminate possible end effects.

The loading and boundary conditions on the elastic roller may be applied in different ways to conduct the plane strain finite element simulations of rolling. Two simulation schemes are presented here: BC-1 and BC-2. For BC-1, a detailed view of the

elastic roller loading and the boundary conditions are shown in Figure 3.2(b). An analytical rigid surface or rigid body of ABAQUS is defined horizontally. The rigid surface is in contact with the upper part of the elastic roller. This top rigid surface is used to apply the rolling load to the elastic roller in the downward direction. The rotational degree of freedom of the rigid surface reference node is constrained but it can move vertically with the applied load and horizontally with an applied motion through a rigid body reference node.

It should be noted that the roller mesh must be sufficiently refined at the contact location between the rigid surface and the roller to avoid numerical convergence issues. The roller is meshed predominantly by quadrilateral elements. In this study, 4-noded quadrilateral elements of size 0.1 mm by 0.16 mm are used for the contact layer of the roller with the 0.1 mm side on the contact side for the given load. The element sizes were selected based on the results of a mesh sensitivity study of the elastic finite element analysis benchmarked with the elastic Hertzian solution as discussed in [25]. The contact between the top rigid surface and the roller is modeled as non-slip (i.e. rough friction) to assist the rigid body rotation of the roller. The arrangement for the rotation of the roller provides the necessary numerical convergence although it is not necessary for the frictionless contact between the roller and the plate as investigated here.

As shown in Figure 3.2(b), the roller center is denoted by L. At any instant, M and M' represent the contact points on the top and bottom surface of the roller, respectively. The distance between M and M' before loading represents the diameter of the elastic roller. A velocity boundary condition v is applied at the roller center L in the x direction to translate the roller in the rolling direction and to overcome the resistance of

the indented surface due to the applied high rolling load. The roller center L is free to move in the vertical direction. The velocity boundary condition of the top rigid surface is chosen to be $2v$ in the x direction based on the rigid body dynamics. With the non-slip condition, the relative velocity of point M is v in the positive x direction with respect to L. On the other hand, the relative velocity of point M' is v in the negative x direction with respect to L. The top rigid surface velocity is chosen here such that there is no relative motion between the roller and the plate at the contact point (near M') according to the rigid body dynamics. This is verified by another finite element analysis that at high rolling load, the roller would be standing still at the rolling start position with only rigid body rotation from the contact at M without the translational motion at the roller center due to frictionless contact between the roller and the plate. This is because the shear traction at point M due to non-slip condition is much smaller than the force necessary to overcome the resistance due to the indented surface at high rolling loads.

It should be noted that the deformed length of LM and LM' would be slightly different under the given rolling load since the elastic roller is contacting the top rigid surface and the lower elastic-plastic plate. The results of the finite element analyses for indentation and rolling indicate that the difference of the deformed lengths of LM and LM' is less than 0.2% of the undeformed roller radius. Therefore, the velocity boundary conditions given at M and L based on the rigid body dynamics appears to be quite acceptable. Figure 3.2(c) shows the Mises stress distribution of the roller for single indentation and rolling to examine the effect of the boundary conditions applied at the roller center L and the contact point M. As shown in the figure, the Mises stress is localized near the roller center L where the velocity boundary condition is applied and it

does not appear to have impact on the stress distributions of the roller near the contact locations. Thus applying the translation motion at the roller center may be acceptable for the current investigation.

Another set of elastic roller loading and boundary conditions (BC-2) is also used for verification purpose and is schematically shown in Figure 3.3. For this set of boundary conditions, there is no top rigid surface and the rolling load is directly applied on the upper side of the roller (near M). The rolling load is evenly divided among a few nodes on the top surface of the roller to avoid numerical problems in the finite element analysis. The selected nodes are the corner nodes of the elements on the roller circumference where the total length of the elements is equivalent to the contact width $2a$ (0.76615 mm for the current case) based on the Hertzian solution for the elastic roller contacting a rigid surface under the given rolling load. The effects of these point loads on the roller are much localized and should not affect the stress and strain distributions near the contact surface between the roller and the plate far away from the applied load based on the Saint-Venant's principle. A velocity boundary condition v is still applied at the roller center L in the x direction to translate the roller in the rolling direction and to overcome the resistance due to the indented surface under the high rolling load. Here, the rigid body rotation of the roller is not necessary since the contact between the roller and the plate is frictionless and this differentiates BC-2 from BC-1 as shown in Figure 3.2(b). The results of the stress distributions in the plate for single indentation and rolling with the BC-2 are found in very good agreement with those of the BC-1. The results of the comparisons are not presented here for brevity. However, for the elastic roller case, the results based on the BC-1 loading and boundary conditions are presented in this paper,

since the BC-1 can also be applied to the cases where the friction between the elastic roller and the plate is considered.

It should be mentioned again that the numerical scheme of a two-dimensional finite element analysis of a rigid cylinder rolling on a finite flat plate was developed, and the details of the loading and boundary conditions for the rigid roller were presented in [23]. One goal of this investigation is to examine the residual stresses in crankshafts after fillet rolling by a rigid and an elastic roller models. The total rolling length 154.264 mm and the plate thickness 24.552 mm are corresponding to the circumferential length and the radius of the main journal of a crankshaft of interest, respectively. The details to determine the rolling load can be found in [23].

Figure 3.4 shows the tensile stress–strain curve of the plate material. The nonlinear kinematic hardening rule of ABAQUS is assumed based on the tensile stress-strain curve shown in Figure 3.4. The nonlinear kinematic hardening rule in ABAQUS is based on the Mises yield function. For the loading/unloading/reloading process, the yield function can be expressed as

$$f\left(\sigma_{ij}-\alpha_{ij},\sigma^{0}\right)=\left[\frac{3}{2}\left(\sigma'_{ij}-\alpha'_{ij}\right)\left(\sigma'_{ij}-\alpha'_{ij}\right)\right]^{\frac{1}{2}}-\sigma^{0}=0 \tag{3.1}$$

where σ_{ij} is the stress tensor, σ'_{ij} is the deviatoric stress tensor, α_{ij} represents the center of the yield surface, α'_{ij} is the deviatoric part of α_{ij}, and σ^{0} represents the size of the yield surface. Here, σ'_{ij} and α'_{ij} are defined, respectively, as

$$\sigma'_{ij}=\sigma_{ij}-\frac{1}{3}\sigma_{kk}\delta_{ij} \tag{3.2}$$

$$\alpha'_{ij} = \alpha_{ij} - \frac{1}{3}\alpha_{kk}\delta_{ij} \tag{3.3}$$

where δ_{ij} is the kronecker delta.

The associated plastic flow is expressed as

$$\dot{\varepsilon}^p_{ij} = \dot{\bar{\varepsilon}}^p \frac{\partial f\left(\sigma_{ij} - \alpha_{ij}, \sigma^0\right)}{\partial \sigma_{ij}} \tag{3.4}$$

where $\dot{\varepsilon}^p_{ij}$ represents the plastic strain rate tensor and $\dot{\bar{\varepsilon}}^p$ is the equivalent plastic strain rate defined as

$$\dot{\bar{\varepsilon}}^p = \left(\frac{2}{3}\dot{\varepsilon}^p_{ij}\dot{\varepsilon}^p_{ij}\right)^{\frac{1}{2}} \tag{3.5}$$

In ABAQUS, the nonlinear kinematic hardening rule is defined to be an additive combination of a purely kinematic term of the Ziegler linear hardening law and a relaxation term which introduces the nonlinearity. The evolution of α_{ij} is expressed as

$$\dot{\alpha}_{ij} = \frac{C}{\sigma_0}\dot{\bar{\varepsilon}}^p\left(\sigma_{ij} - \alpha_{ij}\right) - \gamma\dot{\bar{\varepsilon}}^p\alpha_{ij} \tag{3.6}$$

where σ_0 is constant and represents the size of the initial yield surface, α_{ij} represents the center of the yield surface, $\dot{\bar{\varepsilon}}^p$ is again the equivalent plastic strain rate, and C and γ are material parameters that must be calibrated from cyclic test data. Here, C is the initial kinematic hardening modulus and γ determines the rate at which the kinematic hardening modulus decreases with increasing plastic deformation. When C and γ are zero, the model reduces to the isotropic hardening rule. When γ is zero, the Ziegler

linear hardening law is recovered. Note that, for the nonlinear kinematic hardening rule of ABAQUS, the option of "HALF CYCLE" for data type was adopted in order to use the cyclic stress-strain curve of the material as the input stress-strain data [24].

3.3. Elastic Hertzian solutions and elastic finite element analyses

Consider two infinitely long cylinders with their longitudinal axes both lying parallel are pressed in contact by a force P per unit length as schematically shown in Figure 3.5(a). The Cartesian coordinates are also shown. The two cylinders make contact over a long strip of width $2a$ lying parallel to their axes as shown in Figure 3.5(a). The expressions for the load P, the half contact width a and the pressure $p(x)$ are [26]:

$$P = \frac{\pi a^2 E^*}{4R} \tag{3.7}$$

$$a^2 = \frac{4PR}{\pi E^*} \tag{3.8}$$

where

$$E^* \equiv \left(\frac{1-\nu_1^{\,2}}{E_1} + \frac{1-\nu_2^{\,2}}{E_2} \right)^{-1}$$

and

$$R \equiv \left(\frac{1}{R_1} + \frac{1}{R_2} \right)^{-1}$$

Here, E represents the modulus of elasticity, ν represents the Poisson's ratio, and R represents the radius. The subscripts 1 and 2 represent the upper and lower cylinders, respectively.

The contact pressure distribution is

$$p(x) = \frac{2P}{\pi a^2}\left(a^2 - x^2\right)^{\frac{1}{2}} \tag{3.9}$$

The maximum pressure is expressed as

$$p_0 = \frac{2P}{\pi a} = \left(\frac{PE^*}{\pi R}\right)^{1/2} \tag{3.10}$$

The stresses at a point (x, y) are [26]

$$\sigma_{11} = -\frac{p_0}{a}\left\{m\left(1 + \frac{y^2 + n^2}{m^2 + n^2}\right) - 2y\right\} \tag{3.11}$$

$$\sigma_{22} = -\frac{p_0}{a} m\left(1 - \frac{y^2 + n^2}{m^2 + n^2}\right) \tag{3.12}$$

$$\sigma_{12} = -\frac{p_0}{a} n\left(\frac{m^2 - y^2}{m^2 + n^2}\right) \tag{3.13}$$

where

$$m^2 = \frac{1}{2}\left[\left\{(a^2 - x^2 + y^2)^2 + 4x^2y^2\right\}^{1/2} + (a^2 - x^2 + y^2)\right] \tag{3.14}$$

$$n^2 = \frac{1}{2}\left[\left\{(a^2 - x^2 + y^2)^2 + 4x^2y^2\right\}^{1/2} - (a^2 - x^2 + y^2)\right] \tag{3.15}$$

and the signs of m and n are the same as the signs of y and x, respectively.

Under plane strain conditions, the third principal stress σ_{33} is

$$\sigma_{33} = \nu(\sigma_{11} + \sigma_{22}) \tag{3.16}$$

The von Mises stress is expressed as a function of the stress components as

$$\sigma_{Mises} = \frac{1}{\sqrt{2}}\sqrt{(\sigma_{11} - \sigma_{22})^2 + (\sigma_{22} - \sigma_{33})^2 + (\sigma_{33} - \sigma_{11})^2 + 6\sigma_{12}^2} \tag{3.17}$$

The stresses in equations (3.11)-(3.13), (3.16) and (3.17) based on the elastic Hertzian solution will be plotted in Figures 3.6(a) and 3.6(b) as discussed later. When the radius

R_2 of the lower cylinder becomes infinity, the lower cylinder becomes a semi-infinite solid which is schematically represented by a flat plate as shown in Figure 3.5(b). This corresponds to the case of an elastic flat plate indented by an elastic roller. When the elastic modulus E_1 of the upper roller becomes infinity, the roller becomes rigid as shown in Figure 3.5(c). This corresponds to the case of an elastic flat plate indented by a rigid roller.

For elastic contact analyses, the finite element mesh size of 0.1 mm is used in this study [25]. Figure 3.6(a) shows the distributions of the stresses directly under the roller in the –y direction from the top surface of the plate for indentation by the elastic roller at the full rolling load. Here, the plate is modeled to be linear elastic. Figure 3.6(b) is a zoom-in view of Figure 3.6(a) to show the stresses in the top 5 mm strip of the plate. For the elastic Hertzian solution, at the contact interface $\sigma_{11} = \sigma_{22} = -p(x)$. At the contact point, the stress σ_{22} obtained from the finite element analysis is within 2% of the elastic Hertzian solution. However, the stress σ_{11} obtained from the finite element analysis is 21% lower than the elastic Hertzian solution. This may be attributed to the mesh discretization [9]. The shear stress component σ_{12} should be zero directly under the roller center. However, the stresses are obtained from the nodal points which are not exactly under the center of the roller. Therefore, very small values of σ_{12} are shown in Figures 3.6(a) and 3.6(b) due to a small offset of these nodal points from the centerline of the roller. Accordingly, the elastic Hertzian solutions based on the appropriate value of the x coordinate for these nodal points are also plotted in Figures 3.6(a) and 3.6(b) for comparison purpose. Figure 3.7(a) shows the contact pressure distributions on the plate surface based on the elastic Hertzian solution and the results of the elastic finite element

analysis due to indentation by the rigid roller. Figure 3.7(b) shows the contact pressure distributions on the plate surface based on the elastic Hertzian solution and the results of the elastic finite element analysis due to indentation by the elastic roller. The contact pressure distribution obtained by the elastic finite element analysis is in good agreement with the elastic Hertzian solution except at the corner of the contact point which can be attributed to the mesh discretization [9]. For the case with the elastic roller model, the elastic Hertzian solution showed the maximum contact pressure is about 29% lower and the half contact width is about 40% higher compared to those of the rigid roller model. As shown in Figures 3.7(a) and 3.7(b) the assumption of a rigid roller or a linear elastic roller can have significant effects on the contact pressure distributions and then the subsurface stress distributions when the plate is assumed as linear elastic. Next, the effects of the different roller models on the contact pressure and subsurface stress distributions are examined when the plate is assumed to be elastic-plastic.

3.4. Elastic-plastic finite element analyses

Figure 3.8(a) shows the contact pressure distribution for both roller models between the roller and the plate due to single indentation based on the elastic-plastic finite element analyses conducted in this investigation. The corresponding elastic Hertzian solutions are shown in Figures 3.7(a) and 3.7(b). The results of the elastic-plastic finite element analyses show that the contact pressure distribution is no longer similar to the Hertzian pressure distribution but rather flat and wide. The pressure distributions are in general agreement with the findings of Kral et al. [10] and Komvopoulos [11]. Also the maximum contact pressures and the half contact widths for

both roller models are about the same. This is due to the subsurface plastic flow that leads to a flat and wide pressure distribution. As shown in Figures 3.7(a), 3.7(b) and 3.8(a), although there are notable differences in the elastic Hertzian solutions for the elastic and the rigid rollers indenting an elastic plate, there are no significant differences in the contact pressure distributions for these rollers when indenting an elastic-plastic plate. Figure 3.8(b) shows the representative contact pressure distributions for both roller models between the roller and the plate for rolling after the steady states of the contact pressure distributions are reached when the roller rolls a half rolling length. The results confirm that the contact pressure distributions are neither similar to the Hertzian pressure distribution nor symmetric. The total contact widths ($2a$) for both roller models are with a small difference of 4% and with a slightly larger trailing contact for the elastic roller. The contact pressure distribution for the elastic roller shows a slightly lower (4%) maximum contact pressure value and a smaller pressure on the forward side when compared to that of the rigid roller case. This is due to the deformation of the elastic roller that results in a slightly lower contact pressure in front of the roller whereas the contact pressure near the back of the roller got slightly higher to balance the given rolling load. However, it will be shown later that the impact of these differences is minimal on the stress distribution in the plate directly under the roller center. A finer mesh size of 0.1 mm was used for this purpose to capture the detailed pressure distributions. It should be noted that the computational time for the finite element analysis based on the 0.1 mm mesh is prohibitively high to conduct a full rolling analysis.

Figure 3.9(a) shows the stress distributions directly under the roller center in the – y direction from the top surface of the elastic-plastic plate when the roller is down for the

cases of indentation by the rigid and elastic rollers. For the indentation, the peak values of the compressive stress components σ_{11}, σ_{22} and σ_{33} occur at the contact surface directly under the roller center. Note again that the stresses are obtained from the nodal points which are not exactly under the roller center. Therefore, very small values of σ_{12} exist due to a small offset of these nodal points from the roller centerline. The distributions of the stresses for both roller models are about the same with no significant differences. Figure 3.9(b) shows the displacement components u_1 and u_2 directly under the roller center in the –y direction from the top surface of the elastic-plastic plate for indentation by both rollers. The displacement component u_2 for the rigid roller case is slightly higher (about 3%) than that for the elastic roller case. However, the displacement components u_1 are nearly the same for both cases. Note that the u_1 component exists due to a small offset of these nodal points from the roller centerline as mentioned above.

Figure 3.10(a) shows the stress distributions directly under the roller center in the –y direction from the top surface of the elastic-plastic plate for rolling as the roller is rolled to the half rolling length for both roller models. It should be noted that the rolling distances are about half of the rolling length for the two cases and they are slightly different due to the ABAQUS automatic step increments. However, the results are presented to show the similarity of the stress distributions for the two roller cases. A slightly higher compressive stresses σ_{22} (about 7%) and σ_{33} (about 5%) at the contact surface for the elastic roller case may be attributed to the slightly higher (2%) contact pressure directly under the roller center (Figure 3.8(b)) compared to those of the rigid roller case. On the other hand, a slightly smaller compressive σ_{11} (about 8%) for the rigid roller case may be attributed to a slight forward shift of the maximum contact pressure

distribution for the rigid roller case (Figure 3.8(b)) compared to those of the elastic roller case. A detailed discussion regarding the comparison of the stress distributions directly under the roller center in the –y direction from the top surface of the plate for indentation and rolling can be found in [23]. Figure 3.10(b) shows the displacement components u_1 and u_2 directly under the roller center in the –y direction from the top surface of the elastic-plastic plate for rolling as the roller is rolled to the half rolling length for both roller models. The displacement component u_1 for the rigid roller case is slightly higher than the elastic roller case due to the slight forward shift of the maximum contact pressure distribution for the rigid roller case compared to that for the elastic roller case (Figure 3.8(b)). However, the displacement components u_2 are nearly the same for both cases.

Figure 3.11(a) shows a comparison of the residual stresses distributions in the –y direction from the top surface of the plate after the roller load is removed for both roller cases. The residual stress distributions for both roller cases are nearly identical. The values of the residual stresses at the contact surface for both roller cases are about the same except a slightly (2%) higher peak subsurface compressive residual stress components σ_{11} and σ_{33} for the rigid roller case when compared to that for the elastic roller case. The residual stress components σ_{12} and σ_{22} have very small values near the surface for both cases. These small values could not be shown clearly in Figure 3.11(a) due to the scale of the figure. Figure 3.11(b) shows the residual displacement components u_1 and u_2 in the –y direction from the top surface of the plate for both roller cases after the roller load is removed. The residual value of the displacement component

u_1 for the rigid roller case is higher than that for the elastic roller case. This may be attributed to the accumulation due to a slight forward shift of the maximum contact pressure distribution for rolling for the rigid roller case when compared to that of the elastic roller case (Figure 3.8(b)). The residual values of the displacement components u_2 are nearly the same for both cases. In summary, there are no significant differences for the residual stresses distributions due to rolling for both roller models at very high rolling loads and the rigid roller model can be used to obtain the residual stresses in rolling simulations at very high rolling loads to save computational time.

3.5. Conclusions

In this paper, the differences of the residual stresses due to rolling in a finite elastic-plastic plate by rigid and elastic deformable rollers at very high rolling loads are investigated by two-dimensional plane strain finite element analyses using ABAQUS. In the finite element analyses, the rollers are modeled both as rigid and linear elastic, and have frictionless contact with the elastic-plastic finite plate. The plate material is modeled as an elastic-plastic power-law strain hardening material with a non-linear kinematic hardening rule for loading and unloading. Two new numerical schemes are developed to represent the elastic roller to model the indentation and rolling. The results of the contact pressure and subsurface stress distributions from the two numerical schemes are almost identical. For both roller models, the computational results show that the contact pressure and subsurface stress distributions in the elastic-plastic plate are similar for both indentation and rolling at high rolling loads with extensive plastic deformation. The computational results also indicate that the residual stresses after

rolling are nearly the same for both roller models. The computational results suggest that the rigid roller model can be used to obtain the residual stresses in rolling simulations at very high rolling loads without sacrificing the accuracy.

Acknowledgements

The encouragement of Dr. Jagadish Sorab of Ford Motor Company to conduct this research work is greatly appreciated. Helpful discussions with Dr. Simon Ho of Chrysler LLC are also greatly appreciated.

References

1. Love, R. J. and Waistall, D. N., "The Improvement in the Bending Fatigue Strength of Production Crankshafts by Cold Rolling," M.I.R.A. Report No. 1954/1:1-8, 1954.
2. Spiteri, P., Ho, S., and Lee, Y. L., "Assessment of Bending Fatigue Limit for Crankshaft Sections with Inclusion of Residual Stresses," *Int. J. Fatigue*, **29**:318-329, 2007, doi:10.1016/j.ijfatigue.2006.03.009.
3. Choi, K. S., Pan, J., and Ho, S., "Fatigue Failures of Rollers in Crankshaft Fillet Rolling," SAE Technical Paper 2004-01-1498, 2004.
4. Chien, W. Y., Pan, J., Close, D., and Ho, S., "Fatigue Analysis of Crankshaft Sections under Bending with Consideration of Residual Stresses," *Int. J. Fatigue*, **27**:1–19, 2005, doi:10.1016/j.ijfatigue.2004.06.009.
5. Choi, K. S. and Pan, J., "Simulations of Stress Distributions in Crankshaft Sections under Fillet Rolling and Bending Fatigue Tests," *Int. J. Fatigue*, **31**:544-557, 2009, doi:10.1016/j.ijfatigue.2008.03.035.
6. Choi, K. S. and Pan, J., "A Generalized Anisotropic Hardening Rule Based on the Mroz Multi-Yield-Surface Model for Pressure Insensitive and Sensitive Materials," *Int. J. of Plasticity*, **25**(7):1325-1358, 2009, doi:10.1016/j.ijplas.2008.09.005.
7. Choi, K. S., Pan, J., and Ho, S., "Effects of Roller Geometry on Contact Pressure and Residual Stress in Crankshaft Fillet Rolling," SAE Technical Paper 2005-01-1908, 2005.
8. Ho, S., Lee, Y-L, Kang, H.-T., and Wang, C. J., "Optimization of a Crankshaft Rolling Process for Durability," *Int. J. Fatigue*, **31**:799-808, 2009, doi:10.1016/j.ijfatigue.2008.11.011.
9. Mesarovic, S. Dj. and Fleck, N. A., "Spherical Indentation of Elastic-Plastic Solids," Proc. R. Soc. Lond. A, **455**:2707-2728, 1999.
10. Kral, E. R., Komvopoulos, K., and Bogy, D. B., "Elastic-Plastic Finite Element Analysis of Repeated Indentation of Half-Space by a Rigid Sphere," *J. Appl. Mech.*, **60**:829-841, 1993, doi:10.1115/1.2900991.
11. Komvopoulos, K., "Elastic-Plastic Finite Element Analysis of Indented Layered Media," *J. Tribol.*, **111**(3):430-439, 1989, doi:10.1115/1.3261943.
12. Merwin, J. E. and Johnson, K. L., "An Analysis of Plastic Deformation in Rolling Contact," Proc. Instn. Mech. Engrs., **177**(25):676-690, 1963.
13. Kulkarni, S. M., Hahn, G. T., Rubin, C. A., and Bhargava, V., "Elastoplastic Finite Element Analysis of Three-Dimensional, Pure Rolling Contact at the Shakedown Limit," *J. Appl. Mech.*, **57**:57-65, 1990, doi:10.1115/1.2888324.
14. Kulkarni, S. M., Hahn, G. T., Rubin, C. A., and Bhargava, V., "Elasto-Plastic Finite Element Analysis of Three-Dimensional Pure Rolling Contact Above the Shakedown Limit," *J. of Appl. Mech.*, **58**:347-353, 1991, doi:10.1115/1.2897192.
15. Yu, M., Moran, B., and Keer, L. M., "A Direct Analysis of Two-Dimensional Elastic-Plastic Rolling Contact," *J. Tribol.*, **115**:227–236, 1993, doi:10.1115/1.2920996.
16. Yu, M. M. H., Moran, B., and Keer, L. M., "A Direct Analysis of Three-Dimensional Elastic-Plastic Rolling Contact," *J. Tribol.*, **117**:234–243, 1995, doi:10.1115/1.2831236.

17. Bhargava, V., Hahn, G. T., and Rubin, C. A., "An Elastic-Plastic Finite Element Model of Rolling Contact Part 1: Analysis of Single Contacts," *J. of Appl. Mech.*, **52**:67-74, 1985, doi:10.1115/1.3169028.
18. Bhargava, V., Hahn, G. T., and Rubin, C. A., "An Elastic-Plastic Finite Element Model of Rolling Contact Part 2: Analysis of Repeated Contacts," *J. of Appl. Mech.*, **52**:75-82, 1985, doi:10.1115/1.3169030.
19. Chen, W. W., Wang, Q. J., Wang, F., Keer, L. M., and Cao, J., "Three-Dimensional Repeated Elasto-Plastic Point Contacts, Rolling, and Sliding," *J. of Appl. Mech.*, **75**:021021, 2008, doi:10.1115/1.2755171.
20. Jiang, Y. and Sehitoglu, H., "Rolling Contact Stress Analysis with the Application of a New Plasticity Model," *Wear*, **191**:35-44, 1996, doi:10.1016/0043-1648(95)06663-2.
21. Jiang, Y., Xu, B., and Sehitoglu, H., "Three-Dimensional Elastic-Plastic Stress Analysis of Rolling Contact," *J. Tribol.*, **124**:699–708, 2002, doi:10.1115/1.1491978.
22. Bijak-Zochowski, M. and Marek, P., "Residual Stress in Some Elasto-Plastic Problems of Rolling Contact with Friction," *Int. J. Mech. Sci.*, **39**(1):15-32, 1997, doi:10.1016/0020-7403(96)00018-5.
23. Ali, M. Y. and Pan, J., "Elastic-Plastic Indentation and Flat Plate Rolling under Plane Strain Conditions," *SAE Int. J. Mater. Manuf.,* **4**(1):125-137, 2011, doi:10.4271/2011-01-0035.
24. ABAQUS Version 6.8 User Manual, SIMULIA, Providence, RI, 2008.
25. Ali, M. Y. and Pan, J., Research work to be submitted for publication, 2012.
26. Johnson, K. L, "Contact Mechanics", Cambridge University Press, ISBN 0-521-34796-3, 1987.

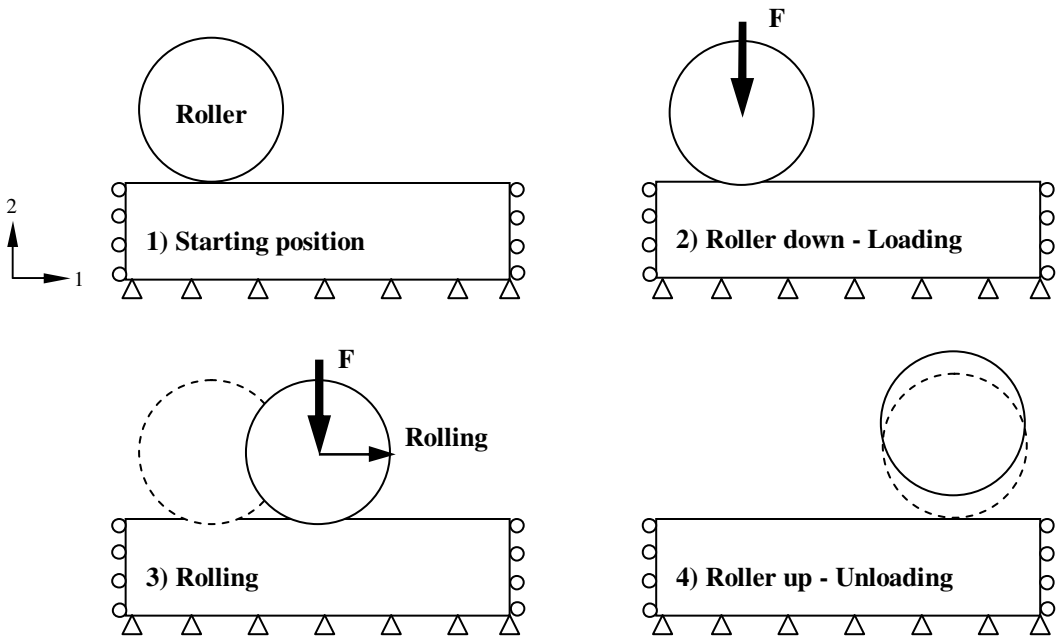

Figure 3.1. A schematic of a two-dimensional model of a flat plate rolling process. The roller is assumed to be both rigid and linear elastic, and the contact between the roller and the plate is frictionless.

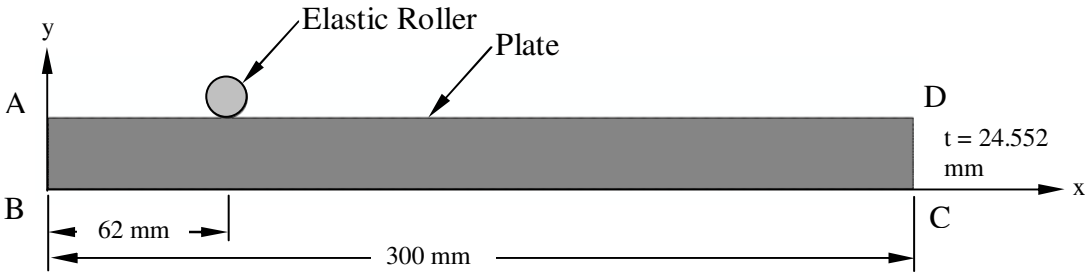
y
Elastic Roller
Plate
A
D
t = 24.552
mm
x
B
C
62 mm
300 mm

(a)

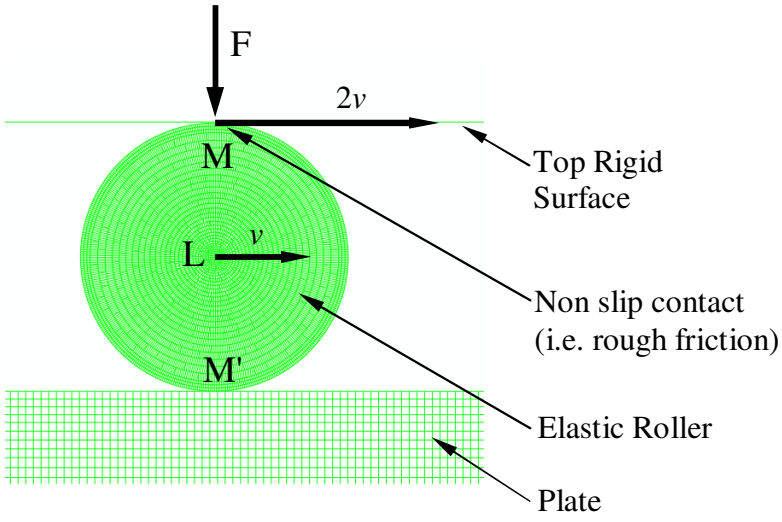
F
2v
M
Top Rigid
Surface
v
L
Non slip contact
(i.e. rough friction)
M'
Elastic Roller
Plate

(b)

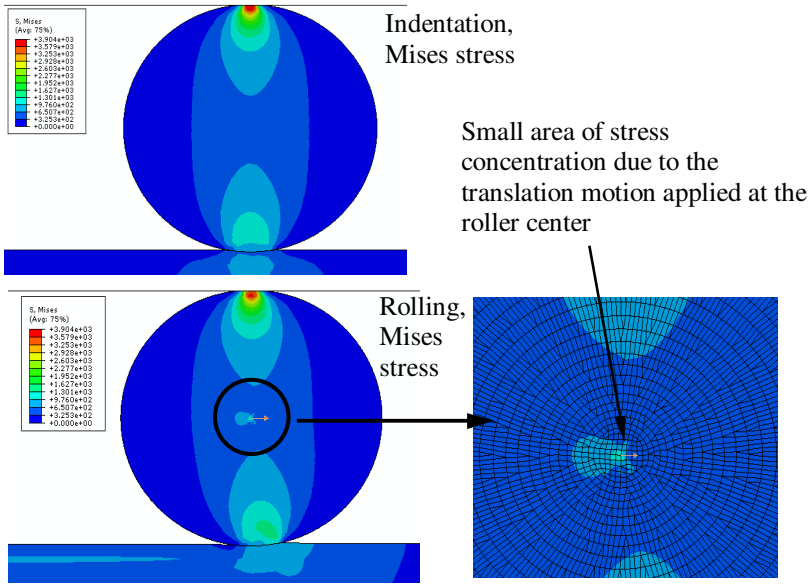

(c)

Figure 3.2. (a) A two-dimensional finite element model of an elastic cylinder rolling on a finite flat plate, (b) a detailed view of the loading and boundary conditions (BC-1) of the elastic roller, and (c) the Mises stress distribution of the roller for single indentation and rolling to examine the effect of the boundary conditions applied at the roller center L and the contact point M.

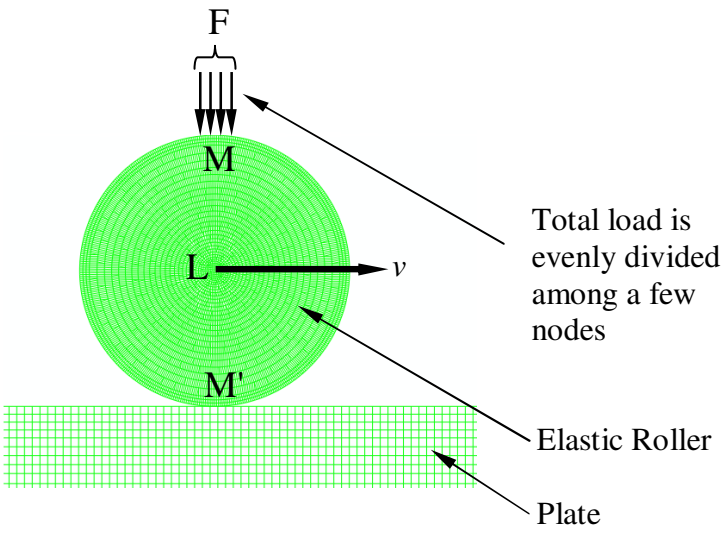

Figure 3.3. A detailed view of the loading and boundary conditions (BC-2) of the elastic roller.

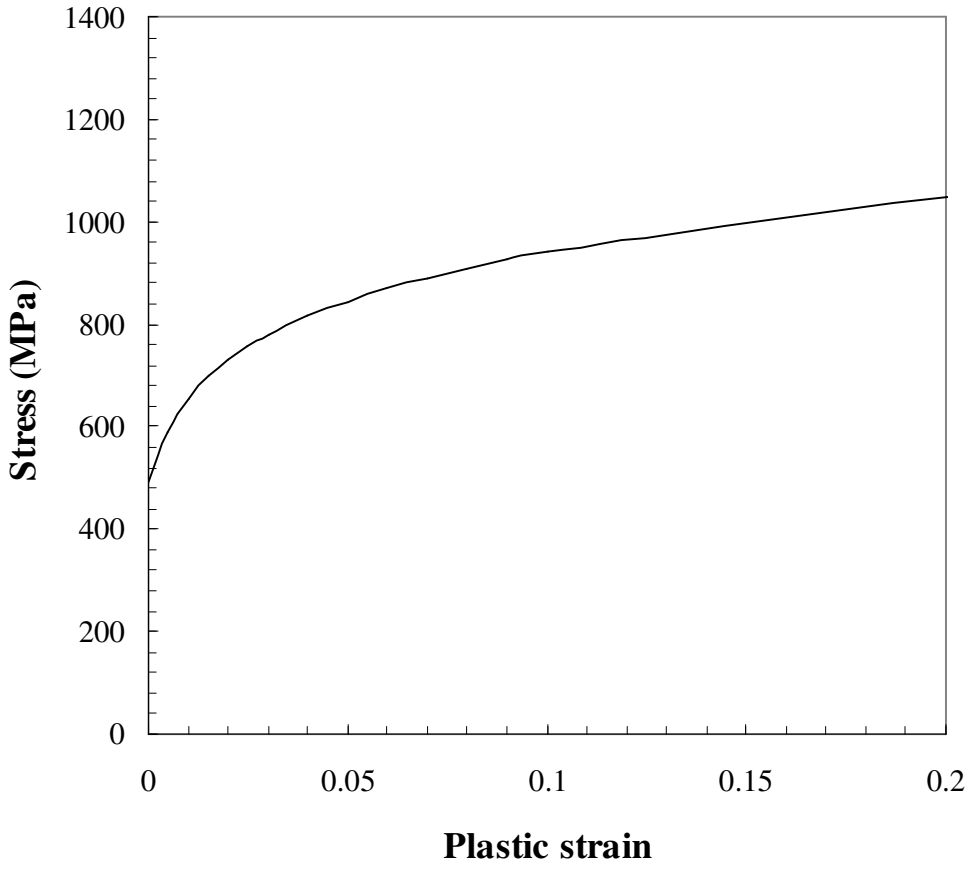

Figure 3.4. The tensile stress–strain curve of the plate material used in the finite element analyses.

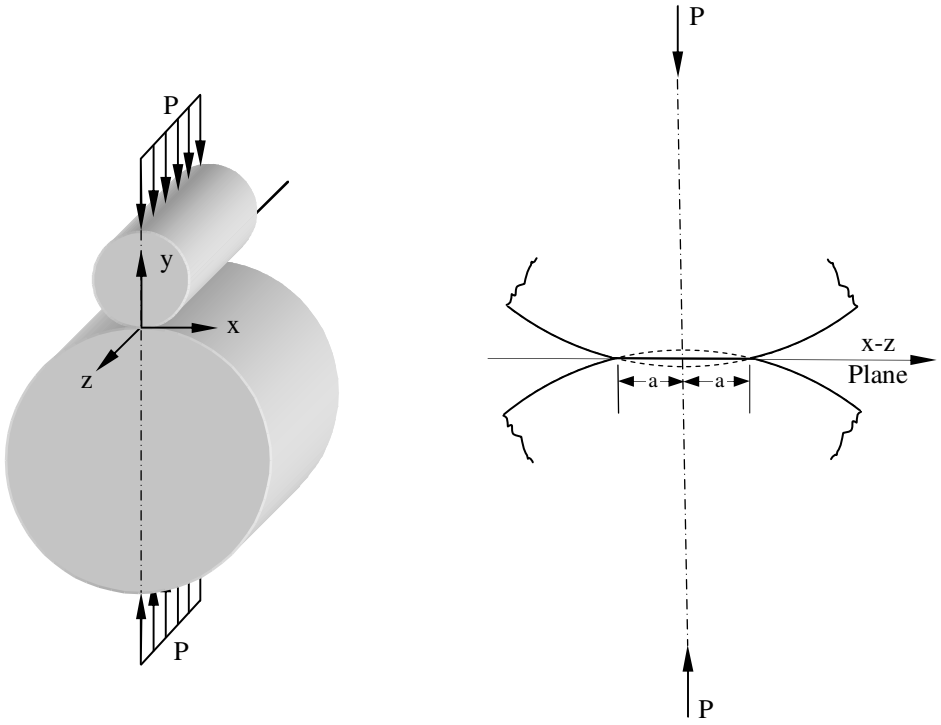

(a)

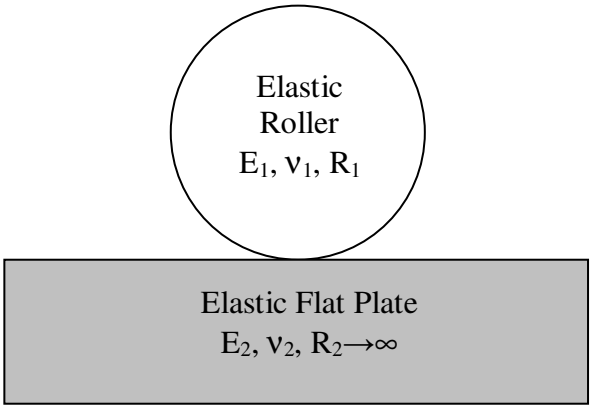

(b)

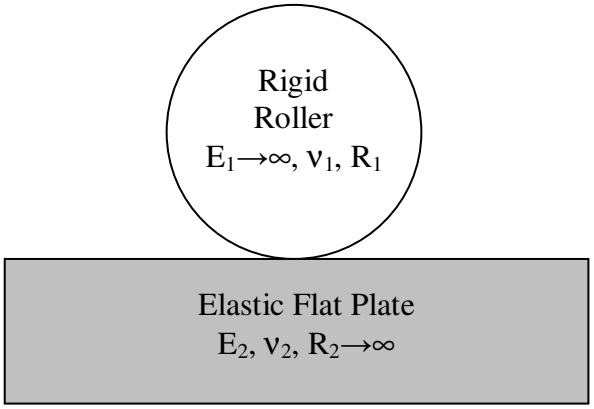

(c)

Figure 3.5. (a) Contact between two elastic cylinders, (b) contact between an elastic roller and an elastic flat plate, and (c) contact between a rigid roller and an elastic flat plate.

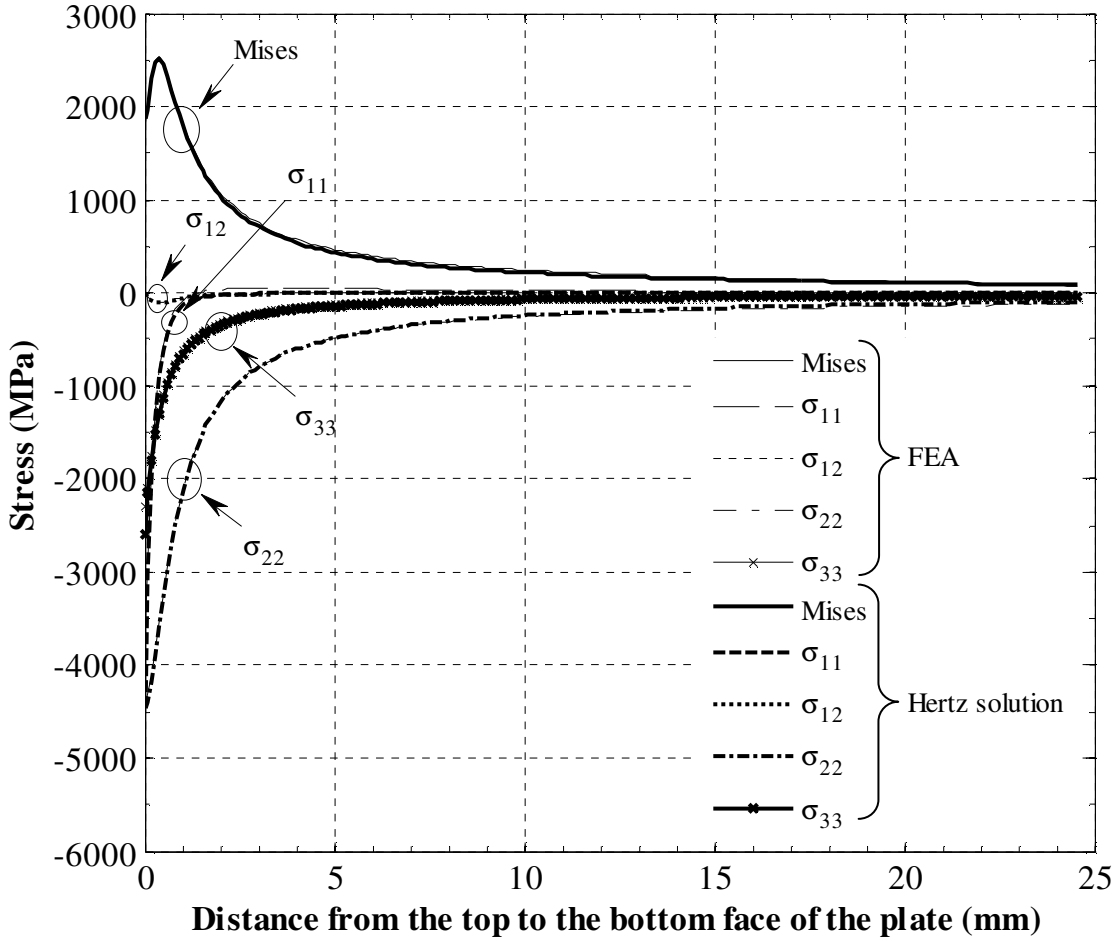
3000
2000
1000
0
-1000
-2000
-3000
-4000
-5000
-6000
0
5
10
15
20
25
Stress (MPa)
Distance from the top to the bottom face of the plate (mm)
Mises
σ11
σ12
σ33
σ22
Mises
σ11
σ12
σ22
σ33
FEA
Mises
σ11
σ12
σ22
σ33
Hertz solution

(a)

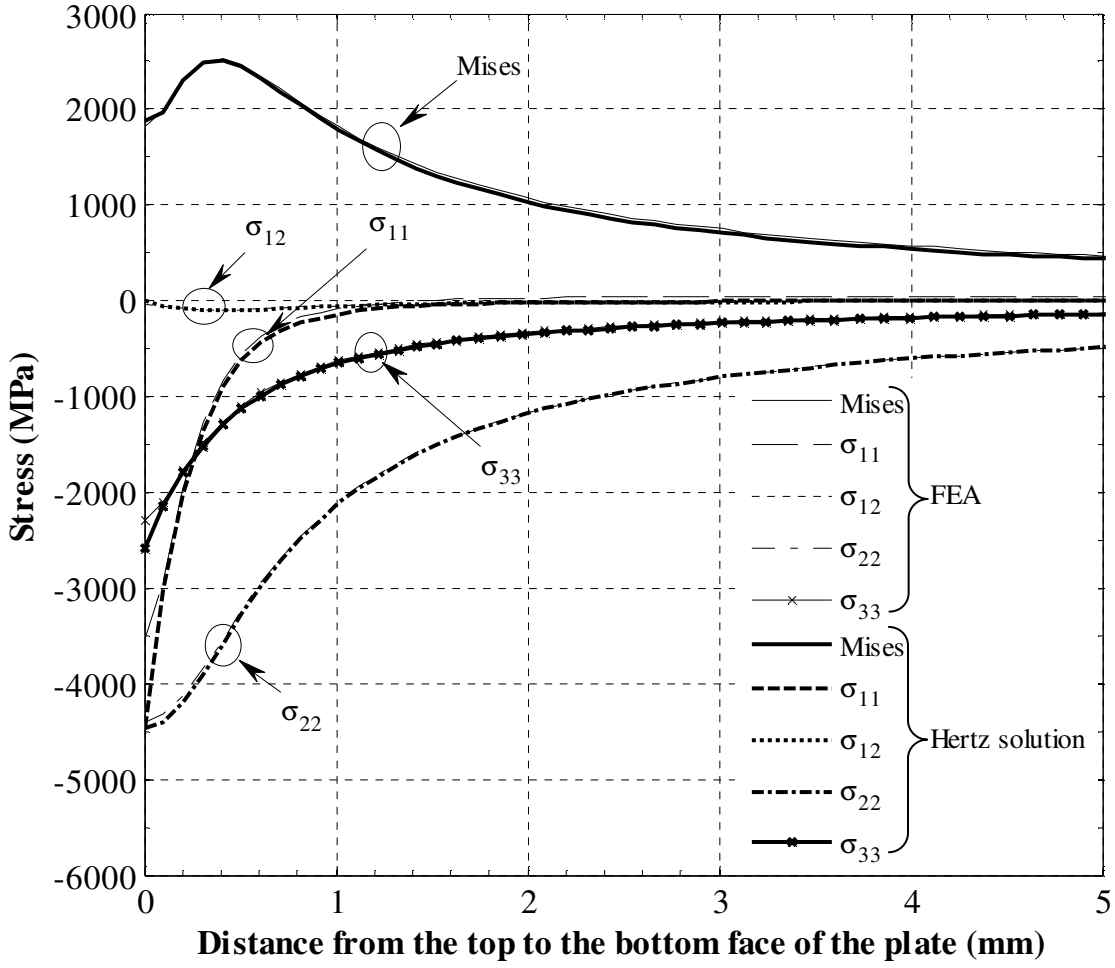

(b)

Figure 3.6. Comparison of the results from the finite element analysis and the elastic Hertzian solution for contact between the elastic plate and the elastic roller. (a) The stress distributions in the –y direction from the top surface for single indentation and (b) a zoom-in view of the stress distribution in the top 5 mm strip of the plate.

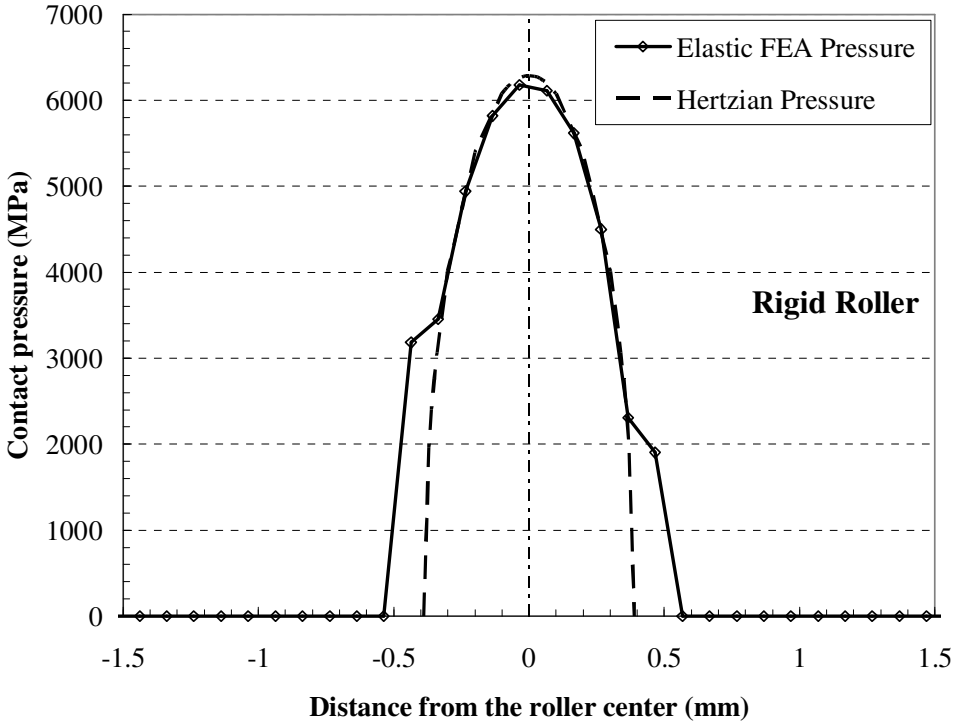

(a)

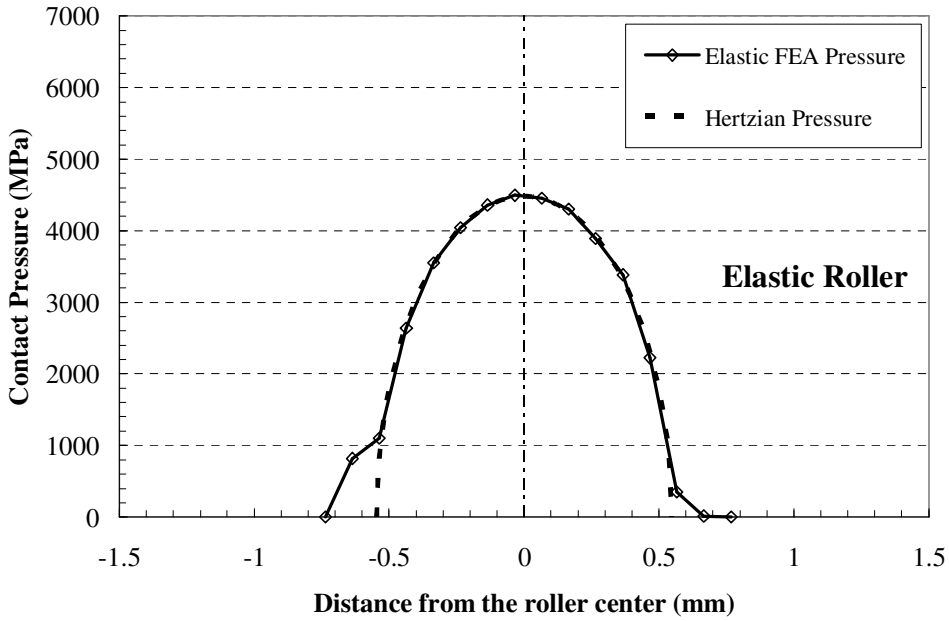

(b)

Figure 3.7. The contact pressure distributions on the plate surface based on the elastic Hertzian solution and the results of the elastic finite element analysis with a fine plate mesh size of 0.1 mm due to single indentation by (a) the rigid roller and (b) the elastic roller.

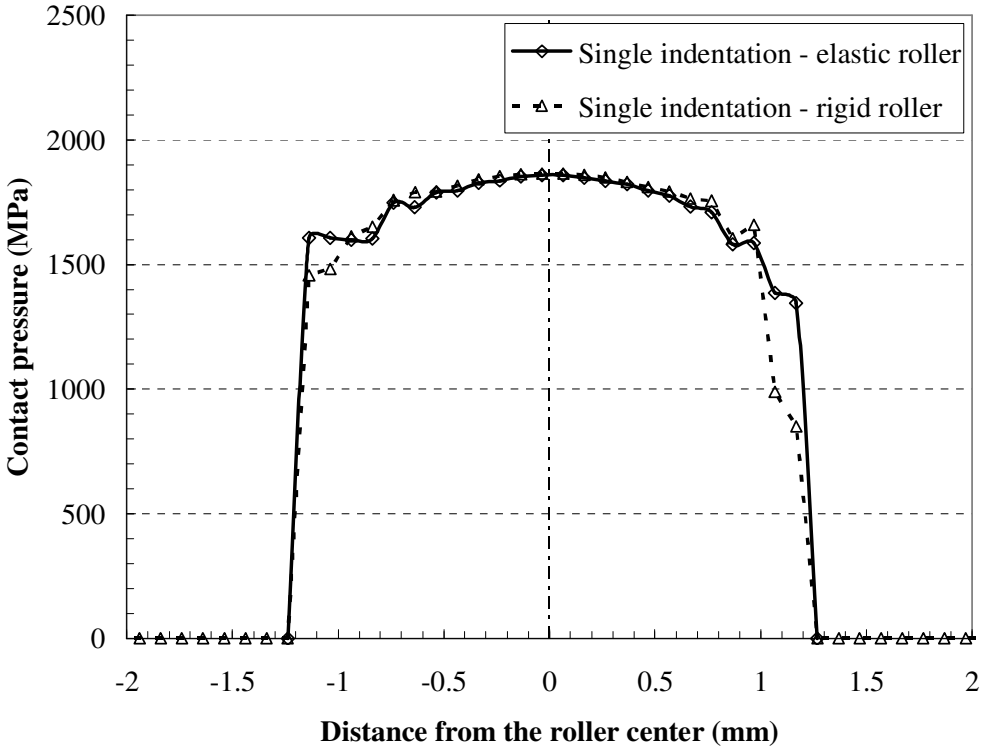
Single indentation - elastic roller
Single indentation - rigid roller
Contact pressure (MPa)
2500
2000
1500
1000
500
0
-2
-1.5
-1
-0.5
0
0.5
1
1.5
2
Distance from the roller center (mm)

(a)

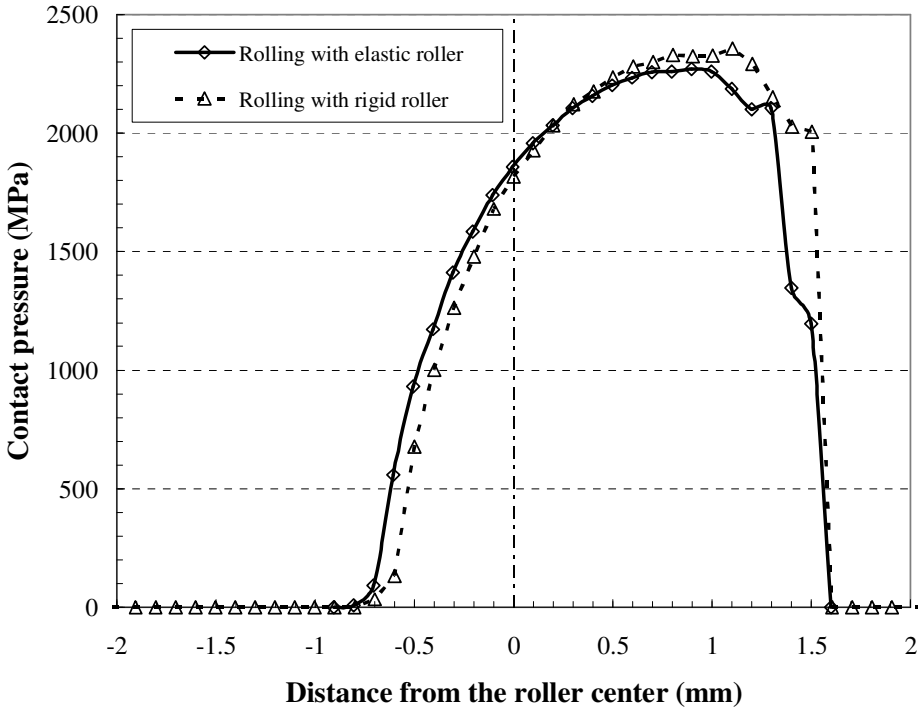

(b)

Figure 3.8. Comparison of the contact pressure distributions from the elastic-plastic finite element analyses with both roller models for (a) single indentation and (b) rolling based on a fine mesh size of 0.1 mm.

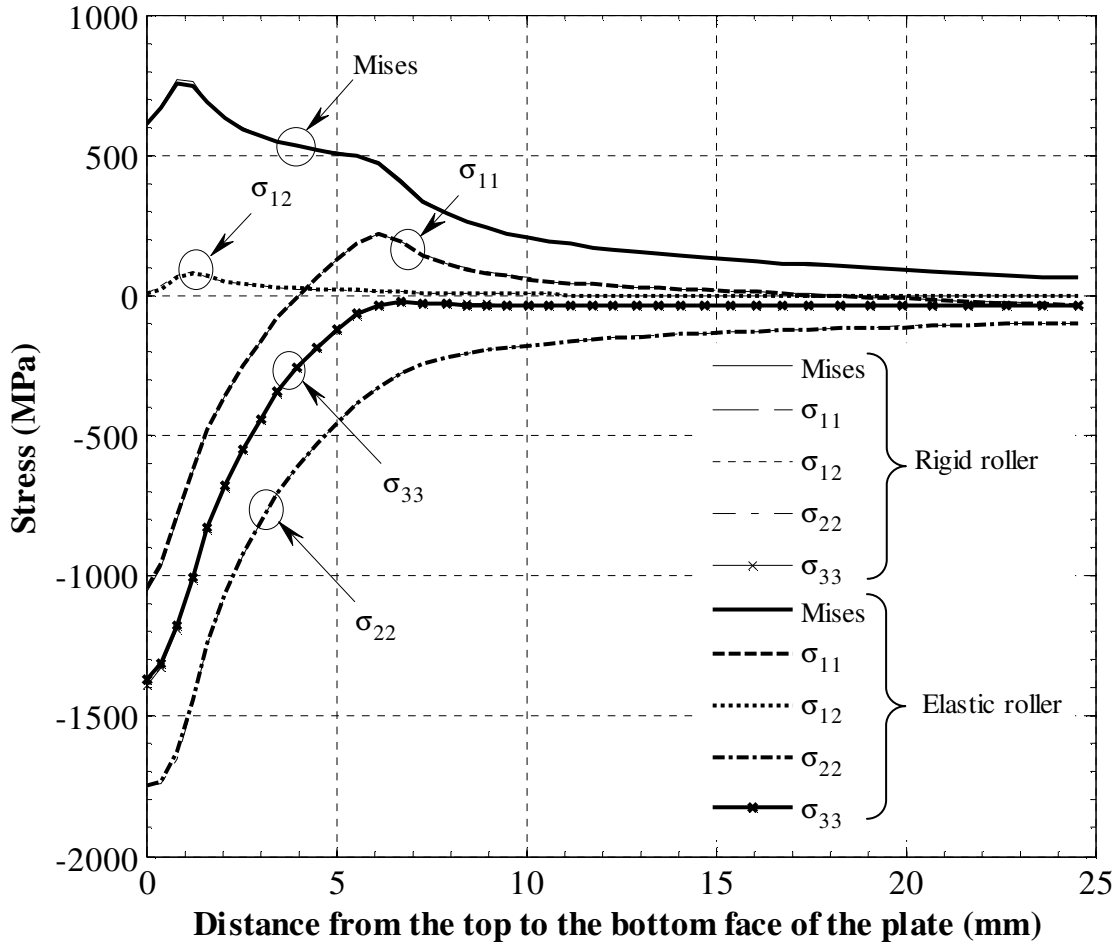
1000
500
0
-500
-1000
-1500
-2000
0
5
10
15
20
25
Stress (MPa)
Distance from the top to the bottom face of the plate (mm)
Mises
σ11
σ12
σ33
σ22
Mises
σ11
σ12
σ22
σ33
Rigid roller
Mises
σ11
σ12
σ22
σ33
Elastic roller

(a)

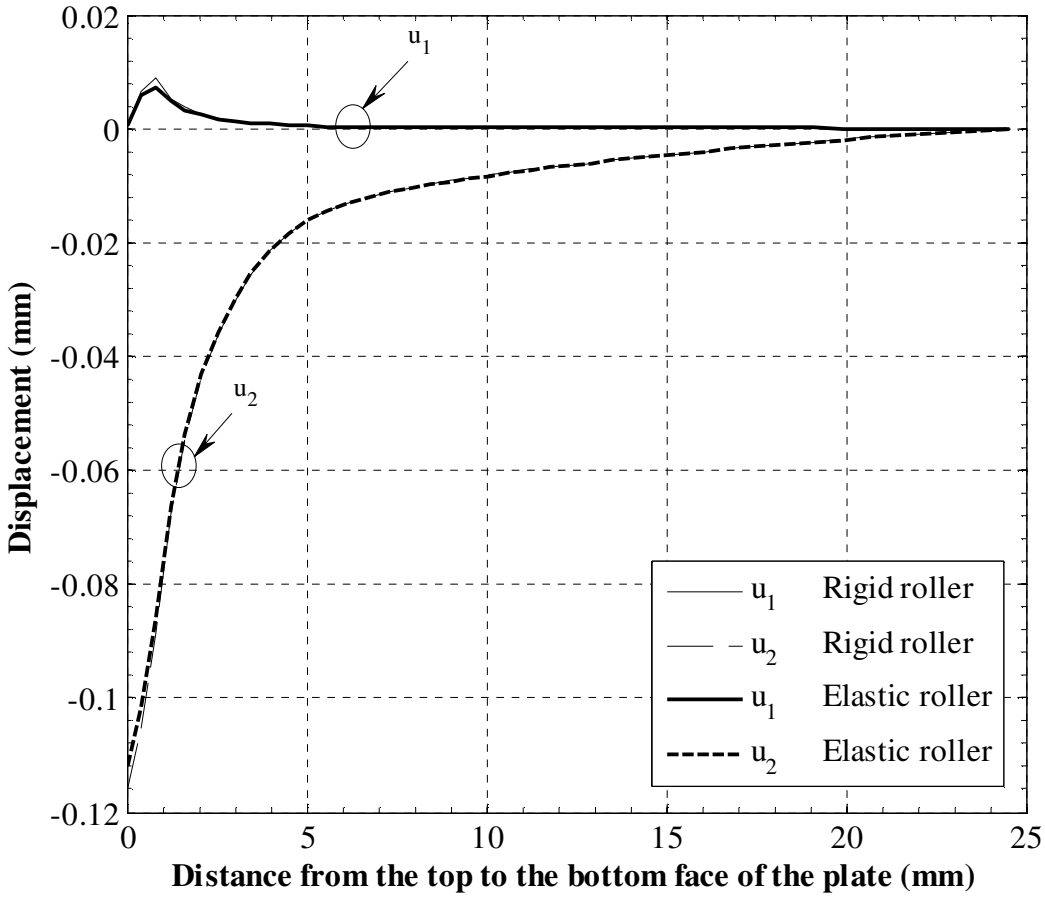

(b)

Figure 3.9. (a) The stress distributions and (b) the displacement components u_1 and u_2 in the –y direction from the top surface of the elastic-plastic plate for single indentation by the rigid and elastic rollers.

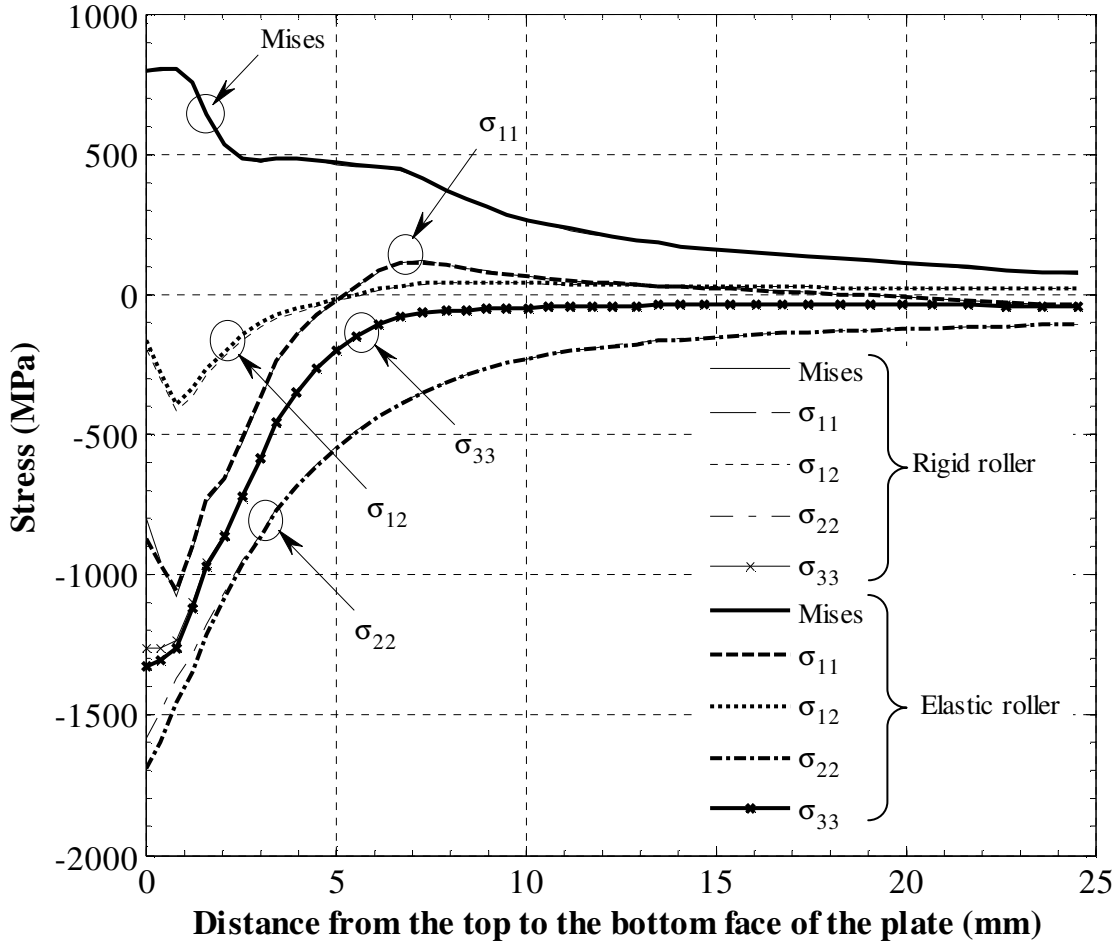
1000
500
0
-500
-1000
-1500
-2000
0
5
10
15
20
25
Stress (MPa)
Distance from the top to the bottom face of the plate (mm)
Mises
σ11
σ33
σ12
σ22
Mises
σ11
σ12
σ22
σ33
Rigid roller
Mises
σ11
σ12
σ22
σ33
Elastic roller

(a)

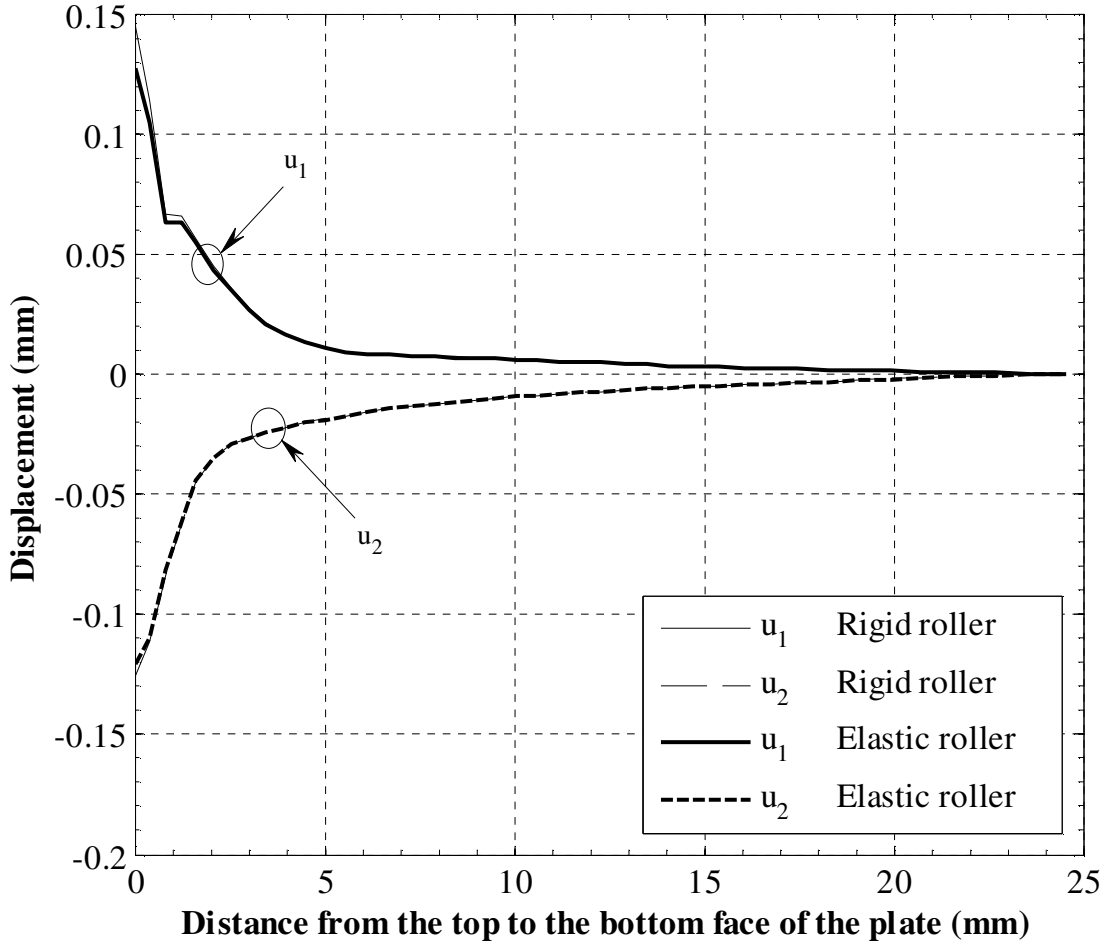

(b)

Figure 3.10. (a) The stress distributions and (b) the displacement components u_1 and u_2 in the –y direction from the top surface of the elastic-plastic plate for rolling at the half rolling length for the rigid and elastic roller cases.

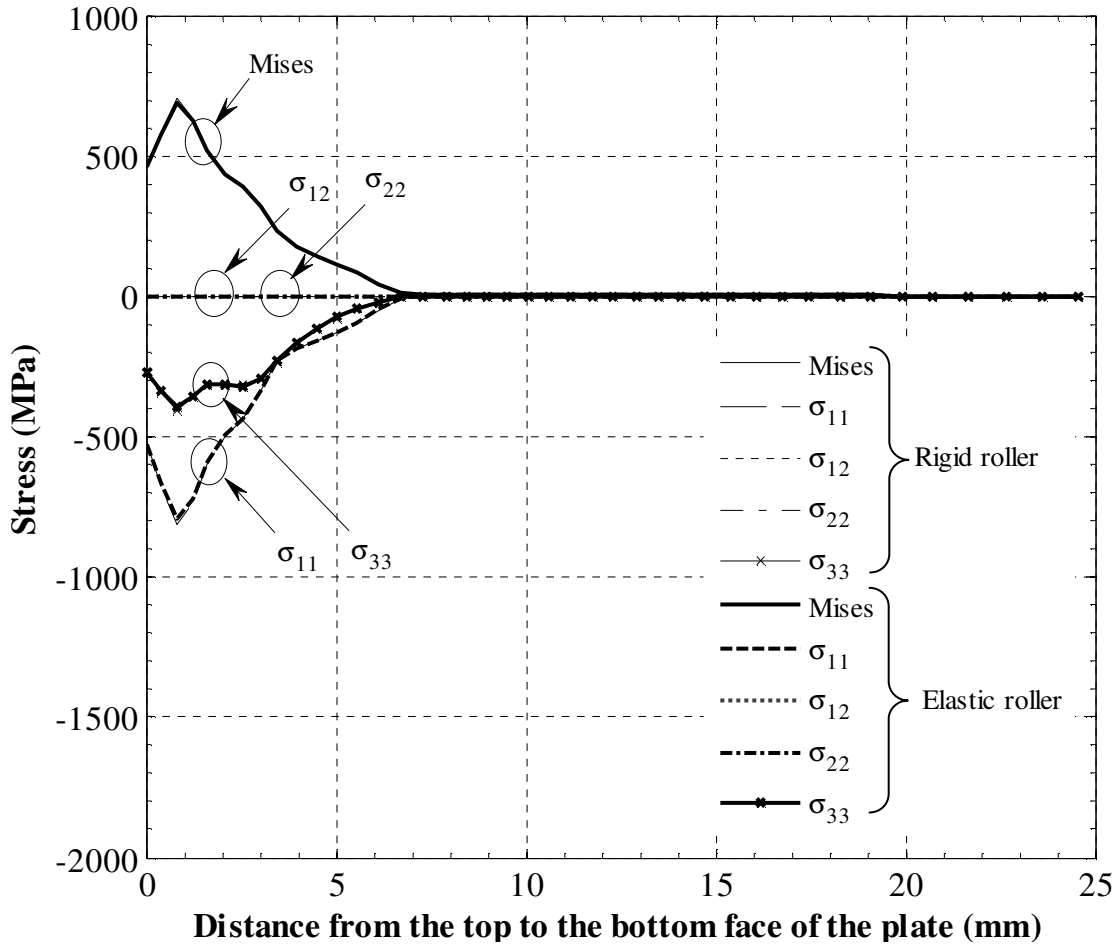
1000
500
0
-500
-1000
-1500
-2000
0
5
10
15
20
25
Stress (MPa)
Distance from the top to the bottom face of the plate (mm)
Mises
σ12
σ22
σ11
σ33
Mises
σ11
σ12
σ22
σ33
Rigid roller
Mises
σ11
σ12
σ22
σ33
Elastic roller

(a)

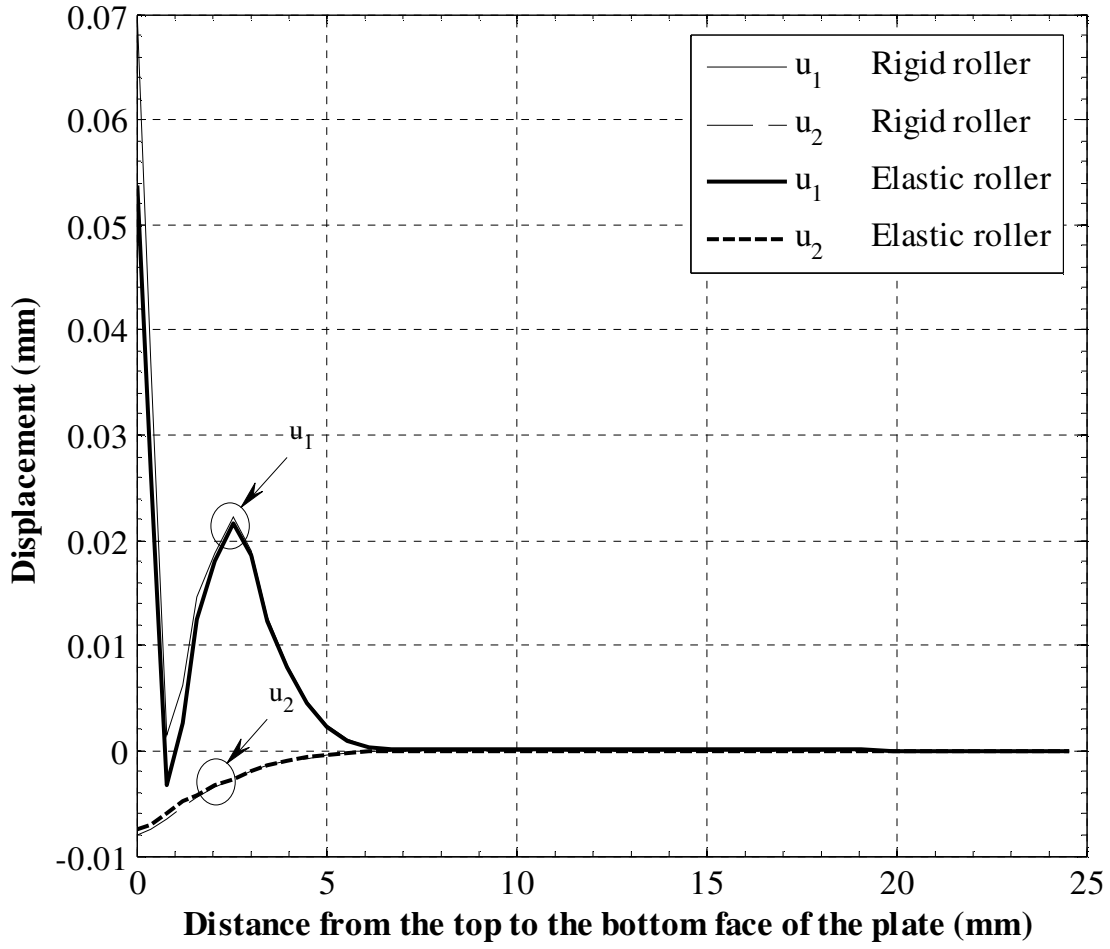

(b)

Figure 3.11. (a) The residual stress distributions and (b) the residual displacement components u_1 and u_2 in the –y direction from the top surface of the elastic-plastic plate after the roller load is removed for the rigid and elastic roller cases.

Chapter 4
Effects of High Rolling Loads on Residual Stress Distributions in a Rectangular Bar

4.1. Introduction

In roller burnishing or deep rolling, a rolling element, which can be a roller as well as a ball, is pressed and rolled against the surface of a work piece. During the rolling process, the material under the roller is loaded into plastic range. Once the rolling load is removed, compressive residual stresses are induced. Rolling improves surface finish and compressive residual stresses by retarding surface or subsurface crack growth of the components under cyclic loading conditions. In this paper the terms "deep rolling" and "roller burnishing" will be used interchangeably even though the terminology "deep rolling" and "roller burnishing" found in the literatures may represent different purposes with the former for the purpose of inducing large plastic deformation and then residual stresses in near-surface layers in contrast to the later which is usually applied with much lower forces and mostly aims to obtain a better surface quality in terms of roughness [1].

In recent publications on the roller burnishing or deep rolling, researchers were more focused on the need for a reliable finite element analyses that can be used to provide a fundamental understanding of the mechanics as well as to understand various parameters effect on the residual stresses in a work piece [2-7]. Sartkulvanich et al. [4] conducted finite element analyses of hard roller burnishing to show the effects of the process parameters upon surface finish and residual stresses. They have used a spherical rigid ball of diameter 6 mm with the maximum burnishing pressure of 40 MPa or about

970 N. Their results show that the burnishing pressure has the most influence, where a high burnishing pressure produces less roughness and more compressive residual stress at the surface. Wu et al. [5] investigated the variation of the residual stresses through the thickness of rolled sheets as a function of the size of the roller relative to the thickness of the sheet both experimentally and numerically for cold-rolled α-brass sheets. Klocke et al. [6] examined the influence of processing and geometry parameters on the surface layer state after roller burnishing of IN718. In their investigation the ball diameter, pressure and specimen thickness varied from 3 to 13 mm, 50 to 250 bar and 1 to 20 mm, respectively. Their measurement results show that the rolling pressure influences the amount and depth of induced residual stresses and strain hardening. Also, with a decreasing thickness, the residual stresses on the surface change from compressive to tensile stresses. Prabhu et al. [7] investigated the influence of deep cold rolling (DCR) and low plasticity burnishing (LPB) on surface hardness and surface roughness of AISI 4140 steel. In their study, the ball diameter and force were in the range of 6 to10 mm and 100 to 750 N, respectively. Their results showed that by using LPB process the surface hardness has been improved by 167% and by using DCR process, the surface hardness has been improved by 442%. Their study also showed that the force, ball diameter, number of tool passes and initial roughness of the work piece are the most pronounced parameters, which have significant effects on the surface of the work piece during the deep cold rolling and LPB processes.

Numerous studies were conducted to understand the stress distributions and deformation patterns near rolling contact surfaces [8-21]. A brief discussion of these works can be found in [22]. Most researchers used the moving Hertzian pressure

distribution to represent the contact pressure for rolling with p_0/k ratios ranging from 5 to 9, where p_0 is the maximum Hertzian pressure and k is the shear yield stress of the material. Ali and Pan [22] investigated the differences between the residual stresses distributions due to single indentation and rolling by a rigid roller on a finite plate under plane strain conditions with very large contact pressure that are relevant to the crankshaft rolling process with the high p_0/k ratio of about 22. The computational results for the rolling case show a significantly higher longitudinal compressive residual stress and a lower out-of-plane compressive residual stress along the contact surface when compared to those for the single indentation case. Their investigation is further extended to examine the effect of an elastic deformable roller on the residual stress distribution due to rolling under plane strain conditions at very high rolling loads [23]. The computational results indicate that the residual stresses after rolling are nearly the same for both roller models and the rigid roller model can be used to obtain the residual stresses in rolling simulations at very high rolling loads without sacrificing the accuracy. Chaise and Nélias [24] investigated the contact pressure and residual strain in three-dimensional elastic-plastic rolling contact for a circular or elliptical point contact. They have used the vertical loading and unloading of an elastic ceramic ball of diameter 9.525 mm over an elastic-plastic flat surface with a normal force of 1150 N applied on the ball that corresponds, in the elastic case, to a Hertzian pressure of 5.7 GPa. They have considered the bodies in contact are semi-infinite. Their results show that the effective contact pressure and subsequent residual strains are strongly dependent on the contact geometry in the elastic-plastic regime.

Furthermore, it is important to realize that compressive residual stresses are largely dependent on the rolling loads, component material and boundary conditions. The current investigation is aimed to quantify the differences between the residual stresses distributions in a finite rectangular bar due to very large contact pressures from two different rolling loads. The rolling parameters for this investigation includes smaller roller radius, high rolling loads (with p_0/k ratio of about 12.5 to 15 with the rigid roller assumption), and finite rectangular bar dimensions. Therefore, a thorough investigation is required to understand the residual stresses due to rolling using three-dimensional finite element analyses. In this paper, a three-dimensional prismatic bar with a rectangular cross section is used for rolling simulations with the appropriate boundary conditions. The roller is assumed to be rigid and the roller rolls on the flat surface of the bar with a low coefficient of friction. Based on the findings in [23], the load or stress distributions for rigid roller should not be significantly different than those for elastic roller at very high rolling loads. The bar material is modeled as an elastic-plastic strain hardening material with a non-linear kinematic hardening rule of ABAQUS [25] for loading and unloading. Effects of the two rolling loads with the material data variability are investigated. A single pass rolling is simulated. The longitudinal residual stress distributions in the bar along the width and the thickness directions are compared for both rolling loads. Also, the longitudinal residual stress distributions in the vertical direction (thickness) are then compared with the measurement data. Finally, some conclusions based on the results of this investigation will be made.

4.2. Experiments

In this paper, the details of the results of finite element analyses for a roll burnishing experiment conducted at Caterpillar are presented. Therefore, a brief review of the roll burnishing experiment is first presented in this section [26]. Figure 4.1(a) shows a schematic of the experimental setup for conducting a burnishing experiment on a rectangular bar of a gray cast iron. Figure 4.1(b) shows a schematic of the gray cast iron bar. The length, width and thickness of the rectangular bar are 200 mm, 20 mm and 18 mm, respectively. The longitudinal edges on the rolling surface of the bar are chamfered (< 0.5 mm). Samples are prepared within a tolerance of ± 5 microns. Figure 4.1(c) shows a front view of the experimental setup with a gray cast iron bar as marked. Figure 4.1(d) shows a closeup view of the roller. The diameter of the steel roller is 25.4 mm. As marked in Figure 4.1(a), the load is applied to the roller by an Instron testing machine. As indicated in Figure 4.1(a), the rectangular bar freely sits inside a rectangular slot of the bottom platen that supports the bar. The bottom platen along with the rectangular bar is pushed to the opposite of the rolling direction using a hydraulic rod. The samples were rolled up to 90% or 180 mm of the total bar length of 200 mm. The burnishing/rolling was by force controlled with two rolling loads at a low roller burnishing (LRB) with 60 kN load and a high roller burnishing (HRB) with 90 kN load. The rolling speed is about 9 mm/sec with single pass rolling. The rolling loads used for this investigation were to obtain given changes of the sample thickness that corresponds to typical dimension changes applied by roller burnishing on large casting components to satisfy the requirements of the surface finish and dimensional tolerance.

Figure 4.2 shows SEM images of graphite morphologies and microstructures of NRB (No Roll Burnishing), LRB (Low Roll Burnishing) and HRB (High Roll Burnishing) samples. At a lower magnification (200x), it appears that HRB load has induced cracks at some of the graphite flake tips as marked by region A in Figure 4.2(c). However, the images of inserts at higher magnifications and a chemical analysis showed that they are indeed graphite flakes. This confirms that no significant microstructure damage was done due to the HRB load used for roller burnishing in this investigation.

Figure 4.3 shows a four-point bending fatigue test setup. Four-point bending fatigue tests were conducted for the following five categories of samples: (i) NRB (No Roll Burnishing), (ii) LRB (Low Roll Burnishing), (iii) HRB (High Roll Burnishing), (iv) LRB samples that were stress relieved at 500 ^{o}C for 50 hrs and v) NRB samples that were stress relieved at 500 ^{o}C for 50 hrs. The goal of the fatigue tests was to compare the fatigue lives of about 1 million cycles for 5 categories of samples for a given load for all samples. The samples were continuously monitored and a failure is determined when the black spots started to appear on ZnO paste as an indicator of surface cracks.

Figure 4.4 shows the fatigue life data obtained from bending tests for 5 categories of samples. The fatigue test results show that the mean life (cycles to failure) for the NRB and HRB samples are nearly the same and is about 0.4 million cycles. On the other hand, the mean life (cycles to failure) for the LRB samples is about 4.3 million cycles. The fatigue test results indicate that the low roller burnishing load (60 kN) improves the fatigue life by almost 10 times than the non-roll burnishing case. However, it appears that the high roll burnishing load does not improve the fatigue life compared to the no roll burnished samples. Moreover, after the residual stress of the LRB samples are relieved,

both the "stress relieved LRB" and NRB samples show almost similar mean fatigue life. A set of "stress relieved NRB" samples are also tested and showed almost similar mean lives as those of the NRB samples.

Figures 4.5(a) and 4.5(b) show the top surfaces of the roll burnished samples after fatigue tests with applications of ZnO paste and penetrating dye, respectively. All broken or unbroken roller burnished samples showed multiple cracks on the rolled surfaces after fatigue tests. The cracks seemed to have either initiated or have grown noticeably at a location few millimeters away from the edges. This observation is also found to be consistent with the results of three dimensional finite element simulations as will be discussed later. Figure 4.6 shows the top surface of NRB samples after fatigue tests with applications of ZnO paste and penetrating dye, respectively. All the NRB samples show failure initiation from the chamfered edges and a single dominating crack. Figure 4.7 shows the top surface of stress-relieved LRB samples after fatigue tests with application of ZnO paste. Unlike the LRB and HRB samples where multiple cracks were observed, the stress-relieved LRB samples have only single dominating crack for each sample similar to that shown in the NRB samples.

Figure 4.8 shows the longitudinal residual stress measurements based on the X-ray diffraction along the centerline of the rolled surface to the subsurface of the bar in the thickness direction for various samples. As shown in the figure, for NRB samples, there was some compressive residual stress on the surface but disappear quickly in the subsurface. The longitudinal residual stress data show that the LRB samples have the highest compressive residual stresses compared to those of the HRB samples in the subsurface. This is consistent with that of the fatigue test results discussed earlier.

However, a detailed finite element analysis will follow shortly to further investigate the findings. It is also found that the compressive residual stress increases from the surface to the subsurface at least up to a depth of 250 microns for LRB and HRB samples.

The average thickness changes of the LRB and HRB samples are 45±5 and 95±10 micrometers, respectively. Figure 4.9 shows the bowing of the bar due to the roller burnishing. In the figure, the bottom surface of the bar was the rolled surface. The bar was held to visualize the bowing for measurement convenience. Depending on the magnitude of a rolling load, plastic deformation occurs on the rolled surface and in the subsurface and thus causing the bowing of the bar. The bar bowing measured by the displacement for the bottom surface from one end to the other as shown in Figure 4.9 for a HRB sample. The average bowing displacements of HRB and LRB samples are 2.79 and 2.38 mm, respectively.

4.3. Modeling procedures

Three-dimensional finite element analyses were conducted to investigate the effects of the burnishing loads on the residual stress distributions in these rectangular bars after the burnishing or rolling. Figure 4.10(a) shows a schematic of a rectangular bar rolling process. The x-y-z coordinate system is also shown. The roller is assumed to be rigid [23] and the roller rolls on the flat surface of the bar with a coefficient of friction (μ) of 0.01. Initially, the roller is sitting on the starting position of the bar at 10 mm from the left end. Then the roller is moved down with a given load. The roller is then moved horizontally in the rolling (z) direction by applying both a translation and rotation to the roller center. After traveling a rolling length of 180 mm before reaching the right

end, the roller is moved up and the rolling is completed. The diameter of the roller is 25.4 mm. The length, width and thickness of the rectangular bar are 200 mm, 20 mm and 18 mm, respectively. The rolling starts on the upper surface from the plane of z = 10 mm and the rolling ends at the plane of z = 190 mm. Similar to the experiment, two burnishing loads are applied to the roller burnishing simulations: a low roller burnishing (LRB) load of 60 kN and a high roller burnishing (HRB) load of 90 kN. The details of applying the rotation and translation to the roller can be found in [22].

Figure 4.10(b) shows a half three-dimensional finite element model of the rectangular bar for rolling simulations with the appropriate boundary conditions. For the finite element model, the displacement in the x direction of the symmetry plane is set to be zero. The displacement of the bottom surface is constrained in the y direction and released after the rolling is completed. The displacement of the right face is constrained in the z direction and released after the rolling. The finite element analyses were performed using the commercial finite element code ABAQUS/standard implicit solver. The Cartesian coordinate system is also shown in the figure. Three-dimensional fully integrated 8-noded (C3D8) elements of size of 0.5 mm by 0.5 mm by 0.5 mm (Mesh-1) were used in this model for a preliminary finite element analysis. Three-dimensional reduced integrated 8-noded (C3D8R) elements were also used. However, the computations using the reduced integrated 8-noded elements converged very slowly and the results were not reported here. In general, the trends of the results based on C3D8 and C3D8R elements are consistent. ABAQUS also provides "selectively reduced" integration for fully integrated lower-order elements where the reduced integration is used for the volume strain and the full integration for the deviatoric strains. As a

consequence, the lower-order elements give an acceptable performance for approximately incompressible behavior [25]. As a starting point, the selection of the sizes of the finite elements to simulate rolling follows the guidelines that were reported in Ali and Pan [27]. A detailed mesh refinement study will be discussed later.

Figure 4.11(a) shows experimental compressive stress-strain curves for the gray cast iron. Since the material under rolling is subject to compression, the experimental compressive stress-strain curve is used for the input of the stress-strain curve for the finite element analyses. The experimental compressive stress-strain data are only available for a limited range of strains. However, for the rolling simulations of our interest, a relatively large range of strains needs to be provided for the stress-strain curve for the input of the finite element analyses. According to common practice, two stress-strain curves for the current investigation are assumed based on a straight line extension beyond the last test data point ('MAT1') and a power-law extension ('MAT2'). 'MAT1' can be considered as a perfectly plastic material whereas 'MAT2' represent a typical power-law strain-hardening material when the plastic deformation becomes large. Figure 4.11(b) shows the two stress-strain curves used in the finite element analyses based on the available experimental compressive stress-strain curve.

The nonlinear kinematic hardening rule of the ABAQUS is assumed based on the compressive stress-strain curves shown in Figure 4.11(b). The nonlinear kinematic hardening rule in ABAQUS is based on the pressure-insensitive Mises yield function. For the unloading/reloading process, the yield function can be expressed as

$$f\left(\sigma_{ij}-\alpha_{ij},\sigma^{0}\right)=\left[\frac{3}{2}\left(\sigma'_{ij}-\alpha'_{ij}\right)\left(\sigma'_{ij}-\alpha'_{ij}\right)\right]^{\frac{1}{2}}-\sigma^{0}=0 \qquad (4.1)$$

where σ_{ij} is the stress tensor, σ'_{ij} is the deviatoric stress tensor, α_{ij} represents the center of the yield surface, α'_{ij} is the deviatoric part of α_{ij}, and σ^0 represents the size of the yield surface. Here, σ'_{ij} and α'_{ij} are defined, respectively, as

$$\sigma'_{ij} = \sigma_{ij} - \frac{1}{3}\sigma_{kk}\delta_{ij} \tag{4.2}$$

$$\alpha'_{ij} = \alpha_{ij} - \frac{1}{3}\alpha_{kk}\delta_{ij} \tag{4.3}$$

where δ_{ij} is the kronecker delta.

The associated flow rule is

$$\dot{\varepsilon}^p_{ij} = \dot{\bar{\varepsilon}}^p \frac{\partial f\left(\sigma_{ij} - \alpha_{ij}, \sigma^0\right)}{\partial \sigma_{ij}} \tag{4.4}$$

where $\dot{\varepsilon}^p_{ij}$ represents the plastic strain rate tensor and $\dot{\bar{\varepsilon}}^p$ is the equivalent plastic strain rate defined as

$$\dot{\bar{\varepsilon}}^p = \left(\frac{2}{3}\dot{\varepsilon}^p_{ij}\dot{\varepsilon}^p_{ij}\right)^{\frac{1}{2}} \tag{4.5}$$

In ABAQUS, the nonlinear kinematic hardening rule is defined to be an additive combination of a purely kinematic term of the Ziegler linear hardening law and a relaxation term which introduces the nonlinearity. The evolution of α_{ij} is expressed as

$$\dot{\alpha}_{ij} = \frac{C}{\sigma_0}\dot{\bar{\varepsilon}}^p\left(\sigma_{ij} - \alpha_{ij}\right) - \gamma\dot{\bar{\varepsilon}}^p\alpha_{ij} \tag{4.6}$$

where σ_0 is constant and represents the size of the initial yield surface, α_{ij} represents the center of the yield surface, and C and γ are material parameters that must be calibrated from cyclic test data. Here, C is the initial kinematic hardening modulus and γ determines the rate at which the kinematic hardening modulus decreases with increasing plastic deformation. When C and γ are zero, the model reduces to the isotropic hardening rule. When γ is zero, the Ziegler linear hardening law is recovered. Note that, for the nonlinear kinematic hardening rule of ABAQUS, the option of "HALF CYCLE" for data type was adopted in order to use the cyclic stress-strain curve of the material as the input stress-strain data [25]. It should be noted that, in ABAQUS, the built-in pressure-sensitive material model such as Cast iron plasticity and Drucker-Prager models are only limited to monotonic loading conditions. For the current investigation, there is a potential for plastic reloading after the rolling is completed [27] and hence these ABAQUS built-in material models may not be suitable for the current investigation. However, a user-material subroutine such as that in Choi et al. [28] to incorporate the pressure dependency and cyclic behavior would have been more appropriate and may be a subject of the future research.

4.3.1 Effect of symmetry

A set of preliminary analyses were conducted to verify the setup and minimize size of the finite element models used for all the subsequent analyses. Due to the symmetry of the bar and the rolling load with respect to the y-z plane, a half bar model can be used to reduce the model size. The preliminary analyses were conducted based on the material data 'MAT1' and 90 kN rolling load. A coarse mesh with the element size of

0.5 mm by 0.5 mm by 0.5 mm denoted as Mesh-1, was used. The boundary conditions used for the full bar model are the same as those for the half bar model. As shown in Figure 4.10(a) for the full bar model, the displacements on the right face CDLK of the bar is constrained in the z direction. The bottom face BCKJ of the bar is constrained in the y direction during the rolling and released later. As shown in Figure 4.10(b), for the half bar model, the displacements on the right face GHLK is constrained in the z direction, the symmetric plane EFGH is constrained in the x direction, and the bottom face FGKJ is constrained in the y direction during the rolling and released later. A comparison of the residual stresses for the both models show that a half bar model can be used instead of a full bar model.

4.3.2 Effects of rolling length

Another preliminary analysis was to examine the results for a full rolled length (equivalent to 14*R*) and partial rolled lengths (about 2*R*, 3*R*, 4*R*, 5*R*, 6*R*, and 8*R*) where *R* is the roller radius. The half bar model described above was used. The rolling loads 40 kN and 90 kN were used in force controlled loading. The 40 kN rolling load was chosen arbitrarily for the verification purpose only. For the given models, the residual stresses for partially rolled lengths equivalent to and above five times of the roller radius were found reasonably comparable to those for a full rolled length. However, a partial rolled length as low as four times of the roller radius still provides acceptable residual stresses. It should be noted that the residual stresses used for the comparisons are based on the values extracted at the middle length of the rolled distance. These computational results are excluded here for brevity.

4.3.3 Effect of the boundary conditions on the bottom surface

Furthermore, two boundary conditions were examined for the bottom face FGKJ as shown in Figures 4.12(a) and 4.12(b). For the boundary condition 'BC DISP' as shown in Figure 4.12(a), the bottom face of the bar is constrained in the y direction during the rolling and released later as mentioned earlier. For the boundary condition 'BC CONT' as shown in Figure 4.12(b), the bottom face of the bar is in frictionless contact with a rigid surface. For a 90 kN rolling load with the mesh size Mesh-1 and the material data 'MAT1', selected longitudinal residual stress distribution are presented and compared for the boundary conditions 'BC DISP' and 'BC CONT'. Figure 4.12(c) shows a comparison of the longitudinal residual stresses on the symmetric plane in the thickness (-y) direction of the bar for the boundary conditions 'BC DISP' and 'BC CONT'. The distributions of the residual stresses are quite similar with slight differences in the magnitudes. Figure 4.12(d) shows a comparison of the longitudinal residual stresses on the top surface in the width (x) direction of the bar for the boundary conditions 'BC DISP' and 'BC CONT'. The distributions of the residual stress are quite similar and within 5%. While the boundary condition 'BC CONT' represents a more realistic boundary condition for the bottom face during rolling or burnishing, the boundary condition 'BC DISP' is much more convenient to model with computational efficiency for multiple analyses. Therefore, a half bar model with rolling distance equivalent to six times of the roller radius for the rolling loads of 60 kN (LRB) and 90 kN (HRB) were adopted for the subsequent analyses. For these models, the rolling started on the upper surface at z = 10 mm rather than z = 0 mm (on the edge) to further reduce the computational time. Referring to Figure 4.10(b), the bottom face of the bar FGKJ is constrained in the y

direction and released after the rolling is completed ('BC DISP'). The right face GHLK of the bar is constrained in the z direction and the symmetric plane EFGH is constrained in the x direction.

4.3.4 Mesh sensitivity study

A mesh sensitivity study was conducted to determine a suitable element size for the subsequent simulations. Figure 4.13 shows the four different mesh sizes that are used for this mesh sensitivity study. The coarse mesh, Mesh-1, consists of elements with the size of $\Delta x = 0.5$ mm, $\Delta y = 0.5$ mm, and $\Delta z = 0.5$ mm for the top layer and in the middle of the bar. This is the mesh size (Mesh-1) used in the preliminary investigations as discussed earlier. The intermediate mesh, Mesh-2, consists of elements with the size of $\Delta x = 0.13$ to 0.25 mm, $\Delta y = 0.126$ mm, and $\Delta z = 0.2$ mm for the top layer and in the middle of the bar. The finest mesh, Mesh-3, is the finest among all the sizes considered here and consists of elements with the size of $\Delta x = 0.1$ mm, $\Delta y = 0.1$ mm, and $\Delta z = 0.1$ mm for the top layer and in the middle of the bar. The fine mesh, Mesh-4, consists of elements with the size of $\Delta x = 0.13$ to 0.25 mm, $\Delta y = 0.126$ mm, and $\Delta z = 0.126$ mm for the top layer and in the middle of the bar. It should be noted that when the mesh size becomes finer, the degree of freedom for the finite element model increases and the computational time becomes prohibitively long to complete the analyses within a reasonable time for multiple analyses. Therefore, this mesh sensitivity study is focused more on finding a reasonable mesh size that balances between the computational time and the accuracy of the results to conduct the subsequent analyses.

With the material data 'MAT1' and boundary condition 'BC DISP', both LRB and HRB loads are used for this mesh sensitivity study. For the 60 kN rolling load, Figure 4.14(a) shows the effect of mesh size on the longitudinal residual stresses on the symmetry plane at the half rolled distance in the thickness (-y) direction. Figure 4.14(b) is a zoom-in view of Figure 4.14(a). For the 90 kN rolling load, Figure 4.15(a) shows the effect of mesh size on the longitudinal residual stresses on the symmetry plane at the half rolled distance in the thickness (-y) direction. Figure 4.15(b) is a zoom-in view of Figure 4.15(a). Even though the longitudinal residual stress results based on Mesh-1 follow the general trend of the four analyses, the magnitudes of the residual stresses on the top surface of the bar are significantly different from those based on the other mesh sizes. The results based on Mesh-4 compared reasonably well with those based on Mesh-3, especially those on the top surface. Figure 4.16 shows the effect of mesh size on the longitudinal residual stresses in the width (x) direction for both rolling loads. Again, the result based on Mesh-4 compared reasonably well with those based on Mesh-3. It should be noted that the computational time for the finite element model based on Mesh-4 is relatively shorter with acceptable accuracy. Therefore, the results that will be reported later in this paper are based on Mesh-4.

4.4. Stress distributions due to bar rolling

4.4.1 Effect of constraint in the width direction

From Figures 4.14, 4.15 and 4.16, the longitudinal residual stresses for the 90 kN rolling load are relatively less compressive or more tensile than those of the 60 kN rolling load. In order to understand the three-dimensional nature of the rolling, the results of the

bar rolling with the assumption of plane strain and plane stress conditions in the x direction are also examined under the conditions that correspond to the 60 and 90 kN rolling loads. Figure 4.17 shows a comparison of the longitudinal residual stress (σ_{33}) obtained from the three dimensional finite element model, and the two-dimensional plane strain and plane stress finite element models with the meshes similar to that of the three-dimensional model for 60 kN rolling load. Figure 4.17 shows that for the 60 kN rolling load, the three-dimensional results are closer to those of under plane strain conditions. On the other hand, Figure 4.18 shows a comparison of the longitudinal residual stress (σ_{33}) obtained from the three-dimensional finite element model and from the two-dimensional plane strain and plane stress finite element model for the 90 kN rolling load. Figure 4.18 shows that for the 90 kN load, the three-dimensional results near the contacting surface are between those under plane strain and plane stress conditions. However, the general trend of the distribution obtained from the three-dimensional finite element model is still quite similar to that from the two-dimensional plane strain finite element model.

4.4.2 Material data variability effect

The material test data for the gray cast iron showed a quite significant variability of the initial yield stress with more than 5% of Coefficient of Variation or CV for a given chemistry specifications. To investigate the effect of the variability of the material yield stress, a "nominal + 3σ" material curve 'MAT2U' for 'MAT2' power law strain hardening model is assumed based on the initial yield stress variability with a CV of about 5%. The mean initial yield stress with the 0.2% offset for the compressive stress-strain curves is

435 MPa. The standard deviation is about 22 MPa for a CV of 5%. Accordingly, the initial yield stress for the 'MAT2U' material curve is set to 501 MPa, with 66 MPa added to the rest of the stress data points for a given strain based on the 'MAT2' power law strain-hardening material curve. This curve represents an upper bound of the material data. A "nominal - 3σ" material curve can be created in a similar way to represent the lower bound of the material data. However, in this investigation the 'MAT1' stress-strain curve represents a lower bound of the material data and hence the "nominal - 3σ" material curve is omitted. It should be noted that the standard deviation (variability) of the stresses at different plastic strain values are not constant. However, in this investigation a constant standard deviation of stresses based on the initial yield stress is used to examine the effect of variability of the material stress-plastic strain curve on residual stresses. Figure 4.19 shows the stress-strain curves of the bar material used in the finite element analyses to examine the effect of the material data variability based on i) a straight line extension beyond the last test data point ('MAT1'), ii) a power-law extension ('MAT2'), and a 'MAT2U' to represent "nominal + 3σ" material data for 'MAT2' for a material yield limit variability.

Figure 4.20(a) shows the effect of the material data variability on the longitudinal residual stresses in the thickness (-y) direction for the 60 kN rolling load. Figure 4.20(b) is a zoom-in view of Figure 4.20(a). The measured longitudinal residual stress data based on the X-ray diffraction (XRD) technique are also shown along with the results of the finite element analyses. The measurement data trend agree well with those based on the 'MAT2' power-law strain hardening curve and falls inside the bound of the results of the finite element analyses. Figure 4.21(a) shows the effect of the material data variability on

the longitudinal residual stresses in the thickness (-y) direction for the 90 kN rolling load. Figure 4.21(b) is a zoom-in view of Figure 4.21(a). The measured longitudinal residual stress data are shown along with the results of the finite element analyses. For the 90 KN rolling load, the results of the finite element analyses show a similar trend as that of the measured residual stresses. However, the magnitudes of the predicted stresses on the surface are more tensile than the measured residual stresses. Figure 4.22 shows a comparison of the longitudinal residual stresses (σ_{33}) for both rolling loads based on the results of the finite element analyses and the measurements. The qualitative trend of the predicted residual stresses also confirm the findings from the measurements that the 90 kN rolling load results in less favorable (less compressive) residual stresses than the 60 kN rolling load. For the 90 kN rolling load, the deviation of the predicted results compared to the measurements may be attributed to the significant pressure sensitivity effect which is not included in the current investigation [28].

Figure 4.23 shows the effect of material data variability on the longitudinal residual stresses in the width (x) direction for both rolling loads. For the 60 kN rolling load, the longitudinal residual stress increases and then decreases as the distance to the edge of the bar increase for 'MAT1', 'MAT2' and 'MAT2U'. However, for the 90 kN rolling load, the trend is still there for 'MAT2U' and 'MAT1', but not for 'MAT2'. It should be mentioned that the experimental results indicate that fatigue cracks were initiated at the locations near the edges, but not from the edges. From this viewpoint, the 'MAT1' stress-strain curve representing a perfectly plastic material gives positive residual stress a few millimeters from edges whereas the 'MAT2' curve does not give this trend for the 90 kN rolling load.

Figure 4.24 shows a comparison of the thickness change of the rolled samples based on the results of the finite element analyses and the measurements. For the 60 kN rolling load, the predicted range for the thickness change by the finite element analyses is in good agreement with the measurement range. However, for the 90 kN rolling load, the trend of the predicted range for the thickness change by the finite element analyses is in agreement with the trend of measurements but the magnitudes are higher than the measured values. This finding indicates that due to the assumption of the hardening rule, material data and strain hardening model, the finite element analyses cannot give the correct thickness change. Since the 90 kN rolling load results in more plastic strain, compressive stress-strain curves cover a larger plastic strain range would be more appropriate for future studies.

A verification analysis is conducted based on the boundary conditions 'BC DISP' and 'BC CONT' (Figures 4.12(a) and 4.12(b)) using the stress-strain curve of 'MAT2U' to examine the effect of the boundary condition on the longitudinal residual stresses. Figure 4.25(a) shows the effect of the boundary condition on the longitudinal residual stresses in the thickness (-y) direction. For the 60 kN and 90 kN rolling loads, the differences of the longitudinal residual stress results are within 10% and 15%, respectively, except a few locations between 1.6 mm and 4.0 mm close to the contact surface where the residual stress value transition from compressive to tensile for the 90 kN rolling load. Similarly, Figure 4.25(b) shows the effect of the boundary condition on the longitudinal residual stresses in the width (x) direction. For the 60 kN rolling load, the differences of the longitudinal residual stress results are within 15% except a few locations where the residual stress magnitudes are below 50 MPa. For the 90 kN rolling load, the differences

of the longitudinal residual stresses are within 10% up to 6 mm from the middle of the bar towards to the edge and there is a slight increase of the differences up to 20% closer to the edge. Overall, the results based on the 'BC DISP' and 'BC CONT' boundary conditions are in good agreement.

Based on the foregoing discussions, in summary, the results of the finite element analyses correlated very well with the test data for the 60 kN rolling load. For the 90 kN rolling load the results of the finite element analyses captured the qualitative trend of the test data but the predicted residual stresses were relatively less compressive.

4.5. Discussions

A few more figures are presented here (Figures 4.26 thru 4.31) to further understand the response of the bar model to the 60 kN and the 90 kN loads. The results presented here are based on the stress-strain curve 'MAT2' and the boundary conditions 'BC DISP'. Figures 4.26(a) and 4.26(b) show the contours of the contact pressure distribution for single indentation and during rolling, respectively. For the visual purpose, a 3X displacement magnification is used and the symmetric half bar model is mirrored using the ABAQUS model viewer post-processing software. For the 90 kN load, the contact length in the longitudinal direction is larger than that of the 60 kN load. However, for the 90 kN load, the higher contact pressure zone in the width direction is relatively shorter than that of the 60 kN load. Similarly, Figures 4.27(a) and 4.27(b) show the distributions of the contact pressure in the longitudinal direction due to single indention with the 60 kN and the 90 kN loads, respectively, based on the three-dimensional, plane strain and plane stress models. For the three-dimensional bar model,

the distributions in the middle and along the edge of the bar are shown. As shown in the figures, the contact pressures are much higher in the middle for the loads. For the 60 kN load, the trend of the contact pressure distribution and the contact length in the middle of the three-dimensional bar model is similar to that of the plane strain model. However, for the 90 kN load, the contact length in the longitudinal direction is larger in the middle of the three-dimensional bar model than that of the plane strain model. Figures 4.28(a), 4.28(b) and 4.28(c) show the contours of the displacement components u_1, u_2 and u_3 during rolling. Here, the displacement magnification is kept to 1X. Figure 4.28(a) shows that for the 90 kN load, the displacement u_1 in the width direction of the material on the two sides of the bar is larger than that of the 60 kN load. For the 90 kN load, displacement u_2 in the y direction indicating the rise up of material in front of the roller is higher than that of the 60 kN load as shown in Figure 4.28(b). For the 90 kN load, the displacement u_3 in the longitudinal direction are much higher than that of the 60 kN load.

Figures 4.29(a), 4.29(b) and 4.29(c) show the contours of the longitudinal stress (σ_{33}), vertical stress (σ_{22}), and transverse stress (σ_{11}) components in the bar during rolling with the 60 and 90 kN rolling loads. For the visual purpose, a 3X displacement magnification is used for these figures. The 90 kN load shows a relatively larger compressive stress zone in front of the roller that is mostly concentrating in the middle of the bar along the width. These figures show that during rolling, when the roller just passes a node, the roller tends to "pull" the material behind the node. At that time, all the stresses components become less compressive, zero or tensile. So the load reversal takes place during rolling process. For the 90 kN load, the indentation depth by the roller during rolling is larger than that of the 60 kN load. Due to the finite dimension of the bar,

this results in a relatively lower compressive stress behind the roller as the roller ploughs through the metal in front of it and that tends to "pull" relatively more material behind it as shown in Figures 4.28(c) and 4.29(a). This may be attributed to the followings: the load interaction with the finite dimension of the bar width and bar height may cause the 90 kN case behave more towards to the plane stress condition; a significant trailing tensile stress with yielding behind the roller have caused the loss of favorable compressive residual stress for the 90 kN load in this investigation. This also underscores the need to incorporate the effect of pressure sensitivity under cyclic loading conditions that may be addressed in the future study. See ref. [22] for further discussion on stress distribution during rolling.

Figures 4.30(a) and 4.30(b) show the contours of the residual Mises stress and the residual longitudinal stress (σ_{33}) at the cross section of the bar after rolling is completed. Here, the displacement magnification is kept to 1X. In Figure 4.30(b), the legend of the contour is set such that the gray color represents the zone of the residual longitudinal stress (σ_{33}) that is tensile and the value is greater than zero. For the 90 kN load, almost the entire rolled surface and a larger portion of the cross section has tensile residual longitudinal stress (σ_{33}), when compared to the 60 kN load. The results qualitatively indicates the reason for better fatigue lives for 60 kN samples than that of the 90 kN samples under four-point bending fatigue tests as shown in Figure 4.4.

Figure 4.31 shows the history of the equivalent plastic strain (PEEQ) for both 60 kN and 90 kN rolling loads at a node located at the top surface and at the symmetry plane of the bar model. At this node the shear stresses are zero (or negligible due to deformed shape effect) and the normal stress components are the principal stress components. For

both rolling load cases, the equivalent plastic strain continues to increase after the rolling load is decreased from the peak value which may indicate plastic reloading takes place after the peak rolling load in the current investigation. Figure 4.32 shows a 3-D line graph to depict the history of the principal stresses of the above mentioned node during and after rolling is completed. This figure is again confirming the findings in Figures 4.29(a) and 4.30(b) that for the 90 kN load, the principal stress components at the node become relatively more tensile than that of the 60 kN load.

4.6. Conclusions

In this paper, residual stress distributions in a rectangular bar due to rolling or burnishing at very high rolling or burnishing loads are investigated by three-dimensional finite element analyses using ABAQUS. First, a roll burnishing experiment conducted at Caterpillar with residual stress measurements are briefly reviewed. In the corresponding finite element analyses, the roller is modeled as rigid and the roller rolls on the flat surface of the bar with a low coefficient of friction. The bar material is modeled as an elastic-plastic strain hardening material with a non-linear kinematic hardening rule for loading and unloading. For rolling loads with extensive plastic deformation, the computational results showed that a higher rolling load does not necessarily always produce higher compressive residual stresses in the desired regions of the bar. The computational results also showed that the longitudinal residual stresses are sensitive to the initial yield stress and the detailed strain hardening assumed at large strains.

References

1. Altenberger, I., "Deep Rolling - the Past, the Present and the Future," Proceedings of 9th International Conference on Shot Peening **ICSP9**: 144-155, Paris, France, 2005.
2. Klocke, F., Bäcker, V., Wegner, H. and Timmer, A., "Innovative FE-Analysis of the Roller Burnishing Process for Different Geometries," X International Conference on Computational Plasticity, COMPLAS X, E. Oñate and D. R. J. Owen (Eds), Ó CIMNE, Barcelona, Spain, 2009.
3. Klocke, F., Bäcker, V., Wegner, H. and Zimmermann, M., "Finite Element Analysis of the Roller Burnishing Process for Fatigue Resistance Increase of Engine Components," Proc. IMechE, **225** Part B: J. Engineering Manufacture, 2010, DOI: 10.1243/09544054JEM2044.
4. Sartkulvanich, P., Altan, T., Jasso, F. and Rodriguez, C., "Finite Element Modeling of Hard Roller Burnishing: An Analysis on the Effects of Process Parameters Upon Surface Finish and Residual Stresses," Journal of Manufacturing Science and Engineering, **129**: 705-716, August 2007.
5. Wu, T., Hartley, C.S., Wang, X.M. and Tsai, C.T., "Residual Stress Distribution in Cold Rolled Brass Sheet," J. Mater. Process. Technol. **45**: 111-116, 1994.
6. Klocke, F., Bäcker, V., Wegner, H., Feldhaus, B., Baron, H.-U. and Hessert, R., "Influence of Process and Geometry Parameters on the Surface Layer State after Roller Burnishing of IN718," Prod. Eng. Res. Devel., German Academic Society for Production Engineering (WGP), 2009, DOI 10.1007/s1 1740-009-0182-0.
7. Prabhu, P. R., Kulkarni, S. M. and Sharma, S. S., "Influence of Deep Cold Rolling and Low Plasticity Burnishing on Surface Hardness and Surface Roughness of AISI 4140 Steel," World Academy of Science, Engineering and Technology, **72**: 619-624, 2010.
8. Mesarovic, S. Dj. and Fleck, N. A., "Spherical Indentation of Elastic-Plastic Solids," Proc. R. Soc. Lond. A, **455**:2707-2728, 1999.
9. Kral, E. R., Komvopoulos, K., and Bogy, D. B., "Elastic-Plastic Finite Element Analysis of Repeated Indentation of Half-Space by a Rigid Sphere," *J. Appl. Mech.*, **60**:829-841, 1993, doi:10.1115/1.2900991.
10. Komvopoulos, K., "Elastic-Plastic Finite Element Analysis of Indented Layered Media," *J. Tribol.*, **111**(3):430-439, 1989, doi:10.1115/1.3261943.
11. Merwin, J. E. and Johnson, K. L., "An Analysis of Plastic Deformation in Rolling Contact," Proc. Instn. Mech. Engrs., **177**(25):676-690, 1963.
12. Kulkarni, S. M., Hahn, G. T., Rubin, C. A., and Bhargava, V., "Elastoplastic Finite Element Analysis of Three-Dimensional, Pure Rolling Contact at the Shakedown Limit," *J. Appl. Mech.*, **57**:57-65, 1990, doi:10.1115/1.2888324.
13. Kulkarni, S. M., Hahn, G. T., Rubin, C. A., and Bhargava, V., "Elasto-Plastic Finite Element Analysis of Three-Dimensional Pure Rolling Contact Above the Shakedown Limit," *J. of Appl. Mech.*, **58**:347-353, 1991, doi:10.1115/1.2897192.
14. Yu, M., Moran, B., and Keer, L. M., "A Direct Analysis of Two-Dimensional Elastic-Plastic Rolling Contact," *J. Tribol.*, **115**:227–236, 1993, doi:10.1115/1.2920996.
15. Yu, M. M. H., Moran, B., and Keer, L. M., "A Direct Analysis of Three-Dimensional Elastic-Plastic Rolling Contact," *J. Tribol.*, **117**:234–243, 1995, doi:10.1115/1.2831236.

16. Bhargava, V., Hahn, G. T., and Rubin, C. A., "An Elastic-Plastic Finite Element Model of Rolling Contact Part 1: Analysis of Single Contacts," *J. of Appl. Mech.*, **52**:67-74, 1985, doi:10.1115/1.3169028.
17. Bhargava, V., Hahn, G. T., and Rubin, C. A., "An Elastic-Plastic Finite Element Model of Rolling Contact Part 2: Analysis of Repeated Contacts," *J. of Appl. Mech.*, **52**:75-82, 1985, doi:10.1115/1.3169030.
18. Chen, W. W., Wang, Q. J., Wang, F., Keer, L. M., and Cao, J., "Three-Dimensional Repeated Elasto-Plastic Point Contacts, Rolling, and Sliding," *J. of Appl. Mech.*, **75**:021021, 2008, doi:10.1115/1.2755171.
19. Jiang, Y. and Sehitoglu, H., "Rolling Contact Stress Analysis with the Application of a New Plasticity Model," *Wear*, **191**:35-44, 1996, doi:10.1016/0043-1648(95)06663-2.
20. Jiang, Y., Xu, B., and Sehitoglu, H., "Three-Dimensional Elastic-Plastic Stress Analysis of Rolling Contact," *J. Tribol.*, **124**:699–708, 2002, doi:10.1115/1.1491978.
21. Bijak-Zochowski, M. and Marek, P., "Residual Stress in Some Elasto-Plastic Problems of Rolling Contact with Friction," *Int. J. Mech. Sci.*, **39**(1):15-32, 1997, doi:10.1016/0020-7403(96)00018-5.
22. Ali, M. Y. and Pan, J., "Elastic-Plastic Indentation and Flat Plate Rolling under Plane Strain Conditions," *SAE Int. J. Mater. Manuf.,* **4**(1):125-137, 2011, doi:10.4271/2011-01-0035.
23. Ali, M. Y. and Pan, J., "Effect of a Deformable Roller on Residual Stress Distribution for Elastic-Plastic Flat Plate Rolling under Plane Strain Conditions," *SAE Int. J. Mater. Manf,* **5**(1):129-142, 2012, doi:10.4271/2012-01-0190.
24. Chaise, T. and Nélias, D., "Contact Pressure and Residual Strain in 3D Elasto-Plastic Rolling Contact for a Circular or Elliptical Point Contact," *J. Tribol.*, **133**:1–9, 2011, doi:2010.1115/1.4004878.
25. ABAQUS Version 6.10 User Manual, SIMULIA, Providence, RI, 2010.
26. Michlik, P., Internal Report, Caterpillar Inc., Peoria, IL, 2009.
27. Ali, M. Y. and Pan, J., Research work to be submitted for publication, 2012.
28. Choi, K.S. and Pan, J., "Effects of pressure-sensitive yielding on stress distributions in crankshaft sections under fillet rolling and bending fatigue tests", *Int. J. of Fatigue*, **31**(10):1588-1597, 2009, doi:10.1016/j.ijfatigue.2009.04.007.

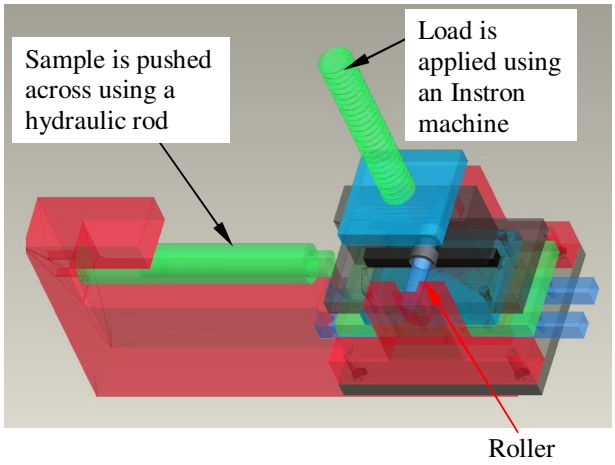

(a)

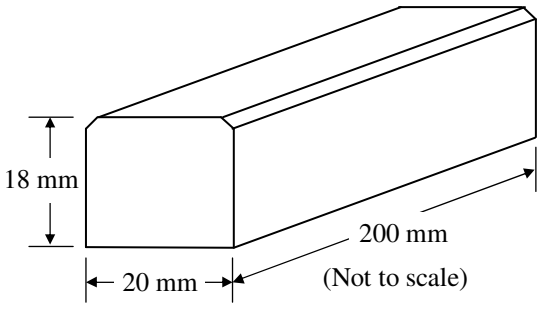

(b)

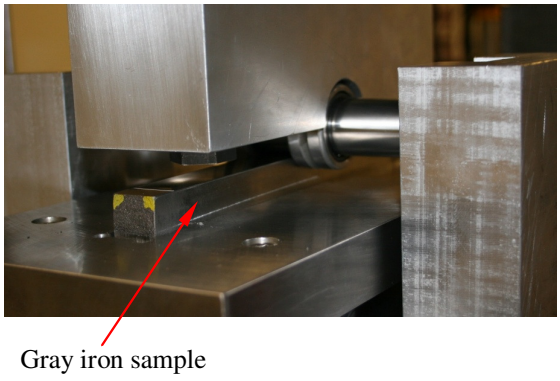

(c)

(d)

Figure 4.1. Schematics of (a) the experimental setup for rolling a rectangular bar, (b) a rectangular bar, (c) a front view of the experimental setup, and (d) a close-up view of the roller.

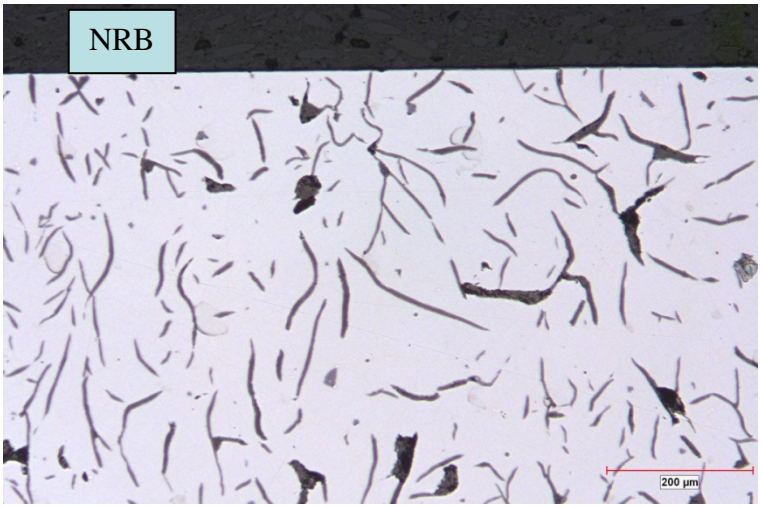

(a)

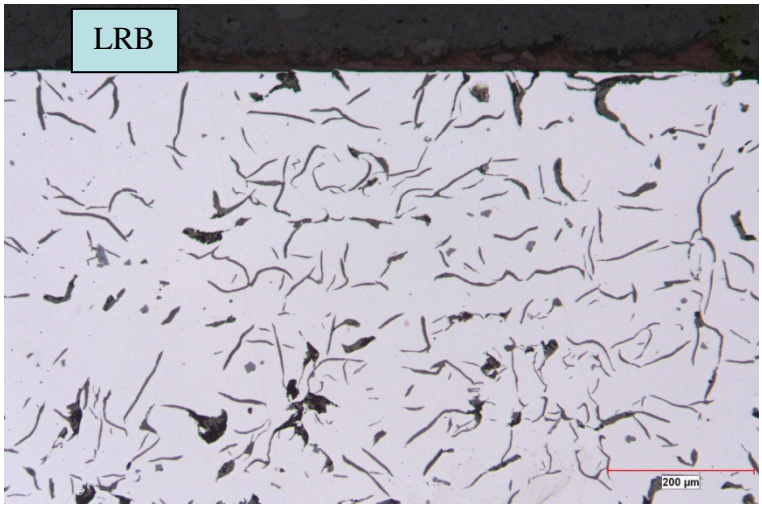

(b)

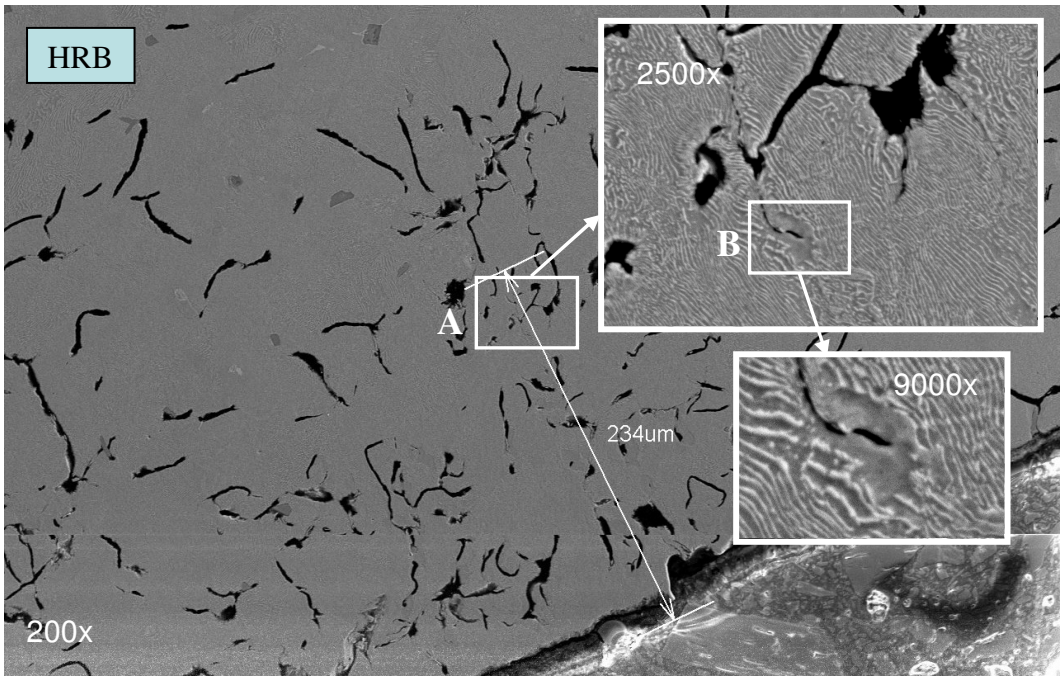

(c)

Figure 4.2. SEM images showing morphologies and microstructures of (a) NRB (No Roll Burnishing), (b) LRB (Low Roll Burnishing) and (c) HRB (High Roll Burnishing) samples.

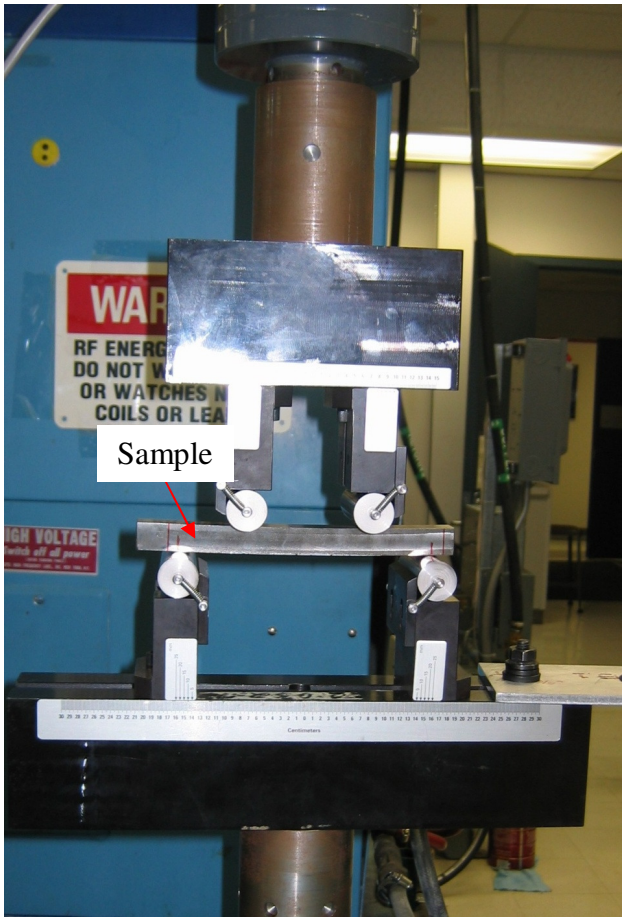

Figure 4.3. A four-point bending fatigue test setup.

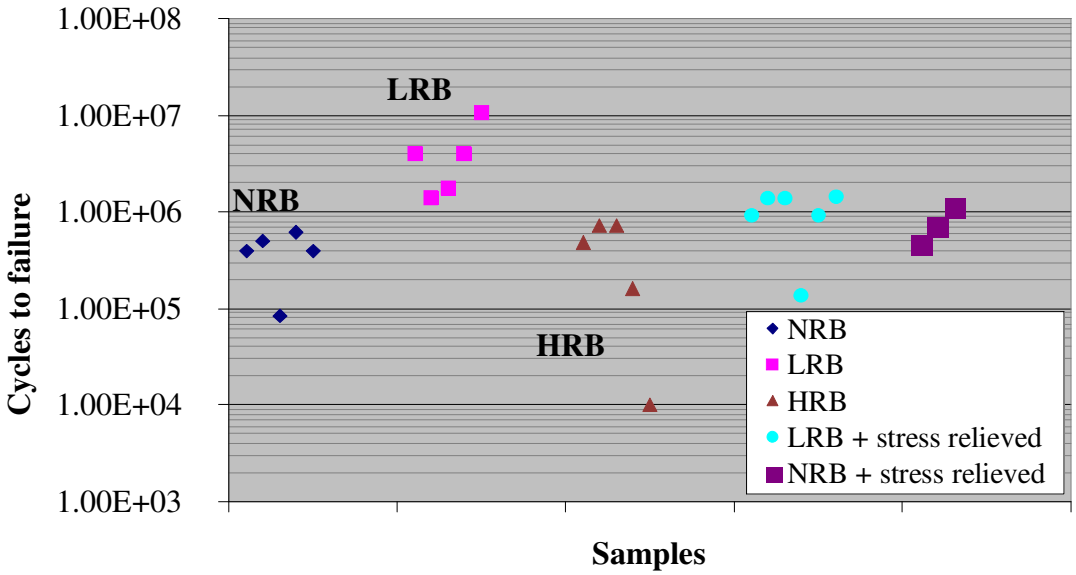

Figure 4.4. Fatigue life data obtained from bending fatigue tests for 5 categories of samples.

(a)

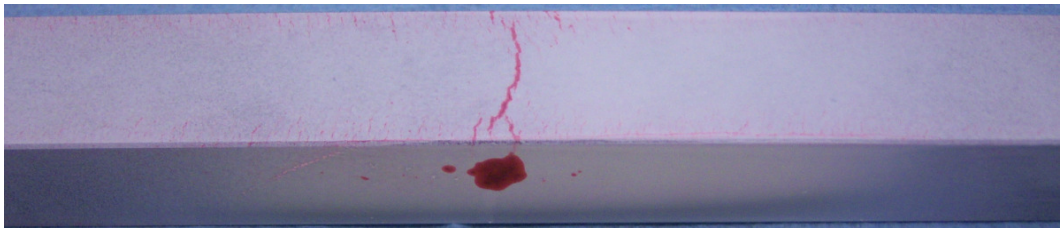

(b)

Figure 4.5. Roll burnished samples after fatigue tests with applications of (a) ZnO paste and (b) penetrating dye.

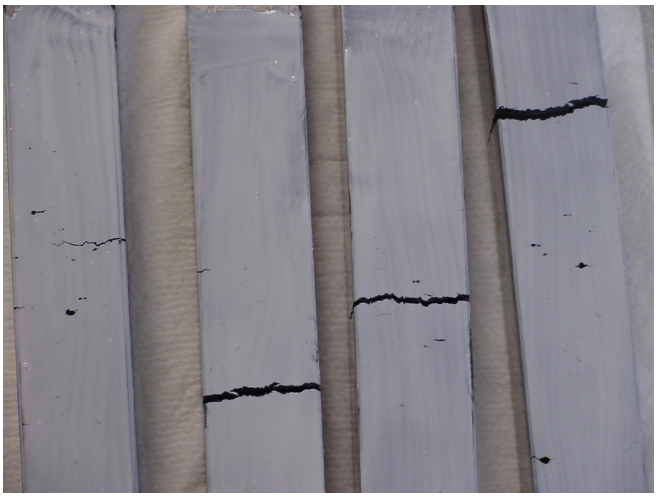

(a)

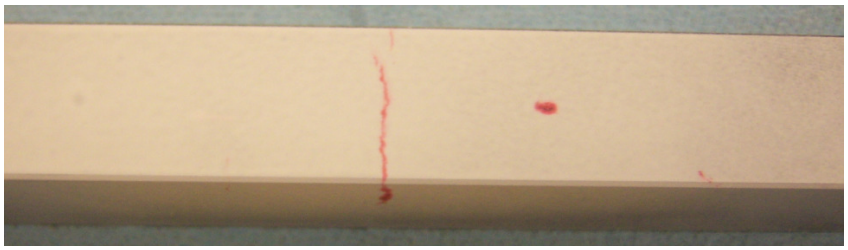

(b)

Figure 4.6. NRB samples after fatigue tests with applications of (a) ZnO paste and (b) penetrating dye.

Figure 4.7. Stress-relieved LRB samples after fatigue tests with applications of ZnO paste.

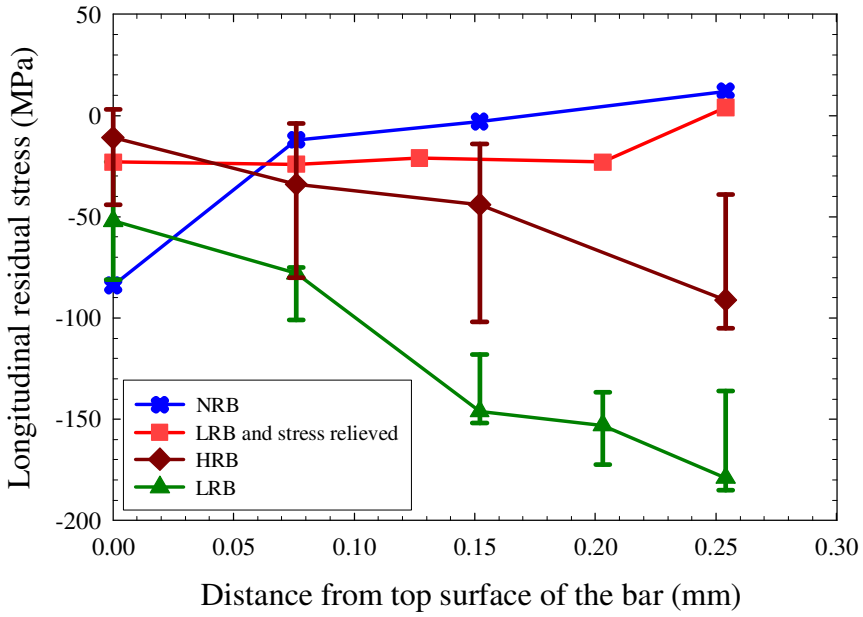

Figure 4.8. Longitudinal residual stress measurements along the centerline of the rolled surface to the subsurface of the bar in the thickness direction for 4 categories of samples.

Figure 4.9. Bowing of a bar due to the roll burnishing.

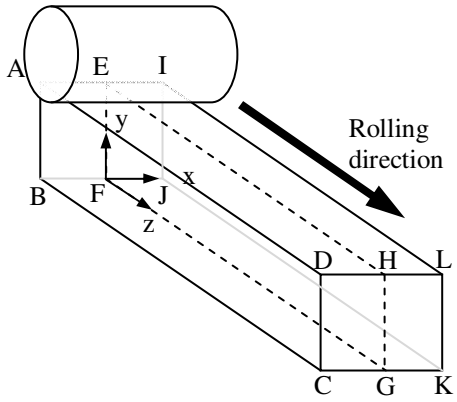

(a)

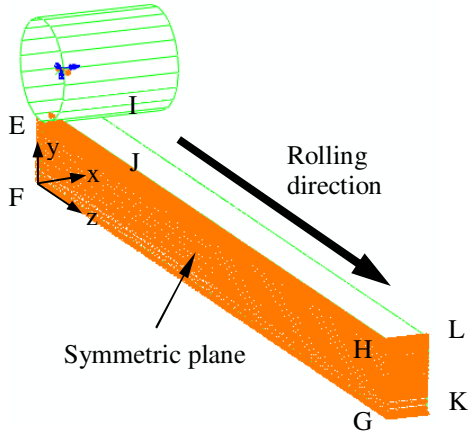

(b)

Figure 4.10. (a) A schematic of a rectangular bar rolling process and (b) a half three-dimensional finite element model of the rectangular bar for rolling simulations.

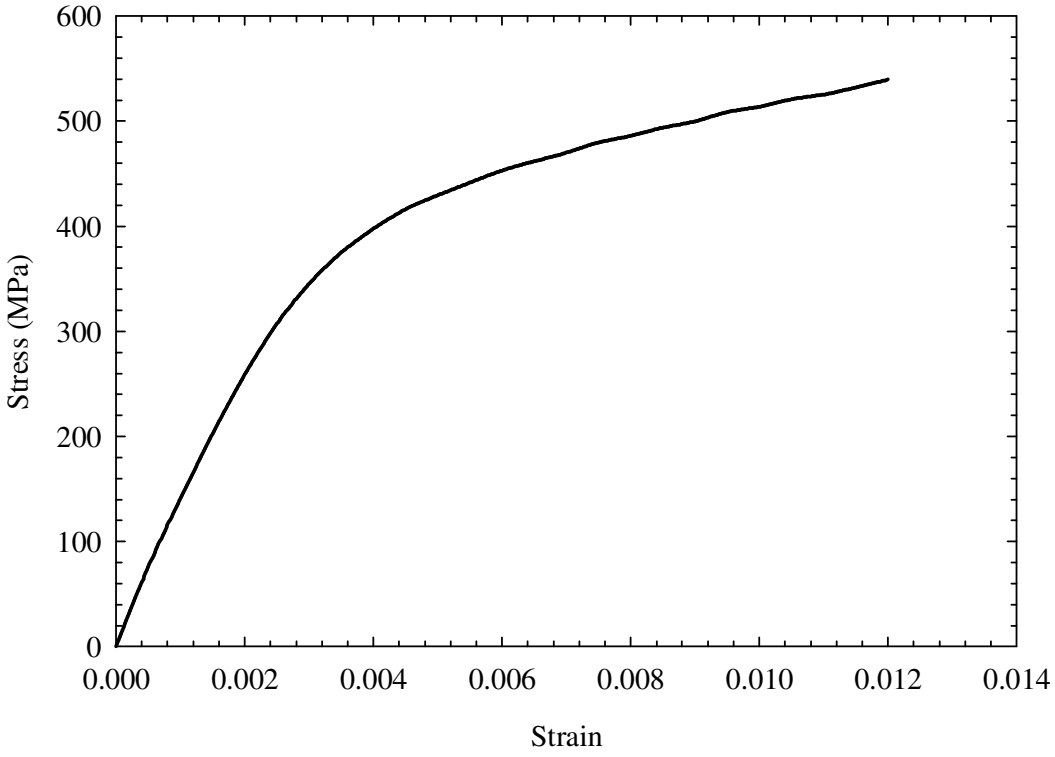
600
500
400
300
200
100
0
Stress (MPa)
0.000
0.002
0.004
0.006
0.008
0.010
0.012
0.014
Strain

(a)

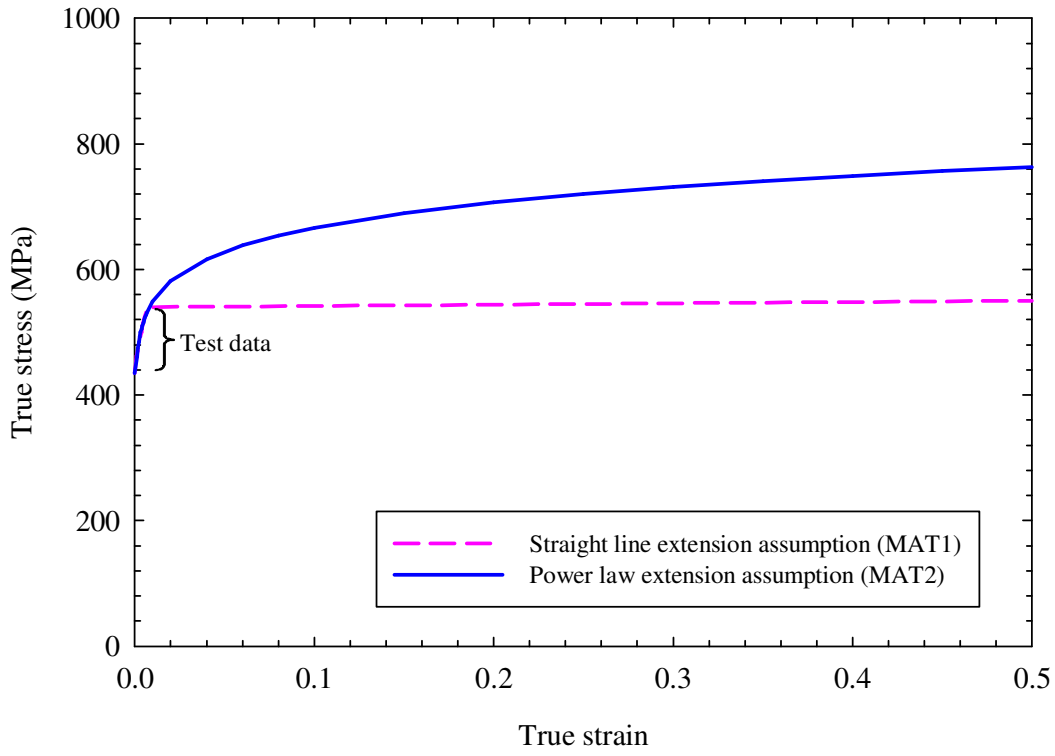

(b)

Figure 4.11. (a) The experimental compressive stress-strain curves for the gray cast iron and (b) the stress-strain curves used in the finite element analyses based on the extensions of the experimental compressive stress-strain curve.

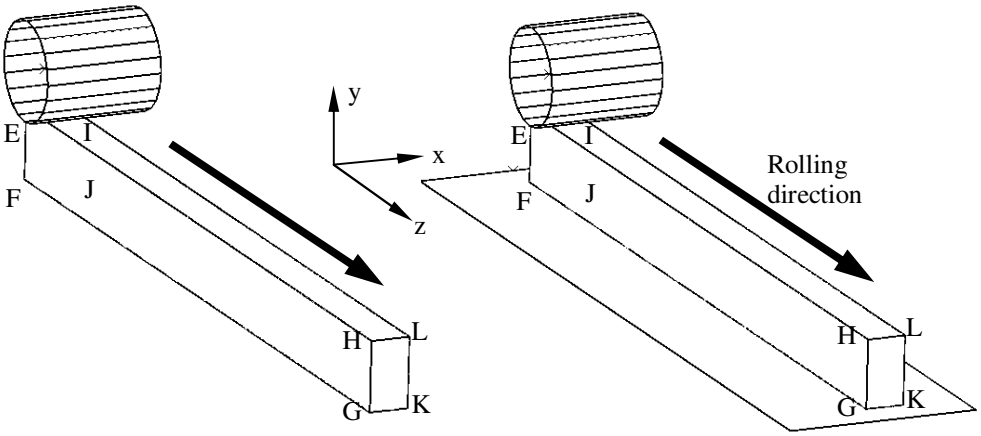
E
I
F
J
y
x
z
H
L
G
K
(a)
E
I
F
J
Rolling
direction
H
L
G
K
(b)

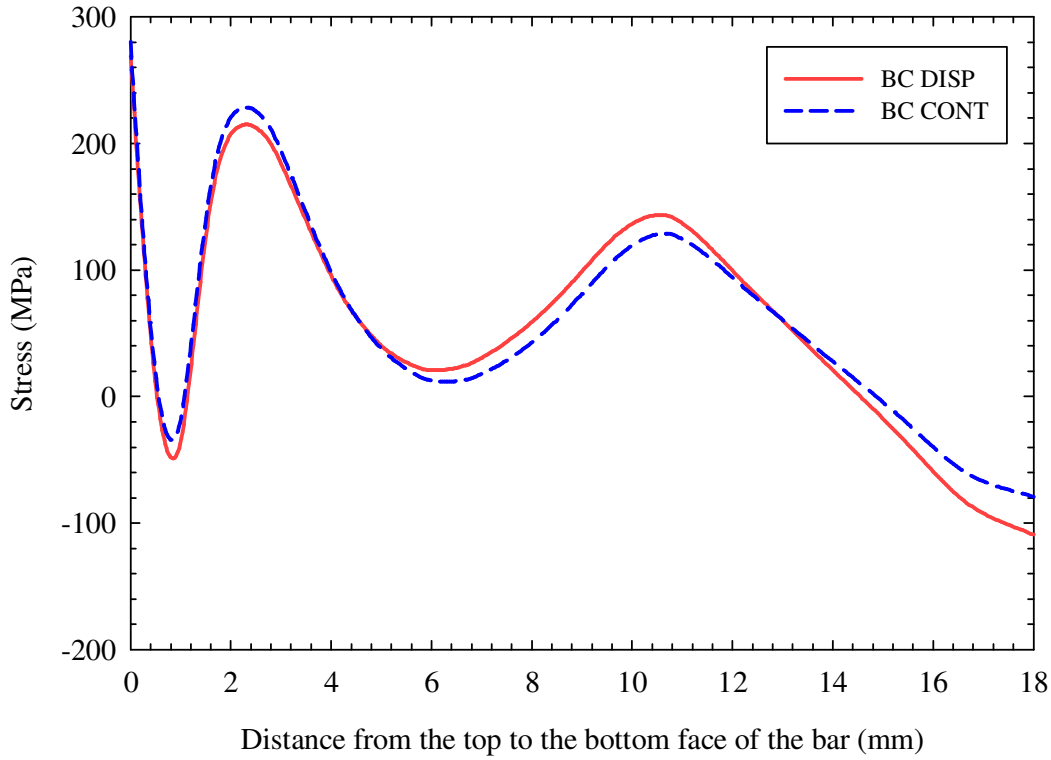
300
200
100
0
-100
-200
0
2
4
6
8
10
12
14
16
18
Stress (MPa)
Distance from the top to the bottom face of the bar (mm)
BC DISP
BC CONT

(c)

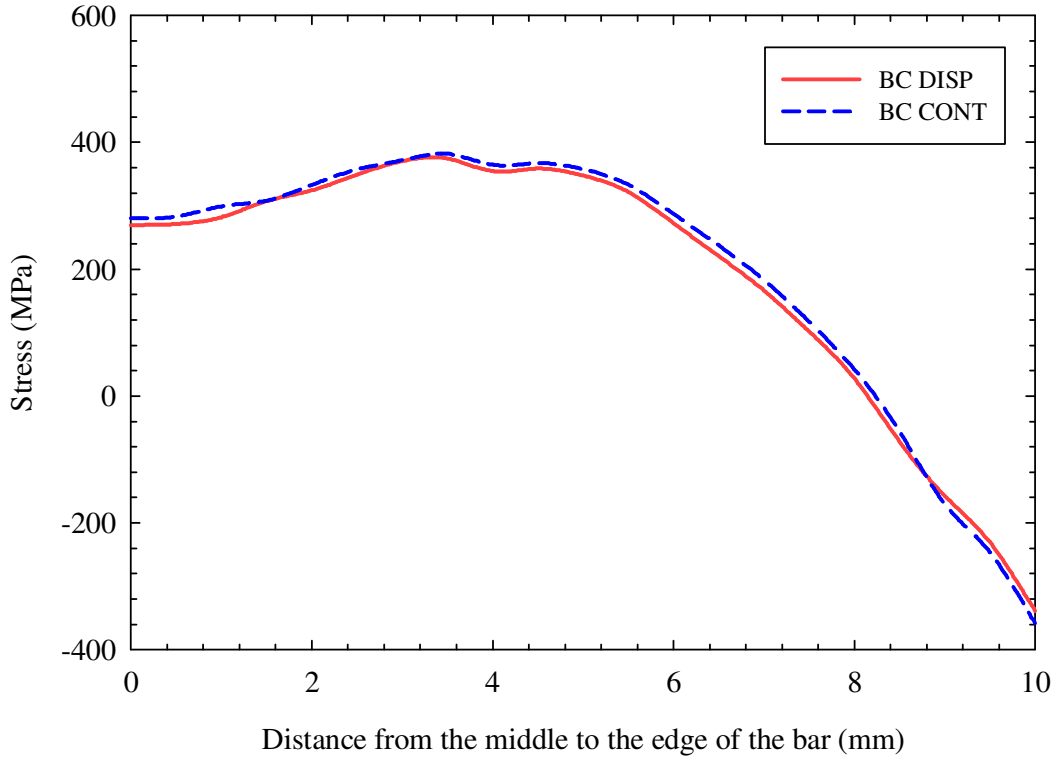

(d)

Figure 4.12. The boundary conditions (a) 'BC DISP' and (b) 'BC CONT' on the bottom face of the bar, and the longitudinal residual stresses (c) in the thickness (-y) direction on the symmetry plane and (d) in the width (x) direction of the bar at the half rolled length for the HRB case.

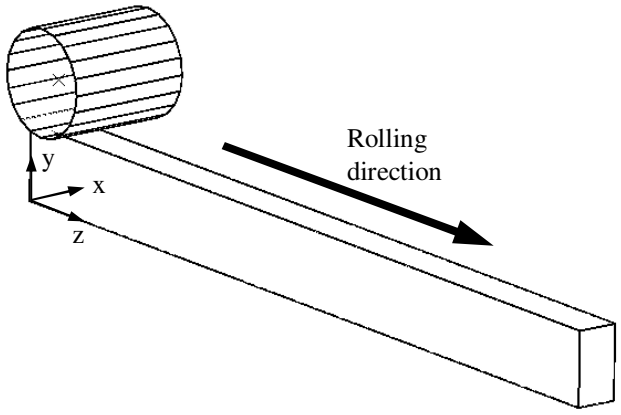

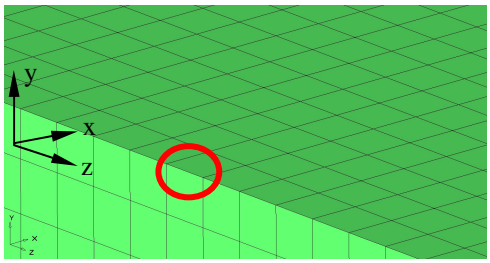

Mesh-1: Coarse mesh element size for the top layer and in the middle of the bar, $\Delta x = 0.5$, $\Delta y = 0.5$, $\Delta z = 0.5$

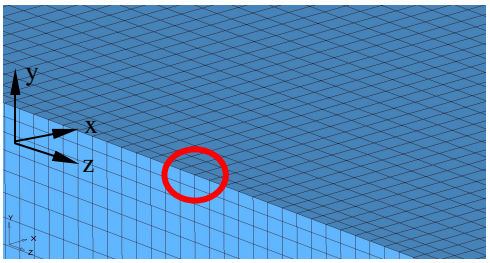

Mesh-2: Intermediate mesh element size for the top layer and in the middle of the bar, $\Delta x = 0.13$ to 0.25, $\Delta y = 0.126$, $\Delta z = 0.2$

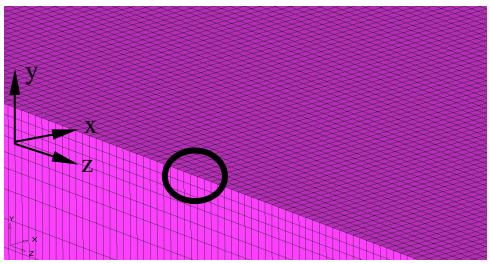

Mesh-3: Finest mesh element size for the top layer and in the middle of the bar, $\Delta x = 0.1$, $\Delta y = 0.1$, $\Delta z = 0.1$

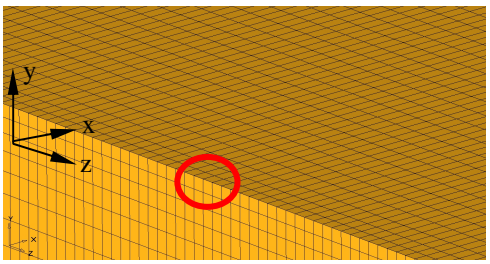

Mesh-4: Fine mesh element size for the top layer and in the middle of the bar, $\Delta x = 0.13$ to 0.25, $\Delta y = 0.126$, $\Delta z = 0.126$

Figure 4.13. Different mesh sizes used for the mesh sensitivity study. All sizes are expressed in mm.

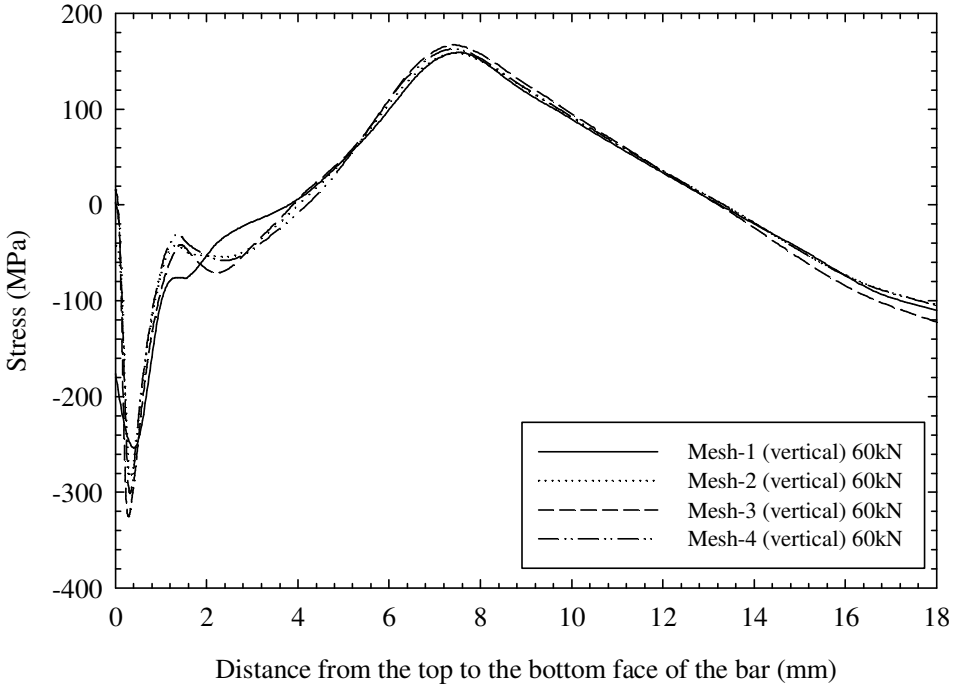

(a)

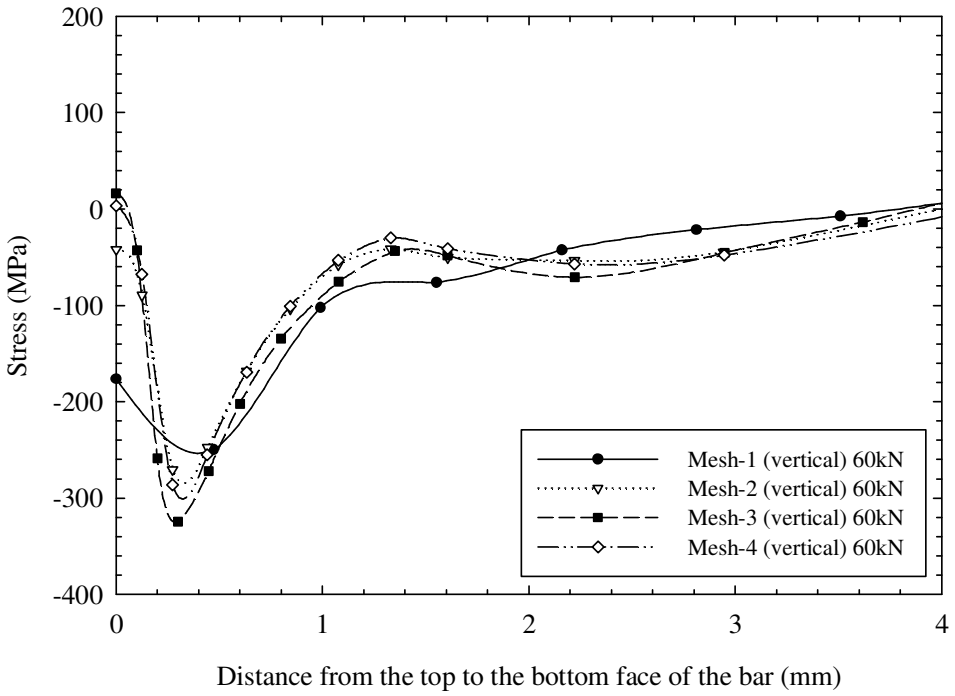

(b)

Figure 4.14. (a) The effect of mesh size on the longitudinal residual stresses in the thickness (-y) direction for the 60 kN rolling load and (b) zoom-in view of (a).

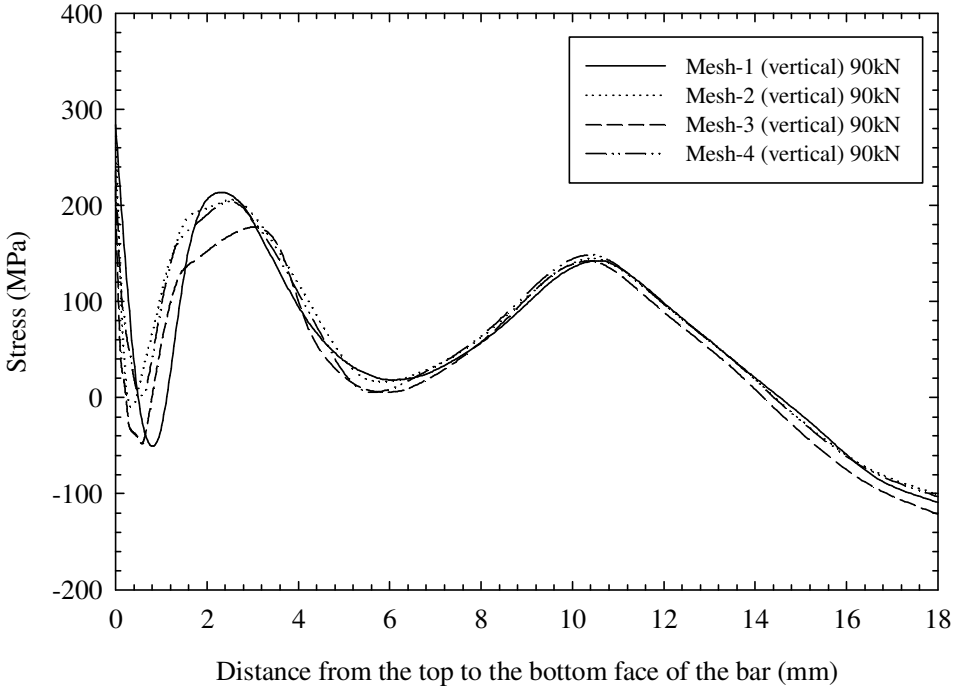

(a)

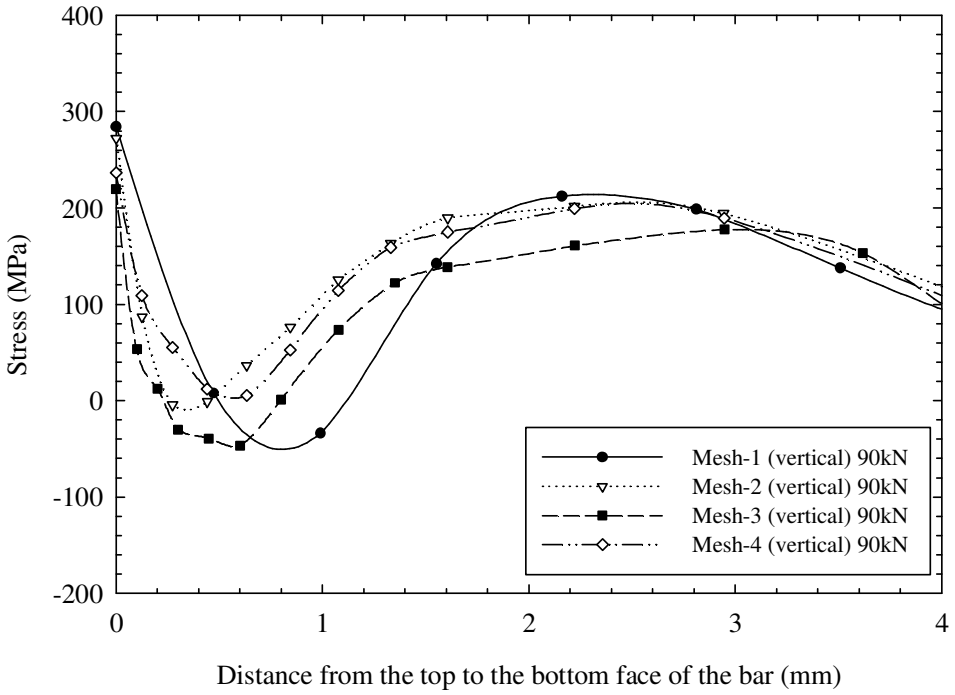

(b)

Figure 4.15. (a) The effect of mesh size on the longitudinal residual stresses in the thickness (-y) direction for the 90 kN rolling load and (b) zoom-in view of (a).

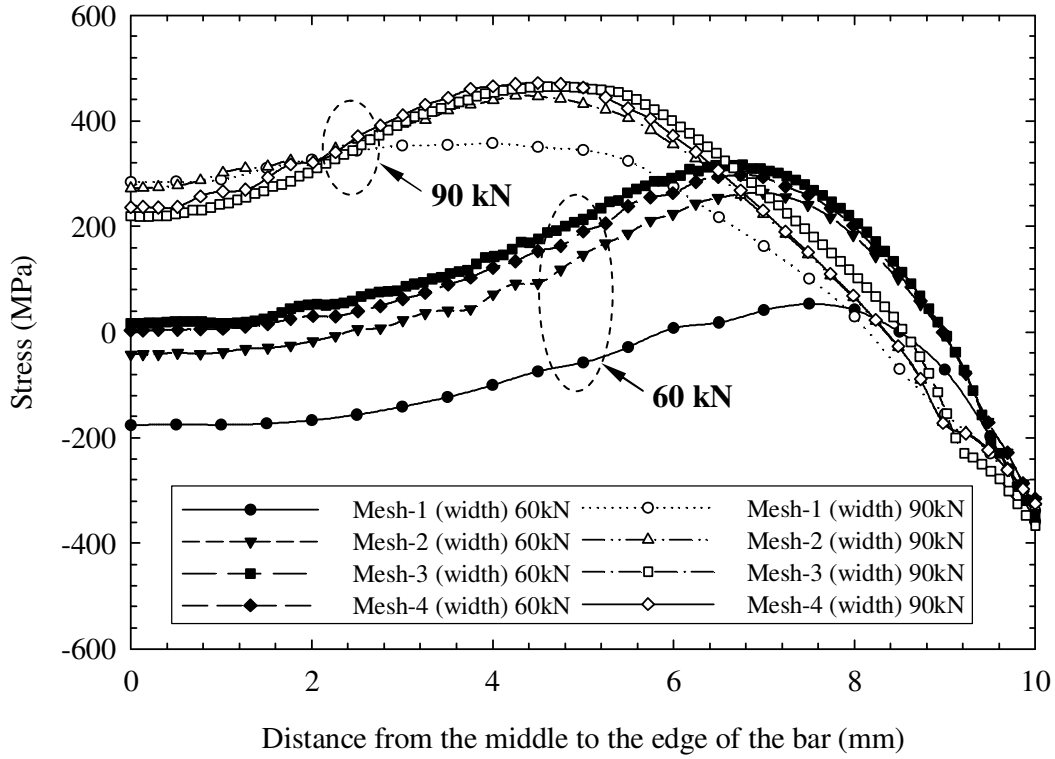

Figure 4.16. The effect of mesh size on the longitudinal residual stresses in the width (x) direction for the 60 kN and the 90 kN rolling loads.

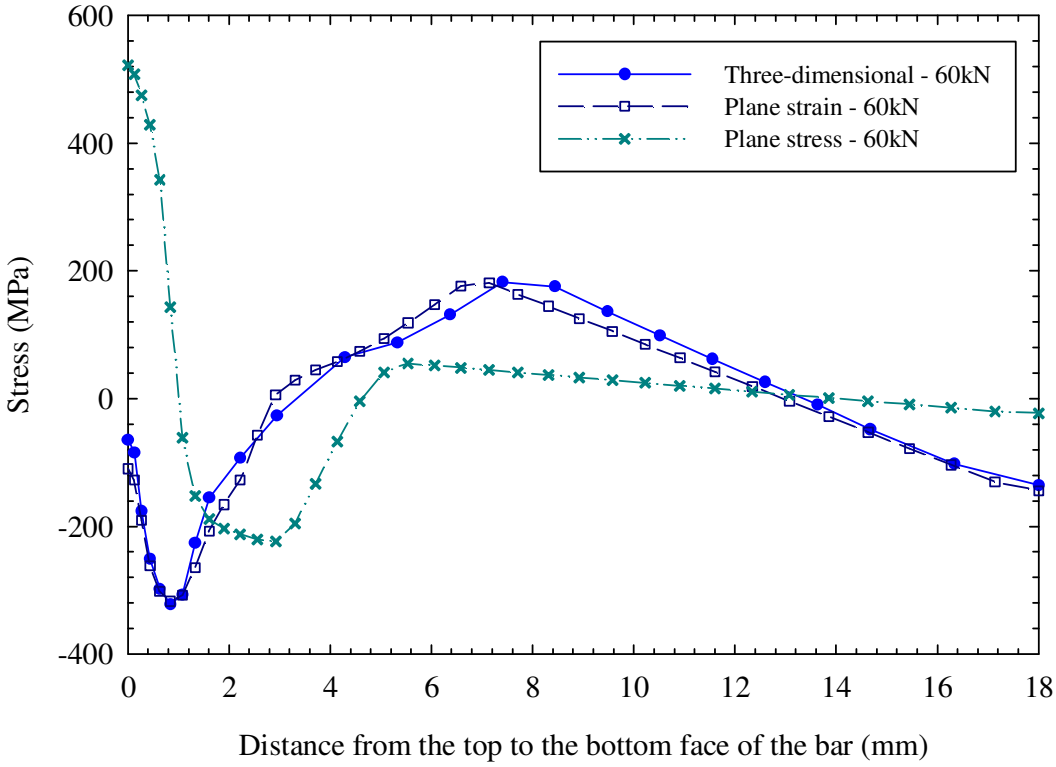

Figure 4.17. A comparison of the longitudinal residual stresses (σ_{33}) obtained from the three-dimensional finite element model and the two-dimension plane strain and plane stress finite element models for the 60kN rolling load.

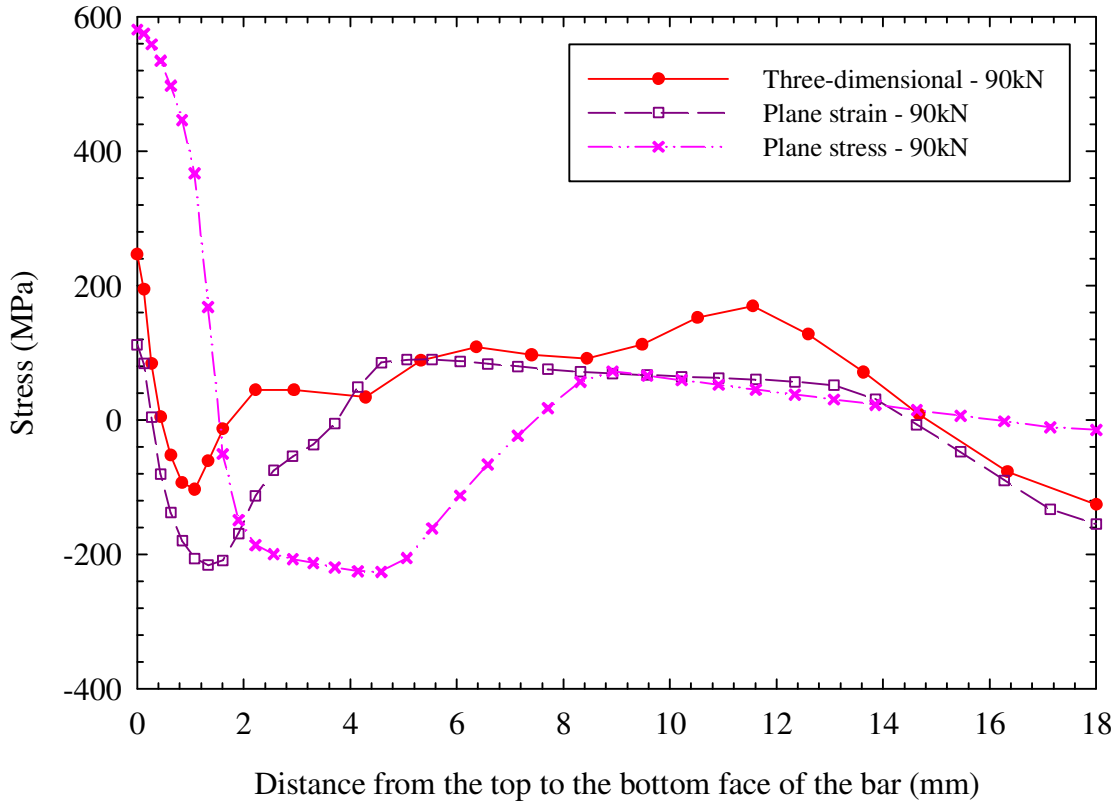

Figure 4.18. A comparison of the longitudinal residual stress (σ_{33}) obtained from the three-dimensional finite element model and the two-dimensional plane strain and plane stress finite element models for the 90kN rolling load.

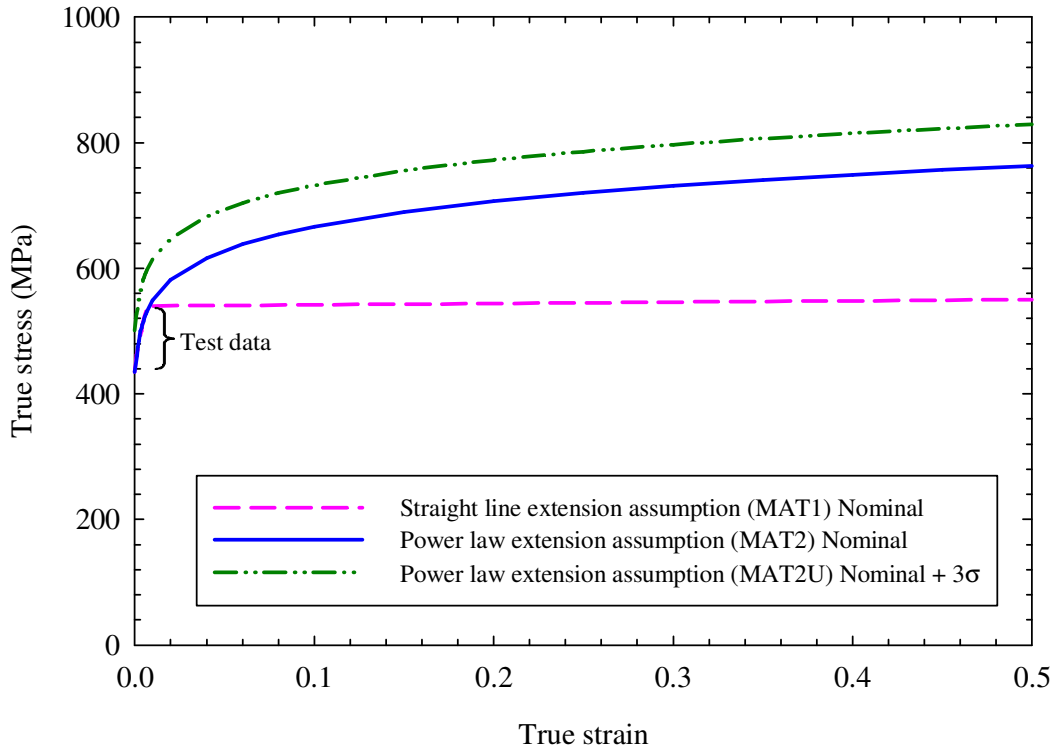

Figure 4.19. The stress-strain curves of the bar material used in the finite element analyses to examine the effect of material data variability.

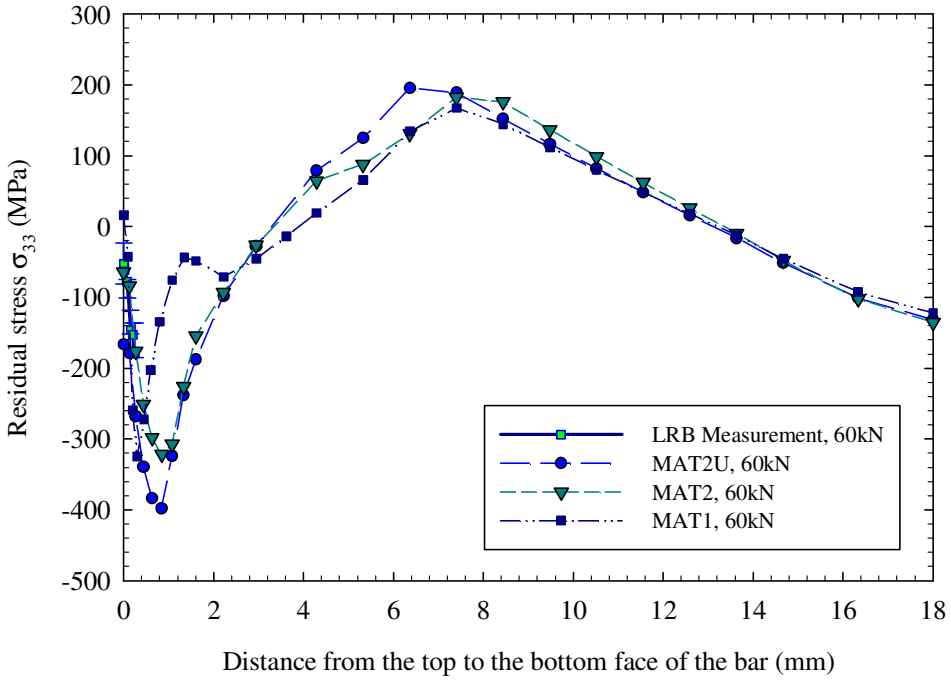

(a)

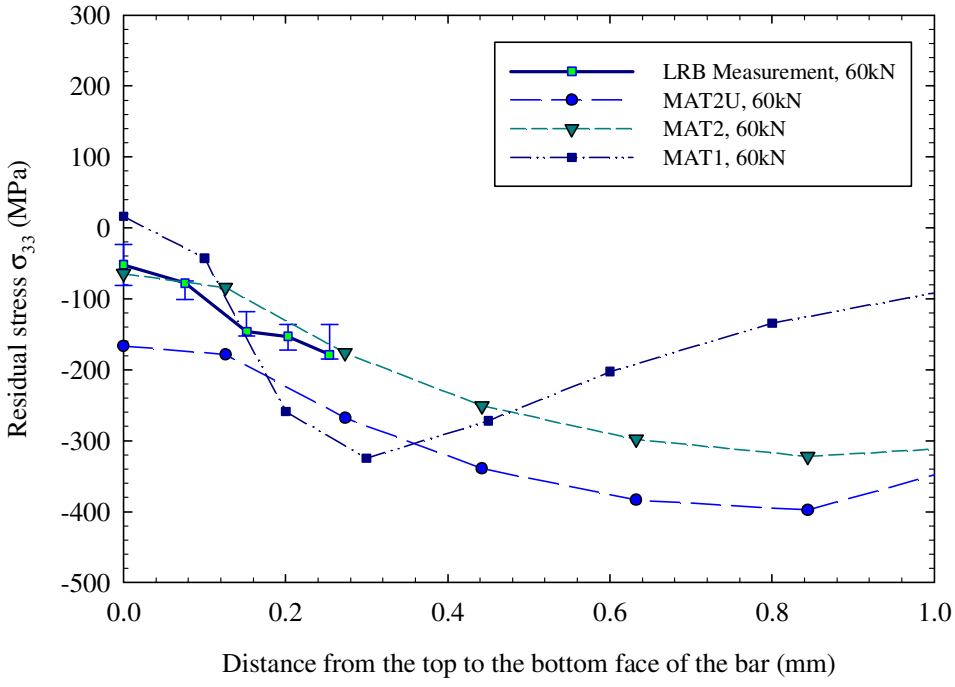

(b)

Figure 4.20. (a) The effect of the material data variability on the longitudinal residual stresses (σ_{33}) in the thickness (-y) direction for the 60 kN rolling load and (b) zoom-in view of (a).

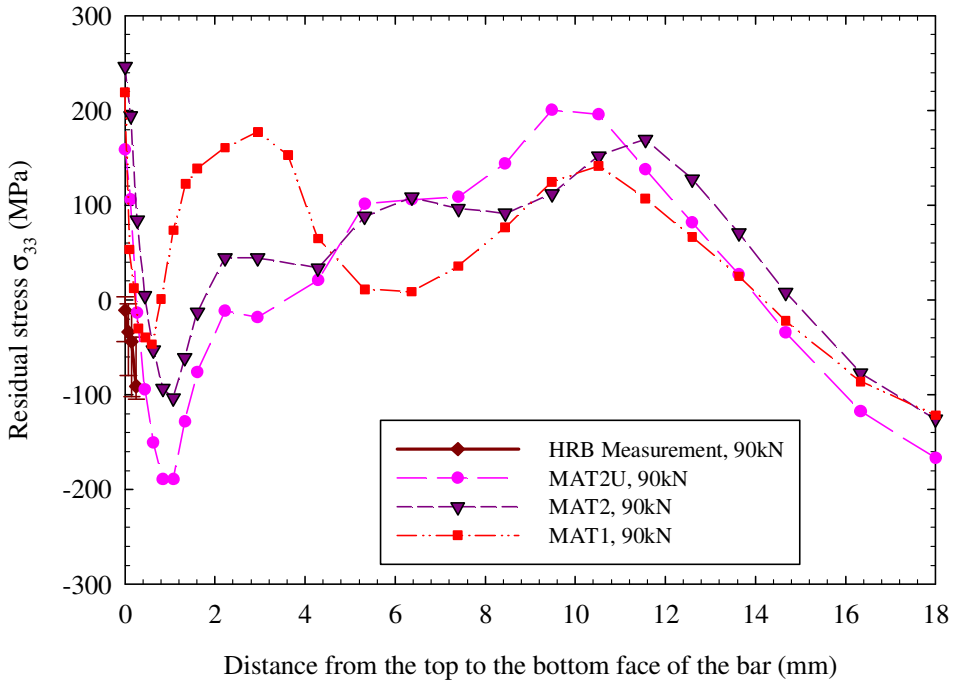

(a)

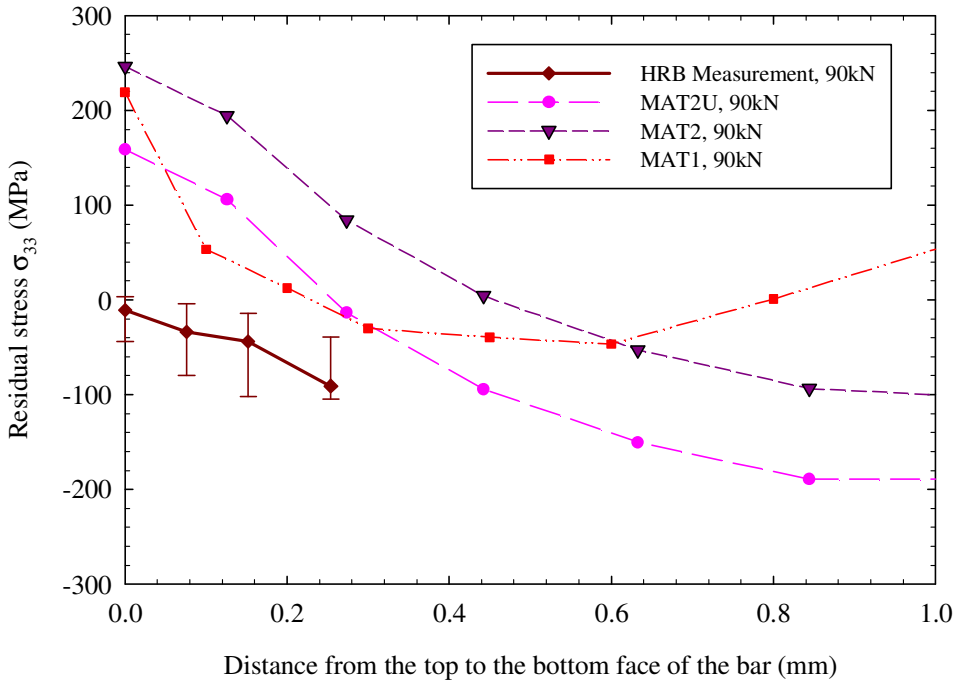

(b)

Figure 4.21. (a) The effect of the material data variability on the longitudinal residual stresses (σ_{33}) in the thickness (-y) direction for the 90 kN rolling load and (b) zoom-in view of (a)

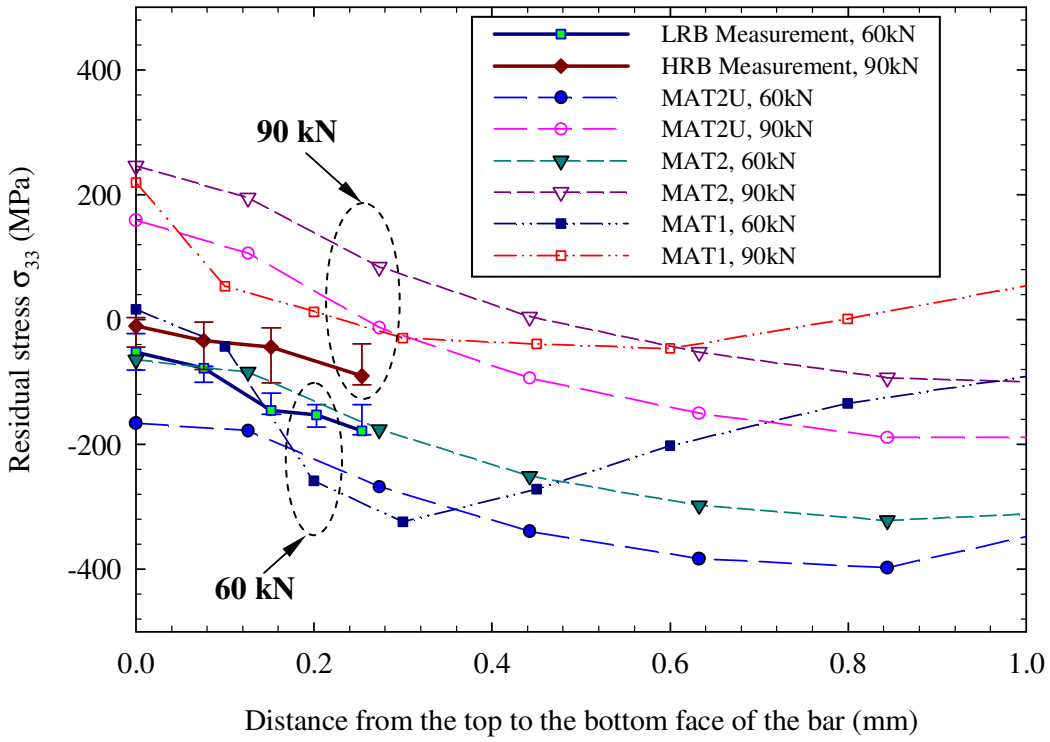

Figure 4.22. A comparison of the longitudinal residual stresses (σ_{33}) in the thickness (-y) direction for both rolling loads based on finite element analysis and measurements.

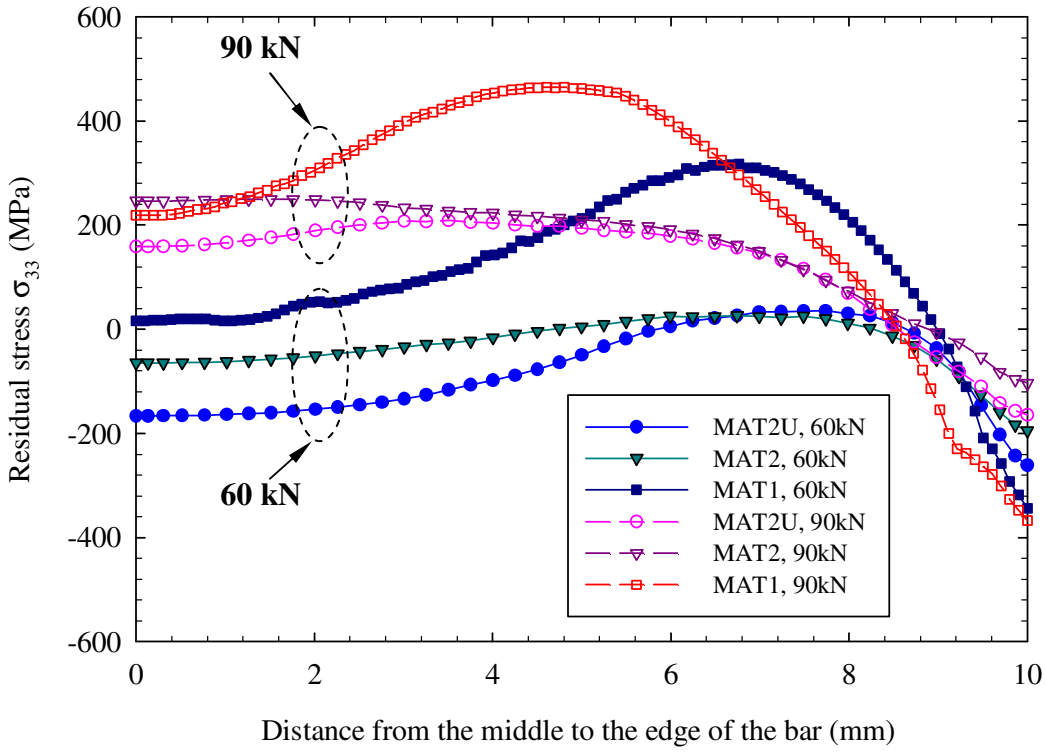

Figure 4.23. The effect of the material data variability on the longitudinal residual stresses (σ_{33}) in the width (x) direction for both rolling loads.

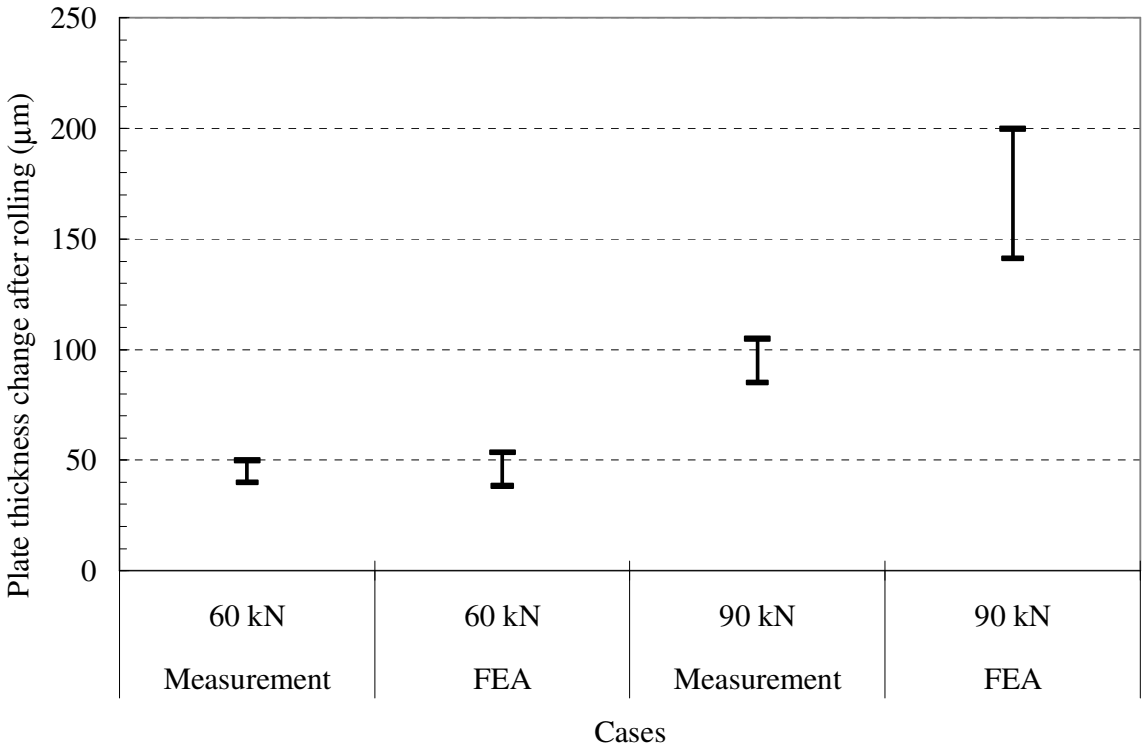

Figure 4.24. A comparison of the results of the finite element analyses with the measurement data for thickness changes of the rolled samples for both rolling loads.

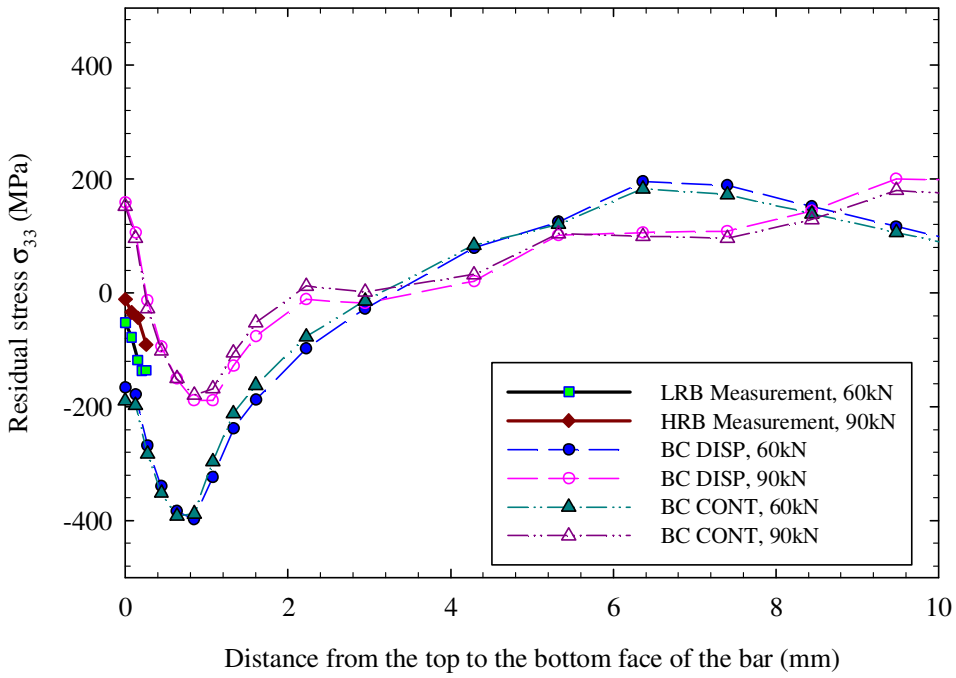

(a)

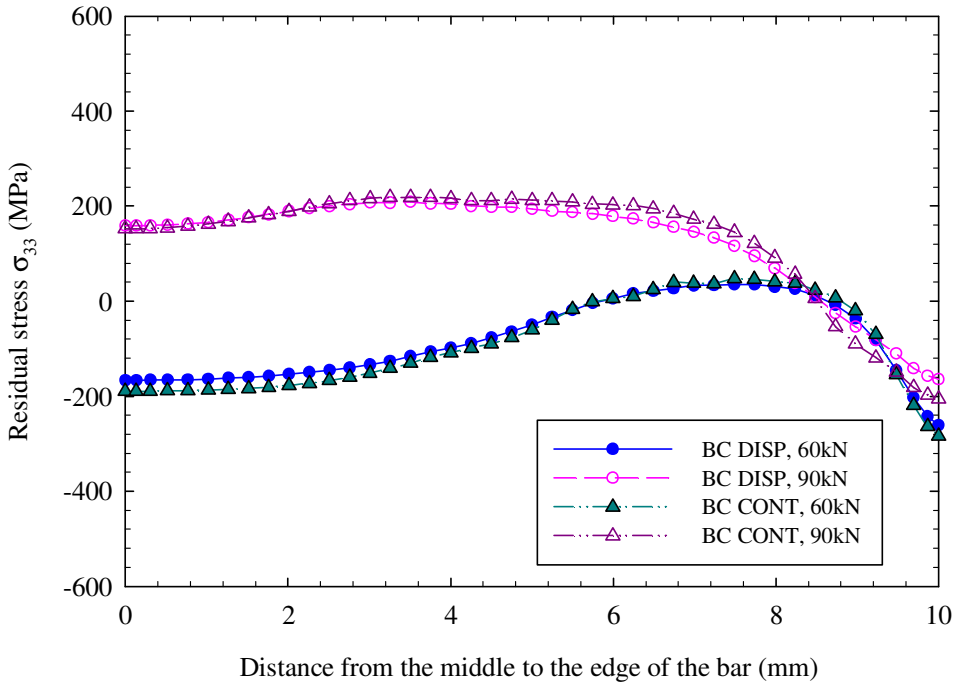

(b)

Figure 4.25. Effect of the boundary conditions on the longitudinal residual stress in the (a) thickness (-y) direction and (b) in the width (x) direction. Material data 'MAT2U' is used.

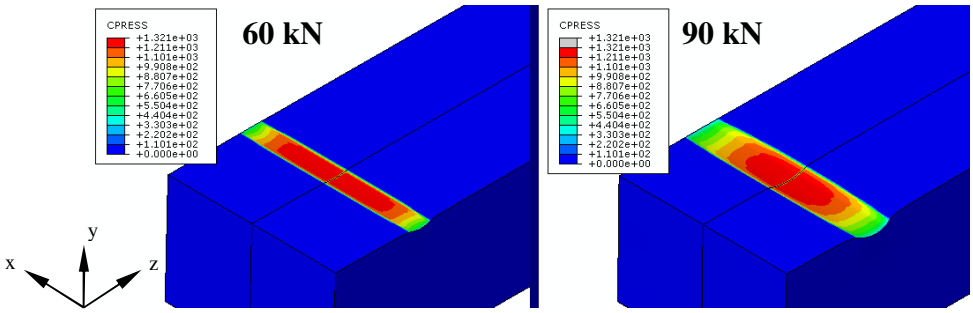

(a)

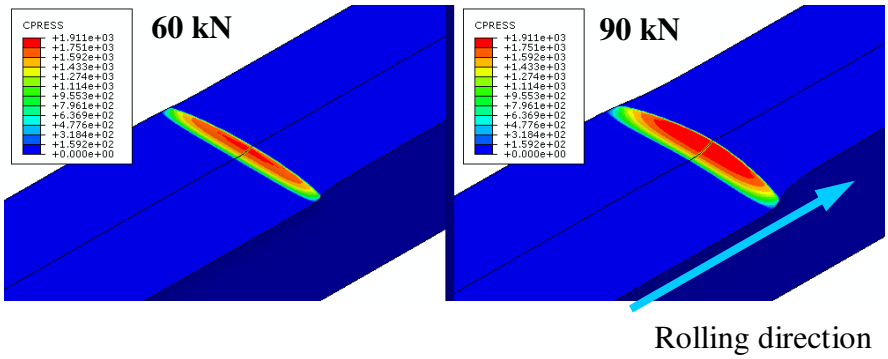

(b)

Figure 4.26. The contours of the contact pressure distribution for (a) a single indentation and (b) during rolling with the 60 and the 90 kN rolling loads. The displacement magnification is 3X and the symmetric half bar model is mirrored for visual purpose.

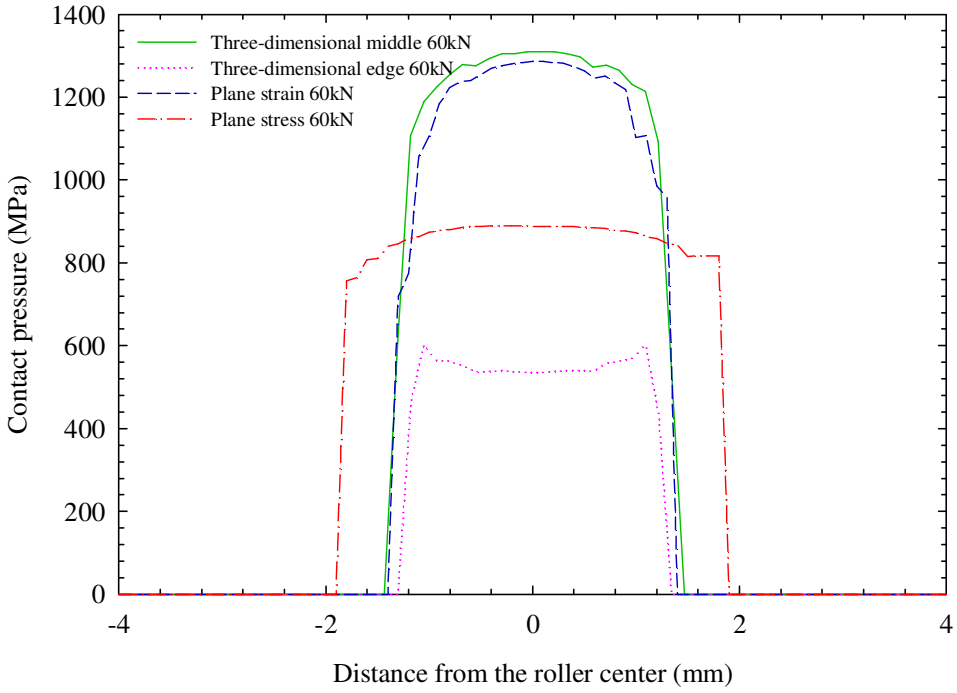

(a)

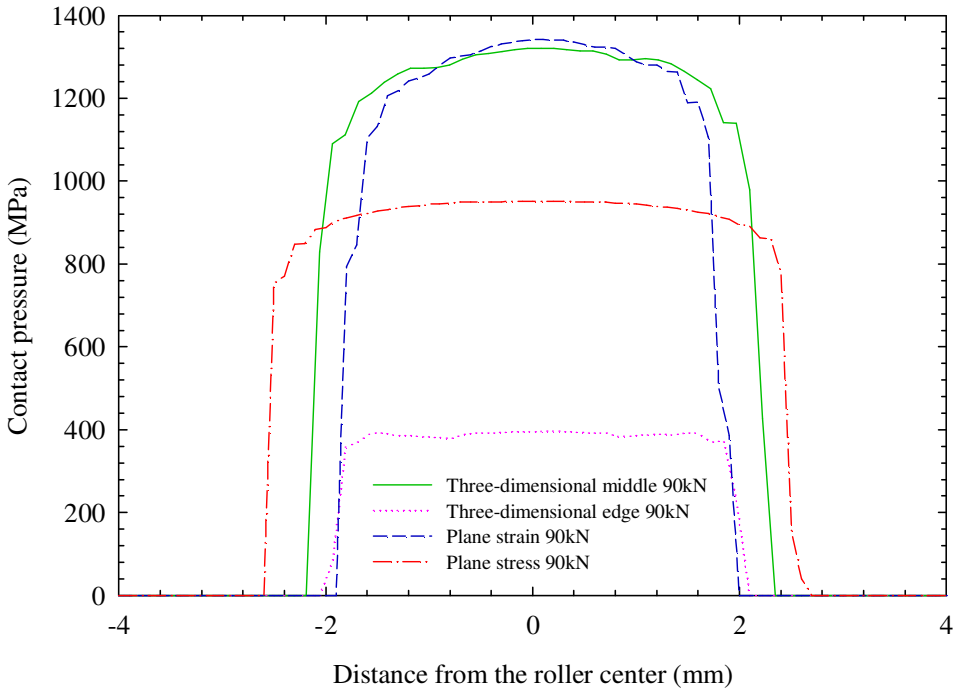

(b)

Figure 4.27. The distributions of the contact pressure due to single indention with the (a) 60 kN and (b) 90 kN loads based on the three-dimensional, plane strain and plane stress models. Material data 'MAT2' is used.

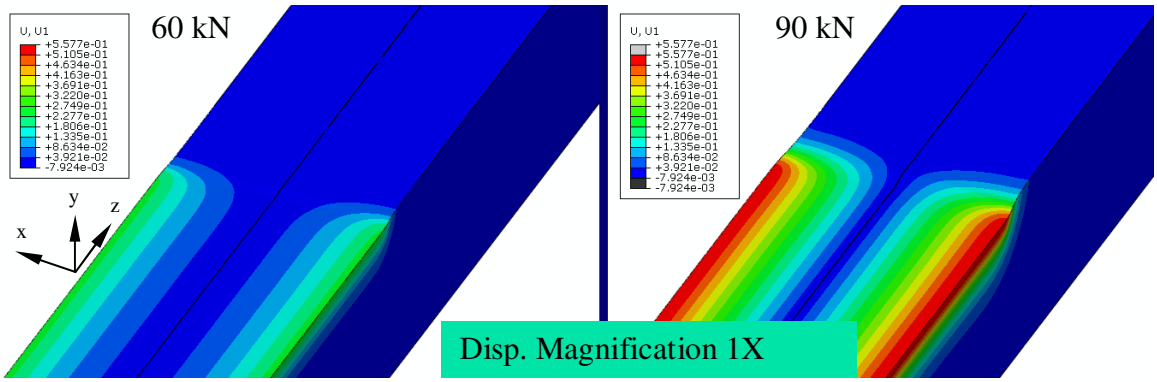

(a)

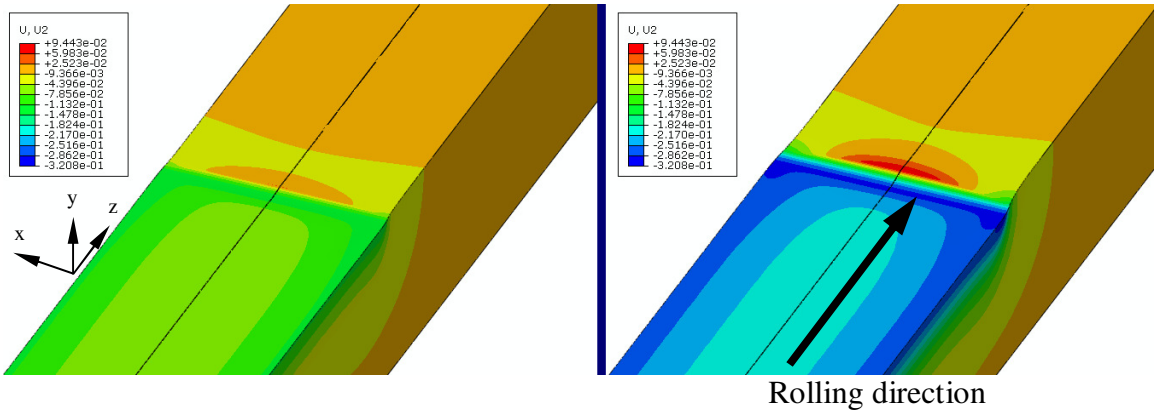

(b)

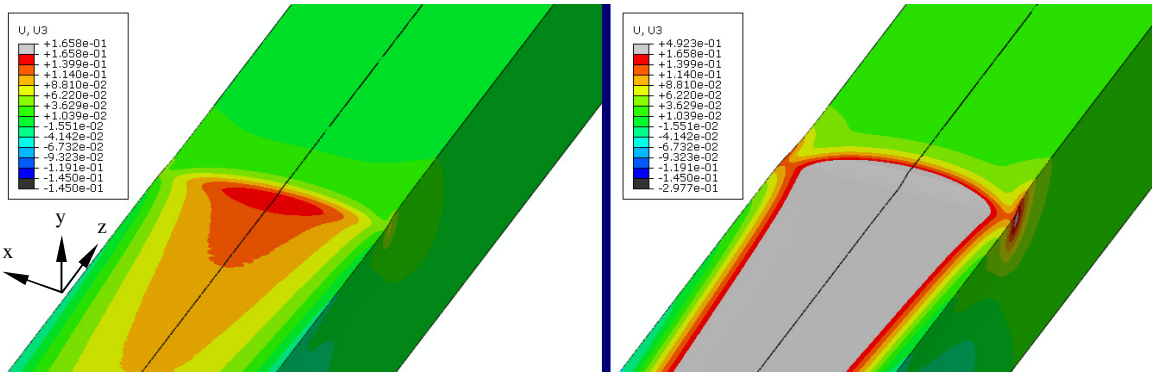

(c)

Figure 4.28. The contours of the displacement components (a) u_1, (b) u_2, and (c) u_3 during rolling under 60 and 90 kN rolling loads.

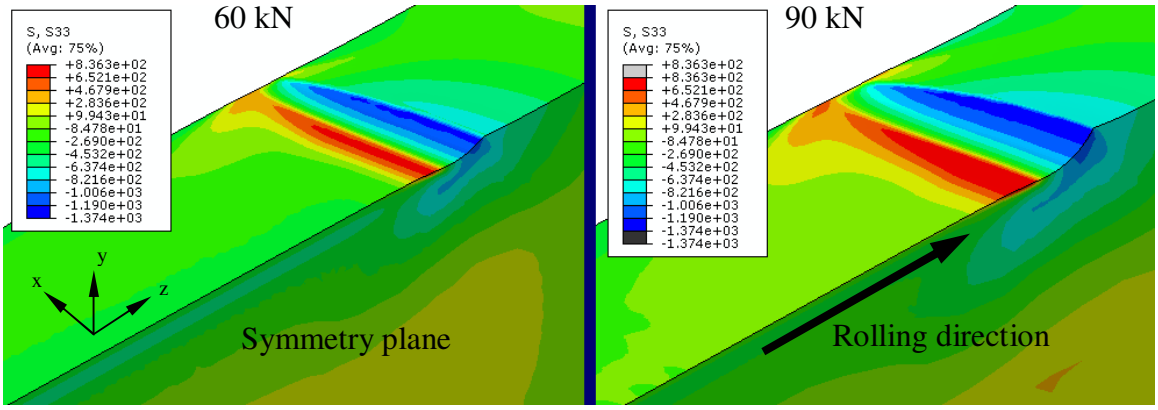

(a)

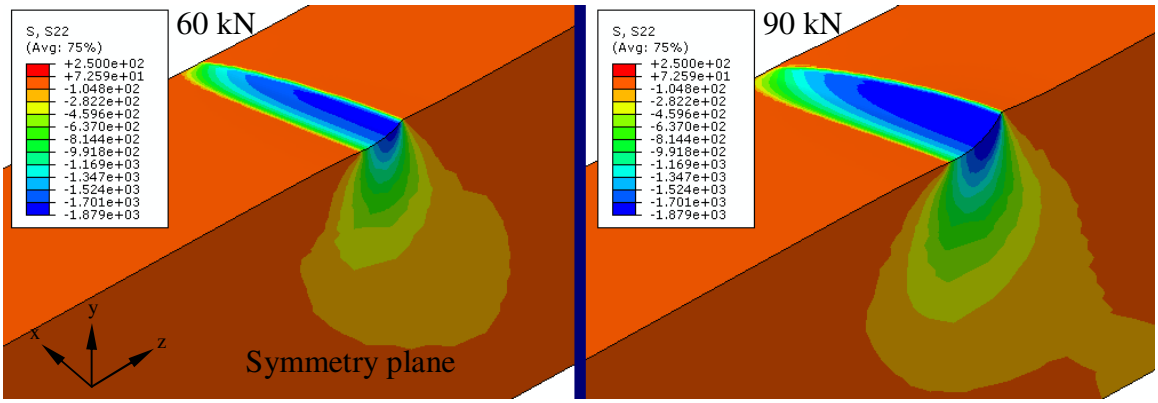

(b)

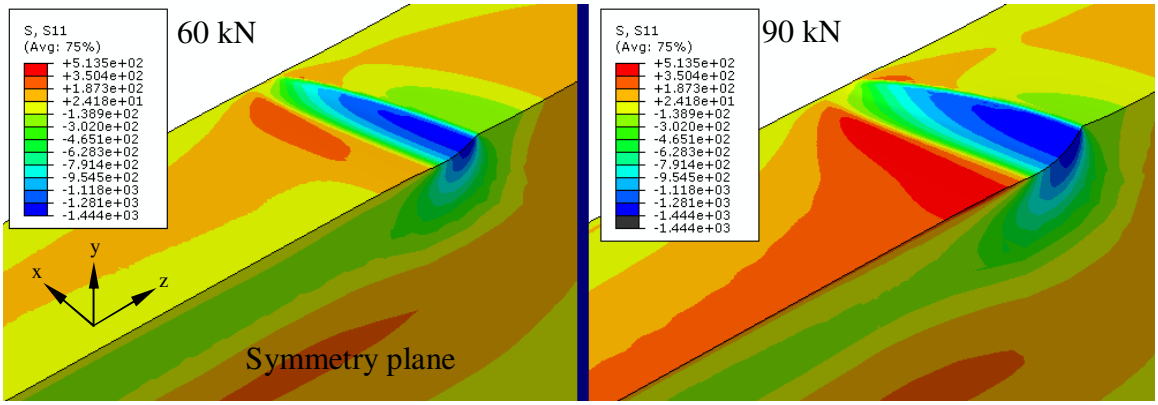

(c)

Figure 4.29. The contours of the (a) longitudinal stress (σ_{33}), (b) vertical stress (σ_{22}), and (c) transverse stress (σ_{11}) components during rolling with 60 and 90 kN rolling loads. A displacement magnification 3X is used for visual purpose.

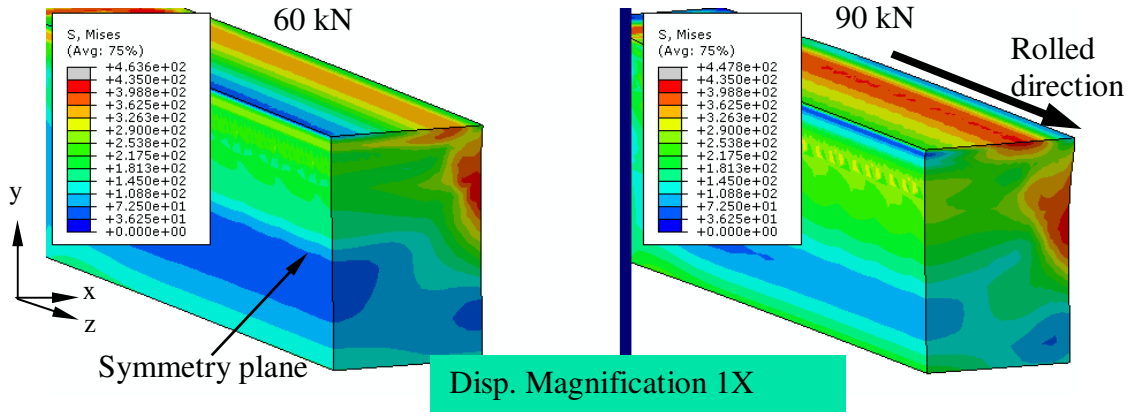

(a)

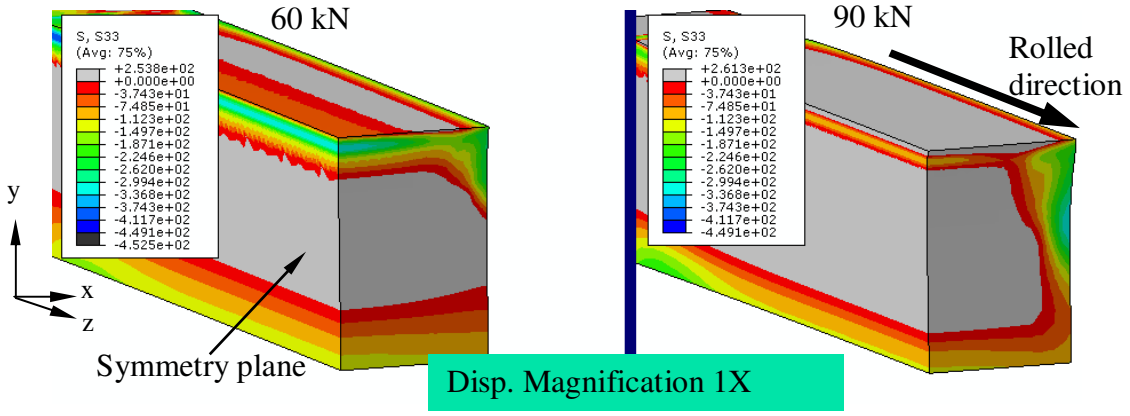

(b)

Figure 4.30. The contours of the (a) residual Mises stress and (b) residual longitudinal stress (σ_{33}) at the cross section of the bar after rolling is completed.

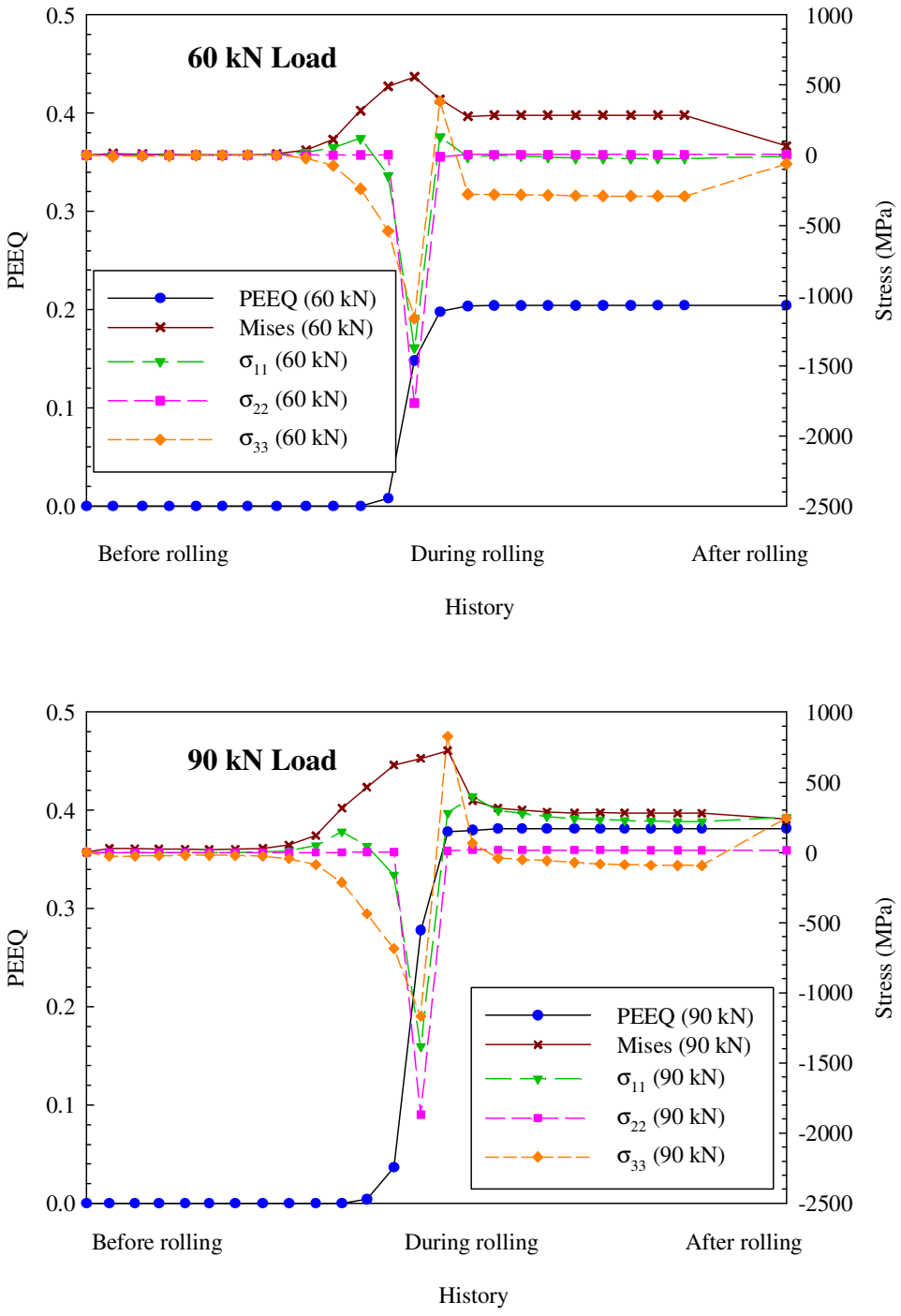

Figure 4.31. The history of equivalent plastic strain (PEEQ) at a node located at the top surface and at the symmetry plane of the bar model for both rolling loads.

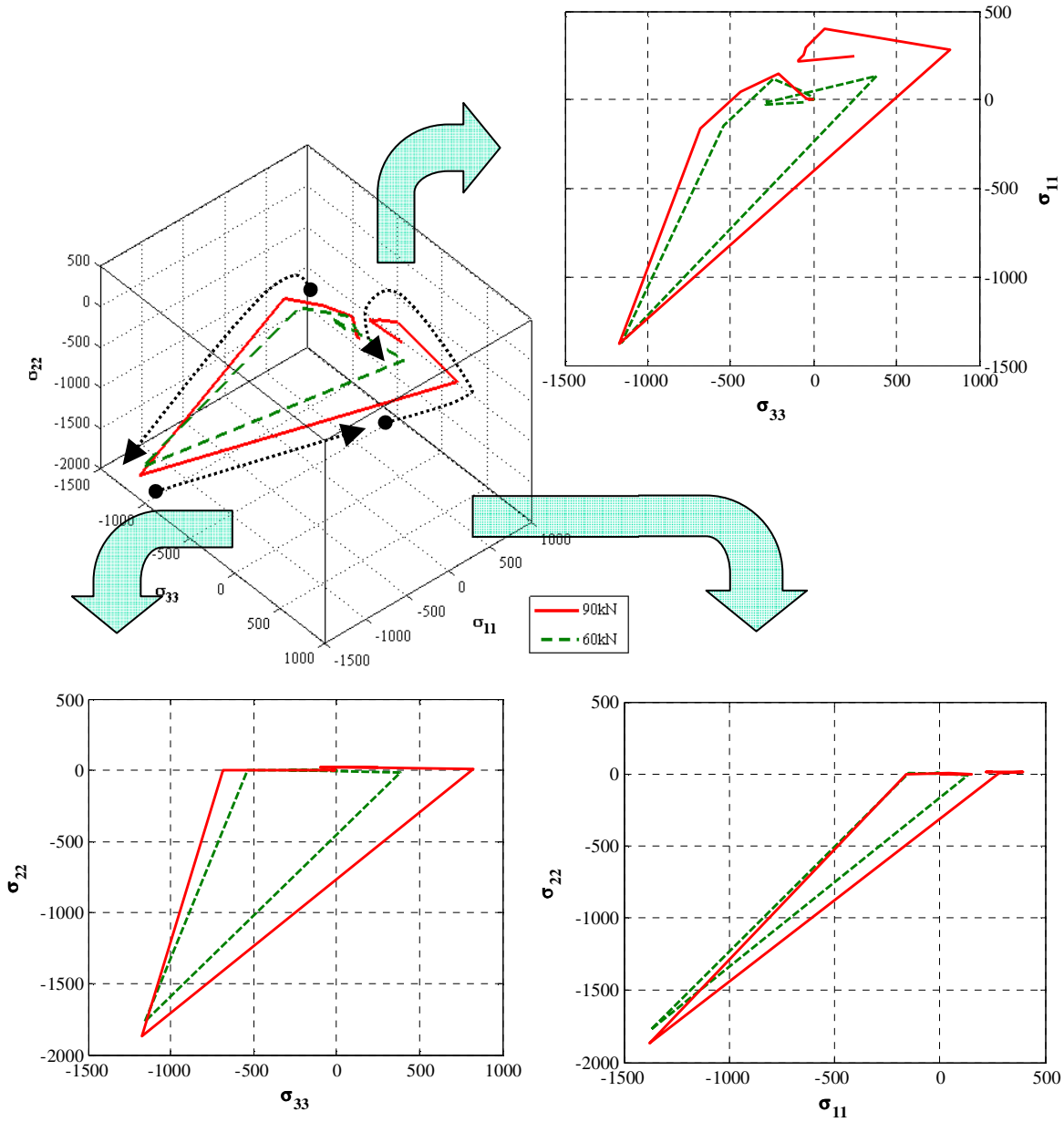

Figure 4.32. History of the principal stresses of a node at symmetry plane and at top surface of the bar is shown in a 3-D line graph – during and after rolling is completed. Material data 'MAT2' is used.

Chapter 5
Computational Models for Simulations of Lithium-Ion Battery Cells under Constrained Compression Tests

5.1. Introduction

Lithium-ion batteries have been considered as the solution for electric vehicles for the automotive industry due to its lightweight and high energy density. The major design considerations of lithium-ion batteries involve electrochemistry, thermal management and mechanical performance. The electrochemistry has been widely studied since it directly determines the battery performance and its life cycle. Different active materials on electrodes give different types of lithium-ion batteries. However, the basic chemical reactions of the cells are similar. For automotive applications, the mechanical performance is of great importance for crashworthiness analyses. Various research works have been focused on the chemical stability under impact, punch, nail penetration, and extreme temperatures [1-5]. However, the research works related to the mechanical behavior of lithium-ion batteries and the corresponding computational modeling are very limited.

Several research works were conducted to understand and model the phenomena related to diffusion or intercalation induced stresses, cracking, debonding, and effect of coating due to reaction in lithium-ion batteries [6-13]. These research works are mainly focused on electrodes or separators and understandably do not cover the global mechanical behavior of battery cells and modules. Sahraei et al. [14] conducted a series

of tests and mechanical modeling on commercial $LiCoO_2$/graphite cells used for cell phones. The results indicate that the compressive mechanical behavior is characterized by the buckling and densification of the cell components. Other testing and modeling data available were also conducted on commercial $LiCoO_2$ cylindrical or prismatic battery cells [15, 16]. However, this information is of limited use for researchers to model the mechanical performance of automotive high-voltage $LiFePO_4$ battery cells and modules for crashworthiness analyses.

Sahraei et al. [14] indicated that computational effort is quite significant to model local buckling phenomenon of battery cells under in-plane compression. Therefore, macro homogenized material models of the representative volume elements (RVEs) for both the battery cells and modules have to be developed for crashworthiness analyses with sacrifice of the accuracy at the micro scale. Other than dealing with the multi-physics problem, one of the challenges of developing the computational models for the battery behavior is to deal with different models at different length scales as indicated in [14]. Therefore, understanding the basic mechanical behavior of the lithium-ion batteries for automotive applications is very important to develop macro homogenized material models for representative volume elements (RVEs) of cells and modules for efficient crashworthiness analyses.

Recently, Lai et al. [17] investigated the mechanical behaviors of lithium-iron phosphate battery cells and modules by conducting tensile tests of individual cell and module components, constrained compression tests of RVE specimens of dry cells and modules, and a punch test of a small-scale dry module specimen. Their results of in-plane tensile tests of the individual cell components indicate that the active materials on

electrodes have a very low tensile load carrying capacity. For in-plane constrained compression tests of cell RVE specimens, the results indicate the load carrying behavior of cell RVE specimens is characterized by the buckling of cells with a wavelength approximately in the order of the thickness of the cells and the final densification of the cell components. They also tested module RVE specimens with different heights and the results indicate that the load carrying behavior of module RVE specimens is also characterized by the buckling of cells with a wavelength approximately in the order of the thickness of the cells and the final densification of the module components but relatively independent of the height of the tested specimens. In addition, they investigated the effects of adhesives between cells and foam/aluminum heat dissipater sheets on the mechanical behavior of module RVE specimens. The results indicate that the adhesive slightly increases the compressive load carrying capacity of the module RVE specimens. Their SEM images of the active materials on electrodes and the results of in-plane compressive and out-of-plane compressive tests suggest the total volume fraction is up to 40% for the microscopic gaps between cell components and the porosity of the separators and the active materials on electrodes. Based on the compressive nominal stress-strain curves in the in-plane and out-of-plane directions, their work suggests that the lithium-ion battery cells and modules can be modeled as anisotropic foams or cellular materials.

The current study is focused on developing the computational models for simulations of RVE specimens of lithium-ion battery cells under in-plane constrained compression tests based on the work of Lai el al. [17] and then comparing the computational results with those of the tests. Figure 5.1 shows a schematic view of the approaches of the developments of the computational models. Two approaches are used

for the modeling of these battery cells and modules: a detailed model (micro approach) and a less detailed model (macro approach). This investigation will focus on the detailed modeling of a cell RVE specimen of lithium-ion batteries. In the detailed model, the pouch cell battery is modeled as a layered composite and the RVE material nominal stress-strain response is obtained based on the properties of the cell components of layered anode, cathode, separator and active sheets. The less detailed models were investigated in a companion study [18] to address the length scale issue in mechanical modeling of the batteries. In those less detailed models, a small-scale battery module was considered as a homogenized material based on the response of the physical testing of the module RVE specimens [17]. Both approaches are useful to investigate the mechanical behavior of lithium-ion pouch cell batteries and modules.

The purpose of this detailed model investigation is twofold: one is to enhance understanding of the mechanical behavior of lithium-ion battery cells used for automotive applications and the other is to pave the groundwork for the development of user material models to represent the battery cells and modules by homogenized materials which are a subject of the future research. Finite element models can be used to simulate the tensile tests for multi-layered cell and module RVE specimens. However, a simple estimation scheme for tensile behavior is presented in [17] based on the rule of mixture (ROM) for composite and thus the tensile behavior of battery cells will not be addressed here. In this investigation, the compressive behavior of cell RVE specimens under quasi-static in-plane compression tests is investigated using the ABAQUS explicit finite element solver [19]. In this paper, the experimental results for cell RVE specimens under in-plane compression tests are first reviewed briefly for understanding the physical deformation

pattern of the porous cell RVE specimens. Next, the Gurson's model for porous material is presented for characterization of the separator and the electrodes with the active materials. Then the available material data are discussed and adopted for the input of the computational model. The details of the computational model are presented. The computational results of the deformation pattern and nominal stress-strain behavior are then compared with the test results. Based on the computational model, the effects of the friction coefficient between the cell components and the constrained surfaces on the deformation pattern, plastic deformation, void compaction, and the load-displacement curve are examined. The usefulness of the computational model is then presented by further exploring the effects of the initial clearance and biaxial compression on the deformation patterns of cell RVE specimens. Finally, some conclusions are made.

5.2. Experiments

A detailed description of the structure of a lithium-ion battery module used for this investigation can be found in [17]. Also note that the following definitions will be used throughout the paper. A *Single unit* cell represents a basic cell containing one cathode, one anode and a separator sheet with two aluminum cover sheets with two accompanying separator sheets. A *Ten unit* cell consists of ten basic cells containing ten cathode, ten anode, twenty one separator and two aluminum cover sheets. In this investigation, the ten unit cell is considered as a general cell RVE specimen that represents a typical assembled pouch cell.

Each cell consists of five major components: cover sheet, anode, cathode, separator and electrolyte. Since the electrolyte is difficult to handle during assembly due

to the safety concern, all the cell and module RVE specimens tested in this study were made without electrolyte at the University of Michigan. Figure 5.2(a) shows a schematic of a pouch cell with two cover sheets and a cell RVE specimen with the x-y-z coordinate system. A cell RVE specimen with the dimensions is shown in Figure 5.2(b). The pouch cell has a layered structure as schematically shown in Figure 5.2(b). The z-coordinate is referred to as the out-of-plane coordinate whereas the x and y coordinates are referred to as the in-plane coordinates. Constrained compression tests were conducted for cell RVE specimens with the dimension of 25 mm x 25 mm x 4.642 mm. The details of the test setup and results of the in-plane constrained compression tests are discussed in [17] and are briefly reviewed in the following.

Figure 5.3 shows three nominal compressive stress-strain curves of the cell RVE specimens tested at a displacement rate of 0.5 mm/min. The specimens showed almost a linear behavior in the beginning with an effective elastic modulus of 188 MPa. Note that the effective elastic modulus obtained from the composite ROM is 190 MPa using the effective elastic moduli obtained from the nominal stress-strain curves of cell components under in-plane constrained compression tests. When the strain reaches about 2%, noticeable change of the slope takes place and the curves continue to increase gradually up to the strains of 34%. Some minor drops were observed during the stage after the linear region due to the development of kinks and shear bands as shown in the deformation patterns recorded as discussed later. The trends of all three curves are quite consistent.

Figures 5.4(a) to 5.4(d) show the deformation patterns of a cell RVE specimen at the nominal strain of 1% in the initial linear stage, at the nominal strain of 2% where the

slope changes, and at the nominal strains of 10% and 15%. Figures 5.4(e) and 5.4(f) show the front and back views of the tested cell RVE specimen at the nominal strain of 34%. A careful examination of the deformation pattern shown in Figure 5.4(a) indicates the initial linear stage corresponds to the development of smooth buckling for the cell components. However, no load drop was observed at the load corresponding to the constrained buckling since it is supposed to occur at the stress of 0.018 MPa (beyond the resolution of the load cell). A detailed calculation of the buckling load or nominal stress of the cell RVE specimen is discussed in [17]. As the displacement increases toward the nominal strain of 2% where the slope starts to level off, the cell RVE specimen shows the development of kinks or plastic hinges of the cell components against the walls, as indicated in Figure 5.4(b). The presence of the kinks promotes the macroscopic shear band formation (strain localization in a narrow zone), as indicated in Figure 5.4(b). The shear band formation creates a physical mechanism to accommodate efficiently for the compression displacement and hence induces the load drop. As the strain continues to increase, more kinks and shear bands form across the cell RVE specimen as shown in Figures 5.4(c) and 5.4(d). Figures 5.4(e) and 5.4(f) show the front and back views of the tested cell RVE specimen at the nominal strain of about 34%. As shown in the figures, the kinks are fully developed as folds and many shear bands can be identified. Since the efficient compaction mechanism of shear band formation has been completed, further compression can only be accomplished by micro buckling of the cell components outside of the shear band regions, as marked in the figures, and the compression and shear in the shear band region.

An idealized deformation process of the cell RVE specimen under an in-plane constrained compression test is proposed in [17] to explain the shear band formation and is briefly reviewed here. Figures 5.5(a) to 5.5(c) show schematics of a cell RVE specimen before, during, and after the shear band formation under in-plane constrained compression, respectively. Figures 5.5(d) to 5.5(f) show the detailed schematics of the shear band formation corresponding to Figures 5.5(a) to 5.5(c), respectively. As shown in Figure 5.5(a), the cell RVE specimen (shown in gray) forms shear bands (between two parallel dashed lines) to accommodate the volumetric reduction under constrained compression. During the deformation, the angle α keeps deceasing towards to zero while the shear band angle θ also decreases by a small amount. In the shear band, the cell components are subjected to a compressive strain in the z' direction, a significant amount of the shear strain in the y'-z' plane and a significant amount of rotation. Here, y' and z' represent the local material coordinates that are fixed to the material. Outside of the shear band, the cell components are subjected to compressive strains in the y direction and z directions. Once α reaches to zero, further compressive strains are achieved by the micro buckling of the cell components outside of the shear bands and the void reduction and shear in the shear band as θ continues to decrease. This is illustrated in Figures 5.5(c) and 5.5(f). It should be noted that Figures 5.5(a) to 5.5(f) are idealized with the periodic shear band structures. In tests, the shear bands do not form at the same time and the shear band angle θ varies due to the imperfections of the specimens.

5.3. Gurson's yield function for porous materials

The anode and cathode for this investigation are graphite coated on copper foil and $LiFePO_4$ coated on aluminum foil, respectively. The copper foil has a thickness of 9 μm and the total thickness of the anode sheet is 0.2 mm. The aluminum foil has a thickness of 15 μm and the total thickness of the cathode sheet is 0.2 mm. Both the anode and cathode sheets are double-side coated. The separator is made of polyethylene with the porosity ranging from 36 to 44% and a thickness from 16 to 25 μm according to the manufacturer specification.

Figure 5.6 shows SEM images of the graphite and $LiFePO_4$ on the anode and cathode sheets, respectively, reported in Lai et al. [17]. It should be noted that both active materials on electrodes are in a powder form held together by the binder and therefore possess a high degree of porosity as seen in the SEM images. The electrodes with the porous active materials can be computationally treated homogenized porous sheets. Therefore, the Gurson's model for porous materials is adopted to model the electrodes with the active materials in the finite element analyses. Also, separator used in the cell is manufactured with a high degree of porosity to hold electrolyte. A brief description of the Gurson's model [19] is presented here.

Gurson [20] proposed a yield function ϕ for porous materials containing a small volume fraction of voids. In porous materials, the void volume fraction f is defined as the ratio of the volume of voids to the total volume of the material. The relative density of a material, r, defined as the ratio of the volume of matrix material to the total volume of the material, can also be used. Note that $f = 1 - r$. The Gurson's yield function ϕ was later modified by Tvergaard [21] to the form

$$\phi = \left(\frac{q}{\sigma_y}\right)^2 + 2q_1 f \cosh\left(-q_2 \frac{3p}{2\sigma_y}\right) - \left(1 + q_3 f^2\right) = 0 \qquad (5.1)$$

where $q \left(= (3\mathbf{S}:\mathbf{S}/2)^{1/2}\right)$ represents the effective macroscopic Mises stress, $p \left(= -\boldsymbol{\Sigma}:\mathbf{I}/3\right)$ represents the macroscopic hydrostatic pressure, σ_y represents the flow stress of the matrix material, which is expressed as a function of the average equivalent plastic strain $\bar{\varepsilon}_m^{pl}$ of the matrix for strain hardening materials, and q_1, q_2 and q_3 are the fitting parameters. Here, $\mathbf{S}$ represent the deviatoric part of the macroscopic Cauchy stress tensor $\boldsymbol{\Sigma}$. The macroscopic Cauchy stress $\boldsymbol{\Sigma}$ is based on the current configuration of a material element with voids. For $f = 0$ ($r = 1$), the material is fully dense, and the Gurson's yield function reduces to the Mises yield function. Tvergaard [21] introduced the fitting constants q_1, q_2 and q_3 to fit the numerical results of shear band instability in square arrays of cylindrical holes and axisymmetric spherical voids. One can recover the original Gurson's yield function by setting up $q_1 = q_2 = q_3 = 1$. In the current investigation, $q_1 = 1.5$, $q_2 = 1$, and $q_3 = q_1^2 = 2.25$ [19].

Figure 5.7(a) shows a schematic of the Gurson's yield contour in the normalized hydrostatic pressure (p) - Mises stress (q) plane for porous materials in comparison with that of the Mises material model. The porous material model reduces to the Mises material model as the void volume fraction f reduces to zero. Figure 5.7(b) shows a schematic of the uniaxial behavior of a porous material with a perfectly plastic matrix material and the initial void volume fraction f_0. Here the yield stress is denoted as σ_{y_0}. The porous material softens in tension and hardens in compression. The porous material

hardens in compression due to the reduction of the void volume fraction. Phenomenological hyperfoam and crushable foam material models are available in ABAQUS. However, more material input data are needed for these foam models and additional material data for the cell components are not available. Therefore, the Gurson's material model is adopted here for modeling the separator and the electrodes with the active materials.

5.4. Available material data for cell components

Tensile tests were conducted for the individual cell components such as anode, cathode, separator and cover sheets, and the test results were discussed in detail in Lai et al. [17]. In-plane constrained compression tests were also conducted for the anode, cathode, separator, and cover sheets to estimate the compressive elastic moduli, and the test results were also discussed in detail in Lai et al. [17]. Although these tests are constrained compression tests, only the apparent elastic part of the stress-strain responses appear to be useful to obtain the effective compressive elastic moduli for individual components. The effective compressive elastic moduli may account for the local micro buckling that occurs at a very small load level for each component sheet and has indistinguishable impacts to the measurable macroscopic response. Due to the compressive loading of the cell RVE specimens, the effective compressive elastic moduli are thus used for the electrodes and separator in the finite element analyses of the cell RVE specimens under constrained compression tests.

For elastic-plastic materials, the plastic strain hardening behavior is essential for the input of elastic-plastic finite element analyses. For the current investigation, the

elastic-plastic tensile stress-strain data for the components obtained in [17] are used to define the strain hardening behavior due to the difficulties to obtain such data under uniaxial 'unconstrained' compression tests. For the ABAQUS solver, the tensile tests data must be converted to the true stress and true strain format for elastic-plastic finite element analyses. There is no simple way to convert the engineering stress-strain curves of the anode, cathode and separator sheets with high porosity. The conversion to the true stress-strain curve is based on the usual assumption of plastic incompressibility for metal plasticity for lack of the detailed information on the detailed microstructure of the anode, cathode and separator. With the composite rule of mixture for the void and matrix and the assumption of the constant total volume of the void and matrix, the engineering stress-strain curve is converted to the true stress-strain curves. The anode and cathode fail at very low strains. The separator is very thin and is expected not to contribute significantly to the overall load carrying capacity of cells and modules. Therefore, the conversion to the true stress-strain curve with the plastic incompressibility seems to be a reasonable option for lack of further information.

The tensile and effective compressive moduli, tensile yield stress and Poisson's ratio of the cell components are listed in Table 1. Poisson's ratios of 0.33 for copper, 0.33 for aluminum, 0.45 for polymer and 0.2 for active layers are used to obtain the effective Poisson's ratio for separator, anode, cathode, and cover sheets using the composite ROM. The Poisson's ratios listed for anode and cathode in Table 1 are corresponding to the assumed void volume fraction f listed in the parenthesis. It should be noted that the void volume fractions of the active materials on electrodes are difficult to measure due to the fact that the graphite and lithium iron phosphate particles are loosely bonded together by

a weak binder. The void volume fraction 44% of the separator provided by the manufacturer is adopted here. For the linear part of each stress-strain curve, the modulus is calculated based on each data point with respect to the origin of the stress-strain curve. A stable average value for a range of the strain of the apparent linear behavior is selected as the tensile modulus for that specific material. The yield stresses for the materials of the cell components are selected where the stresses deviate from the apparent linear ranges. The thickness and the densities of the cell components are also listed in Table 2.

Figures 5.8(a) and 5.8(b) show the representative tensile nominal and true stress-true strain data of the cell components, respectively, and Figure 5.8(c) shows the stress-plastic strain curves of the cell components used in the finite element analyses. For the electrodes, the stress-plastic strain curves are provided up to the strain of failure in the tests. In ABAQUS, the stresses are kept constant outside the input strain range. In this case, this represents a perfectly plastic extension of the stress-plastic strain curves of the electrodes since they are apparently flat near the failure strains. This automatic extension of the input material data is used to avoid numerical issues that may arise due to error tolerance check used in regularizing the user-defined data in ABAQUS/explicit code. It should be mentioned again that the stress-plastic strain curves are estimations based on the available information. Many assumptions are made to obtain these curves. One goal of this investigation is to understand the physical mechanisms of these RVE specimens under constrained compressive tests. The details of the various aspects of compression tests simulations for cell RVE specimens are described in the following sections.

5.5. Computational models

The results of the compression tests of cell RVE specimens show that the layers of the RVE specimens are deformed by multiscale buckling phenomenon - both layer micro buckling and global macro buckling. Ideally, in a confined space with no clearance and only with the presence of the porosity in the separator and the active materials on the electrodes, the dense parts of the layers (copper foils in anodes, aluminum foils in cathodes, and aluminum and polymers in cover sheets) would get the room for buckling only by compressing the relatively softer and porous active materials on electrodes and separator layers laterally or in the out-of-plane direction. However, the initial microscopic gaps between the cell components also allow some rooms for buckling. The following approach is adopted and tested in developing the buckling model presented here. As the load increases, the local buckling of the individual sheets of the specimens develops and then the kinks of the cell components start to form laterally adjacent to the wall of the fixture. The kinematics of development of kinks and shear bands is an efficient way to compact these porous sheets with plastically incompressible inner copper or aluminum foils. Based on the experimental observations [17], the cell global buckling or shear bands come from the plastic hinges or sharp bending due to the rigid constraint of the fixture wall and the module global buckling comes from the smooth bending due to a more relax environment from the soft foam padding. The formation of these kinks and shear bands in computational simulations is the key to properly simulate the buckling behavior of the cell RVE specimens under constrained compression tests.

The simulation of the cell RVE (ten units) specimens under compression tests will be presented here. The similar approach can be used for module RVE specimens under

compressive loading to estimate the nominal stress-strain response that can be used as an input for a less detailed modeling [18]. Figure 5.2(b) shows a schematic of a cell RVE specimen with the dimensions. It should be noted that the stack-up of the cell components gives a total thickness of 4.642 mm. However, the constrained compression test fixture has a confinement dimension of 25 mm x 25 mm x 5 mm. In the beginning of the compression test, a clearance of 0.358 mm was present in the lateral or thickness direction, and is modeled accordingly in the finite element analyses.

Figure 5.9(a) shows the finite element model setup for a cell RVE specimen compression test using the ABAQUS/Explicit commercial finite element code. The x-y-z coordinate system is also shown. The explicit finite element solver is used for this simulation for a better contact stability among all the thin sheets during the buckling and under large deformation. The vertical length 25 mm and the thickness 4.642 mm of the finite element model are similar to the cell RVE specimen. For computational efficiency, only a half of the cell RVE specimen width of 25 mm is used in the finite element model. However, it should be noted that the symmetric boundary condition was not applied in the model due to the nature of the problem. The nominal stress vs. nominal strain curves of the computational simulations will be compared with those of the tests.

The compression test fixture is made of steel that has a very high stiffness compared to the cell components. Therefore, the confinement surfaces are assumed to be rigid and modeled by planar rigid surfaces. In the finite element model setup, the specimen mesh is surrounded by six rigid surfaces. The rigid surfaces contacting with the edges of the cell RVE component sheets with the normals in the x and y directions have zero clearance. The rigid surfaces contacting the cover sheets with the normal in the z

direction are 5 mm apart and provide a total of 0.358 mm initial lateral clearance with 0.179 mm on each side. The reference nodes of all the rigid surfaces except the top one have six degrees of freedom constrained. The top rigid surface can only move in the vertical direction and is given a velocity boundary condition. The general contact algorithm of ABAQUS/Explicit is used to model the contact interaction between the surfaces of the cell components that contact with one another and with the rigid surfaces. All the contact surfaces are assumed to be in friction contact with each other and an appropriate value of the coefficient of friction is used in the simulations as a fitting parameter. Figure 5.9(b) shows a detailed view of the meshes of each layer. The anode, cathode and cover sheets are modeled by linear hexahedral full integration solid elements (C3D8 of ABAQUS). Only a single layer of elements are used to model each layer and a mesh size of $\Delta x = 0.25$ mm and $\Delta y = 0.25$ mm is used. For the cathode and anode sheets, $\Delta z = 0.2$ mm. For the cover sheets, $\Delta z = 0.111$ mm. The thin separator is modeled by linear quadrilateral reduced integration shell elements (S4R of ABAQUS) with a thickness of 0.02 mm for convergence and computational efficiency.

The compression test speed of 0.008 mm/s is considered as a quasi-static condition. Using the explicit dynamics solver to model a quasi-static event requires some special considerations. It is computationally impractical to model the process by a time step to satisfy the Courant-Fredrich-Levy condition of numerical stability. A solution is typically obtained either by artificially increasing the loading rate or the speed of the process in the simulation, or increasing the mass of the system, or both. A general recommendation is to limit the impact velocity to less than 1% of the wave speed of the specimen, and a mass scaling of 5 to 10% is typical to achieve a desirable stable time

increment. Also the kinetic energy of the deforming specimen should not exceed a small fraction (1 to 5%) of the internal energy throughout the quasi-static analysis. The densities of the cell components are very low and the mesh size in this simulation is fine enough to capture the micro and macro buckling behaviors. Therefore, for a reasonable computational time, the finite element analysis is conducted at a speed of 200 mm/s and with a uniform mass scaling of 100 times of the actual mass. The deformation speed and the kinetic energy are very low and meet the recommendations of the quasi-static analysis for the explicit solver even though a higher mass scaling is used for computational efficiency. Different percentages of mass scaling were examined. The results showed some impact on the initial part of the stress-strain response up to a strain of about 1.5% and the results are generally comparable.

For the micro and macro buckling analyses as mentioned earlier, the compressive elastic moduli of the cell components are used and are listed in Table 1. The cover sheet is modeled as the Mises material with the isotropic hardening rule of ABAQUS and the elastic-plastic true stress-strain curve shown in Figure 5.8(b) is used. For the separator sheets, the initial void volume fraction f is set at 0.44 based on the manufacturer specification. The plastic behaviors for these components are provided based on the stress-plastic strain curves shown in Figure 5.8(c). The effect of the void volume fraction on the Poisson's ratio is estimated by treating the void as a component with zero Poisson's ratio using the ROM as

$$\nu_{\text{ROM}} = \sum_{i=1}^{n} \nu_i V_i \tag{5.2}$$

where ν_i and V_i are the Poisson's ratio and the volume fraction of the *i*-th component, respectively. Table 1 lists the Poisson's ratios for the cell components for different values of the initial void volume fraction f. The strain hardening behavior for the matrix material is obtained by scaling the tensile stress-plastic strain curves using the ROM

$$\sigma_{y_{Gurson}} = \frac{\sigma_y}{1-f} \tag{5.3}$$

where σ_y and $\sigma_{y_{Gurson}}$ represent the flow stress and adjusted flow stress of the matrix, respectively. The stress-plastic strain curve based on equation (5.3) will be referred as 'adjusted strain hardening curve'.

5.6. Computational results

Figure 5.10 shows the initial and deformed shape of the battery cell model under quasi-static in-plane compression and the corresponding experimental results. Initially, the cell RVE model is confined by six rigid surfaces as described earlier as shown in Figure 5.10(a). The top rigid surface is moved downward in the –y direction with a velocity boundary condition. Figure 5.10(b) shows the deformed shape of the model after the compressive displacement boundary condition is applied and held with the initial void volume fraction of f = 0.2 for the electrodes with the active materials at the nominal strain of 34%. In this case, the initial void volume fraction of f = 0.2 is used in estimating the Poisson's ratios and adjusting the strain hardening curves for the anode and cathode sheets with the active materials. In the model, a coefficient of friction of 0.1 is adopted for all the contacting surfaces as a general value. Many simulations with

multiple combinations of the parameters such as the void volume fraction and coefficient of friction were conducted. Only the combinations of parameters giving reasonable results will be presented here. Figure 5.10(c) is a zoom-in view of Figure 5.10(b). Figure 5.10(d) shows a deformed cell RVE test specimen after the in-plane compression test. The cell RVE specimen after the compression test shown in 10(d) is one of the three cell RVE specimens tested. Note that a different tested specimen is shown in Figure 5.4. The specimen showed here has a fairly regular buckling pattern and was selected for comparison of the buckling pattern with that of the computational results. Regular buckling patterns are obtained from the computational models since these computational models do not have significant irregularities or imperfections. The buckling patterns of the deformed finite element model are found similar and comparable to that of the test specimen.

Figures 5.11(i) through 5.11(vi) show successive snapshots of the deformation of the cell RVE specimen during the buckling simulation. Figures 5.12(i) through 5.12(vi) show the successive snapshots of the equivalent plastic strain (PEEQ) of the cell RVE during the buckling simulation. In Figure 5.11(ii) for the strain of 1.7%, the cover sheets on both sides of the cell specimen appear to buckle independently but the buckling is restricted by the rigid walls. The computational results not shown here indicate that the five buckles shown in Figure 5.11(ii) develop successively one by one from the top to the bottom and the neighboring softer separator, anode and cathode sheets buckle with the stiffer cover sheets. In Figure 5.11(iii) for the strain of 3.4%, the buckling peaks or valleys appear to adjust and synchronize with the macro buckling mode of the cell RVE specimen as a homogenized beam or plate. The absolute value of the nominal stress starts

to drop at the strain of about 2% with the increasing compressive nominal strain based on the computational results and this appears to be related to the starting of the macro buckling of the cell RVE specimen as a homogenized beam or plate.

Figure 5.11(iv) for the strain of 11.9% show that kinks starts to form adjacent to the cover sheets and shear bands are formed between the opposite pairs of kinks. As shown in Figures 5.11(v) and 5.11(vi) for the strains of 22.1% and 34%, respectively, the kinks become folds and the folds have different depths. The spacing between the folds in fact is not the same due to the friction and imperfections. The plastic hinges or bends of the cell components are found smoother in the computational models due to the large size of the elements in the finite element analyses compared to those of the tests where the bends are sharper with almost rectangular corners as shown in Figures 5.4(d) and 5.10(d) for two different tested cell RVE specimens.

The shear bands are formed in the sheets between the two opposite kinks as schematically shown in Figure 5.11(iv). As the deformation progresses, the shear bands in the computational models become slightly wider in the middle of the specimen compared to those of the tests due to the smoothing of the bends coming from the large element size in the finite element analysis. It should be noted that in order to capture the local bending more accurately, more layers of linear elements would have been appropriate to model each sheet. However, for computational efficiency and for a very high length to thickness ratio of each sheet, only a single layer of element is used for modeling each sheet to sufficiently capture the micro and macro deformation patterns.

The compaction of the voids in the components and microscopic gaps between the components, along with the initial clearances, allows room for further compression in a confined space. The kinks grow up to certain depths and the surfaces collapse with further compressive loading as shown in Figure 5.11(v). On the other hand, the stack of sheets that apparently are vertical between the two kinks on the same side are carrying loads by further deformations as shown in Figures 5.11(iv) to 5.11(vi), and Figures 5.12(iii) to 5.12(vi). The shape of this vertical zone across the thickness direction appears to be triangularly shaped whose apex is at the tip of the kink on the opposite side. Figure 5.12(vi) shows that at the end of the compression, the values of the PEEQ are higher near the top of the specimen compared to those near the bottom. This can be attributed to the friction effect on the top portion due to the progress of compressive deformation.

Figures 5.13(i) and 5.13(ii) show the distributions of the void volume fraction at the nominal strains of 8.5% and 34% of the constrained compression simulation, respectively. Only the void volume fractions of the anode and cathode sheets of the cell RVE specimen are displayed in these plots. Figure 5.13(i) shows that during the deformation at the nominal strain of 8.5%, the voids in the kink compaction bands are consumed. Figure 5.13(ii) shows that at the end of the compression at the nominal strain of 34%, the void volume fraction decreases more near the top of the specimen compared to that near the bottom. This can be attributed to the friction effect on the top portion due to the progress of compressive deformation.

Figure 5.14 shows a comparison of the nominal stress-strain curve from the finite element analysis with that of the test results obtained from Lai et al. [17]. As mentioned

earlier, the nominal stress-strain curve of the finite element analysis is based on the Gurson's material model with the initial void volume fraction $f = 0.2$ for the electrodes with the active materials and a friction coefficient of 0.1 based on a parametric study. The results of the parametric study show that the formation of the kinks and shear bands affects the stress where the slope of the nominal stress-strain curve of the computational results changes whereas a higher coefficient of friction raises the nominal stress to a higher value at a large strain. The results of the parametric study will not be reported here for brevity. The SAE 60 class filter has been used to post-process the computational stress-strain responses to filter the computational noise if present and for consistency in comparing the curves from computations [19]. The computational results show that the stresses drop slightly after the first noticeable global buckling at a strain of about 2% and this is in agreement with the experimental results. After reaching a strain of about 2%, the global buckling for the cell RVE specimen as a homogeneous beam begins. The stress then gradually increases as the densification or compaction continues as the strain increase. The results are compared fairly well with the test results in general. However, the computational response drops slightly after the strain of 25%.

The importance of the establishment and validation of the detailed computational model in this investigation can be demonstrated by exploring two example cases in order to visualize the effect of clearance and biaxial compression on the deformation patterns of cell RVE specimens under constrained compression. Only the deformation patterns of the two example cases are briefly presented here for demonstrating the usefulness of the computational model to understand the underlying physics of the cell RVE specimens under constrained compression.

The effect of the initial clearance on the shear band formation of a cell RVE specimen is demonstrated by using three initial clearances of zero, 0.358 mm for the current model and 0.716 mm in the finite element analyses. Figures 5.15(a) to 5.15(c) show the deformation patterns of the cell model under quasi-static in-plane compression for the three clearance cases at the nominal strain of 34%. As the initial clearance in the finite element models decreases from 0.716 mm to 0.358 mm and then to zero, the number of kinks increases, the kink depth decreases, and the number of shear bands increases from 8, 10 to 15, respectively. The details of the computational results will be reported with the corresponding experimental results in the future.

Figure 5.16 shows the deformation pattern of a cell RVE specimen under equal biaxial constrained compression based on the model shown in Figure 5.10(a). Here, the top and front rigid surfaces are moved downward in the –y direction and horizontally in the –x direction, respectively, with the velocity boundary conditions such that compressive nominal strains are equal in both x and y directions. The kinks and shear bands are formed inclined to both x and y directions in Figure 5.16. The number of kinks and shear bands on side S is about half compared to that of the side L due to the length ratio of one half for sides S and L in the computational model. Figure 5.16 also shows the pattern of interactions of the shear bands initiated from sides L and S. The details of the computational results will be reported with the experimental results for biaxial compression in the future.

5.7. Conclusions

In this paper, computational models are developed for simulations of representative volume element (RVE) specimens of lithium-ion battery cells under constrained compression tests. First, the load-displacement data and deformation patterns for cell RVE specimens under in-plane constrained compression tests are briefly reviewed. For the corresponding finite element analyses based on ABAQUS, the effective compressive moduli for cell components are obtained from constrained compressive tests, the Poisson's ratios for cell components are based on the rule of mixture, and the stress-plastic strain curve of the cell components are obtained from the tensile tests and the rule of mixture. The Gurson's material model is adopted to account for the effect of porosity in separators and in the active layers of anodes and cathodes. The results of the computations show that the computational models can be used to examine the micro buckling of the component sheets, the macro buckling of the cell RVE specimens, and the formation of the kinks and shear bands observed in experiments, and to simulate the load-displacement curves of the cell RVE specimens. Based on the computational models, the effects of the friction coefficient between the cell components and the constrained surfaces on the deformation pattern, plastic deformation, void compaction, and the load-displacement curve are identified. Finally, the usefulness of the computational model is demonstrated by further exploring the effects of the initial clearance and biaxial compression on the deformation patterns of cell RVE specimens.

Acknowledgements

Helpful discussions with Yibing Shi, Guy Nusholtz, and Ronald Elder of Chrysler, Saeed Barbat, Bill Stanko, Mark Mehall and Tau Tyan of Ford, Jenne-Tai Wang, Ravi Nayak, Kris Yalamanchili and Stephen Harris of GM, Christopher Orendorff of Sandia National Laboratory, Seung-Hoon Hong of University of Michigan, and Natalie Olds of USCAR are greatly appreciated.

References

1. Ashtiani, C., "Design and Development for Production of the Think EV Battery Pack," *Proceeding of the AABC-09 Conference*, CA, USA, 2009.
2. Cai, W., Wang, H., Maleki, H., Howard, J., Lara-Curzio, E., "Experimental Simulation of Internal Short Circuit in Li-Ion and Li-Ion-Polymer Cells," *Journal of Power Sources*, **196** 7779-7783 (2011).
3. Nguyen, J., Taylor, C., "Safety Performance for Phosphate Based Large Format Lithium-Ion Battery, Telecommunications Energy Conference," *INTELEC 2004. 26th Annual International*, 146-148, 2004.
4. Oh, J., "Large Lithium-Ion Battery for Automotive Applications," *Proceeding of the AABC-09 Conference*, CA, USA, 2009.
5. Otsuki, M., Ogino, T., Amine, K., "Investigation of Flame-Retardant Additives for Safety Usage of Lithium-Ion Batteries," *ECS Transactions*, **1** 13-19 (2006).
6. Deshpande, R., Cheng,Y.-T., Verbrugge, M. W., "Modeling Diffusion-Induced Stress in Nanowire Electrode Structures," *J. Power Sources* **195** 5081–5088 (2010), doi: 10.1016/j.jpowsour.2010.02.021.
7. Hu, Y., Zhao, X., Suo, Z., "Averting Cracks Caused by Insertion Reaction in Lithium-Ion Batteries," *Journal of Materials Research* **25**, 1007-1010 (2010).
8. Xiao, X., Wu, W., Huang, X., "A Multi-Scale Approach for the Stress Analysis of Polymeric Separators in a Lithium-Ion Battery," *J. Power Sources* **195** 7649–7660 (2010).
9. Zhang,L.Q., Liu, X., Liu, Y., Huang, S., Zhu, T., Gui, L., Mao, S., Ye, Z., Wang, C., Sullivan, J. P., Huang, J. Y., " Controlling the Lithiation-Induced Strain and Charging Rate in Nanowire Electrodes by Coating," *ACS Nano* **5** 4800–4809 (2011).
10. Zhang, X., Shyy, W. and Sastry, A. M., "Numerical Simulation of Intercalation-Induced Stress in Li-Ion Battery Electrode Particles," *Journal of The Electrochemical Society* **154** (10) A910-A916 (2007), doi: 10.1149/1.2759840.
11. Zhang, X., Sastry, A. M., and Shyy, W. "Intercalation-Induced Stress and Heat Generation within Single Lithium-Ion Battery Cathode Particles," *Journal of The Electrochemical Society* **155** (7) A542-A552 (2008), doi: 10.1149/1.2926617.
12. Zhao, K., Wang, W. L., Gregoire, J., Pharr, M., Suo, Z., Vlassak, J. J., Kaxiras, E., "Lithium-Assisted Plastic Deformation of Silicon Electrodes in Lithium-Ion Batteries: A First- Principles Theoretical Study", *Nano Letters* **11** 2962–2967 (2011), dx.doi.org/10.1021/nl201501s.
13. Zhao, K., Pharr, M., Hartle, L., Vlassak, J. J., Suo, Z., "Fracture and Debonding in Lithium-ion Batteries with Electrodes of Hollow Core-Shell Nanostructures," *J. Power Sources* **218** 6-14 (2012), doi:10.1016/j.jpowsour.2012.06.074.
14. Sahraei, E., Hill, R., and Wierzbicki, T., "Calibration and Finite Element Simulation of Pouch Lithium-Ion Batteries for Mechanical Integrity," *J. Power Sources* **201** 307–321 (2012), doi:10.1016/j.jpowsour.2011.10.094.
15. Hill, R., "Development for a Representative Volume Element of Lithium-Ion Batteries for Thermo-Mechanical Integrity, Department of Mechanical Engineering," Massachusetts Institute of Technology, 2011.

16. Sahraei, E., Wierzbicki, T., Hill, R., and Luo, M., "Crash Safety of Lithium-Ion Batteries Towards Development of a Computational Model," *SAE Technical Paper 2010-01-1078*, 2010, doi:10.4271/2010-01-1078.
17. Lai, W., Ali, M. Y. and Pan, J., Research work to be published, 2012
18. Ali, M. Y., Lai, W. and Pan, J., "Computational Models for Simulation of a Lithium-Ion Battery Module Specimen under Punch Indentation", Research work to be published, 2012
19. ABAQUS Version 6.11 User Manual, SIMULIA, Providence, RI, 2012.
20. Gurson, A. L., "Continuum Theory of Ductile Rupture by Void Nucleation and Growth: Part I-Yield Criteria and Flow Rules for Porous Ductile Materials," *Journal of Engineering Materials and Technology*, **99** 2-15, 1977.
21. Tvergaard, V., "Influence of Voids on Shear Band Instabilities under Plane Strain Condition," *International Journal of Fracture Mechanics*, **17** 389-407, 1981.

Table 5.1. Material properties used in the finite element analyses

	Tensile modulus (MPa)	Effective compressive modulus (MPa)	Tensile Yield stress (MPa)	Poisson's ratio
Anode, Graphite/Cu	4700	83	2.11	0.21 (f = 0%) 0.17 (f = 20%) 0.13 (f = 40%)
Cathode, Li-$FePO_4$/Al	5100	275	1.48	0.21 (f = 0%) 0.17 (f = 20%) 0.14 (f = 40%)
Separator	500	90	10.53	0.25 (f = 44%)
Cover sheet	5600	575	9.74	0.41

Table 5.2. Thickness and densities of the battery cell components

	Thickness, mm	Density, kg/m^3
Anode, Graphite/Cu	0.2	934
Cathode, Li-$FePO_4$/Al	0.2	1712
Separator	0.02	795
Cover sheet	0.111	1338

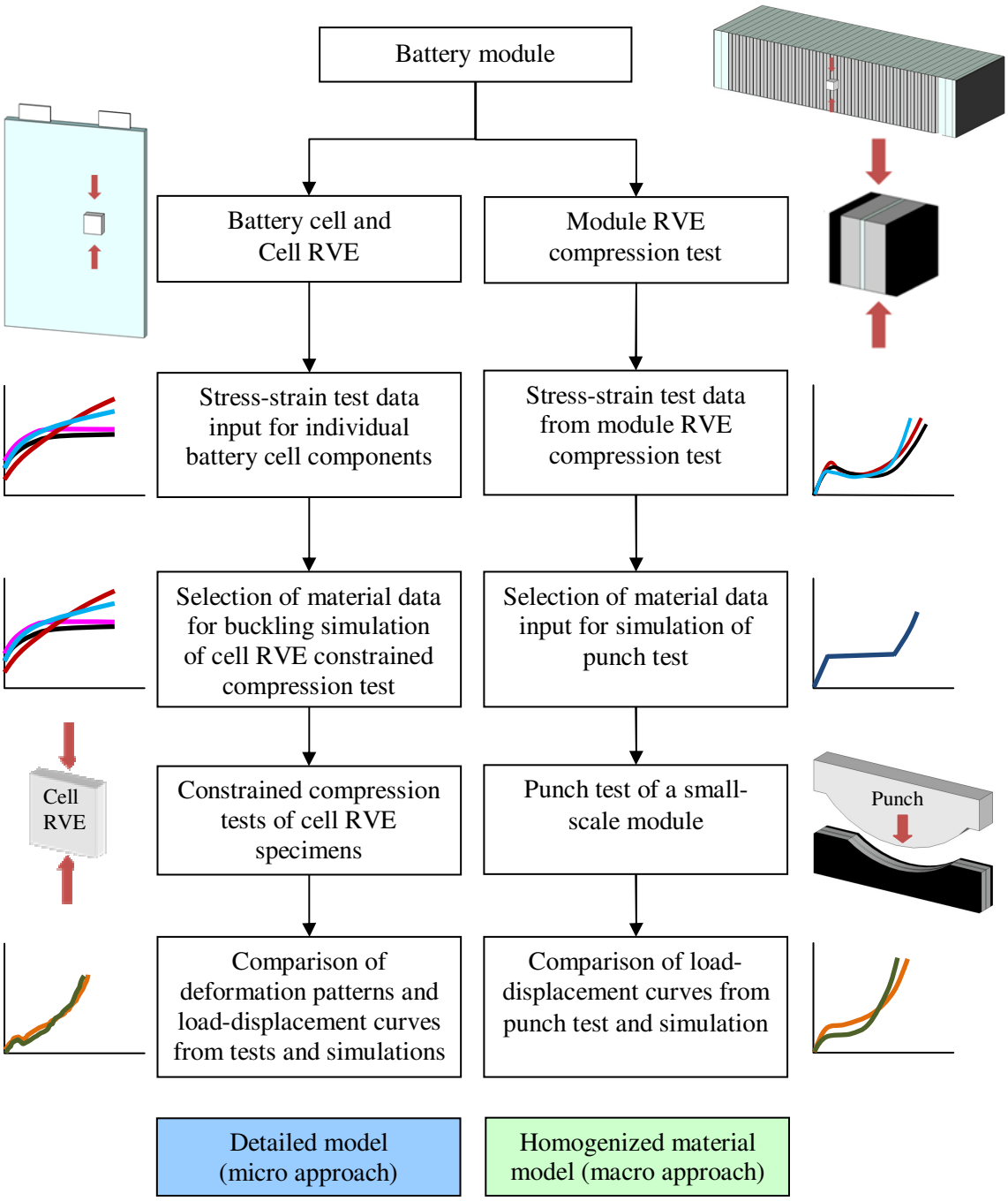

Figure 5.1. A schematic view of the approaches for computational model developments.

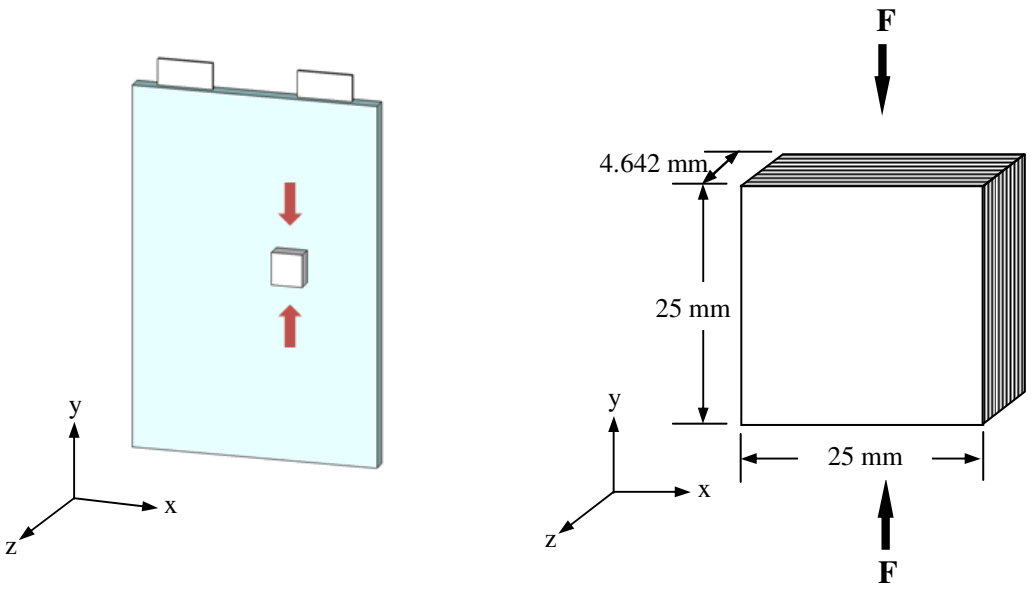

(a) (b)

Figure 5.2. A schematic of (a) a pouch cell and (b) a cell RVE (ten units) specimen with the dimensions.

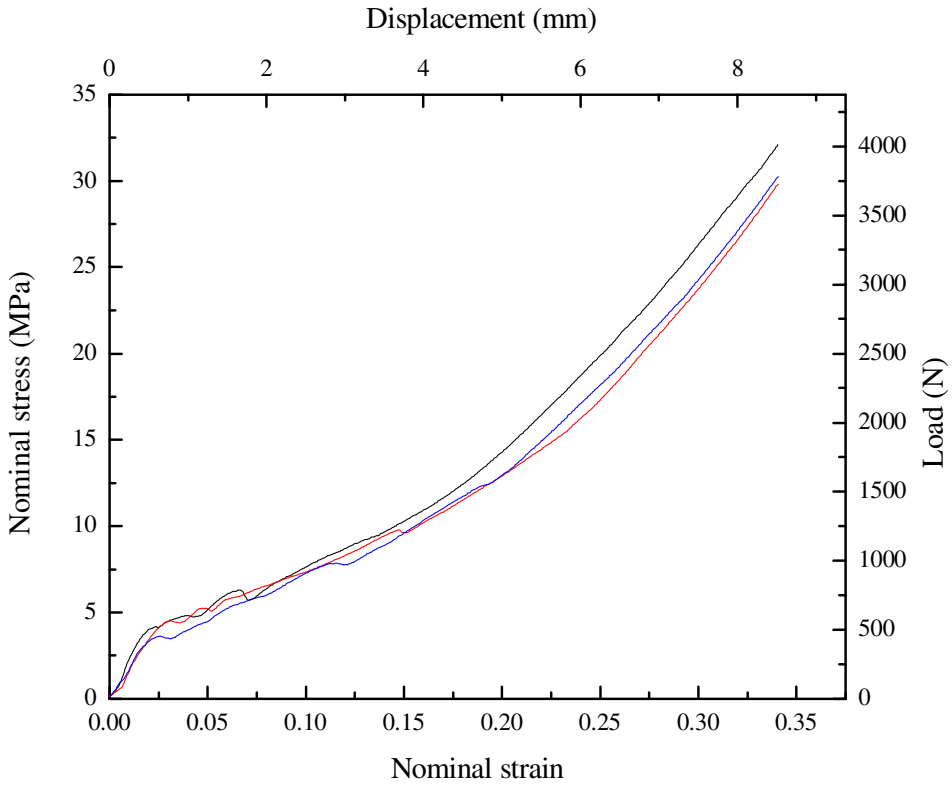

Figure 5.3. Nominal compressive stress-strain curves of the cell RVE specimens tested at a displacement rate of 0.5 mm/min (nominal strain rate of 0.0003 s^{-1}).

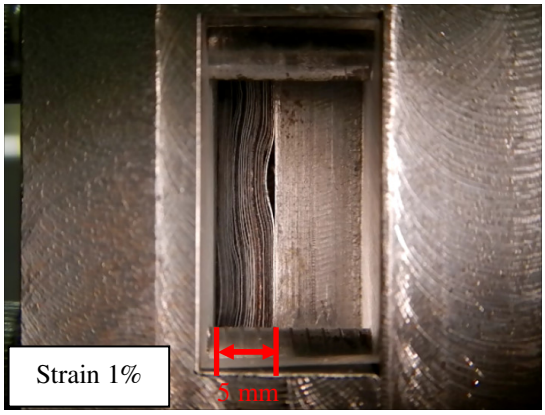
Strain 1%
5 mm

(a)

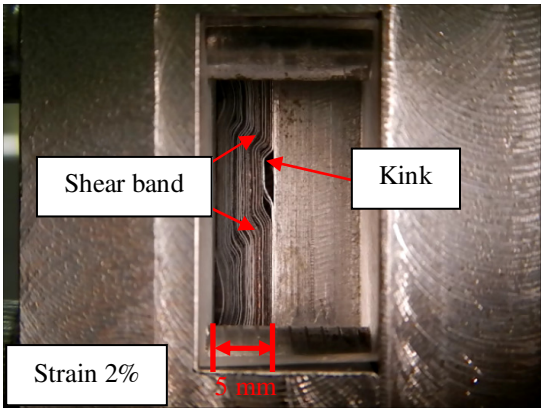
Shear band
Kink
Strain 2%
5 mm

(b)

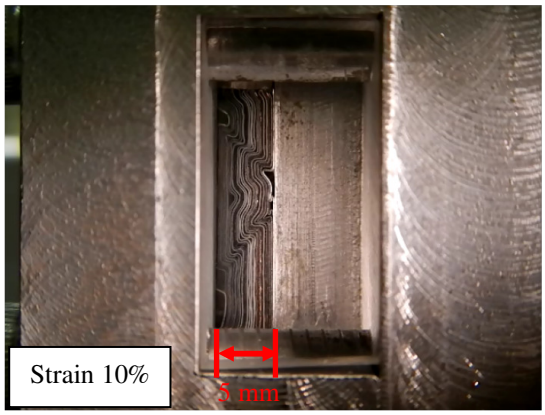
Strain 10%
5 mm

(c)

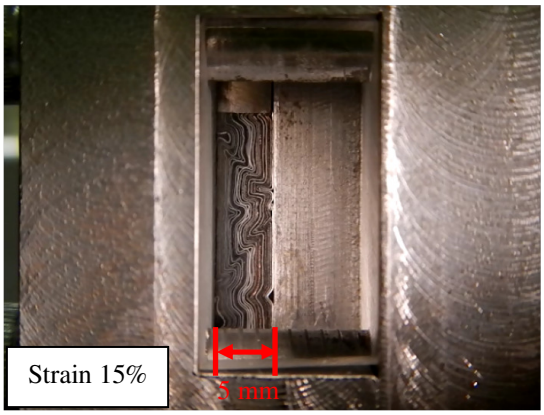
Strain 15%
5 mm

(d)

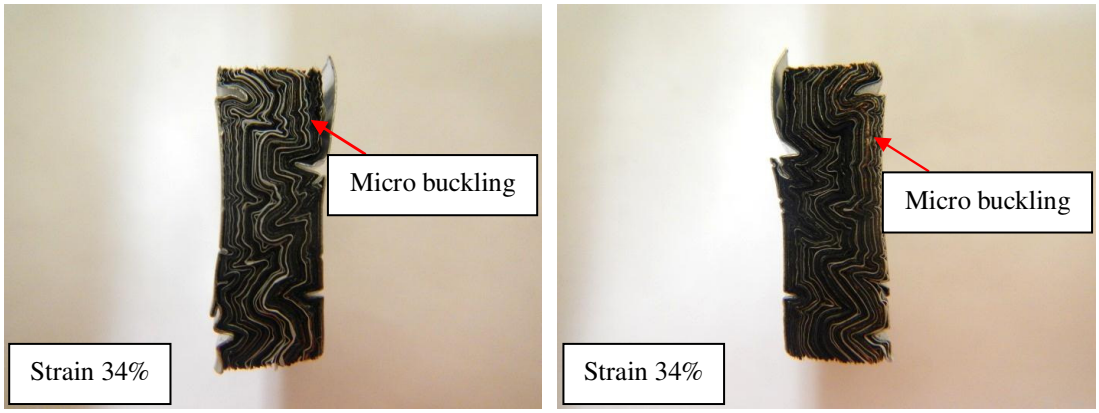

(e) (f)

Figure 5.4. Deformation patterns of a cell RVE specimen during a compression test at the displacement rate of 0.5 mm/min: (a) at the nominal strain of 1% in the initial linear stage, (b) at the nominal strain of 2% where the slope changes, (c) at the nominal strain of 10%, (d) at the nominal strain of 15%, (e) at the nominal strain of 34% after the test (front view), and (f) at the nominal strain of 34% after the test (back view).

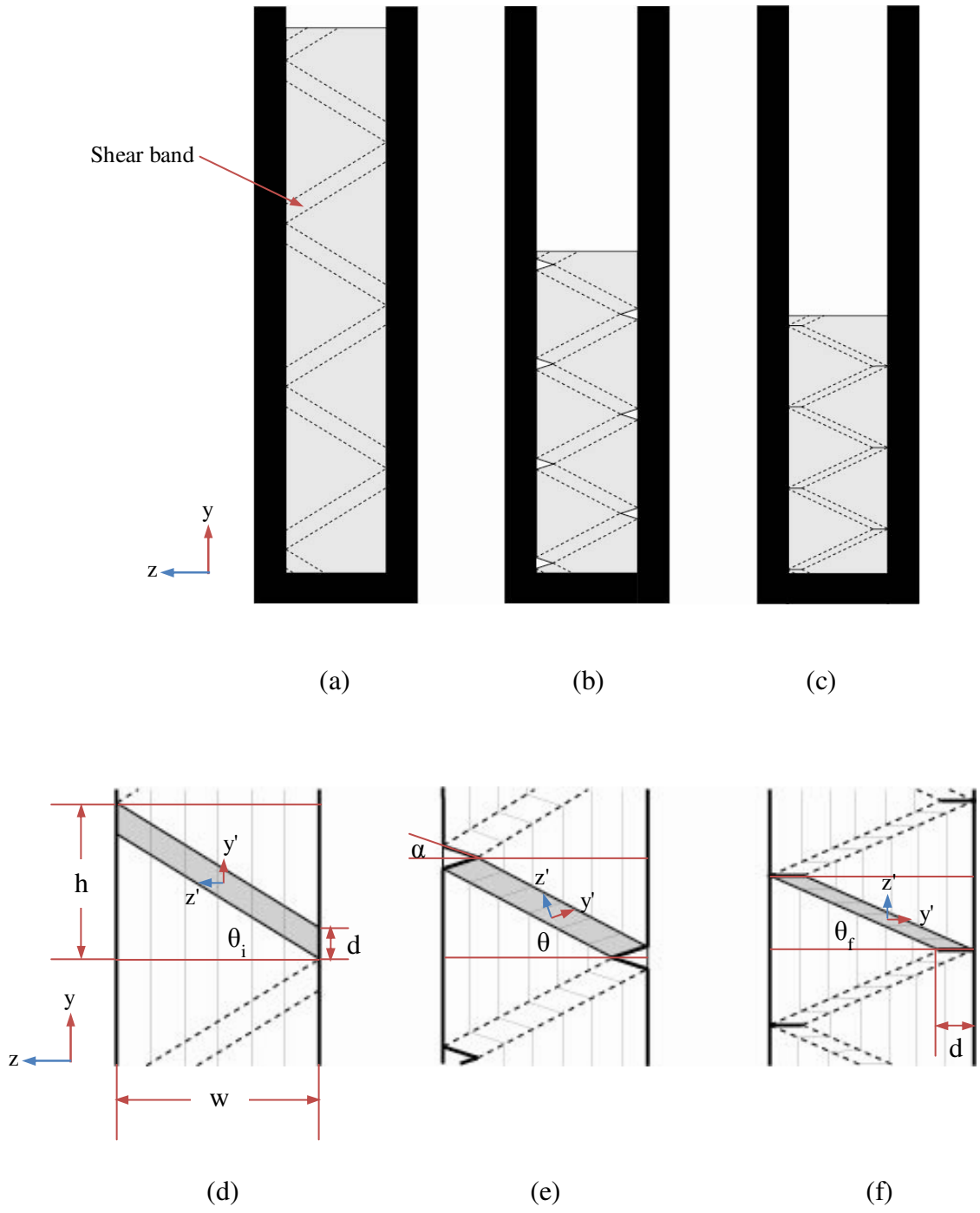

Figure 5.5. Schematics of a cell RVE specimen (a) before, (b) during, and (c) after in-plane constrained compression. (d) to (f) are detailed schematics showing the shear band formation corresponding to (a) to (c), respectively. The y and z coordinates are the global coordinates and the y' and z' coordinates in (d) to (f) are the local material coordinates rotate with the cell components.

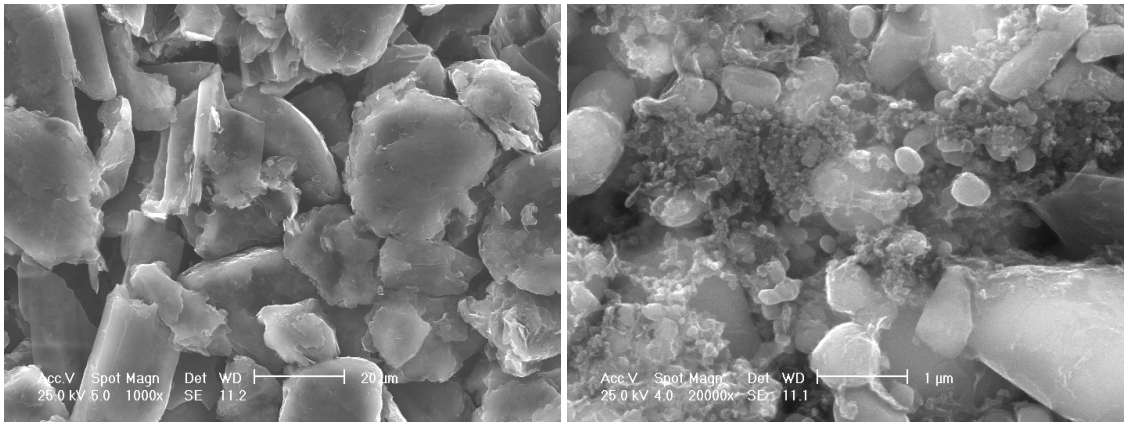

(a) **(b)**

Figure 5.6. SEM images of (a) graphite and (b) $LiFePO_4$ on the anode and cathode sheets, respectively.

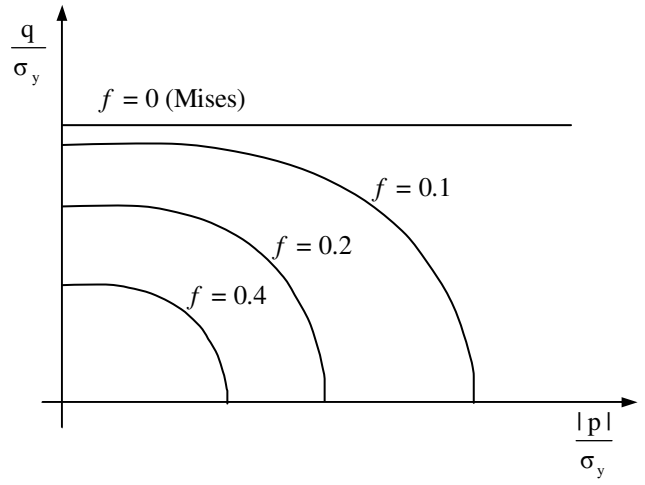

(a)

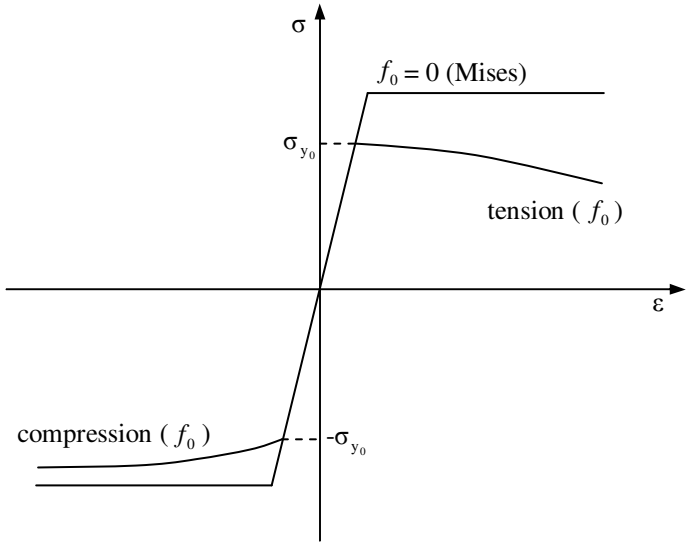

(b)

Figure 5.7. (a) A schematic of the Gurson's yield contour in the normalized hydrostatic pressure (p) - Mises stress (q) plane [19], and (b) a schematic of uniaxial behavior of a porous material with a perfectly plastic matrix material and the initial void volume fraction f_0 [19].

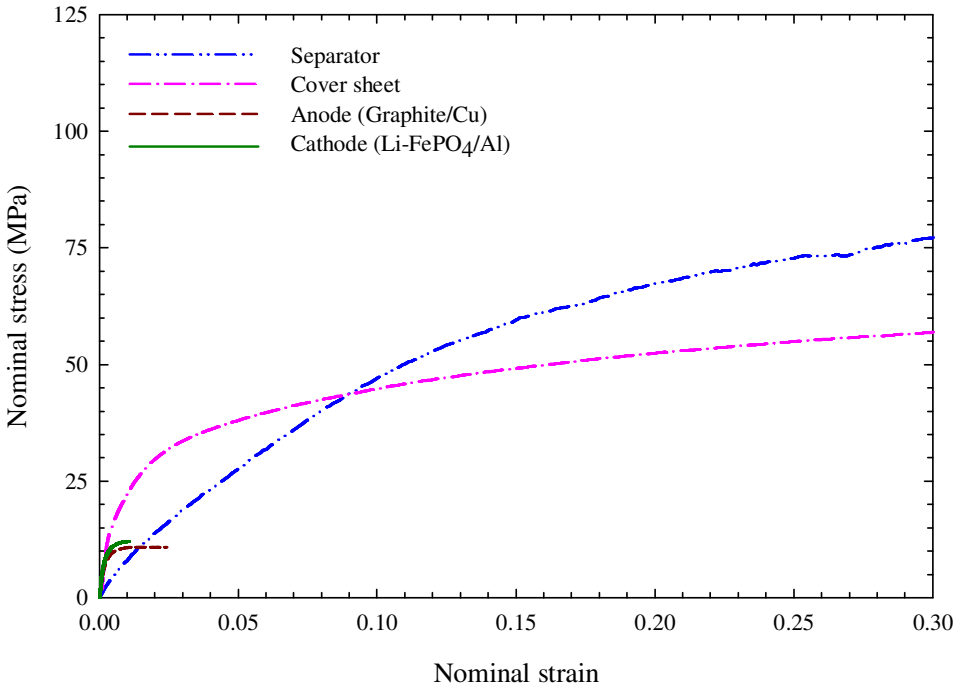
Separator
Cover sheet
Anode (Graphite/Cu)
Cathode (Li-FePO4/Al)
Nominal stress (MPa)
Nominal strain
0
25
50
75
100
125
0.00
0.05
0.10
0.15
0.20
0.25
0.30

(a)

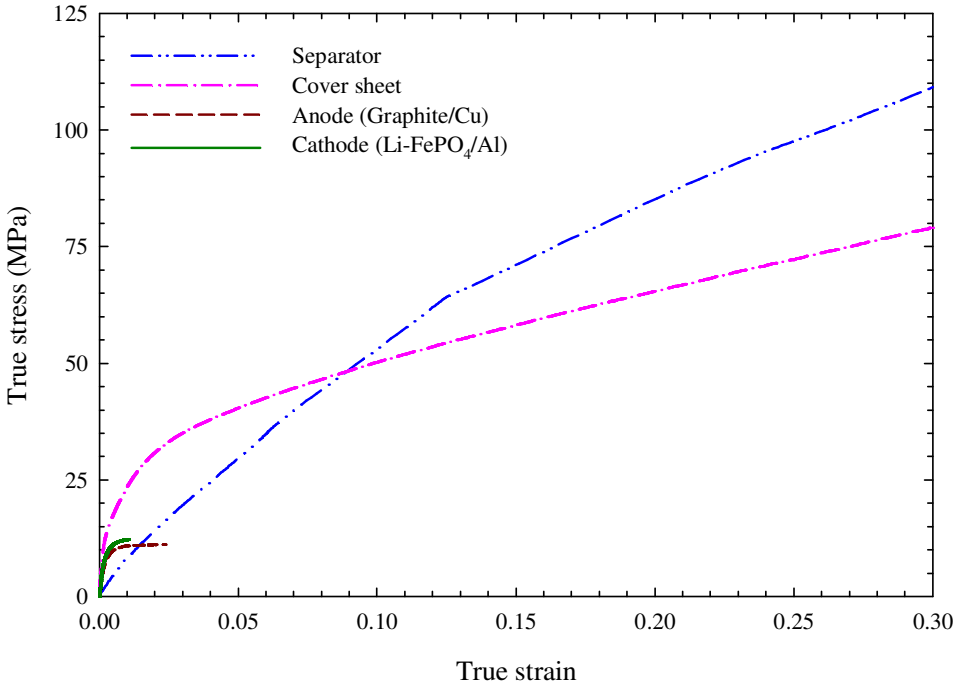
Separator
Cover sheet
Anode (Graphite/Cu)
Cathode (Li-FePO4/Al)
True stress (MPa)
True strain
0
25
50
75
100
125
0.00
0.05
0.10
0.15
0.20
0.25
0.30

(b)

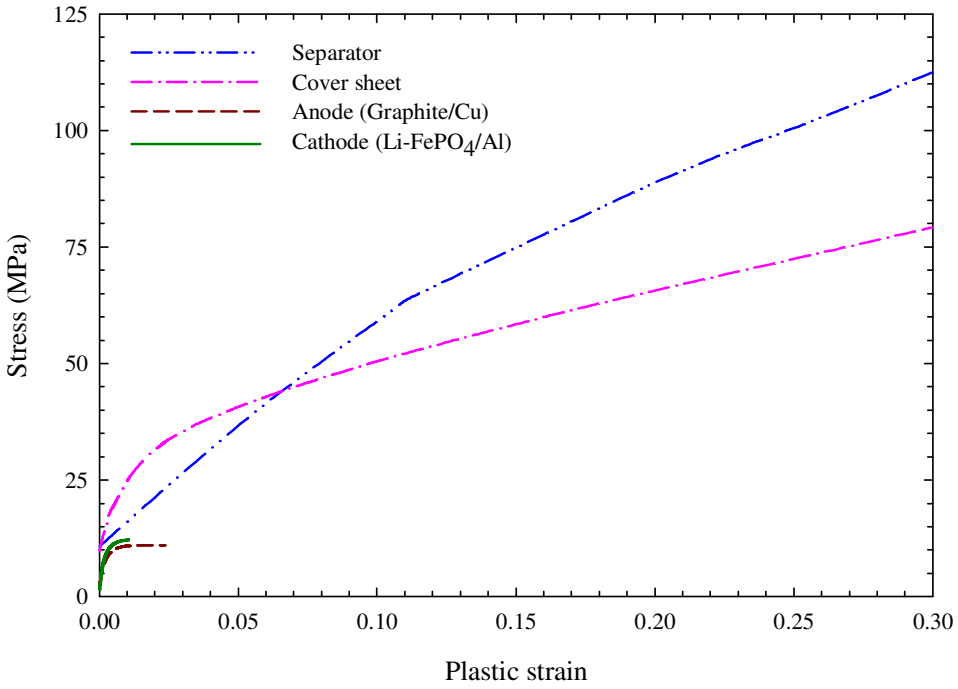

(c)

Figure 5.8. (a) The representative tensile nominal stress-strain data of the cell components obtained from [17], (b) estimated true stress-true strain data based on (a), and (c) the stress-plastic strain curves of the cell components used in the finite element analysis.

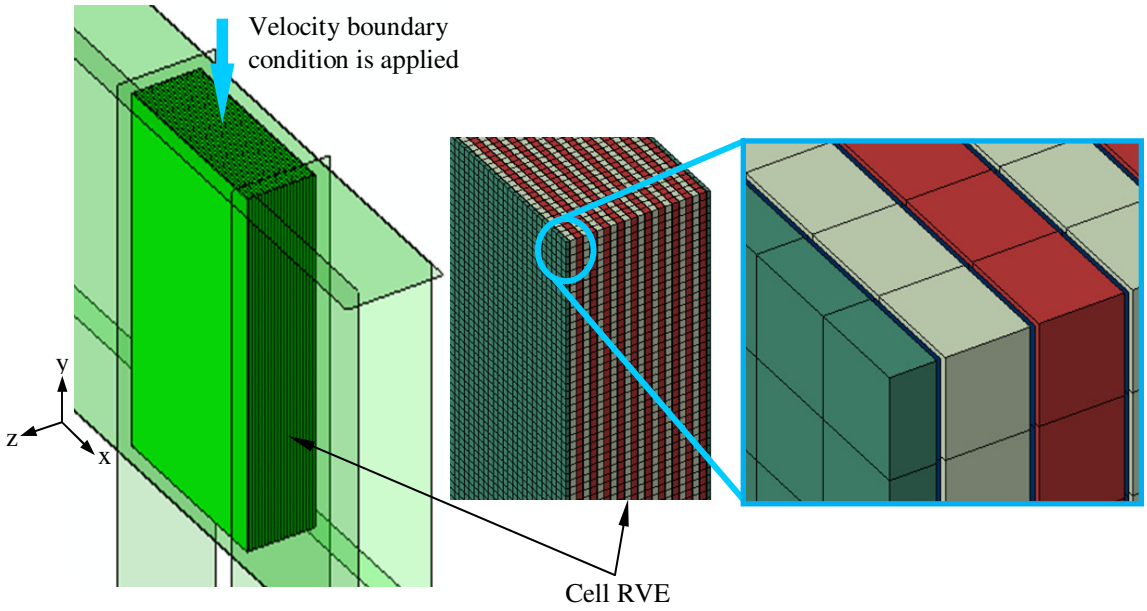

Figure 5.9. (a) The finite element model setup for a cell RVE specimen under constrained compression, and (b) the detailed view of meshes where the anode (light yellow), cathode (red) and cover sheets (green) are modeled by linear hexahedral solid elements and the separator sheet (dark blue) is modeled by linear quadrilateral reduced integration shell elements.

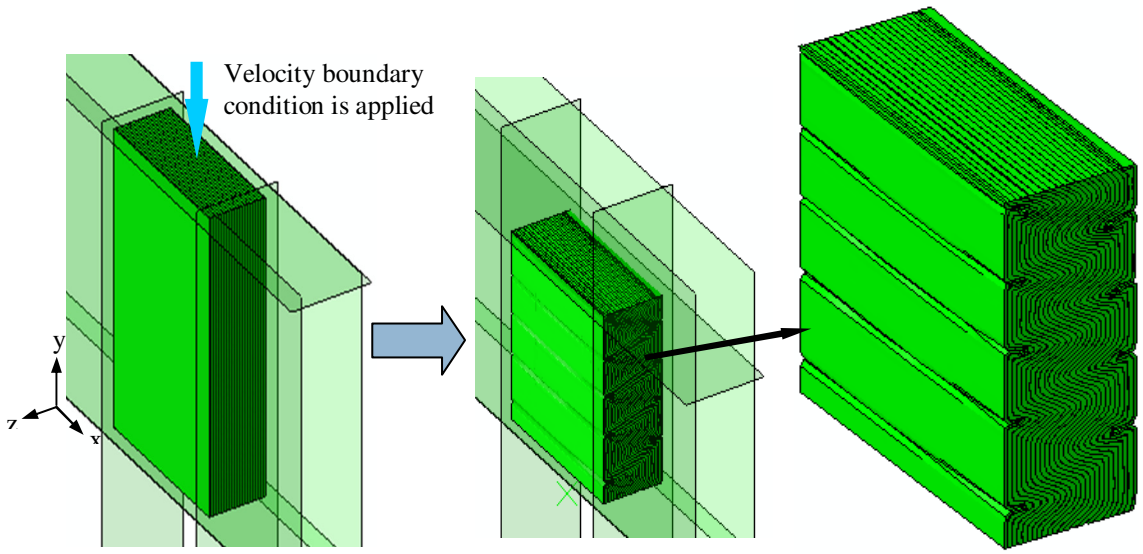

(a) (b) (c)

(d)

Figure 5.10. (a) A cell RVE half model is confined by six rigid surfaces, (b) the deformed shape of the model after the compressive displacement is applied (with the effective elastic compressive modulus and $f = 0.2$ for the electrode sheets with the active materials at the nominal strain of 34%), (c) a zoom-in view of (b), and (d) a deformed cell RVE specimen after the in-plane compression test.

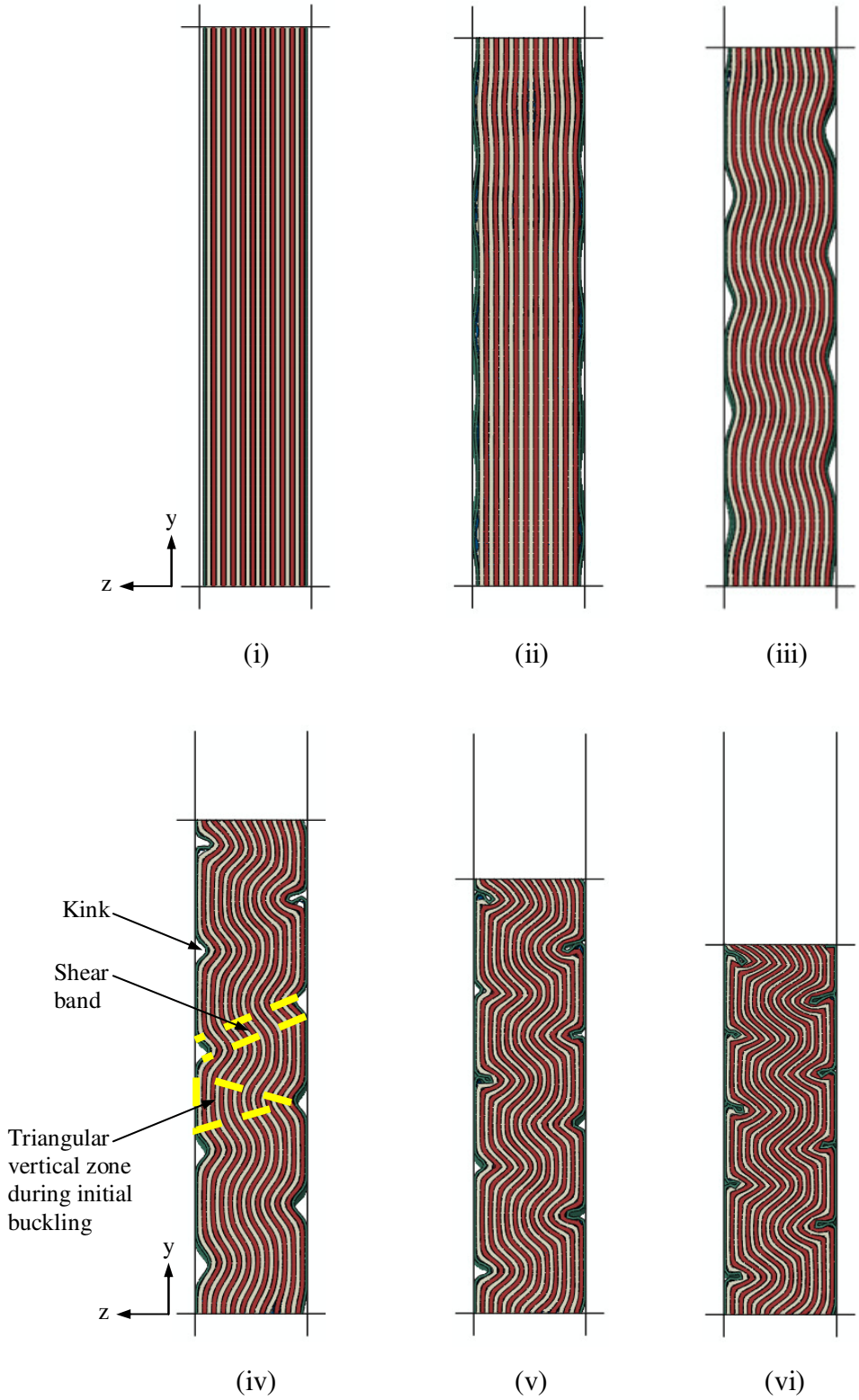

Figure 5.11. The successive snapshots of the deformation of the cell RVE specimen during the buckling simulation at the nominal strains of (i) 0%, (ii) 1.7%, (iii) 3.4%, (iv) 11.9%, (v) 22.1% and (vi) 34%.

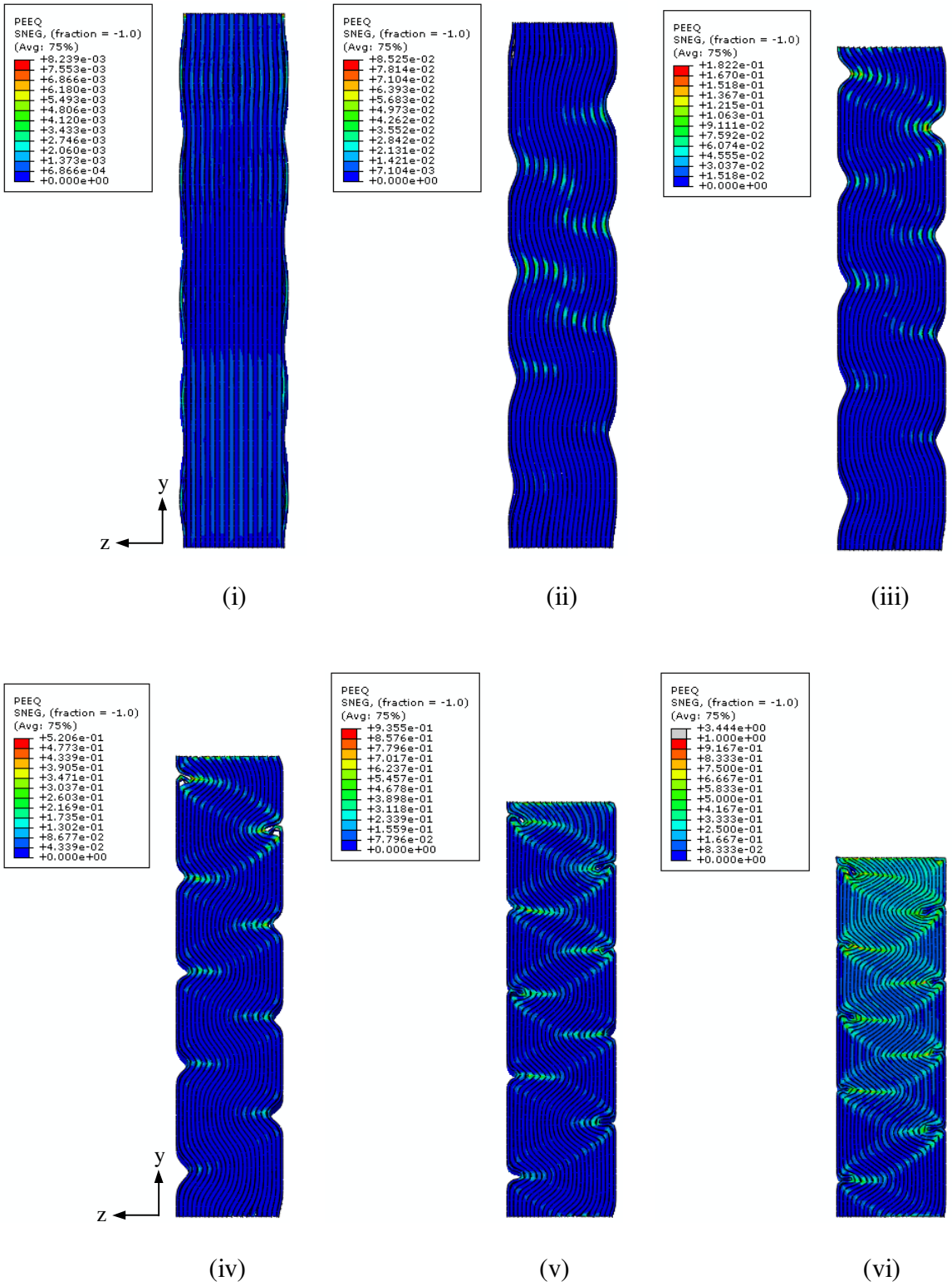

Figure 5.12. The successive snapshots of the equivalent plastic strain (PEEQ) of the cell RVE specimen during the buckling simulation at the nominal strains of (i) 1.7%, (ii) 3.4%, (iii) 6.8%, (iv) 13.6%, (v) 23.8% and (vi) 34%.

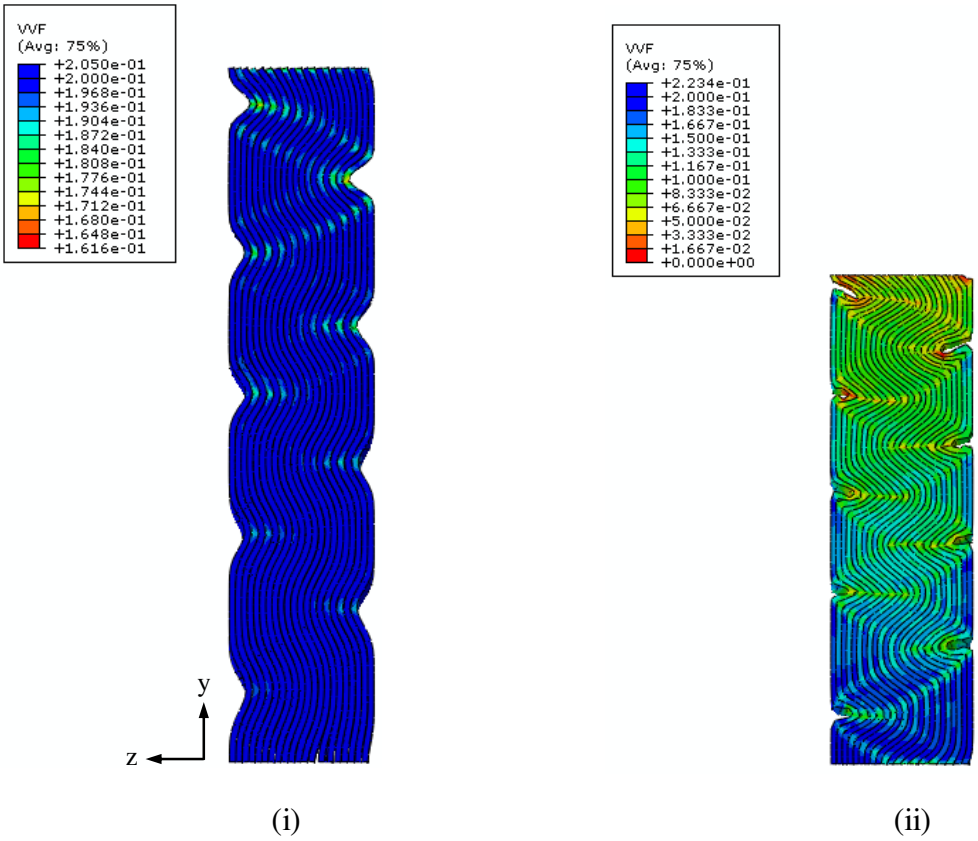

(i) (ii)

Figure 5.13. The distributions of the void volume fraction at the nominal strains of (i) 8.5% and (ii) 34% of the constrained compression simulation. Only the void volume fractions of the anode and cathode sheets of the cell RVE specimen are shown.

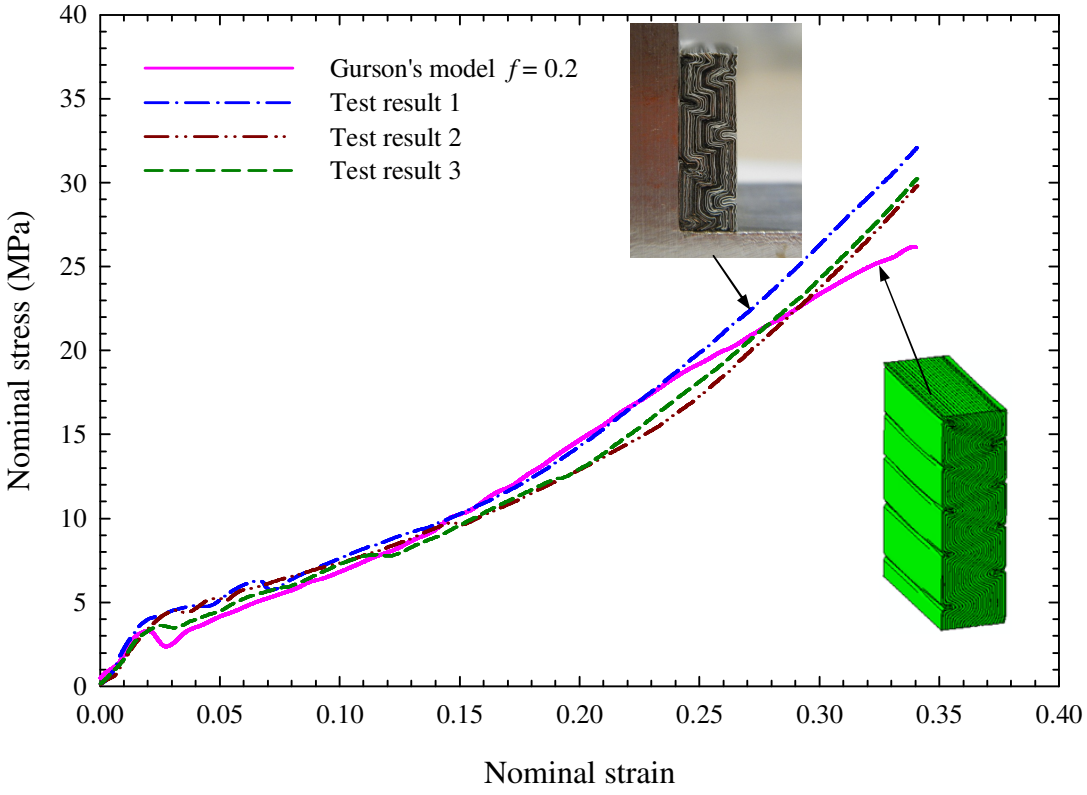

Figure 5.14. A comparison of the nominal stress-strain curve from the finite element analysis using the Gurson's material model with those of the test results. In the finite element analyses, all the contact surfaces are assumed to be in friction contact with a friction coefficient of 0.1.

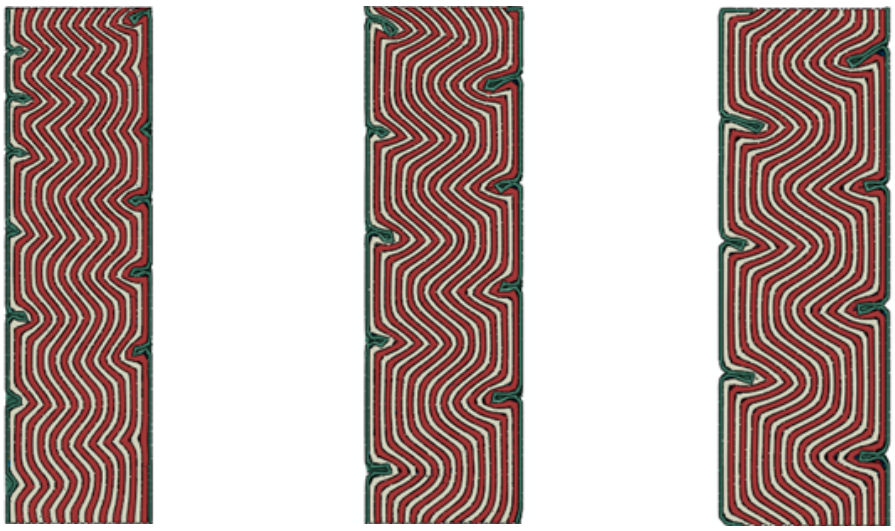

Figure 5.15. The deformation patterns of a battery cell under quasi-static in-plane compression for three initial clearances of (a) zero, (b) 0.358 mm of the current model and (c) 0.716 mm at the nominal strain of 34%. The finite element models are similar to the model described in Figure 5.10(a) with different initial clearances.

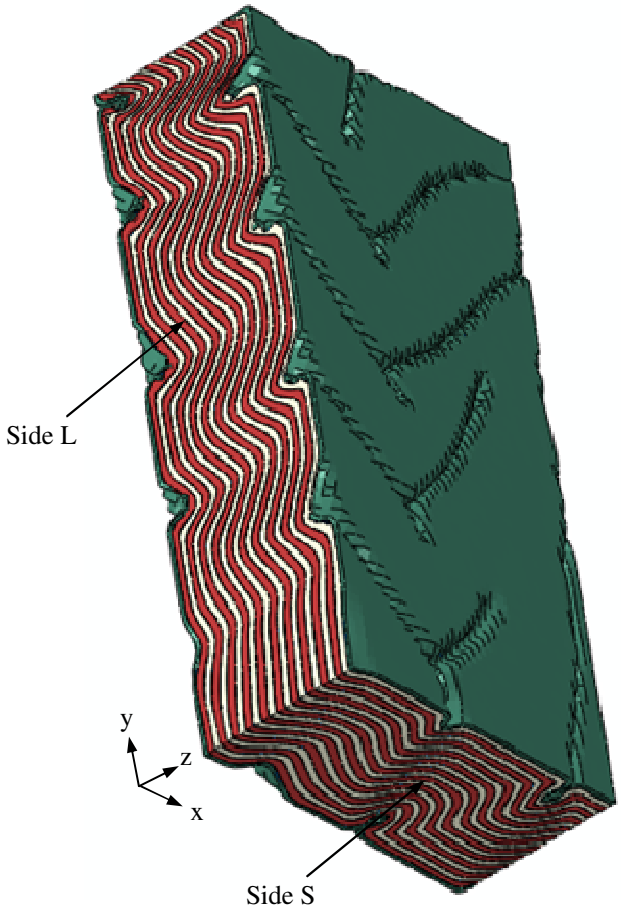

Figure 5.16. The deformation pattern of the cell RVE specimen under equal biaxial constrained compression based on the model shown in Figure 5.10(a) at the nominal strain of 22% in the x and y directions.

Chapter 6
Computational Models for Simulation of a Lithium-Ion Battery Module Specimen under Punch Indentation

6.1. Introduction

Lithium-ion batteries have been considered as the solution for electric vehicles for the automotive industry due to their lightweight and high energy density. The major design considerations of the lithium-ion batteries involve electrochemistry, thermal management and mechanical performance. The electrochemistry has been widely studied since it directly determines the battery performance and its life cycle. Different active materials on electrodes give different types of lithium-ion batteries. However, the basic chemical reactions of the cells are similar. For automotive applications, the mechanical performance is of great importance for crashworthiness analyses. Various research works have been focused on the chemical stability under impact, punch, nail penetration, and extreme temperatures [1-5]. However, the research works related to the mechanical behavior of lithium-ion batteries and the corresponding computational modeling are very limited.

Several research works were conducted to understand and model the phenomenon related to diffusion or intercalation induced stresses, cracking, debonding, and effect of coating due to reaction in lithium-ion batteries [6-13]. These research works are mainly focused on electrodes or separators and understandably do not cover the global mechanical behavior of battery cells and modules. Sahraei et al. [14] conducted a series

of tests and mechanical modeling on commercial $LiCoO_2$/graphite cells used for cell phones. The results indicate that the compressive mechanical behavior is characterized by the buckling and densification of the cell components. Other testing and modeling data available were also conducted on commercial $LiCoO_2$ cylindrical or prismatic battery cells [15, 16]. However, this information is of limited use for researchers to model the mechanical performance of automotive high-voltage $LiFePO_4$ battery cells and modules for crashworthiness analyses.

Sahraei et al. [14] indicated that computational effort is quite significant to model local buckling phenomenon of battery cells under in-plane compression. Therefore, macro homogenized material models of the representative volume elements (RVEs) for both the battery cells and modules have to be developed for crashworthiness analyses with sacrifice of the accuracy in the micro scale. Other than dealing with the multi-physics problem, one of the challenges of developing the computational models for the battery behavior is to deal with different models at different length scales as indicated in [14]. Therefore, understanding the basic mechanical behavior of the lithium-ion batteries for automotive applications is very important to develop macro homogenized material models for representative volume elements (RVEs) of cells and modules for efficient crashworthiness analyses.

Recently, Lai et al. [17] investigated the mechanical behaviors of lithium-iron phosphate battery cells and modules by conducting tensile tests of individual cell and module components, constrained compression tests of RVE specimens of dry cells and modules, and a punch test of a small-scale dry module specimen. Their results of in-plane tensile tests of the individual cell components indicate that the active materials on

electrodes have a very low tensile load carrying capacity. For in-plane constrained compression tests of cell RVE specimens, the results indicate the load carrying behavior of cell RVE specimens is characterized by the buckling of cells with a wavelength approximately in the order of the thickness of the cells and the final densification of the cell components. They also tested module RVE specimens with different heights and the results indicate that the load carrying behavior of module RVE specimens is also characterized by the buckling of cells with a wavelength approximately in the order of the thickness of the cells and the final densification of the module components but relatively independent of the height of the tested specimens. They also investigated the effects of adhesives between cells and foam/aluminum heat dissipater sheets on the mechanical behavior of module RVE specimens. The results indicate that the adhesive slightly increases the compressive load carrying capacity of the module RVE specimens. Their SEM images of the active materials on electrodes and the results of in-plane compressive and out-of-plane compressive tests suggest the total volume fraction up to 40% for the space between components and the porosity of the separator and the active materials on electrodes. Based on the compressive nominal stress-strain curves in the in-plane and out-of-plane directions, their work suggests that the lithium-ion battery cells and modules can be modeled as anisotropic foams or cellular materials.

Figure 6.1 shows a schematic of the approach for the computational model development in this chapter. The purpose of this investigation is two fold: one is to enhance understanding of the mechanical behavior of lithium-ion batteries used for automotive applications and the other is to pave the groundwork for the development of more accurate material models to represent the battery cells and modules by

homogenized material models which are a subject of the future research. In this investigation, less detailed macro homogenized material models are adopted to simulate a small-scale module specimen under the punch test. Here, the test data of module RVE specimens [17] were used to calibrate the inputs of the hyperfoam and crushable compressible foam models available in commercial finite element code ABAQUS [18] for the punch test simulation. The computational results of the load-displacement responses of the punch test are then compared with the experimental results. Finally, some comments are made.

6.2. Module RVE specimens under constrained compression tests

A detailed description of the structure of the lithium-ion battery module used for this investigation can be found in Lai et al. [17]. The following definitions will be used throughout the paper. A *Single unit* cell represents a basic cell containing one cathode, one anode and a separator sheet with two aluminum cover sheets with two accompanying separator sheets. A *Seven unit* cell consists of seven basic cells containing seven cathode, seven anode, fifteen separator and two aluminum cover sheets. This seven unit cell represents a typical assembled pouch cell. A *Module* consists of two pouch cells (seven unit cells) separated by an aluminum heat dissipater sheet and with two foam sheets on both sides. The name 'module' will be used throughout the paper to represent this definition (Figure 6.1).

Each cell consists of five major components: cover sheet, anode, cathode, separator and electrolyte. Since the electrolyte is difficult to handle during assembly due to the safety concern, all the cell and module RVE specimens tested in this study were

made without the electrolyte at the University of Michigan. Tensile tests were conducted for the individual cell components such as anode, cathode, separator and cover sheets, and the test results were discussed in detail in Lai et al. [17]. Tensile tests were also conducted for the aluminum heat dissipater sheets located between the cells and compression tests were conducted for the foam sheets in battery modules.

Since a less detailed homogenized model would require treating the battery cells and modules as homogenized materials, the nominal stress-strain curves of module RVE specimens under quasi-static in-plane compression tests reported in [17] will be used as the input for the homogenized material models in the finite element analyses. Figure 6.2(a) shows a schematic of a battery module and a module RVE specimen for the in-plane constrained compression test. A small module RVE specimen is shown in Figure 6.2(b) with the dimensions. Figure 6.2(c) shows a side view of the module RVE specimen with individual components. The large red arrows shown in the figure indicate the in-plane compressive direction. The simulation of the in-plane quasi-static punch test of a small-scale module is modeled here by treating the battery module as a homogenized material.

Figure 6.3 shows representative nominal stress-strain curves for two module RVE specimens with two different heights of 10 mm and 20 mm under quasi-static in-plane compression tests. These curves have similar trends or patterns as those of cell RVE specimens under quasi-static in-plane compression as shown in [17]. The characteristics of these compression stress-strain curves are similar to that of a typical hyperfoam. Lai et al. [17] also reported that for the module RVE specimens, the curves for in-plane compression is higher by about 5 to 8 MPa than the one for out-of-plane compression due

to the stiffening effects of the aluminum and copper foils and the cover and aluminum heat dissipater sheets under in-plane compression. The results indicate that the module RVE specimens can be modeled in general as anisotropic foam materials (for example, see Wang and Pan [19]). However, in the current investigation, only in-plane compression tests are addressed and the scope will be limited to isotropic homogenized material models only. The details of the various aspects of punch test simulations using macro homogenized material models for battery modules are described later in this paper.

6.3. A small-scale module specimen under a punch indentation test

The experimental results of module RVE specimens under in-plane compression tests will be used to develop macro homogenized material models for battery modules. However, the macro homogenized material models need validations. A limited validation will be presented here by comparing the computational results based on the macro homogenized material models with the test data from a punch test of a small-scale module specimen. The quasi-static in-plane punch test is conducted by indenting a small-scale module specimen by a semicircular punch. Figure 6.4 shows a schematic of a module specimen under a punch test. The travel speed of the punch is very low and the test is considered as a quasi-static test. The detailed description of the punch test can be found in Lai et al. [17]. It should be noted that the stress and strain distribution of the module specimen under the punch are quite nonuniform and under biaxial loading conditions, in contrast to the nearly uniform macroscopic stress and strain distributions in the module RVE specimens as homogenized materials under in-plane compression. The objectives of creating and validating such macro homogenized material models are to

provide a general understanding of the effects of the macro homogenized material models for battery cells and modules used in crashworthiness analyses. Next, a hyperfoam material model will be examined in detail as a candidate for a macro homogenized material model for lithium-ion battery modules.

6.4. Macro homogenized hyperfoam material model

For foams or cellular materials, three stages of the compression stress-strain curve can usually be observed. In the beginning at small strains, the foam deforms in a linear elastic manner due to cell wall bending. The next stage is a plateau at almost constant stress, caused by the buckling of the columns or plates that make up the cell edges or walls. Finally, a region of densification occurs, where the cell walls crush together, resulting in a rapid increase of compressive stress.

A brief description of a hyperfoam material model in ABAQUS is presented below. The hyperfoam strain energy function in ABAQUS [18] has the following form

$$U = \sum_{i=1}^{N} \frac{2\mu_i}{\alpha_i^2}\left[\hat{\lambda}_1^{\alpha_i} + \hat{\lambda}_2^{\alpha_i} + \hat{\lambda}_3^{\alpha_i} - 3 + \frac{1}{\beta_i}\left(J_{el}^{-\alpha_i\beta_i} - 1\right)\right] \tag{6.1}$$

where μ_i, α_i, and β_i are temperature dependent material parameters, and $\hat{\lambda}_i$ are the principal stretches. The strain energy can be fitted up to the order of $N = 6$. The deformation modes are characterized in terms of the principal stretches and the volume ratio *J*. The elastomeric foams are not incompressible. Therefore,

$$J = \lambda_1\lambda_2\lambda_3 \neq 1 \tag{6.2}$$

The transverse stretches λ_2 and/or λ_3 are independently specified in the test data either as individual values depending on the lateral deformations or through the definition of an effective Poisson's ratio.

For uniaxial mode, the stretch ratios are expressed as

$$\lambda_1 = \lambda_U,\ \lambda_2 = \lambda_3,\ \ J = \lambda_U \lambda_2^2,\ \ \lambda_U = 1 + \varepsilon_U \tag{6.3}$$

For equibiaxial mode, the stretch ratios are expressed as

$$\lambda_1 = \lambda_2 = \lambda_B,\ \ J = \lambda_B^2 \lambda_3,\ \ \lambda_B = 1 + \varepsilon_B \tag{6.4}$$

For planar mode, the stretch ratios are expressed as

$$\lambda_1 = \lambda_P,\ \lambda_2 = 1,\ \ J = \lambda_P \lambda_3,\ \ \lambda_P = 1 + \varepsilon_P \tag{6.5}$$

where the subscripts *U*, *B* and *P* represents the uniaxial, equibiaxial and planar mode, respectively. The nominal stress-stretch ratio relation for the three deformation modes mentioned above is

$$T_j = \frac{\partial U}{\partial \lambda_j} = \frac{2}{\lambda_j} \sum_{i=1}^{N} \frac{\mu_i}{\alpha_i} \left(\lambda_j^{\alpha_i} - J^{-\alpha_i \beta_i} \right) \tag{6.6}$$

where T_j is the nominal stress and λ_j is the stretch ratio in the direction of loading.

For the punch test simulation, a general elastomeric foam model “Hyperfoam” in ABAQUS is used as a preliminary case. This material is highly compressible in contrast to the incompressibility for usual hyperelastic materials. Only the uniaxial compression test data based on the module RVE uniaxial compression test data is available to fit the strain energy potential for the Hyperfoam material model. There is no shear and biaxial test data. ABAQUS performs a nonlinear least-squares fitting of the test data to determine the hyperfoam coefficients. The uniaxial compression test data shown in Figure 6.3 for the module RVE specimen with dimensions of 10 mm x 10 mm x 20 mm is used as the

material data input in the subsequent finite element simulations. However, Figure 6.5 shows two different scenarios that are considered for the homogenized material data input for the ABAQUS hyperfoam data fitting. The first one is the test data used "as-is" and the other is adjusted without softening.

The uniaxial compression curve (marked as "as-is") shown in Figure 6.5 can be broken down into three stages. At small strains ($< 3\%$), the module deforms in a linear elastic fashion. This is followed by a plateau of stress with a relatively small range of stress caused by the buckling of the module component sheets. At higher strains, a region of densification occurs where the module component sheets crush together resulting in a rapid increase of the compressive stress. The effective Poisson's ratio is considered to be zero for the homogenized hyperfoam model, since the data used is based on a constrained compression test.

It is essential to evaluate whether the hyperfoam constants determined by the finite element solver (ABAQUS) are acceptable, based on the correlation between the finite element solver predictions and the experimental data. A three-dimensional single-element test is used to calculate the nominal stress-nominal strain response of the material model. Figures 6.6(a) and 6.6(b) show the fitted stress-strain curves for the hyperfoam material model with different orders of N and the compression test data for a module RVE specimen. For the battery module RVE specimens, $N = 2$ seems to be adequate in providing good correlations since $N = 2$ usually provides numerical stability for most material models.

6.4.1 Model fitting procedure

In ABAQUS, the test data are specified as nominal stress–nominal strain data pairs using combinations of the *UNIAXIAL TEST DATA, *BIAXIAL TEST DATA, *SIMPLE SHEAR TEST DATA, *PLANAR TEST DATA, and *VOLUMETRIC TEST DATA sub-options of the *HYPERFOAM option with the TEST DATA INPUT parameter. In addition, the effective Poisson's ratio can be specified through the POISSON parameter. For each stress-strain data pair, ABAQUS generates an expression for the stress in terms of the stretch ratio and the unknown hyperfoam constants. For the uniaxial, equibiaxial, planar, and volumetric deformation cases, the nominal stress T_C is

$$T_C = \frac{\partial U}{\partial \lambda_C} = \frac{2}{\lambda_C} \sum_{i=1}^{N} \frac{\mu_i}{\alpha_i} \left(\lambda_C^{\alpha_i} - J_{el}^{-\alpha_i \beta_i} \right) \tag{6.7}$$

where U is the strain energy potential and λ_C is the stretch in the primary displacement direction. For the simple shear case, the nominal shear stress T_S is

$$T_S = \frac{\partial U}{\partial \gamma} = \sum_{j=1}^{2} \left[\frac{2\gamma}{2(\lambda_j^2 - 1) - \gamma^2} \sum_{i=1}^{N} \frac{\mu_i}{\alpha_i} (\lambda_j^{\alpha_i} - 1) \right] \tag{6.8}$$

where γ is the shear strain and λ_j are the two principal stretches in the plane of shearing and are related to the shear strain by

$$\lambda_{1,2} = \sqrt{1 + \frac{\gamma^2}{2} \pm \gamma \sqrt{1 + \frac{\gamma^2}{4}}} \tag{6.9}$$

For the n stress-strain pairs the following error measure E is minimized as

$$E = \sum_{i=1}^{n} (1 - T_i^{th} / T_i^{test})^2 \tag{6.10}$$

where T_i^{test} is a stress value from the test data and T_i^{th} is one of the stress expressions described above.

As the energy potential is a nonlinear function of α_i and β_i, a nonlinear least squares procedure similar to that of Twizell and Ogden [20] is used in ABAQUS to determine μ_i, α_i, and β_i simultaneously. If the POISSON parameter is specified as the effective Poisson's ratio ν, then all the β_i constants are directly computed as

$$\beta_i = \frac{\nu}{1-2\nu}.$$

After a set of material constants is obtained, ABAQUS performs material stability checks along the primary deformation modes using the Drucker stability criterion as

$$d\boldsymbol{\tau} : d\boldsymbol{\varepsilon} > 0 \quad \Rightarrow \quad d\boldsymbol{\varepsilon} : \mathbf{D} : d\boldsymbol{\varepsilon} > 0 \tag{6.11}$$

where $d\boldsymbol{\tau}$ is the Kirchhoff stress increment due to the logarithmic strain increment, $d\boldsymbol{\varepsilon}$, and $\mathbf{D}$ is the tangential material stiffness.

For the stability criterion to be satisfied, $\mathbf{D}$ must be positive-definite. The analysis input file processor will give warning messages if $\mathbf{D}$ loses its positive-definite property, thereby defining strain states that are likely to result in unstable material behavior. The deformation modes examined are uniaxial, equibiaxial, planar, and volumetric deformation in tension and compression and the simple shear mode [18].

6.5. Finite element analyses using a macro homogenized hyperfoam material model

Figure 6.7 shows a two-dimensional plane strain finite element model for simulation of the quasi-static semicircular punch test using a macro homogenized

hyperfoam material model. The implicit finite element solver ABAQUS/Standard commercial finite element code is used for the punch test simulation. The length, height, and thickness of the specimen are 80 mm, 20 mm, and 10 mm respectively. Two-dimensional plane strain 4-noded CPE4R elements of size 0.1 mm by 0.1 mm with hourglass control are used. Preliminary analyses show that a symmetric half model can be used in the subsequent analyses. The punch is modeled as a rigid body and the contacts between the punch and the specimen is modeled with a friction coefficient of 0.2. The specimen is in frictionless contact with the three bounding rigid surfaces represented by the three rigid lines BA, AC and CD in the two-dimensional plane strain model shown in Figure 6.7. The reference nodes of these rigid lines are constrained for all available degrees of freedom. The effective Poisson's ratio is considered to be zero, and for the hyperfoam model, the input data fitting with $N = 2$ is used. A vertical downward displacement boundary condition in the –y direction is applied at the rigid punch center. The maximum travel depth of the punch center is 10 mm. The punch is displaced statically downward to indent the specimen, and the reaction force-displacement response is obtained.

Figure 6.8 shows a comparison of the load-displacement curves from the finite element analyses of the quasi-static in-plane semicircular punch test based on the homogenized hyperfoam model and the experimental results. The load based on the hyperfoam model with "as-is" input is lower than the experimental results at small displacements but agree well the experimental results at large displacements. On the other hand, based on the hyperfoam model with the test data adjusted without softening, the load-displacement response at small displacements gives the general trend of the

experimental results without the distinctive peak and plateau due to buckling. However, at large displacement, the computational results match with the experimental data. The computational scheme presented here using the homogenized hyperfoam model for the lithium-ion battery module appear to show the capability to model the response of the battery module under punch indentation tests. It should be noted that a three-dimensional computational model is also developed and the computational results match well with those under plane strain conditions presented in Figure 6.8.

The hyperfoam material model is based on the hyperelastic theory that uses the strain energy function and is suitable for quasi-static loading conditions. The hyperfoam model cannot be used to account for the strain rate sensitivity for the foam. However, it could be combined with a viscoelastic model to capture a certain degree of the strain rate sensitivity for foam materials [18, 21].

6.6. Macro homogenized crushable foam material model

The crushable foam model in ABAQUS is based on the plasticity theory and can be used to model crushable materials other than foams [18]. It could also be used to model the compressible behavior of lithium-ion battery cells and modules. This model can be used when rate-dependent effects are important and could be useful for crashworthiness simulations of battery cells and modules. Next, the crushable foam material model will be examined in detail as a candidate for a homogenized material model for lithium-ion battery modules. The isotropic hardening crushable foam model [22] uses an elliptical yield surface centered at the origin in the p–q stress plane. Here, p represents the pressure and q represents the Mises stress. The yield surface evolves in a

self-similar manner, and the evolution is governed by the equivalent plastic strain. The yield surface for the isotropic hardening model is defined as

$$F = \sqrt{q^2 + \alpha^2 \, p^2} - B = 0 \tag{6.12}$$

where

$$B = \alpha \, p_c = \sigma_c \sqrt{1 + \left(\frac{\alpha}{3}\right)^2} \tag{6.13}$$

Here, B is the size of the yield ellipse, α is the shape factor of the yield ellipse, that defines the relative magnitude of the minor axis to the major axis, p_c is the yield stress in hydrostatic compression, and σ_c is the absolute value of the yield stress in uniaxial compression.

Figure 6.9 shows the yield surface in the *p*-*q* plane. The shape factor α can be computed using the initial yield stress in uniaxial compression, σ_c^0, and the initial yield stress in hydrostatic compression, p_c^0 (the initial value of p_c), using the relation [18]

$$\alpha = \frac{3k}{\sqrt{9 - k^2}} \tag{6.14}$$

where

$$k = \frac{\sigma_c^0}{p_c^0}$$

6.7. Finite element analyses using a macro homogenized crushable foam material model

Figure 6.10(a) shows a three-dimensional finite element model for the simulation of the quasi-static semicircular punch test using a macro homogenized crushable foam material model. The implicit finite element solver ABAQUS/Standard commercial finite element code is used for the punch test simulations. A symmetric half model is used with the half length of 40 mm, the height of 20 mm, and the thickness of 10 mm. Three-dimensional linear 8-noded hexahedral C3D8 elements of size 1 mm x 1 mm x 1 mm are used. The punch is modeled as a rigid body and the contacts between the punch and the specimen is modeled with a friction coefficient of 0.2. The specimen is in frictionless contact with the four bounding rigid surfaces as shown in Figure 6.10(a). The reference nodes of these rigid surfaces are constrained for all available degrees of freedom. A vertical downward displacement boundary condition is applied at the punch center. The maximum travel depth of the punch center is 10 mm. The punch is displaced statically downward to indent the specimen as shown in Figure 6.10(b), and the reaction force-displacement response is obtained.

The uniaxial compression test data shown in Figure 6.3 for a module RVE specimen with dimension 10 mm x 10 mm x 20 mm is used for the material input data of the finite element analyses. The crushable foam model requires the plastic strain to be provided in the ascending order. Thus the uniaxial compression test data input for the finite element analysis needed to be adjusted. Similar to the hyperfoam material model cases, two scenarios are also considered here. Figure 6.11 shows two sets of input data for the elastic-plastic material data. The first one has the test data adjusted in the

ascending order but the rise and fall segment due to initial buckling is flattened to a lower bound of the curve. The second one has the test data adjusted in the ascending order and the curve is adjusted higher at the peak point due to the initial buckling and is flattened to a higher bound of the curve.

For the crushable foam model, the isotropic hardening rule is used. The elastic part of the material is specified by the elastic modulus 305.5 MPa based on the initial linear parts of the input stress-strain curve and Poisson's ratio of 0.2 based on the rule of mixture for an aggregate with a void volume fraction of 0.4 and the effective Poisson's ratio of the matrix as 0.33. The ratio of the initial yield stress in uniaxial compression, σ_c^0 to the initial yield stress in hydrostatic compression, p_c^0 for compression loading $k = \sigma_c^0 / p_c^0$, $(0 \le k < 3)$ is assumed to be 1.1 as an approximation. However, based on the experimental data of Lai et al. [17] with the assumption that the in-plane yield stresses are equal while the out-of-plane yield stress is nearly zero, then k becomes 1.5. It is found that for the current investigation, both k values give almost similar results. The plastic Poisson's ratio ν_p is assumed to be zero. The CRUSHABLE FOAM HARDENING option is used with the stress-plastic strain input to define the hardening data for the crushable foam plasticity model [18].

Figure 6.12 shows a comparison of the load-displacement curves from the finite element analyses of the quasi-static semicircular punch indentation test based on a crushable foam material model and the experimental results. For both scenarios of material data inputs, the computational results give upper and lower bounds of the experimental results. In general, the computational scheme presented here using the homogenized crushable foam model appear to be able to model the experimental results

of the punch test. However, the computational results based on the macro homogenized crushable foam model could not catch the distinctive peak and the plateau due to buckling. The investigation shows that the material models in commercial software can be used for simulation of lithium-ion battery modules under punch indentation. But the investigation can be used to underscore the need to develop better material models to represent more accurately for lithium-ion battery cells and modules as homogenized materials, which is a subject of the future research. The results of the simulation presented here are geared towards to that objective and to layout some ground work for future investigations.

6.8. Conclusions

In this paper, macro homogenized material models are adopted to model a small-scale lithium-ion battery module specimen under an in-plane constrained punch indentation test. The macro material models are based on the compressive stress-strain curves obtained from the representative volume element (RVE) module specimens under in-plane constrained compression tests. The ABAQUS implicit solver is used for the punch test simulations. The hyperfoam and the crushable foam material models in ABAQUS are adopted to fit the nominal stress-strain curves of the module RVE specimens under in-plane compression. The load-displacement responses of the simulation results based on the hyperfoam and crushable foam material models compare fairly well with the experimental results of the punch test in general. However, the initial yielding and the corresponding plateau of the load-displacement curves of the punch test due to micro buckling could not be modeled distinctively by the macro homogenized

models. The computational results show that the material models available in commercial finite element software can be used to reasonably model lithium-ion battery modules under non-uniform compression loading conditions.

Acknowledgements

Helpful discussions with Yibing Shi, Guy Nusholtz, and Ronald Elder of Chrysler, Saeed Barbat, Bill Stanko, Mark Mehall and Tau Tyan of Ford, Jenne-Tai Wang, Ravi Nayak, Kris Yalamanchili and Stephen Harris of GM, Christopher Orendorff of Sandia National Laboratory, Seung-Hoon Hong of University of Michigan, and Natalie Olds of USCAR are greatly appreciated. Special assistance of Yibing Shi and Ronald Elder of Chrysler is especially appreciated.

References

1. Ashtiani, C., "Design and Development for Production of the Think EV Battery Pack, "*Proceeding of the AABC-09 Conference*, CA, USA, 2009.
2. Cai, W., Wang, H., Maleki, H., Howard, J., Lara-Curzio, E., "Experimental Simulation of Internal Short Circuit in Li-Ion and Li-Ion-Polymer Cells," *Journal of Power Sources*, **196** 7779-7783 (2011).
3. Nguyen, J., Taylor, C., "Safety Performance for Phosphate Based Large Format Lithium-Ion Battery, Telecommunications Energy Conference," *INTELEC 2004. 26th Annual International*, 146-148, 2004.
4. Oh, J., "Large Lithium-Ion Battery for Automotive Applications," *Proceeding of the AABC-09 Conference*, CA, USA, 2009.
5. Otsuki, M., Ogino, T., Amine, K., "Investigation of Flame-Retardant Additives for Safety Usage of Lithium-Ion Batteries," *ECS Transactions*, **1** 13-19 (2006).
6. Deshpande, R., Cheng,Y.-T., Verbrugge, M. W., "Modeling Diffusion-Induced Stress in Nanowire Electrode Structures," *J. Power Sources* **195** 5081–5088 (2010), doi: 10.1016/j.jpowsour.2010.02.021.
7. Hu, Y., Zhao, X., Suo, Z., "Averting Cracks Caused by Insertion Reaction in Lithium-Ion Batteries," *Journal of Materials Research* **25**, 1007-1010 (2010).
8. Xiao, X., Wu, W., Huang, X., "A Multi-Scale Approach for the Stress Analysis of Polymeric Separators in a Lithium-Ion Battery," *J. Power Sources* **195** 7649–7660 (2010).
9. Zhang,L.Q., Liu, X., Liu, Y., Huang, S., Zhu, T., Gui, L., Mao, S., Ye, Z., Wang, C., Sullivan, J. P., Huang, J. Y., " Controlling the Lithiation-Induced Strain and Charging Rate in Nanowire Electrodes by Coating," *ACS Nano* **5** 4800–4809 (2011).
10. Zhang, X., Shyy, W., Sastry, A. M., "Numerical Simulation of Intercalation-Induced Stress in Li-Ion Battery Electrode Particles," *Journal of The Electrochemical Society* **154** (10) A910-A916 (2007), doi: 10.1149/1.2759840.
11. Zhang, X., Sastry, A. M., Shyy, W. "Intercalation-Induced Stress and Heat Generation within Single Lithium-Ion Battery Cathode Particles," *Journal of The Electrochemical Society* **155** (7) A542-A552 (2008), doi: 10.1149/1.2926617.
12. Zhao, K., Wang, W. L., Gregoire, J., Pharr, M., Suo, Z., Vlassak, J. J., Kaxiras, E., "Lithium-Assisted Plastic Deformation of Silicon Electrodes in Lithium-Ion Batteries: A First- Principles Theoretical Study", *Nano Letters* **11** 2962–2967 (2011), dx.doi.org/10.1021/nl201501s.
13. Zhao, K., Pharr, M., Hartle, L., Vlassak, J. J., Suo, Z., "Fracture and Debonding in Lithium-Ion Batteries with Electrodes of Hollow Core-Shell Nanostructures," *J. Power Sources* **218** 6-14 (2012), doi:10.1016/j.jpowsour.2012.06.074.
14. Sahraei, E., Hill, R., Wierzbicki, T., "Calibration and Finite Element Simulation of Pouch Lithium-Ion Batteries for Mechanical Integrity," *J. Power Sources* **201** 307–321 (2012), doi:10.1016/j.jpowsour.2011.10.094.
15. Hill, R., "Development for a Representative Volume Element of Lithium-Ion Batteries for Thermo-Mechanical Integrity," Department of Mechanical Engineering, Massachusetts Institute of Technology, 2011.

16. Sahraei, E., Wierzbicki, T., Hill, R., Luo, M., "Crash Safety of Lithium-Ion Batteries Towards Development of a Computational Model," *SAE Technical Paper 2010-01-1078*, 2010, doi: 10.4271/2010-01-1078.
17. Lai, W., Ali, M. Y., Pan, J., Research work to be published, 2012
18. ABAQUS Version 6.11 User Manual, SIMULIA, Providence, RI, 2012.
19. Wang, D.A., Pan, J., "A Non-Quadratic Yield Function for Polymeric Foams," *International Journal of Plasticity*, **22** 434-458 (2006).
20. Twizell, E. H., Ogden, R. W. "Non-Linear Optimization of the Material Constants in Ogden's Stress-Deformation Function for Incompressible Isotropic Elastic Materials," *J. Austral. Math. Soc. Ser. B*, **24** 424–434 (1983).
21. Pan, F., "Modeling of the Rate Responsive Behavior of Elastomer Foam Materials," *Journal of Engineering Materials and Technology* **130** 014501/1- 014501/6 (2008), doi: 10.1115/1.2807047.
22. Deshpande, V.S., Fleck, N.A., "Multi-Axial Yield Behaviour of Polymer Foams," *Acta Materialia*, **49** 1859-1866 (2001).

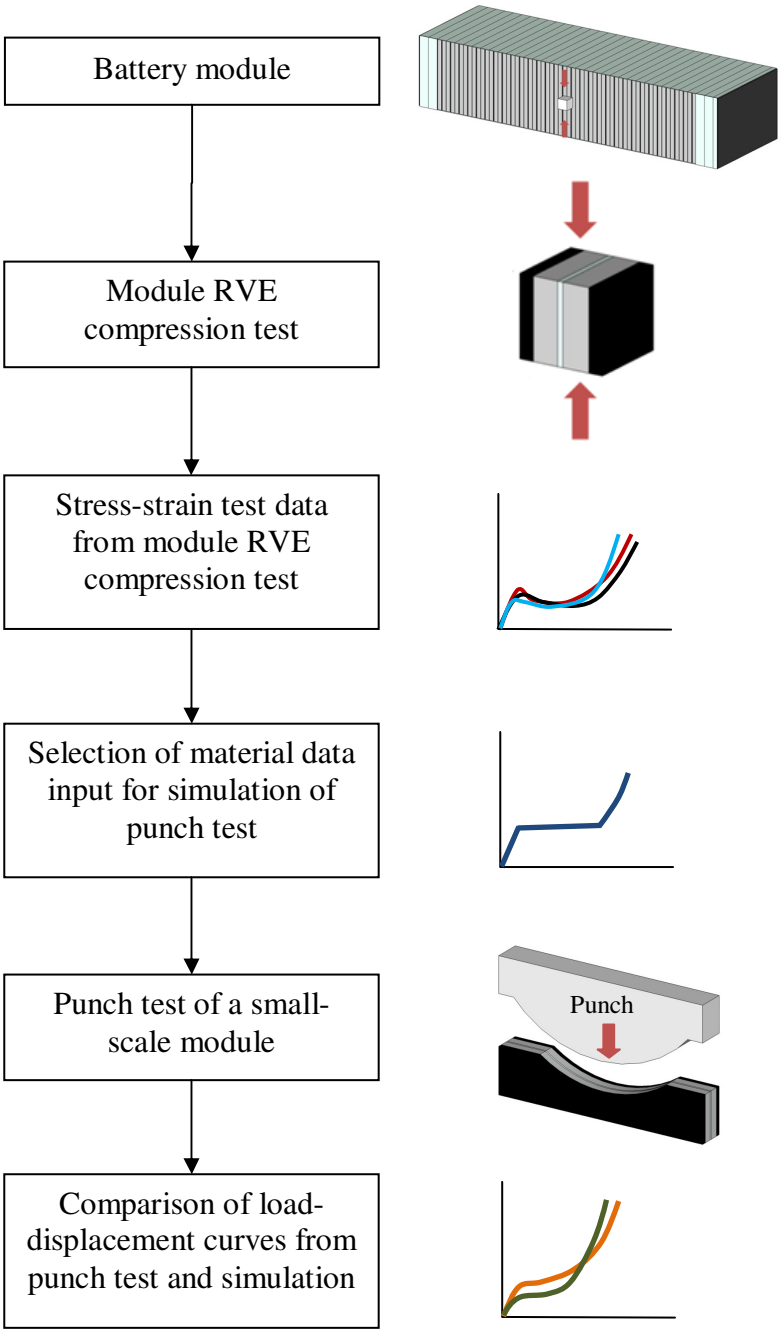

Figure 6.1. A schematic view of the approach of the computational model development.

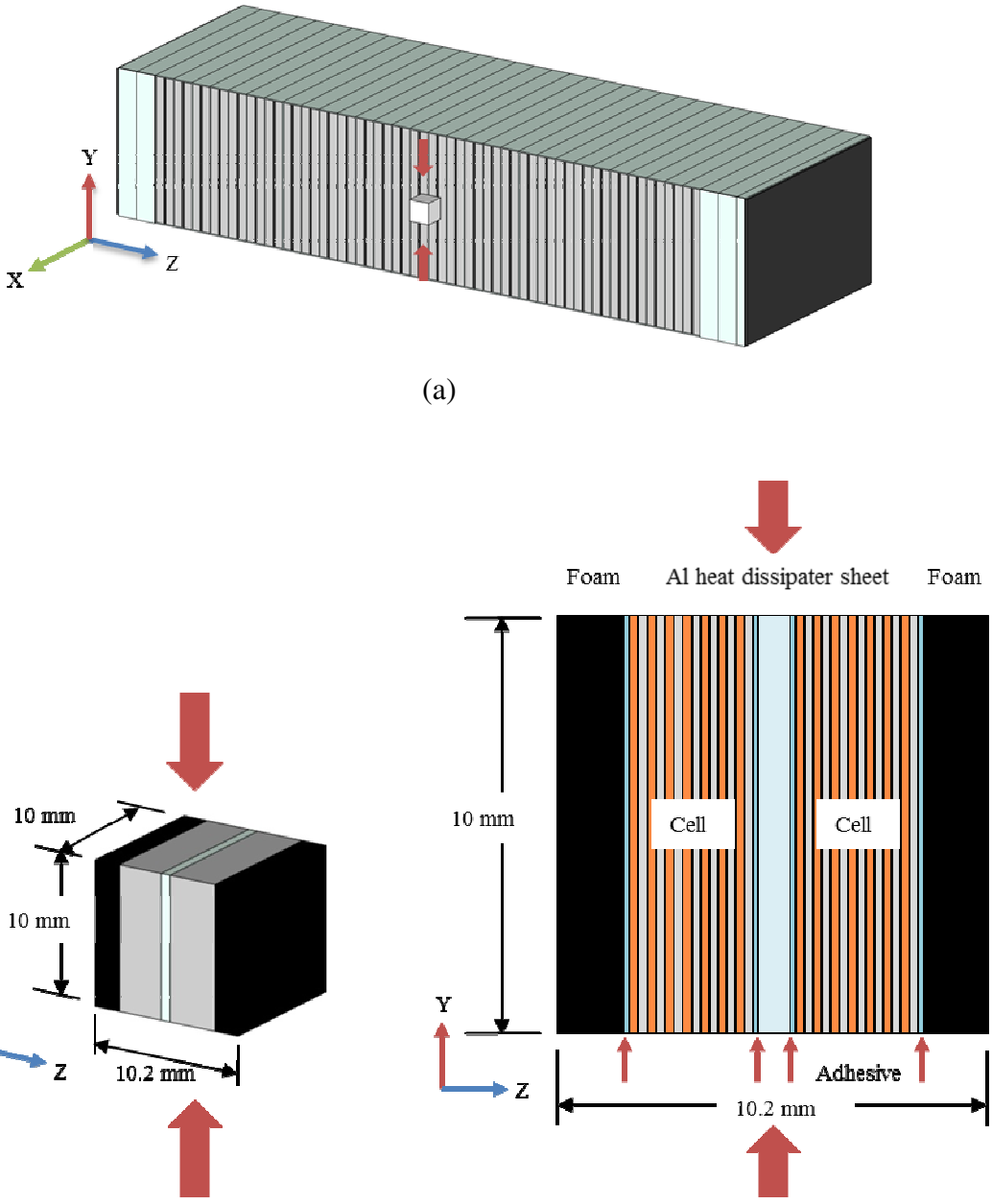

Figure 6.2. A schematic of (a) a battery module and a module RVE specimen for the in-plane constrained compression test, (b) a module RVE specimen with the dimensions, and (c) a side view of the module RVE specimen showing the individual components. The large red arrows indicate the compressive direction.

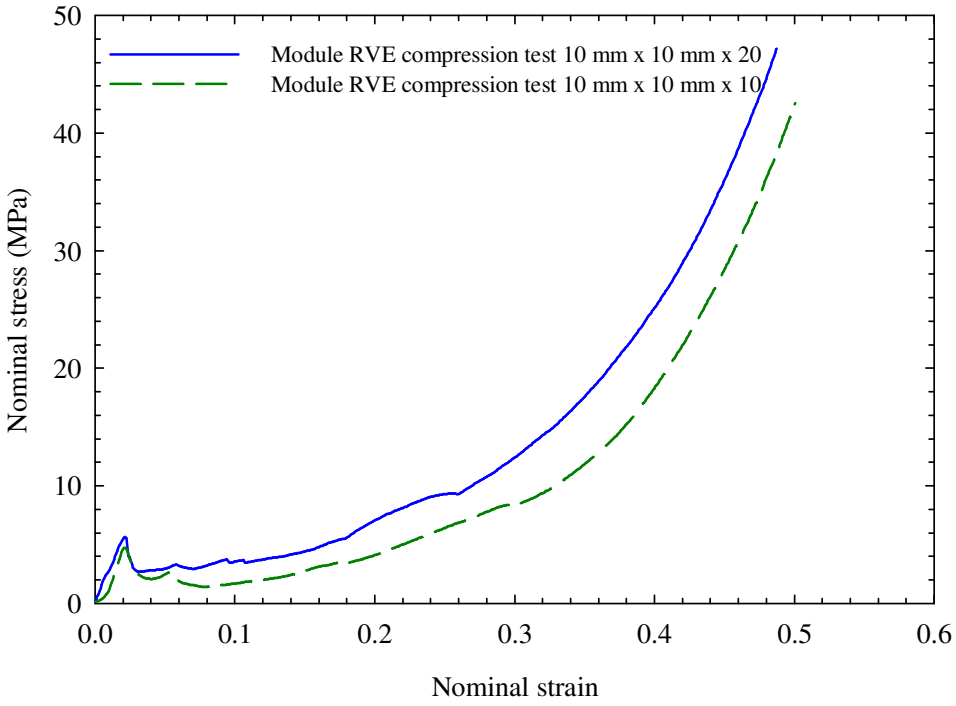

Figure 6.3. Quasi-static in-plane constrained compression test data for module RVE specimens.

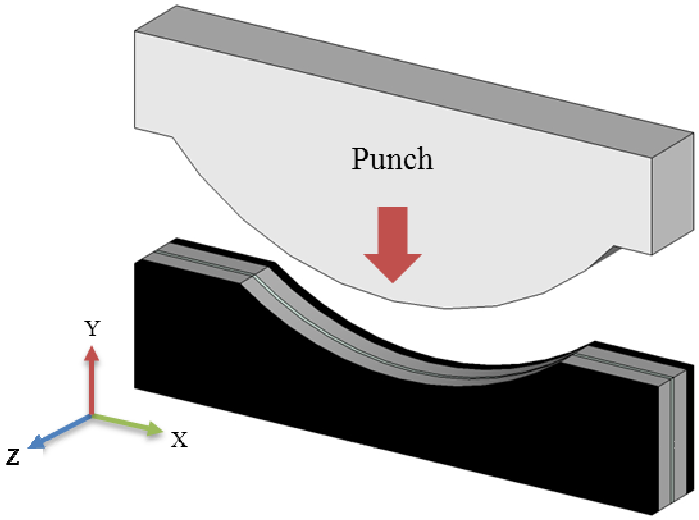

Figure 6.4. A schematic of a module specimen under a punch test.

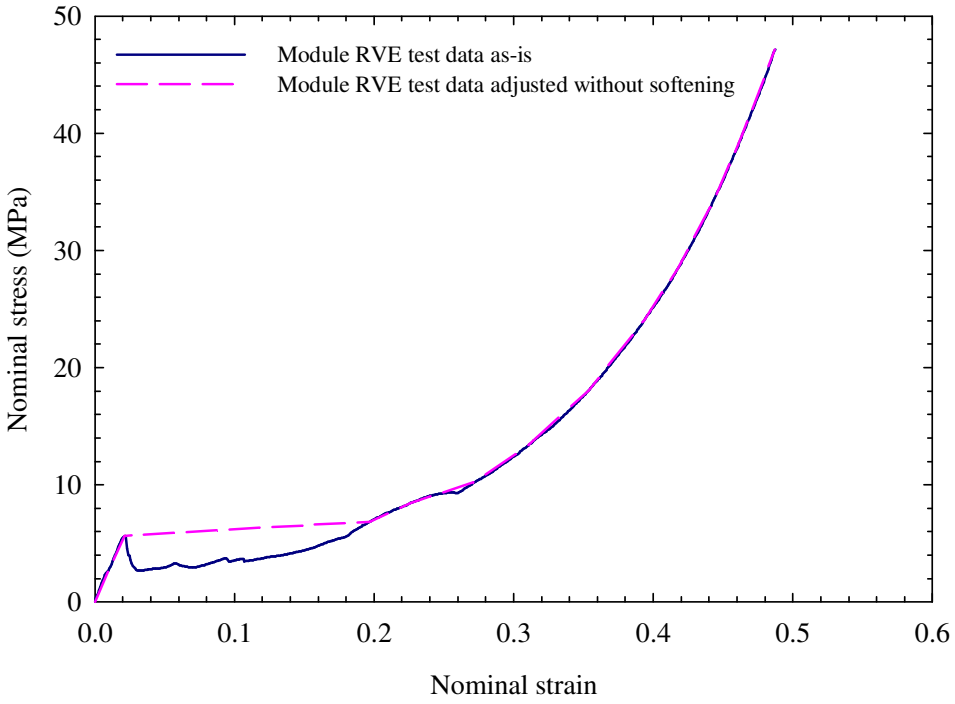

Figure 6.5. Two different sets of material data input for the ABAQUS hyperfoam data fitting. The first one is the test data used "as-is" and the other is adjusted without softening.

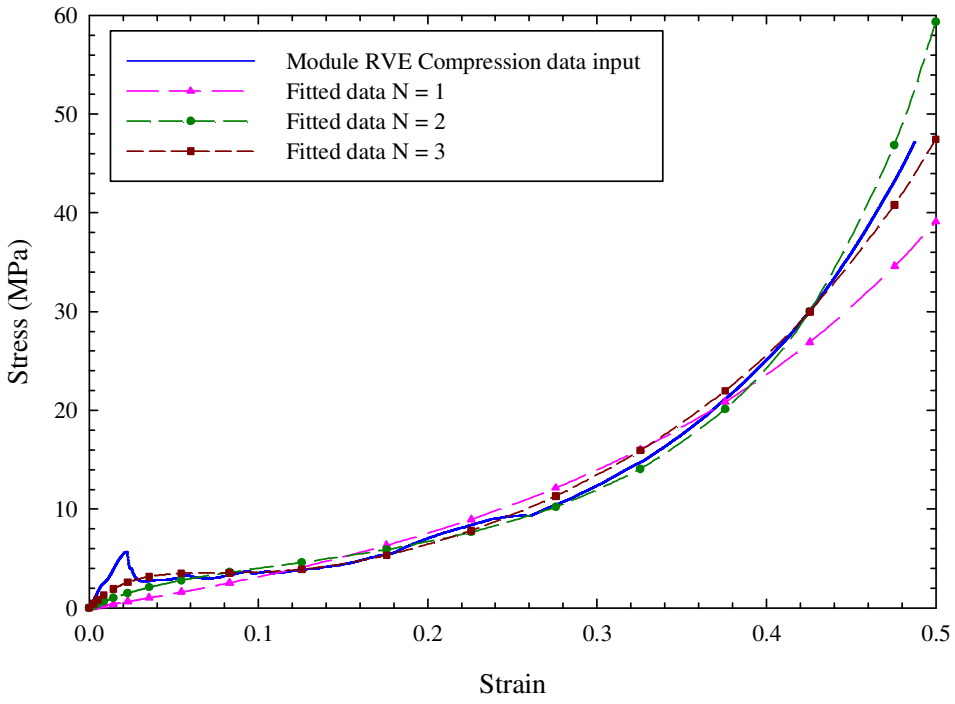
Module RVE Compression data input
Fitted data N = 1
Fitted data N = 2
Fitted data N = 3
Stress (MPa)
Strain
0
10
20
30
40
50
60
0.0
0.1
0.2
0.3
0.4
0.5

(a)

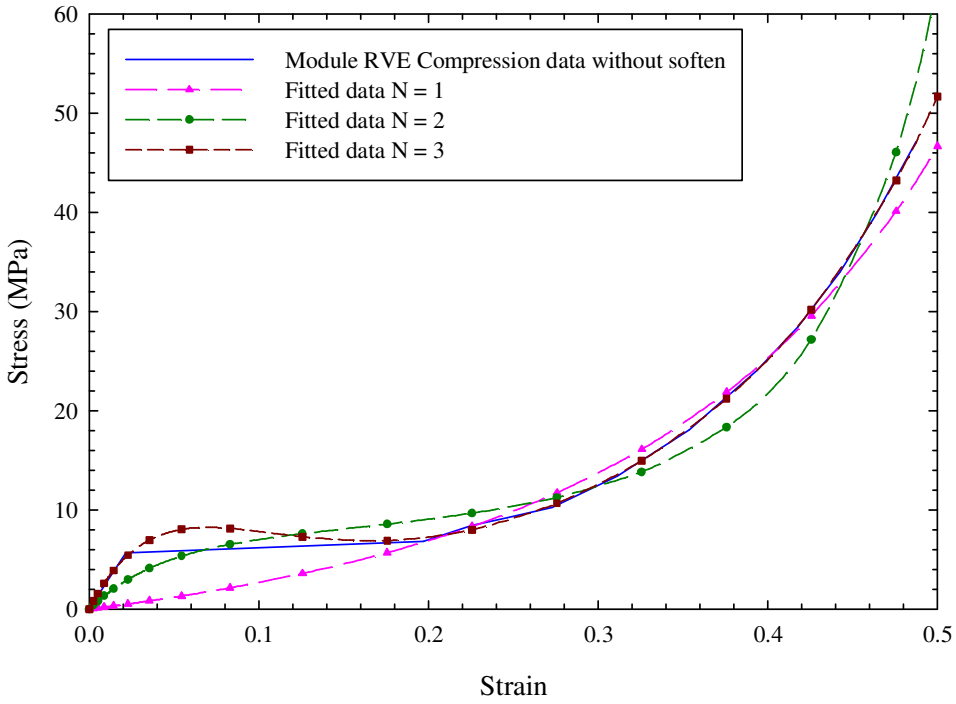

(b)

Figure 6.6. The fitted stress-strain curves by the hyperfoam material model with different values of N for (a) the "as-is" compression test data and (b) the "adjusted without softening" compression test data for a module RVE specimen.

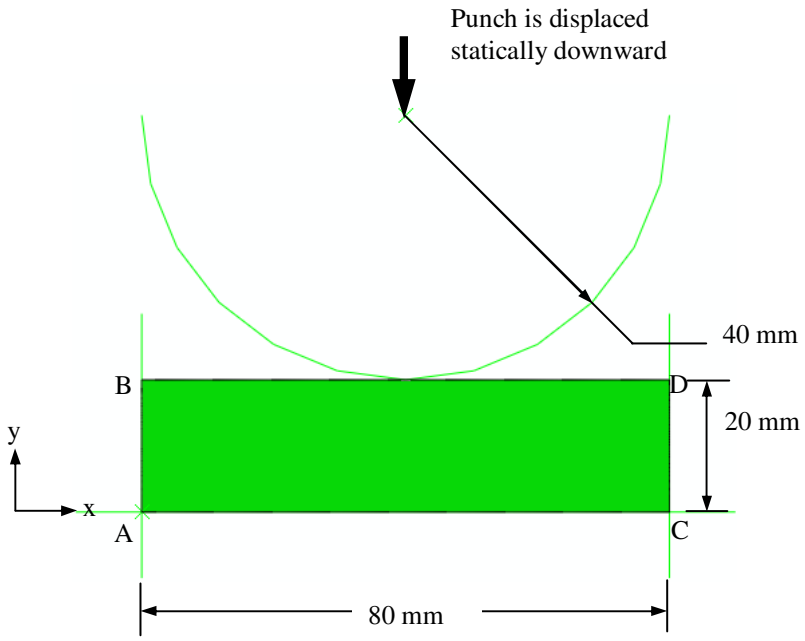

Figure 6.7. A two-dimensional plane strain finite element model for simulation of the quasi-static semicircular punch test using a macro homogenized material model.

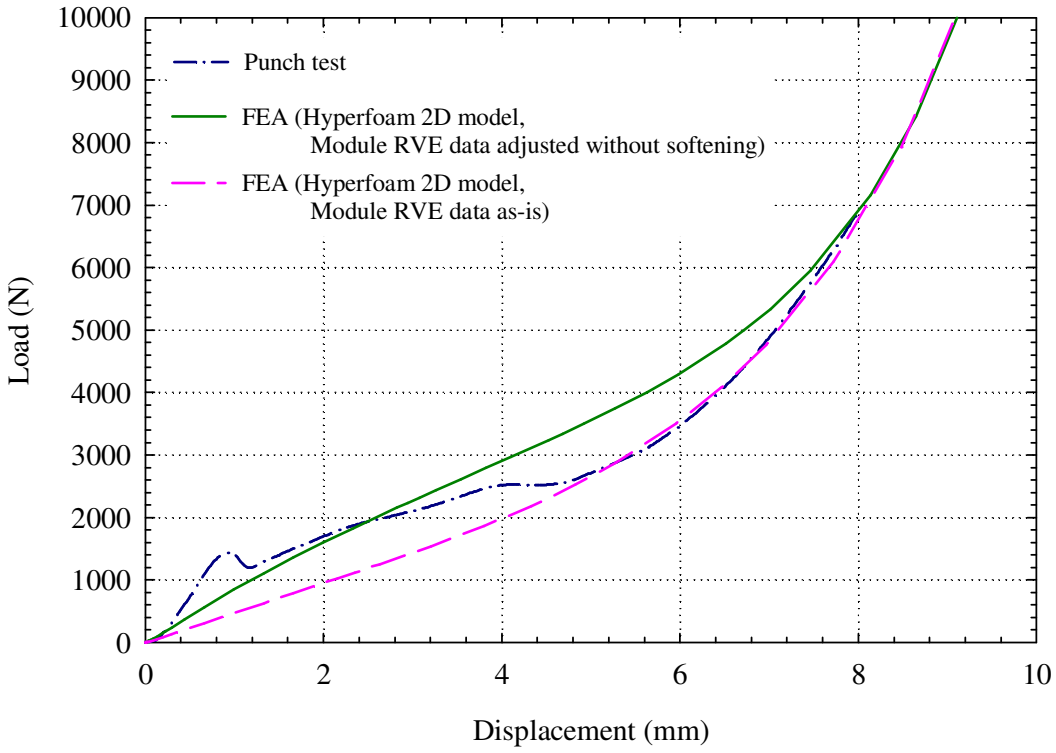

Figure 6.8. The load-displacement curves from the finite element analyses of the quasi-static in-plane semicircular punch test based on the homogenized hyperfoam model and the experimental results.

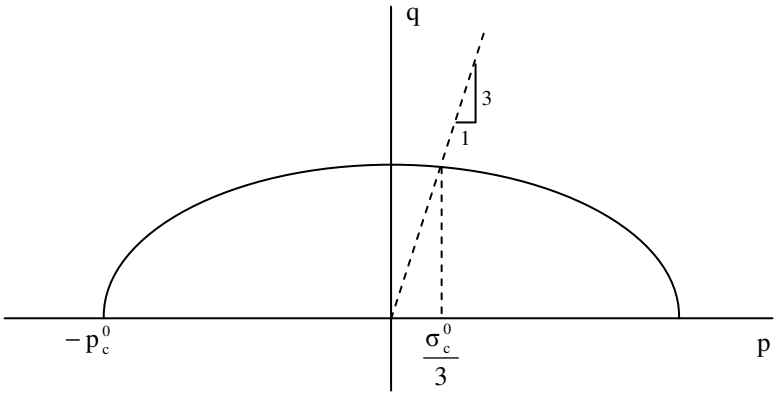

Figure 6.9. A crushable foam model with the yield surface in the *p*–*q* plane [18].

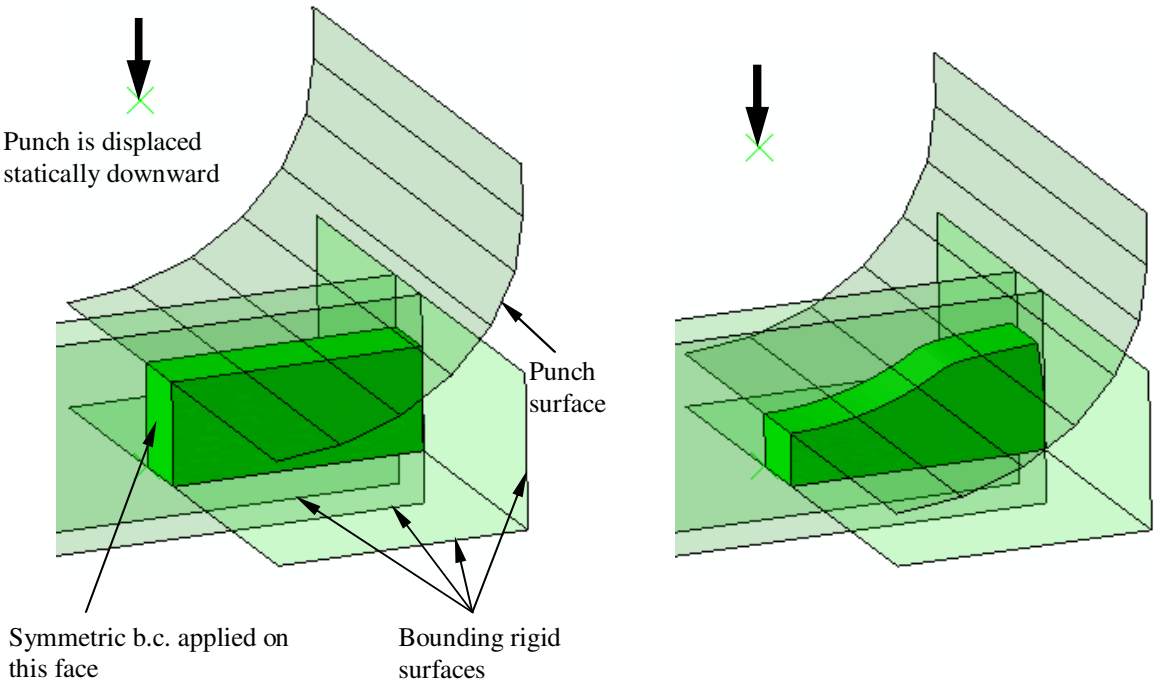

Figure 6.10. (a) A three-dimensional finite element model for the simulation of the quasi-static semicircular punch test using a macro homogenized crushable foam material model, and (b) a deformed view after the punch is displaced statically downward.

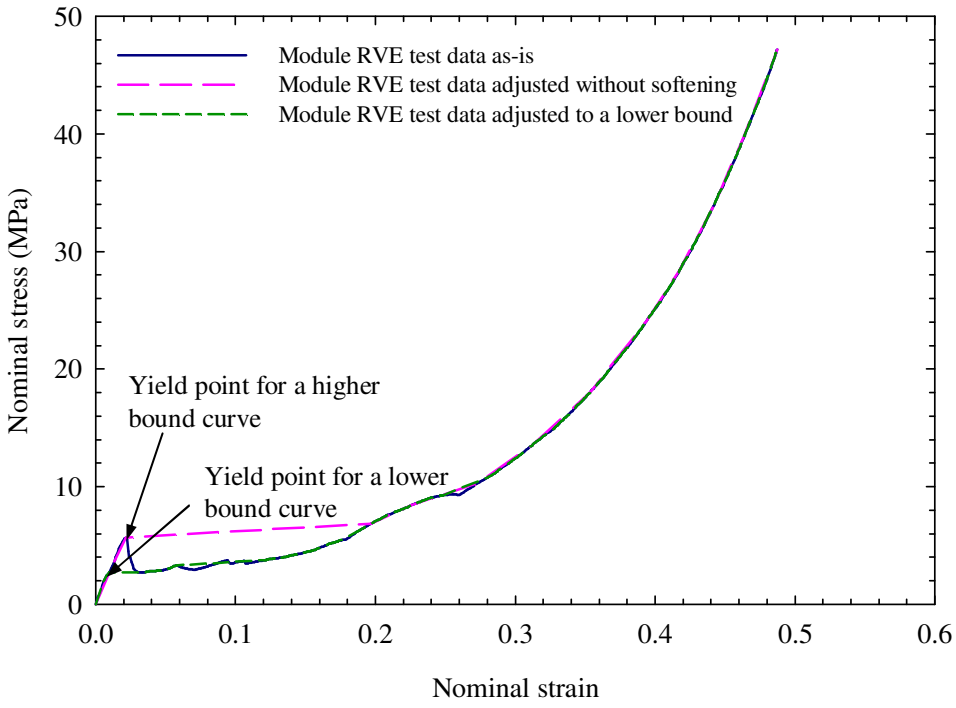

Figure 6.11. Two scenarios are considered here for the elastic-plastic material data input with the test data adjusted in the ascending order. The rise and fall segment due to initial buckling is flattened to a lower bound and a higher bound of the segment.

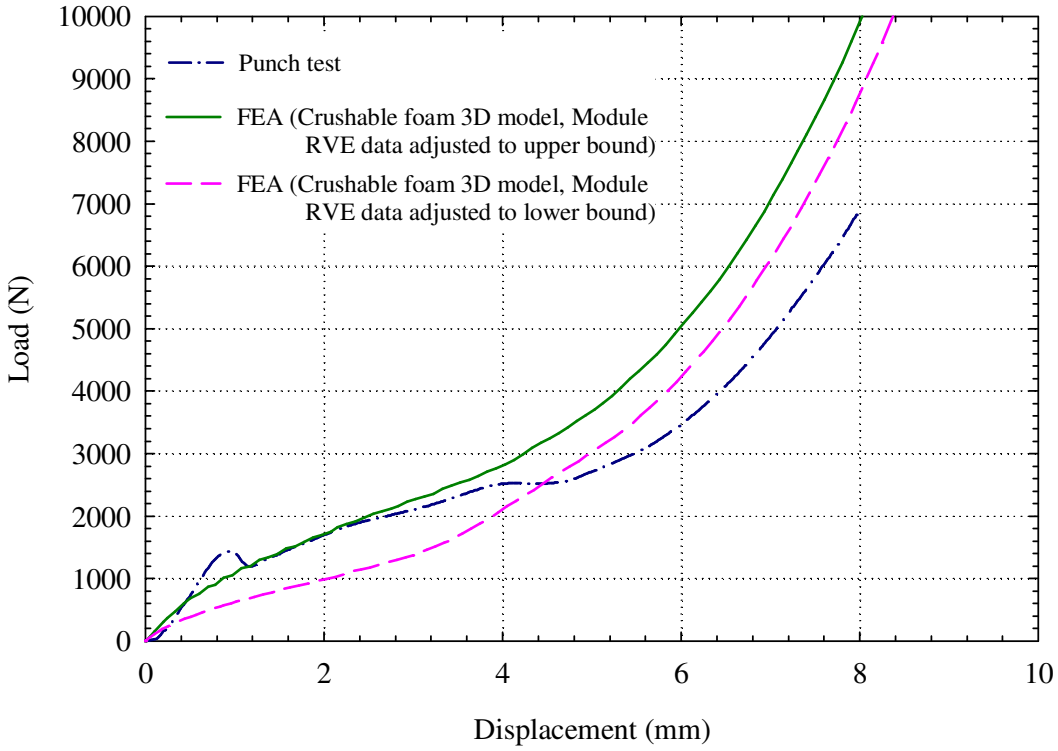

Figure 6.12. The load-displacement curves from the finite element analyses of the quasi-static semicircular punch indentation test based on a crushable foam material model and the experimental results.

Chapter 7
Conclusions

In chapter 2, residual stresses due to single indentation and rolling on a finite plate at very high rolling loads are investigated by two-dimensional plane strain finite element analyses using ABAQUS. In the finite element analyses, the roller is modeled as rigid and has frictionless contact with the finite plate. Finite element analyses with different meshes for single indentation on elastic flat plate under plane strain conditions are first carried out and the results are compared with those of the elastic Hertzian solutions to understand the need of the finite element model for elastic-plastic analyses of indentation and rolling. Then the plate material is modeled as an elastic-plastic power-law strain hardening material with a non-linear kinematic hardening rule for loading and unloading. Finite element analyses with different meshes for single indentation on an elastic-plastic flat plate under plane strain conditions are also carried out to validate the finite element models. Based on the computational models for indentation and rolling at high rolling loads with extensive plastic deformation, the computational results show that the contact pressure distributions are quite different and they are also significantly different from the elastic Hertzian pressure distribution. The computational results for the rolling case show a significantly higher longitudinal compressive residual stress and a lower out-of-plane compressive residual stress along the contact surface when compared to those for the single indentation case. Moreover, the residual stresses at the boundary surfaces due to

rolling are found to be four to five times higher than those of the single indentation case. Also, the longitudinal residual stress distribution under the roller is no longer in self equilibrium due to a length change of the top portion of the plate by rolling and the boundary reaction forces which are no longer negligible compared to those of the single indentation case. The results suggest that the effects of rolling must be accounted for when two-dimensional finite element analyses of crankshaft sections are used to investigate the residual stresses due to fillet rolling of the crankshafts under prescribed loading conditions.

In chapter 3, the differences of the residual stresses due to rolling in a finite elastic-plastic plate by rigid and elastic deformable rollers at very high rolling loads are investigated by two-dimensional plane strain finite element analyses using ABAQUS. In the finite element analyses, the rollers are modeled both as rigid and linear elastic, and have frictionless contact with the elastic-plastic finite plate. The plate material is modeled as an elastic-plastic power-law strain hardening material with a non-linear kinematic hardening rule for loading and unloading. Two new numerical schemes are developed to represent the elastic roller to model the indentation and rolling. The results of the contact pressure and subsurface stress distributions from the two numerical schemes are almost identical. For both roller models, the computational results show that the contact pressure and subsurface stress distributions in the elastic-plastic plate are similar for both indentation and rolling at high rolling loads with extensive plastic deformation. The computational results also indicate that the residual stresses after rolling are nearly the same for both roller models. The computational results suggest that

the rigid roller model can be used to obtain the residual stresses in rolling simulations at very high rolling loads without sacrificing the accuracy.

In chapter 4, residual stress distributions in a rectangular bar due to rolling or burnishing at very high rolling or burnishing loads are investigated by three-dimensional finite element analyses using ABAQUS. First, a roll burnishing experiment conducted at Caterpillar with residual stress measurements are briefly reviewed. In the corresponding finite element analyses, the roller is modeled as rigid and the roller rolls on the flat surface of the bar with a low coefficient of friction. The bar material is modeled as an elastic-plastic strain hardening material with a non-linear kinematic hardening rule for loading and unloading. For rolling loads with extensive plastic deformation, the computational results showed that a higher rolling load does not necessarily always produce higher compressive residual stresses in the desired regions of the bar. The computational results also showed that the longitudinal residual stresses are sensitive to the initial yield stress and the detailed strain hardening assumed at large strains.

In chapter 5, computational models are developed for simulations of representative volume element (RVE) specimens of lithium-ion battery cells under constrained compression tests. First, the load-displacement data and deformation patterns for cell RVE specimens under in-plane constrained compression tests are briefly reviewed. For the corresponding finite element analyses based on ABAQUS, the effective compressive moduli for cell components are obtained from constrained compressive tests, the Poisson's ratios for cell components are based on the rule of mixture, and the stress-plastic strain curve of the cell components are obtained from the tensile tests and the rule of mixture. The Gurson's material model is adopted to account

for the effect of porosity in separators and in the active layers of anodes and cathodes. The results of the computations show that the computational models can be used to examine the micro buckling of the component sheets, the macro buckling of the cell RVE specimens, and the formation of the kinks and shear bands observed in experiments, and to simulate the load-displacement curves of the cell RVE specimens. Based on the computational models, the effects of the friction coefficient between the cell components and the constrained surfaces on the deformation pattern, plastic deformation, void compaction, and the load-displacement curve are identified. Finally, the usefulness of the computational model is demonstrated by further exploring the effects of the initial clearance and biaxial compression on the deformation patterns of cell RVE specimens.

In chapter 6, macro homogenized material models are adopted to model a small-scale lithium-ion battery module specimen under an in-plane constrained punch indentation test. The macro material models are based on the compressive stress-strain curves obtained from the representative volume element (RVE) module specimens under in-plane constrained compression tests. The ABAQUS implicit solver is used for the punch test simulations. The hyperfoam and the crushable foam material models in ABAQUS are adopted to fit the nominal stress-strain curves of the module RVE specimens under in-plane compression. The load-displacement responses of the simulation results based on the hyperfoam and crushable foam material models compare fairly well with the experimental results of the punch test in general. However, the initial yielding and the corresponding plateau of the load-displacement curves of the punch test due to micro buckling could not be modeled distinctively by the macro homogenized models. The computational results show that the material models available in commercial

finite element software can be used to reasonably model lithium-ion battery modules under non-uniform compression loading conditions.